Modeling of complex microcracking in cement based materials by combining numerical simulations based on a phase-field method and experimental 3D imaging

Thanh Tung Nguyen

UNIVERSITÉ PARIS-EST

ÉCOLE DOCTORALE SCIENCE INGÉNIERIE ET ENVIRONNEMENT

THÈSE

présentée pour l'obtention du diplôme docteur de

L'UNIVERSITÉ PARIS-EST

Spécialité: *Mécanique des Matériaux et des Structures*

par

Thanh Tung NGUYEN

Sujet de la thèse :

Modeling of complex microcracking in cement based materials by combining numerical simulations based on a phase-field method and experimental 3D imaging

Version finale

Thèse soutenue le 5 novembre 2015 devant le jury composé de :

C. STOLZ	Directeur de recherche CNRS Ecole Centrale de Nantes	Président
R. De BORST	Professeur Université de Glasgow	Rapporteur
J.Y. BUFFIÈRE	Professeur INSA de Lyon	Rapporteur
J. RÉTHORÉ	Chargé de recherche CNRS INSA de Lyon	Examinateur
C. CHATEAU	Chargée de recherche Ecole des Ponts ParisTech	Encadrante
M. BORNERT	Ingénieur en Chef des Ponts, Eaux et Forêts Ecole des Ponts ParisTech	Co-directeur de thèse
J. YVONNET	Professeur Université Paris-Est Marne-la-Vallée	Directeur de thèse

Acknowledgments

Je tiens tout d'abord à remercier Monsieur Claude STOLZ, qui m'a fait l'honneur de présider le jury de ma soutenance de thèse ainsi que Messieurs Réne de Borst et J.Y BUFFIERE qui ont accepté la longue et lourde tâche d'être rapporteurs de ma thèse. Leurs rapports très détaillés ainsi que leurs remarques et questions très intéressantes ont suscité ma réflexion en ouvrant d'autres perspectives à mon travail. Je tiens également à remercier Monsieur Julien RETHORE qui a examiné mon travail et dont les questions et remarques étaient autant pertinentes que constructives.

Je voudrais remercier vivement mon encadrante, Mademoiselle Camille CHATEAU, pour tes connaissances, tes conseils, tes explications dans la partie expérimentale et traitant d'image, pour tes aides sans limite à la réalisation des essais.

Un grand merci donc à Michel BORNERT, pour sa direction de ce travail de recherche tout au long de ces trois années. Je remercie pour sa confiance, et pour son aide scientifique, ainsi que les nombreuses discussions pour résoudre les problèmes. Ses soutiens et encouragements m'ont permis de mener à bien ce travail.

Je souhaite exprimer ma profonde reconnaissance à mon directeur de thèse, Monsieur Julien YVONNET, qui m'a suivi durant ces trois années de thèse, et aussi dans mon stage en partant des premières notions de la mécanique, avec ses précieux conseils et son encadrement, j'ai pu mener à bien ce travail. Les mots ne peuvent pas exprimer tous ce qu'il a faits pour moi, du fond de mon coeur, je le remercie.

Je tiens aussi à exprimer mon amitié à tous mes collègues et de mes amis qui m'ont beaucoup aidé pendant ma thèse et avec qui j'ai passé de très bons moments.

Je tiens enfin à remercier ma famille pour leur patience et leurs encouragements tout au long de l'élaboration de ce travail.

Abstract

An approach combining numerical simulations and experimental techniques is developed to model complex microcracking in heterogeneous cementitious materials. The proposed numerical model allowed us to predict accurately in 3D the initiation and the propagation of microcracks at the scale of the actual microstructure of a real sample subjected to compression. Its predictions have been validated by a direct comparison with the actual crack network characterized by 3D imaging techniques. In a first part, the numerical simulation tools are developed and tested. More specifically, the phase-field method is applied to microcracking simulations in highly heterogeneous microstructures and its advantages for such simulations are discussed. Then, the technique is extended to account for interfacial cracking, possibly occurring at inclusion/matrix interfaces. In a second part, the experimental methods used and developed in this work are described. The procedures to obtain the evolution of the 3D crack network within the samples by means of X-rays computed microtomography and in-situ mechanical testing are presented. Then, we focus on the developed image processing tools based on digital volume correlation to extract with good accuracy the cracks from the grey level images. In a third part, we compare the predictions of the numerical model with experimental results obtained, first, with a model material made of expanded polystyrene beads embedded in a plaster matrix, and second, to a more complex lightweight concrete. More precisely, we use the experimental data to identify by inverse approaches the local microstructural parameters, and use the experimental displacements measured by digital volume correlation to define boundary conditions to be applied on sub-domains within the sample for the simulations. The obtained direct comparisons of 3D microcrack networks and their evolutions demonstrate the very good predictive capability of the numerical model.

Résumé

Une approche combinant simulation numérique et expérimentation est développée pour modéliser la microfissuration complexe dans des matériaux hétérogènes cimentaires. Le modèle numérique proposé a permis de prévoir précisément en 3D l'initiation et la propagation des microfissures à l'échelle de la microstructure réelle d'un échantillon soumis à un chargement de compression. Ses prévisions ont été validées par une comparaison directe avec le réseau de fissures réel caractérisé par des techniques d'imagerie 3D. Dans une première partie, nous développons et testons les outils de simulation numérique. Plus précisément, la méthode de champ de phase est appliquée pour simuler la microfissuration dans des milieux fortement hétérogènes et ses avantages pour ce type de modélisation sont discutés. Ensuite, une extension de cette méthode est proposée pour tenir compte d'un endommagement interfacial, notamment aux interfaces inclusion/matrice. Dans une deuxième partie, les méthodes expérimentales utilisées et développées au cours de cette thèse sont décrites. Les procédures utilisées pour obtenir l'évolution du réseau de fissures 3D dans les échantillons à l'aide de microtomographie aux rayons X et d'essais mécaniques in-situ sont présentées. Ensuite, les outils de traitement d'image utilisant la corrélation d'images volumiques, pour extraire les fissures des images en niveaux de gris avec une bonne précision, sont détaillés. Dans une troisième partie, les prévisions du modèle numérique sons comparées avec les données expérimentales d'un matériau modèle en billes de polystyrène expansé intégrées dans une matrice de plâtre dans un premier temps, et, dans un second temps, d'un béton léger plus complexe. Plus précisément, nous utilisons les données expérimentales pour identifier les paramètres microscopiques inconnus par une approche inverse, et utilisons les déplacements expérimentaux déterminés par corrélation d'images volumiques pour définir des conditions limites à appliquer sur les bords de sous-domaines dans l'échantillon pour les simulations. Les comparaisons directes de réseaux de microfissures 3D et de leur évolution montrent une très bonne capacité prédictive du modèle numérique.

Contents

List of Figures

.

List of Tables

Chapter 1

Introduction

Contents

1.1 Background and motivations

Modeling the fracture process in civil engineering materials and structures until complete failure is of formidable interest. Even though engineering-oriented rules are available to design concrete structures, predicting the formation of cracking and design the components to avoid failure or damage requires advanced methodologies based on numerical simulations. However, such procedures are far to be integrated, due to many difficulties inherent to the modeling and simulation of crack propagation, to the complex nature of cementitious materials, and to the need to develop experimental procedures to identify the related models.

It has been shown that many macroscopic brittle damage phenomena originate from micro-cracking of the underlying microstructure, leading to a multi-scale problem. An example of cracking problem in a civil engineering structure at three different scales is illustrated in Fig. 1.1, where typical crack networks are shown to range from the microscopic scale of the granular structure of concrete to the macroscopic one of a building. It has been generally accepted

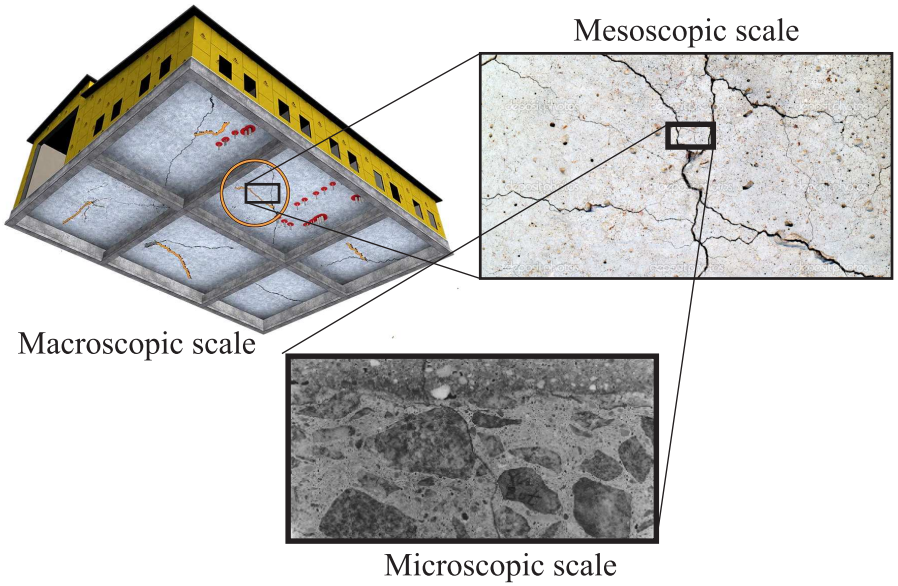

Figure 1.1: Damage phenomena in civil engineering material

that many macroscopic damage phenomena originate from micro-cracking of the underlying microstructure.

Materials like cement, concrete or plaster are quasi-brittle, and in contrast to metallic materials, characterized by very complex microstructures regarding the morphologies, the multiple scales involved, the different fracture processes (matrix cracking, inclusion-matrix decohesion...), the highly stochastic distribution and size of constituents, and possible evolutions due to hydric, thermal and chemical effects.

The use of experimental techniques such as X-ray microtomography [72, 189] setups has been democratized in the recent years and realistic models of microstructures obtained from 3D imaging techniques can now be routinely generated for many materials at various scales. They have allowed to construct realistic microstructural models of materials like concrete, biological tissues (cortical bones), or composites, among many others. Developing damage models for these highly heterogeneous materials, taking into account the real microstructure offers new avenues to predict more accurately fracture processes in related structures. These models are nowadays used in numerical simulations to evaluate linear mechanical and other physical properties of complex materials like bones [191, 56], concrete [232, 175], coke blend [211], filled elastomers [10], among many others.

Unfortunately, because of the possible occurrence of multiple arbitrary branching cracks in such materials, several obstacles remain to develop reliable simulation methods of fracture nucleation and propagation in highly complex heterogeneous materials.

To summarize, the following obstacles remain to develop predictive, micromechanically-based models of fracture propagation in civil engineering materials:

- Develop robust and efficient numerical methods for crack propagation in complex hetero-

geneous brittle materials.

- Develop accurate experimental imaging techniques to follow crack propagation in complex 3D samples to provide reference solutions for the models.
- Develop combined experimental-numerical procedures to analyze and model the fracture process in cementitious materials, using the numerical simulations to identify by inverse approaches parameters of the developed models and to validate them.

The purpose of the present PhD work will be to provide contributions to the above-mentioned challenges.

In this introduction, we will first review available numerical methods for crack propagation modelling in brittle materials. Then, we will review the experimental systems available to characterize damage in such materials at different scales. Finally, an outline of the thesis work will be described.

1.2 Literature review on numerical crack propagation simulation methods for brittle materials

The theoretical methods to predict brittle fractures, like the ones based on the classical Griffith theory [83, 77, 84, 85], have been useful to develop criteria for crack propagation in simple configurations and have shown good predictive capacities with respect to experimental tests in these cases. However, such approaches have the drawback to fail in describing crack initiation or more complex propagation modes like branching. Furthermore, the sharp representation of cracks requires the identification of a crack growth law, which is a complex task in the general case. On the other hand, many numerical simulation methods for crack propagation have been developed in the recent decades, but each faces well-known issues and drawbacks, as presented in the following.

1.2.1 Damage models: smeared cracks representation

One way for describing brittle fracture is to assume a homogenized representation of the damage due to an underlying diffuse propagation of microcracks. In such approaches, damage models with softening [99, 173] are employed. These damage models suffer from strong drawbacks when implemented in numerical solving methods such as the finite element method, like mesh dependency and lack of convergence of the fracture energy as the element size goes to zero [167, 22]. This has been shown to yield from a loss of ellipticity of the associated mechanical problem [210, 117, 36]. To circumvent these issues, regularization schemes must be applied, such as nonlocal damage models [168, 23] and higher-order deformation gradient schemes [165, 125].

Non-local damage models have been proposed in [168]. The key idea of this approach is to introduce an internal length into the constitutive law that may be related to the characteristic

size of the material (i.e. aggregate size). In addition to this added length, the approach creates a non-locality by means of a convolution product of the strain tensor. This regularization remedies the issues of well-posedeness of softening behavior in finite element implementations [100] and related mesh issues. In non-local damage model, the stress-strain relationship is expressed by:

$$\boldsymbol{\sigma} = (1 - d)\mathbb{C} : \boldsymbol{\varepsilon} \tag{1.1}$$

where, $\boldsymbol{\sigma}$ and $\boldsymbol{\varepsilon}$ are the Cauchy stress and strain tensors, respectively and $\mathbb{C}$ is elastic tensor. The damage variable takes a value from 0 (undamage material) to 1 (fully damaged material). The evolution of d is a function of a non-local estimation of the equivalent strain $\overline{\varepsilon}_{eq}$, and is defined in [168] by:

$$\overline{\varepsilon}_{eq}(\mathbf{x}) = \frac{\int_\Omega \phi(\mathbf{x} - \mathbf{s})\varepsilon_{eq}(\mathbf{s})ds}{\int_\Omega \phi(\mathbf{x} - \mathbf{s})ds} \tag{1.2}$$

where $\phi(\mathbf{x} - \mathbf{s})$ is kernel function, depending on an internal length l_c:

$$\phi(\mathbf{x} - \mathbf{s}) = \exp\left(-\left(\frac{2 \parallel \mathbf{x} - \mathbf{s} \parallel}{l_c}\right)^2\right). \tag{1.3}$$

However, such models have the following drawbacks: (a) an incorrect prediction of damage initiation; (b) diffusion of damaged zones after complete failure of the structure; (c) spurious nonlocal interactions across macroscopic cracks; (d) a deficiency to describe fragmentation. A more in-depth review of such difficulties is described in [169].

Gradient-damage models [43, 164] introduce higher-order strain gradient in the constitutive model to regularize the problem of softening in damage FEM problems and remove the mesh issues. However, an important problem for their practical application is the proper experimental determination of the model parameters, which must be computed by inverse analyses.

These models can be used in tandem with finite element deletion techniques, also called "kill-elements" methods (see e.g. [107]), or "elements erosion" [101, 24, 71].

Recently, an alternative of such techniques to brittle materials has been introduced in [161] and called "eigenerosion" method. This technique is mainly based on the *eigenfracture* approach in [194], and converges to Griffith fracture theory as the mesh size converges. However, this method still suffers from mesh sensitivity and still needs to be developed for dynamic fracture.

1.2.2 Direct tracking of the crack front

1.2.2.1 Remeshing methods and related techniques

Sharp description of cracks, and direct tracking of the crack front using the classical theory of brittle fracture, requires very complex remeshing algorithms [96], which are hardly tractable for complex 3D morphologies, or multiple crack fronts. The problem can be alleviated by means of recent local/global meshes superposition [105], or bridging domain/Arlequin methods [68]. To

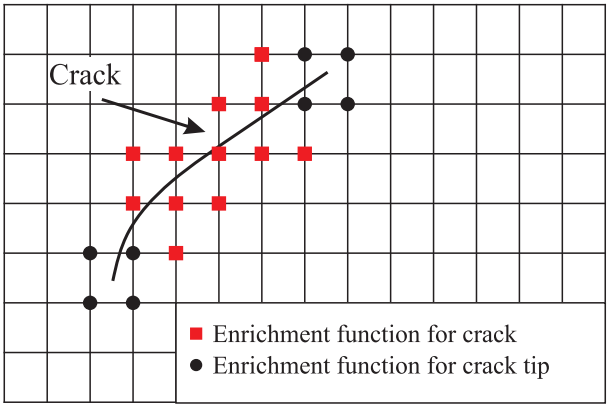

Figure 1.2: Illustration of XFEM discretization for describing sharp cracks.

overcome these difficulties, enriched FEM discretizations or embedded discontinuity techniques have been introduced in the last decades.

1.2.2.2 X-FEM

The eXtended Finite Element Method (XFEM) [208, 149, 150, 63] is a particular case of the Partition of Unity Method (PUM) [135] where the finite element discretization is enriched with additional nodal degrees of freedom, which carry local discontinuous functions, able to describe cracks within elements. Then, cracks can be described accurately in regular or non-conforming meshes, removing the need for continuous remeshing as the crack propagates. In XFEM, the approximation of the displacement field $\mathbf{u}(\mathbf{x})$ is expressed with the presence of n_c cracks and m_t crack tips in the form:

$$\mathbf{u}(\mathbf{x}) = \sum_{I\in S} N_I(\mathbf{x})\mathbf{u}_I + \sum_{N=1}^{n_c}\sum_{I\in S_c} N_I(\mathbf{x})\psi_I^{(N)}\mathbf{a}_I^{(N)} + \sum_{M=1}^{m_t}\sum_{I\in S_t} N_I(\mathbf{x})\sum_{K=1}^{N_K}\phi_{KI}^{(M)}\mathbf{b}_{KI}^{(M)} \tag{1.4}$$

where S is the set of nodes in whole mesh, S_t is the set of nodes of elements containing the crack tip, and S_c is the set of nodes whose support is intersected by the crack. The functions $\psi_I^{(N)}$ and $\phi_{KI}^{(M)}$ are enrichment functions for crack N and crack tip M, respectively, and $\mathbf{a}_I$, $\mathbf{b}_{KI}$ are additional degrees of freedom. Such enriched approximation is illustrated in Fig. 1.2.

However, this technique has shown difficulties to describe crack nucleation and requires level-set function construction to describe the crack, which can be cumbersome when multiple cracks interact. Applications and developments of XFEM for 3D fracture problems can be found e.g. in [150, 82, 216, 94] and in [93] in a multiscale framework. Works involving multiple cracks propagation using XFEM are rare [234, 44]. Some examples of crack branching using XFEM require ad-hoc techniques (see e.g. [203, 25]) and lead to cumbersome algorithms.

1.2.3 Cohesive elements and cohesive layers

Because of its versatility, cohesive zone modeling (CZM) [229, 50, 233] is one of the primary method to handle discrete crack propagation in diverse types of materials. This concept was introduced by Barenblatt [20] and Dugdale [70] to address the stress singularity at a crack tip. In these models, all nonlinearities take place in a cohesive zone ahead of the main crack tip, which is associated with the physical fracture process zone of the material. The cohesive laws have been embedded into finite element analysis in Needleman [153] and Tvergaard and Hutchinson [214] or have been modeled by cohesive finite elements like in Camacho and Ortiz [50], Xu and Needleman [229], and Ortiz and Pandolfi [159], or in a dynamic context by Zhou and Molinari in [233]. An overview of cohesive elements techniques can be found in Chandra et al [54].

1.2.4 Thick level-set

A new method, called Thick Level-Set method (TLS) [151, 27, 53] has been recently introduced to tackle the issue of crack initiation in numerical crack simulations, in which a level-set function is employed to separate the undamaged zone from the damaged one, and where the crack is a consequence of the damage front motion, allowing crack initiation. The damage variable and its evolution are functions of the level-set function. In contrast to crack models, the width of the damage band is here a parameter which is independent from the mesh. This damage models is able to describe complex crack morphologies like branching.

1.2.5 Phase field method

Recently, a new approach for the description of crack propagation has been developed. Starting from the pioneering work of Francfort and Marigo [75], difficulties arising in the classical fracture framework can be overcome by a variational-based energy minimization framework for brittle fracture (see also [39, 166, 38, 48, 16]). An important ingredient of the method relies on a regularized description of the discontinuities related to the crack front: the surface of the crack is replaced by a smooth function, using a Mumford-Shah functional [152], the original functional being substituted by an Ambrosio-Tortorelli approximation [13, 14]. It has been shown that the solution of the associated variational problem converges to the solution of the sharp crack description implying discontinuities, in the $\Gamma-$ convergence sense [129, 41, 42]. The approximation then regularizes a sharp crack surface topology in the solid by a scalar auxiliary variable, interpreted as a phase field describing broken and unbroken parts of the solid. Such a method has the quality that it does not require any prescription of the shape geometry and allows crack nucleation and branching, providing a very robust framework for crack propagation simulation. It has been adapted to quasi-static fracture problems in [38, 37], dynamic crack propagation [40, 92], and in a multiphysic context in [142, 6]. Remarkably, the regularized model may be regarded as a damage model of the gradient type [121, 125, 26, 165, 76] with critical differences in the choice of the free energy and dissipation function. Recently, the problem of cohesive

fracture has been reformulated in the context of phase field [217].

The phase field method has been used successfully for describing 2D and 3D quasi-static fracture [142, 138, 143, 110, 109], dynamic crack propagation [40, 32, 31, 193], cracks in media undergoing finite strains [140], brittle fracture under multiphysics environment [137, 141] and applied to cohesive fracture [218, 220].

In this work, we have choosen this numerical technique because of its various advantages over other above mentioned methods:

1. Its ability to describe arbitrary crack front in 2D and 3D, without sensitivity to the mesh.
2. The possibility to easily handle crack initiation.
3. Its simplicity in implementation.
4. Its robustness for handling softening, due to the its damage gradient nature.
5. Its consistency with Griffith theory in the $\Gamma-$ convergence sense.

We have used the computational framework as proposed by Miehe et al. [142] and have developed some extensions and original applications.

1.3 Review of some experimental methodologies for damage characterization in materials and structures

Damage characterization methods can be classified into destructive and non-destructive testing (NDT). Non-destructive methods are more efficient and usefull, so this section will mostly focus on them. Their advantage is their ability to follow damage evolution during a mechanical loading.

1.3.1 Damage characterization methods at macroscopic structure or sample scale

Several methods have been developed to study the cracking of a structure at macroscopic or sample scale. These include Acoustic Emission (AE), ultrasonic methods, vibration-based methods and thermography. In this subsection, we will present their principle and several applications on damage characterization.

1.3.1.1 Acoustic emission (AE)

AE refers to the generation of transient elastic waves produced by a sudden redistribution of stress in a material [225]. This changing stress field can be attributed to growth in structural damage. In practice, this technique relies on the use of one or several piezoelectric sensors which are placed against the sample, and a electronic systems that records the electronic pulses that are induced in these sensors by the transient waves. Pulses (or so-called acoustic events) can

be characterized by various quantities such as energy, length, number of peaks, etc A detailed analysis of these features for a given material might allow to identify the type of damage that induced the event. Prosser et al. [171] used AE to detect damage in crossly graphite/epoxy composite test specimens. Wevers [225] noted that AE provided good capabilities to identify fiber breakage, delaminations, matrix cracking, and debonds in a loaded composite as compared to other conventional nondestructive evaluation techniques.

Acoustic emission can provide local information on damage mechanisms such as reinforcement cracking but the precise identification of the damage for which a signal is detected often requires destructive observations. The AE technique has been successfully applied to damage detection in various materials such as metals, alloys, concrete, polymers and other composite materials. Localization of damage is possible by the use of several sensors, and the accurate analysis of the temporal shifts of the events recorded on these sensors. In the most advanced setups, spatial accuracy can be of the order of one millimeter in centimetric samples. In the work of Fortin et al [73, 74], this method has been used to localize the compaction bands (a mode of damage) in sandstone. The author noted that the elastic wave velocities are very sensitive to the presence of cracks, and can be used to detect formation of new cracks. Recently, AE has been applied to detect the initiation of compaction bands in the work of Stanchits et al [199]. However, an accurate characterization of damage phenomena in heterogeneous material at micro scale is hardly possible with such technique because of its low spatial resolution.

1.3.1.2 Ultrasonic Methods

Ultrasonic testing is based on high energy acoustic waves generated using a pulser receiver and transducer in frequency ranges typically between 1 and 50 MHz (contrary to X-ray testing that uses electromagnetic waves). The analysis of transmitted and/or reflected waves allows to detect in the bulk of the materials, various sources of mechanical heterogeneity, among which cracks or porosities. The ultrasonic transducer can be operated in contact or non-contact mode and in either pulse echo or through-transmission modes. The advantage of this arrangement is that any potential flaw location is interrogated from a variety of angles, maximizing the probability that it can be detected.

This method has been used to identify flaw existence and to determine their geometric dimensions, and characterize material properties [108, 181]. It is also applied to detect defects in many materials, for example in welds [86] and concrete [9]. A relative follow-up of damage can be performed but it is at present difficult to have a quantitative assessment of the damage from ultrasonic indications. A recent work [104] shows a first investigation of quantitative evaluation of distributed damage in concrete. However, for a real structure with complex geometry, this method is quasi inapplicable, because the recorded signals become too complex for specific echoes to be readily identified, especially small echoes typical of those scattered from damage.

1.3.1.3 Vibration-based methods

This method is based on changes in the dynamic behavior. More specifically, it relates changes in modal parameters such as natural frequency, mode shape, and damping to the mass, stiffness, and damping parameters associated with a structure. Mechanical damage (e.g., cracks, delamination, and loose bolts) can change stiffness and/or damping. Therefore, measurement of their dynamic characteristics (that is the natural frequencies and damping of a structure) is a technique for damage detection.

Vibration-based methods was found to be more effective than ultrasonic attenuation or radiographic transmission methods. Many works in literature have applied this technique to study structures and materials, e.g. in the form of resin-bound shear cracks [8]. Cawley and Adams [52] located defects in composite structures (macroscopic scale) using changes in natural frequencies through a detailed sensitivity analysis study. Yao [231] reviewed the techniques used at that time for studying structural damage and reliability assessment.

1.3.1.4 Thermography

Thermal methods define another family of techniques used to detect damage. Thermography [95] is based on the detection and measurement of the infrared range of the electromagnetic spectrum emitted from objects. Thanks to the different thermal properties of structural components and defects, they have mainly different specific heat constants, thermal diffusivity, and thermal conductivity. This difference is amplified when the components are hotter. Thermal wave propagation methods such as lock-in thermography [188] and pulsed thermography [128] have been used to detect delaminations, corrosion, surface cracks, and voids. Combined approaches such as vibrothermography where thermal wave propagation is used in conjunction with elastic wave propagation, has been used to effectively detect microcracks [136]. When compared with other classical NDT techniques such as ultrasonic or X-Rays, the thermal method is more safe. It can work non intrusive, non contact and in a fast manner (from a fraction of a second to a few minutes depending in the configuration). However, this technique allows only the detection of relatively shallow subsurface defects (a few millimeters in depth). It is also limited in terms of spacial resolution and is not adapted for a detection of damage at a microstructural scale, even though some recent investigations into this direction have shown some potential of thermography for the thermoemecanical analysis of metals at grain scale [29].

1.3.2 Damage characterization methods at microstructural scale

Several methods have been used to study the microcracking of a materials. These mainly include three broad approaches: (a) Impregnation techniques,and post-mortem surface or bulk observations; (b) methods based on optical observation and/or scanning electron microscopy to detect the damage phenomena at the surface of samples; (c) X-ray computed tomography to characterize the damage in the bulk of the materials.

1.3.2.1 Impregnation techniques

Impregnation techniques are among oldest techniques used to study damage at microstructural scale in materials like concrete. In this method, samples are impregnated with a fluorescent dye or epoxy resin to facilitate detection and identification of cracks, which are expected to fill the whole open portal space and replace water that might be present. After polymerization of the resin, samples are cut and/or polished for a surface observation with optical methods or electron microscopy. The dye provides a contrast in the images which permits the detection and identification of cracks, and eventually a quantitative analysis of the crack network with appropriate image analysis tools. In order to reduce difficulty in viewing cracks in dense microstructures, a fluorescent dye was used by [106]. However, pre drying of the specimen in an electric oven before impregnation, which could alter the specimen condition, remained a major inhibition to this process. Methods developed by [81, 201] overcome drying of the specimen by using counter diffusion method for the replacement of pore water by a dye-impregnated organic solution. However, this process could increase the duration of the test. Nevertheless, Bisschop et al [28] and other studies have indicated that the impregnation of the whole sample and then cutting thin samples from fully impregnated samples would introduce less microcracks. Specimen preparation techniques involve cutting, drying, lapping, grinding, and polishing. Improper handling of these operations results in induction of additional microcracks. Impregnation of sample with Wood metal has also been proposed in [155] to characterize cracks at a small scale in an SEM. This technique however raises similar questions about the perturbation of the crack network by the impregnation process or the sample preparation.

1.3.2.2 Optical Microscopy and Scanning Electron Microscopy

Digital images from a sample surface can be recorded at various scales by a macroscopic optical camera, an optical microscope or a scanning electron microscope. These images can be analyzed for detection of microcracks and quantified to determine the density of cracks and other features of the crack network. The microstructural observations are mainly based on both last methods, their principles and several applications to study microcracking will be presented bellow.

Optical microscope (OM)

Optical microscopy (OM) is one of the favored techniques for observation of damage at microstructural scale [205]. With this instrument, the image is recorded either in grey level or in full color mode. Because of the inherent limitations of its physical principles, the spatial resolution of optical microscopy is limited to a few tens of micrometers making it a more suitable technique for observing features with typical sizes of several micrometers, within regions of interest with millimetric sizes, or larger.

Optical microscopy can be used for ex-situ or post-mortem analyses (see next section for a more detailed explanation of these concepts), in particular after impregnation as explained in previous section. In this context, specimens prepared by thin−sectioning and fluorescent

microscopy techniques can be viewed under the optical microscope with the use of reflected ultraviolet lights. The image acquisition was performed in [106] by placing a Tri−CCD camera linked to a personal computer acquisition system; in the obtained color images, the fluorescent dye exhibits a color very different from the surrounding cement based materials, so that the crack extraction by image processing could be performed very efficiently.

A more efficient use of optical microscopy for the analysis of the evolution at microstructural scale of a network of cracks under mechanical loading conditions consists in combining it with in-situ testing devices. Various configurations can be used to combine mechanical testing and optical observation, including the use of small specifically designed tensile stages that fit on the sample holder of a standard microscope, or conversely, the use of a custom optical microscope that fits on a standard tensile test machine.

Optical microscopy methods have thus been chosen for many applications due to their reasonably high spatial resolution, high sensitivity, fast imaging capability, compatibility with various sample environments (including control of temperature or humidity) and their non-contacting nature. It has for instance been used recently for the investigation of hydromechanical behaviour of clayey rocks in [35], or the study of a porous carbonate, Estaillades limestone, in [62]. In these studies, crack initiation and propagation could be detected at the surface of the samples. The recourse to image processing tools like digital image correlation (described later in this manuscript) often facilitates the detection of such phenomena.

However, optical microscopy techniques have a shallow depth of field and limited resolution capacity, so that a highly smooth and polished surface is required to produce a sharp focused image with this technique. These limitations are overcome with scanning electron microscopy.

Scanning Electron Microscopy (SEM)

Scanning electron microscopy (SEM) is one type of electron microscopy which images a sample by scanning it with a beam of electrons in a raster scan pattern. This technique is based on the interaction between the incident electrons and the atoms at and near the sample's surface [174], producing various signals that can be used to obtain information about the surface topography and composition. Many types of signals generated by these interactions can be recorded to produce images: back-scattered electrons, secondary electrons, X-rays,... The two most used signals in SEM are secondary electrons (resulting from inelastic electron-sample collisions) and back-scattered electrons (elastic interaction of incident beam electrons with sample). The secondary electrons mode image contains typically the topography information of the sample surface, and back-scattered electrons image can provide an information about the distribution of different chemical elements in the sample. Images of SEM can be obtained with very high special resolution, with a pixel size that can be of the order of 1 nm in recent high end SEMs equiped with a Field Emission electron Gun. The advantage of the SEM is its great depth of field in comparison of the light microscope. Observations can be made over a much wider range of magnifications including those above the range of light microscopes.

SEMs have a variety of applications in a number of scientific and industry-related fields,

especially where characterizations of materials is beneficial. Again, damage mechanisms can be characterized by SEM imaging either within a post-mortem or an ex-situ protocol, or in combination with in-situ mechanical testing. In the latter case, specifically designed micro-testing devices that fit into the chamber of the SEM are required. It is noted that, unless recent so-called "environmental" SEM techniques are used, only materials that are not sensitive to the secondary vacuum conditions of the SEM chamber can be analyzed this way. Diamond et al [147] used the SEM to observe the growth of surface cracks in mortar during loading, or to analyze the fracture mechanism of concrete in [154]. This technique is also applied to study damage in various materials as in geomaterial [222] or in composites like SiC/SiC [55]. Recently, Das et al [61] used SEM to investigate the influence of elongated metallic iron particulate reinforcements on the propagation of cracks in cementitious mortars.

However, two strong disadvantages of both OM and SEM investigations are that only surface damage is documented and that special sample preparation procedures are required, which might have an influence on the mechanical response of the material.

Image Processing Techniques

As already noticed, we can use SEM and OM coupled with various characterization testing protocols as *post-mortem, in-situ,...* (as described in next subsection) to observe damage evolution. An important step after image acquisition by OM/SEM is the processing of the microstructural image to obtain a qualitative/quantitative analysis of the sample. Many techniques have been developed in literature to this aim. Darwin et al [60] researched quantification of microcracks of cement mortar samples by the backscatter electron technique of the scanning electron microscope. The identification of cracks was based on local changes in grey level. A line scan was taken perpendicular to the images for the identification of potential cracks. Soroushian et al [197] used segmentation of images from grey level to binary images by using the thresholding approach for viewing microcracks in concrete samples. Roli [178] and Hatada et al.[87] considered the direction of cracks as a feature in a local window and then attempted to detect cracks on granite slabs and drains. Fujita et al. [78] proposed two preprocessing methods using a subtraction method and a Hessian matrix. Since the used local window was fixed, these methods cannot be flexibly applied to different widths. Among these techniques, digital image correlation (DIC) is one of the most efficient and versatile tool. This procedure is based on the comparison of images acquired at different stages of a mechanical test and provides qualitative and quantitative descriptions of local responses. The principles of this technique will be presented in Chapter 4. DIC could be used instead of, or in addition to the prevailing methods to detect defects, by observing the singularity due to the change in the strain distribution, or a step jump in the displacement field across the cracks. Many works in literature have applied this technique to study fracture mechanics [133, 5, 176, 183, 215, 62], crack growth [131, 170]. This technique allows local information to be obtained on the mechanical behaviour of materials, not only at the macroscopic scale but also the microscopic one, e.g. on micromechanisms such as strain localisation, damage localisation, crack initiation and propagation [180].

However the main limitation of these observations and measurements is that they are relative to the outer faces of the specimen and could be a poor approximation of what occurs in the bulk of the sample, unless additional analyses are performed to confirm the accuracy of surface measurements with respect to 3D behavior.

1.3.3 X-ray computed tomography and in-situ testing

X-ray computed tomography (XR-CT) is a nondestructive characterization technique which provides images of the bulk of the materials. The principles of this technique will be presented in Chapter 4. The benefits of 3D maps to characterize internal structures led to a rapid adaptation of this technique to many fields including materials science, in particular for the study of damage phenomena. Moreover, X-ray tomography is particularly effective to get 3D quantitative information concerning each step of the damage.

Because X-ray tomography is a non-destructive technique, many scans of the same sample can be made under different conditions. As a consequence, a wide variety of mechanical tests have been coupled with X-ray tomography characterization [202]. Indeed several procedures can be considered to investigation the evolutions of a material under mechanical load.

Post-mortem characterization: This procedure consists in performing the same test on many specimens and stopping these test at different stages to follow evolution of the material. Samples are then imaged after unloading and, if necessary, specific preliminary preparation (such as impregnation, cutting or polishing). Evolution of damage can be assessed by a comparison, in terms of statistical quantities, of the observed damage in the set of samples. This procedure assumes that the material does not change from one specimen to another.

Ex-situ characterization: A unique specimen is tested up to a given level of deformation. It is thereafter unloaded and imaged. It is then mounted again on the testing device, loaded up to a next deformation level, unmounted and imaged again. This procedure can be repeated several times. This procedure assumes that the unloading process and interruption of the deformation do not influence the test. The test can be performed on only one sample. This provides a strong advantage of this procedure compared with the *post-mortem* procedure. However, as sample are observed in their unloaded stage, cracks might be closed and hard to detect.

In-situ characterization: This procedure is similar to *ex-situ*, but the sample is here loaded in a device, which is placed on the X-ray beam. Therefore, during scanning, the state of sample is kept constant (deformation is stopped and maintained constant). The detail of this procedure will be presented in Chapter 4.

The combination of XR-CT with the above testing procedure has been applied to study damage phenomena in many works. Buffière et al [47] used X-ray synchrotron phase contrast microtomogrphy to characterize damage in metal matrix composites material. The work of Babout et al [18] has introduced the detection of damage initiation in metallic materials. This technique was used to examine damage in civil engineering materials (mortar, concrete, cement paste)[111, 113, 126, 163], that were observed under mechanical loading. These work aimed at

establishing a the quantitative relationships between internal damage of sample and external load on specimen. Especially in the study [114], by coupling load-deformation response with crack surface areas determined from an analysis of the tomographic image, several fracture parameters could be identified, e.g fracture toughness. In the application for polymer composites, XR-CT has been used to study 3D woven composites [67, 127], to assess the damage in composite laminates arising from drilled holes [212] and to examine micro-damage mechanisms in uni-directional laminates [228, 192].

Crack evolutions under fatigue loading conditions, including closure phenomena, have also been studied by XRCT combined with in-situ fatigue testing. Stock et al [200] investigate how the topology of the fracture surface of AlLi alloy determines the onset and extent of closure during unloading from the maximum load. A number of crack closure studies have followed for various material, e.g. cast iron [122, 123], Ti-SiC [226]. The application of this technique to study crack growth rate has been introduced in the work of Buffiere et al [46, 45], Authors looked at the morphology of cracks and correlated this to the crack growth rate of longer cracks as a function of fatigue cycling. XR-CT is also capable to quantify separately the nucleation of new cavities [115], their growth and finally their coalescence [116]. This technique has also renewed the interest of the experimental study of ductile damage during tensile deformation at room and high temperature in engineering materials.

XR-CT is particularly interesting when most of the damage development occurs within the bulk of the studied material (e.g., nucleation, growth and coalescence of damage in 3D experiments). Many techniques have been developed in literature to characterize quantitatively damage. Among these techniques, Digital Image Correlation (or Digital Volume Correlation in 3D) is more and more used. By measuring the displacement field, this technique is used to evaluate crack crack closure and crack propagation [122]. It can also be used to extract fracture parameters e.g. stress intensity factors [185], energy release rates [130]... Damage mechanisms and their quantification have been reported for particulate composites by resorting to DVC analyses [89, 91].

To date, the study of cracking phenomena in concrete at micro scale in 3D is still under development. In this work, XR-CT imaging combined with compression tests will be used to characterize damage on EPS concrete (or plaster) sample. The obtained CT images are analyzed by image processing based on DVC to localize micro cracks within microstructure and to investigate their evolution.

1.4 Outline of the thesis

The outline of this thesis is as follows.

In a first part, we develop numerical simulation tools based on the phase field method to model microcracking in voxel-based models of complex microstructures.

In Chapter 2, the phase field method is introduced and described in details. Then, a shifted

algorithm is proposed to decrease computational times. The numerical method is then validated on several benchmarks and applied for the first time to our knowledge to XR-CT image-based models of real cementitious materials, characterized by highly complex microstructures, some obtained in this work through our XR-CT system. We show the capability of the phase field method to be applied to such complex microstructural models and its advantages in voxel-based models simulations of crack propagation.

In Chapter 3, we propose an extension of the phase field method for handling interfacial damage, and appropriate algorithms to describe interfacial decohesion in voxel-based models of microstructures. More specifically, the formulation that we propose does not imply additional variables for describing the displacement jump at the interfaces and permits the use of the phase field as an internal variable for describing the irreversible damage of interfaces. Benchmarks for validation and applications to microcracking in complex microstructures are proposed.

In a second part, we describe the experimental imaging and testing procedures used to provide the experimental data and construct the initial models for the numerical simulations.

In Chapter 4, a procedure to manufacture sample of plaster containing EPS beads is described. The objective is to obtain a benchmark specimen, which can be used to validate the numerical tool developed in part I. The new set-up for compression test and sample preparation with several enhancement are introduced to optimize condition for a true uni axial compression test. They will be used to perform the in-situ test combined with XR-CT. We present also the procedures to determine elastic properties of plaster using compression tests monitored with a digital image correlation (DIC) method. The results of this chapter will be analyzed in Chapter 5 and Chapter 8.

In Chapter 5, we propose a novel approach for the detection of cracks in the CT images of an expanded polystyrene (EPS) light-weight concrete sample under compressive loading. The crack network and its evolution through the heterogeneous microstructure can be characterized by an adapted "DVC-assisted image subtraction" techniques, with the capacity to detect very tiny cracks, decohesion in the porous region and provide a good reference to compare the crack evolution at different loading steps. The new method can be a generic and promising experimental tool to detect the crack initiation and propagation in any heterogeneous material.

In a third part, we develop procedures combining the simulations and the experiments for constructing the initial numerical models from the experimental XR-CT images, for describing the boundary conditions to be applied on sub-volumes within simulations from 3D image correlation, for inverse identification of material parameters of the model, and for validation of the numerical simulations.

In Chapter 6, we study by numerical simulation the influence of experimental conditions defects (lack of parallelism, roughness on the faces of the sample...) to correct the experimental conditions and obtain crack morphologies within the samples that can be compared with the simulations. Then, a method using 3D image correlation is described to provide experimental kinematic boundary conditions to be applied on sub-volumes of sample to address cases where

the whole sample cannot be meshed with microstructural details.

In Chapter 7, we validate the phase field method by comparing the simulation results of simple 2D tests on plaster samples, where experimental data are available from previous works [179]. We provide direct qualitative and quantitative predictions of crack initiation levels and crack propagation (length) which show the very good accuracy of the method to describe cracking in brittle materials.

Finally, we provide in Chapter 8 direct comparisons between numerical simulations and experimental results of 3D crack propagation in heterogeneous brittle cementitious materials. First, plaster samples with embedded EPS beads are considered. The experimental XR-CT images are first used to construct the initial models, and then the recorded 3D crack evolution obtained from the in-situ test within the XR-CT is compared with the obtained numerical simulations. Then we provide similar comparisons in much more complex cases of lightweight concrete, where 3 phases are involved. There, a sub-volume is studied using the above-mentioned techniques to again provide direct comparisons of 3D crack propagation between experiments and numerical simulations using phase field.

Finally, some conclusions and perspectives are drawn.

Part I

Numerical modeling of crack propagation

Chapter 2

A phase field method to simulate crack nucleation and propagation in strongly heterogeneous materials from direct imaging of their microstructure

---

Contents

The main content of this chapter has been adapted from our published paper [158].

2.1 Introduction

The numerical simulation of crack propagation in highly heterogeneous materials is a very challenging problem. Recently, the use of experimental techniques such as X-ray microtomography [72] has allowed to construct realistic microstructural models of material like concrete, biological tissues (cortical bones), or composites, among many others. Developing damage models for these highly heterogeneous materials taking into account the real microstructure offers new avenues to predict more accurately fracture processes in related structures and is of formidable interest in engineering.

The challenges and difficulties of microcracking in highly complex materials, as well as a review of available numerical techniques for crack propagation simulation, have been reviewed in Chapter 1. Furthermore, the advantages of the phase field method over other techniques has been discussed.

In this chapter, crack propagation in highly heterogeneous microstructures, such as segmented X-ray CT images of real material, which are used as direct input of the simulations, is investigated by means of the phase field method, which here follows the algorithmic framework proposed by Miehe et al. [138, 143]. To increase the computational efficiency of the method, a modified shifted algorithm has been introduced, to compute the strain tensor split which leads to a very simple and fast algorithm. The advantages of such an approach are demonstrated for crack nucleation and propagation in voxel based models. Several applications to 2D and 3D images of porous cement-based materials are provided.

The overview of this chapter is as follows. In sections 2.2 and 2.3, the main idea and thermodynamic foundations of the phase field method such as presented in Miehe et al. [138, 143] are reviewed. In section 2.4, the computational and algorithmic framework based on finite elements is presented. A shifted strain tensor split algorithm is introduced to simplify the treatment of damage, assumed to be only induced by the tensile strain, to provide an efficient algorithm. Finally, numerical examples are presented in section 2.7.

2.2 Regularized representation of free discontinuities

Let $\Omega \subset \mathbb{R}^D$ an open domain describing a cracked solid, with D the space dimension and $\partial\Omega$ its boundary. Let Γ a curve of dimension $D-1$ within Ω (see Fig. 3.7). In a regularized framework, the crack geometry is approximated by a smeared representation defined by a scalar parameter $d(\mathbf{x})$, $\mathbf{x} \in \Omega$, taking a unit value on Γ and vanishing away from it. It can be shown (see e.g. [138]) that such a function can be determined by solving the following boundary value problem on Ω:

$$\begin{cases} d - l^2 \triangle d = 0 \ \text{ in } \Omega, \\ d(\mathbf{x}) = 1 \ \text{ on } \Gamma, \\ \nabla d(\mathbf{x}) \cdot \mathbf{n} = 0 \ \text{ on } \partial\Omega, \end{cases} \tag{2.1}$$

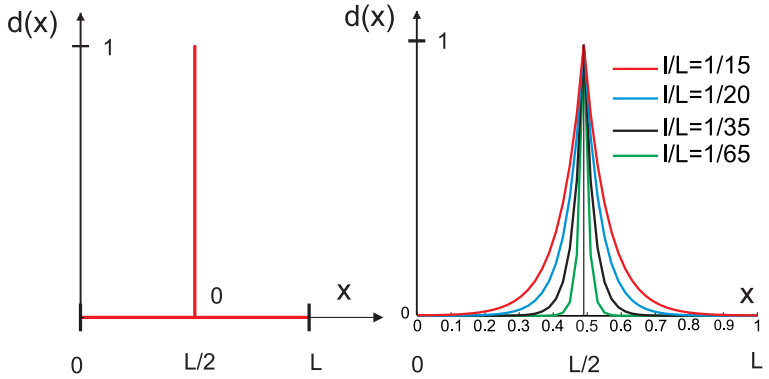

(a) (b)

Figure 2.1: Regularized representation of a crack: one dimensional case: (a) sharp crack model, taking unitary value of $d(x)$ at $x = x_\Gamma = L/2$ (crack); (b) regularized representation through phase field.

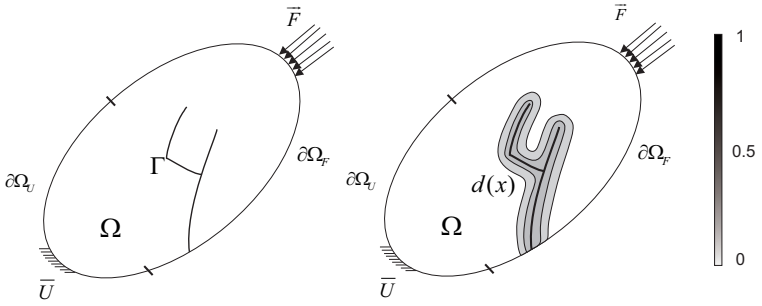

(a) (b)

Figure 2.2: Regularized representation of a crack: two-dimensional case: (a) sharp crack model; (b) regularized representation through phase field.

where $\Delta(.)$ is the Laplacian, l is a regularization parameter describing the actual width of the smeared crack, and $\mathbf{n}$ the outward normal to $\partial\Omega$. A one-dimensional illustration of this

concept is depicted for different widths l in Fig. 2.1. In two and three dimensions, the solution of (2.1) produces a smooth representation of the crack morphology (see Fig. 3.7(b)). It can be shown that (2.1) is the Euler-Lagrange equation associated with the variational problem:

$$d(\mathbf{x}) = Arg\left\{\inf_{d\in\mathcal{S}_d}\Gamma_l(d)\right\}, \tag{2.2}$$

with $\mathcal{S}_d = \{d|d(\mathbf{x}) = 1 \text{ on } \Gamma\ \forall\mathbf{x}\in\Gamma\}$ and where

$$\Gamma_l(d) = \int_\Omega \gamma(d,\nabla d)d\Omega \tag{2.3}$$

represents the total crack length. In (2.3), $\gamma(d,\nabla d)$ denotes the crack density function per unit volume, defined by:

$$\gamma(d,\nabla d) = \frac{1}{2l}d^2 + \frac{l}{2}\nabla d\cdot\nabla d. \tag{2.4}$$

The $\Gamma-$ limit [41] of the principle (2.5) gives:

$$\lim_{l\to 0}\left\{\operatorname*{Inf}_{d\in\mathcal{S}_d}\Gamma_l(d)\right\} = |\Gamma|\,. \tag{2.5}$$

The variation of Γ_l is defined as:

$$\delta\Gamma_l = \frac{\partial\Gamma_l}{\partial d}\cdot\delta d\int_\Omega\left(\frac{\partial\gamma}{\partial d}\delta d + \frac{\partial\gamma}{\partial\nabla d}\nabla\delta d\right)d\Omega \tag{2.6}$$

Then, by using the integration by parts, we obtain:

$$\delta\Gamma_l = \int_\Omega\left(\frac{\partial\gamma}{\partial d} - \nabla\frac{\partial\gamma}{\partial\nabla d}\right)\delta d d\Omega + \int_S \mathbf{n}\cdot[\![\nabla d\delta d]\!]_\Gamma\, dS \tag{2.7}$$

suppose that d is continuous, so δd is continuous. Therefore, the variation of Γ_l include a volume distribution and another of surface distribution:

$$\frac{\partial\Gamma_l}{\partial d} = \frac{\partial\gamma}{\partial d} - \nabla\frac{\partial\gamma}{\partial\nabla d} + \mathbf{n}\cdot[\![\nabla d]\!]_\Gamma\,\delta S \tag{2.8}$$

We denote the density of volume distribution:

$$Y_c(d) = \frac{d}{l} - l\Delta d. \tag{2.9}$$

2.3 Review of the Phase field method

2.3.1 Regularized variational framework

The variational approach to fracture mechanics provided by Francfort and Marigo [75] introduces the following energy functional for cracked body:

$$E(\mathbf{u},\Gamma) = E_u(\mathbf{u},\Gamma) + E_s(\Gamma) = \int_{\Omega\setminus\Gamma} W_u(\boldsymbol{\varepsilon}(\mathbf{u}))d\Omega + g_c\mathcal{H}^{d-1}(\Gamma) \tag{2.10}$$

where W_u is the strain energy density function, $\boldsymbol{\varepsilon} = \frac{1}{2}\left(\nabla \mathbf{u} + \nabla \mathbf{u}^T\right)$, $\mathbf{u}$ is the displacement field, g_c is the fracture toughness, and $\mathcal{H}^{d-1}$ is the Hausdorff surface measure giving the crack length ($d = 2$) or surface ($d = 3$). The term $E_u(\mathbf{u}, \Gamma)$ represents the elastic energy stored in the cracked body, and $E_s(\Gamma)$ is the energy required to create the crack according to the Griffith criterion. Then, the state variables are the displacement field $\mathbf{u}$ and the geometry of the crack Γ. In a regularized framework (phase field method), fracture energy is regularized by the crack density function $\gamma(d, \nabla d)$ and the strain energy is replaced by energy of damageable material $W_u(\boldsymbol{\varepsilon}(\mathbf{u}), d)$, the above functional is substituted by the functional:

$$E(\mathbf{u}, d) = \int_\Omega W_u(\boldsymbol{\varepsilon}(\mathbf{u}), d) d\Omega + g_c \int_\Omega \gamma(d) d\Omega, \tag{2.11}$$

where $\gamma(d)$ is defined by (2.4). The total energy is then rewritten as $E = \int_\Omega W d\Omega$ in which

$$W = W_u(\boldsymbol{\varepsilon}(\mathbf{u}), d) + g_c \gamma(d) \tag{2.12}$$

2.3.2 Basics of thermodynamics and evolution of phase field

Assuming isothermal process, the Clausius-Duhem inequality states that:

$$\phi = \boldsymbol{\sigma} : \dot{\boldsymbol{\varepsilon}} - \dot{W} \geq 0 \tag{2.13}$$

where $\boldsymbol{\sigma}$ is the Cauchy stress and ϕ is the dissipation. We can re-write (2.13) as:

$$\boldsymbol{\sigma} : \dot{\boldsymbol{\varepsilon}} - \frac{\partial W}{\partial \boldsymbol{\varepsilon}} : \dot{\boldsymbol{\varepsilon}} - \frac{\partial W}{\partial d}\dot{d} = \left(\boldsymbol{\sigma} - \frac{\partial W}{\partial \boldsymbol{\varepsilon}}\right) : \dot{\boldsymbol{\varepsilon}} - \frac{\partial W}{\partial d}\dot{d} \geq 0. \tag{2.14}$$

It follows that if no damage occurs, i.e. for $\dot{d} = 0$, then $\phi = 0$ and

$$\boldsymbol{\sigma} = \frac{\partial W}{\partial \boldsymbol{\varepsilon}} = \frac{\partial W_u}{\partial \boldsymbol{\varepsilon}} \tag{2.15}$$

A reduced form of the Clausius-Duhem inequality can be re-written as:

$$-\frac{\partial W}{\partial d}\dot{d} \geq 0 \tag{2.16}$$

The damage parameter d is an increasing function, i.e $\dot{d} \geq 0$, the E.q.(2.16) become:

$$F = -\frac{\partial W}{\partial d} = -gc\left(\frac{d}{l} - l\Delta d\right) - \frac{\partial W_u}{d} = Y - g_c Y_c(d) \leq 0 \tag{2.17}$$

where $Y = -\frac{\partial W}{\partial d}$, and Y_c is defined in E.q. (3.22). F is here the thermodynamic force associated with d

With the conditions on the discontinuous surfaces for $d \neq 1$:

$$[\![d]\!]_\Gamma = 0, \qquad \mathbf{n} \cdot [\![\nabla d]\!]_\Gamma = 0 \tag{2.18}$$

and on the boundary $\partial\Omega$

$$\mathbf{n} \cdot \nabla d = 0 \tag{2.19}$$

Dissipation due to crack propagation is regularized by $g_c \Gamma_l$, while the total dissipation due to damage is defined by:

$$D_m = -\int_\Omega -\frac{\partial W_u}{\partial d} \dot{d} \geq 0 \tag{2.20}$$

This definition corresponds to quality of the dissipation rest on an equilibrium trajectory, when $\dot{d} \geq 0$:

$$\frac{\partial E}{\partial d} \dot{d} = \frac{d}{dt} \Gamma + \frac{\partial W_u}{\partial d} \dot{d} = 0 \tag{2.21}$$

which corresponds to the classical expression of the dissipation:

$$D_m = -\int_\Omega \frac{\partial W}{\partial d} \dot{d} d\Omega = \frac{d}{dt} \Gamma_l \tag{2.22}$$

The integration of a local normality law based on Y is now defined by:

$$F(Y, d) = Y - g_c Y_c(d) \leq 0, \quad \dot{d} \geq 0, \quad F\dot{d} = 0 \tag{2.23}$$

For $\dot{d} > 0$, $F = 0$ which gives:

$$F = -\frac{\partial W_u(\mathbf{u}, d)}{\partial d} - g_c Y_c(d) = 0. \tag{2.24}$$

2.3.3 Unilateral contact formulations

In what follows, we review several models for handling unilateral contact in cracks, to prevent interpenetration in compression mode.

2.3.3.1 Modified deviatoric fractures model

This model has been proposed for the first time in the work of Ramtani et al. [172], and applied to predict the behaviour of rocks up to failure in the work of Comi [57]. This model has been used in the regularized framework for brittle fracture of Amor et al. [16]. The main idea is to decompose the trace of the strain tensor into positive and negative parts:

$$\operatorname{tr} \boldsymbol{\varepsilon} = \langle \operatorname{tr}(\boldsymbol{\varepsilon}) \rangle_+ + \langle \operatorname{tr}(\boldsymbol{\varepsilon}) \rangle_- \tag{2.25}$$

where the operator $\langle x \rangle_+ = (x + |x|)/2$ and $\langle x \rangle_- = (x - |x|)/2$. Then, it is assumed that damage is created by expansion or shear. The strain energy density function then reads:

$$W_u(\mathbf{u}, d) = \{g(d) + k\} \left(\frac{\lambda + 2\mu}{2n} \langle \operatorname{tr}(\boldsymbol{\varepsilon}) \rangle_+^2 + \mu \boldsymbol{\varepsilon}_{dev} : \boldsymbol{\varepsilon}_{dev} \right)$$

$$+\frac{\lambda+2\mu}{2n}\langle \mathrm{tr}(\boldsymbol{\varepsilon})\rangle_-^2+\mu\boldsymbol{\varepsilon}_{sph}:\boldsymbol{\varepsilon}_{sph}. \tag{2.26}$$

where $n=2$ for 2D case, and $n=3$ for 3D case.

However, in general this model is not able to avoid material interpenetration in proximity of the crack when combined compression and shear loading are involved.

2.3.3.2 Tensile fractures

Use of computing the eigenvalues of the elastic strain tensor to separate compressive and tensile parts of the strain has been introduced, e.g. in [162]. The application of this assumption to concrete material is discussed in the work of Contrafatto et al [58]. Following the work of Miehe [139], we have adopted this model in this thesis work. In that case, the strain density energy function is given by:

$$W_u(\mathbf{u},d)=\Psi^+(\boldsymbol{\varepsilon}(\mathbf{u}))\{g(d)+k\}+\Psi^-(\boldsymbol{\varepsilon}(\mathbf{u})). \tag{2.27}$$

The strain field is then decomposed into extensive and compressive modes as

$$\boldsymbol{\varepsilon}=\boldsymbol{\varepsilon}^+ +\boldsymbol{\varepsilon}^- \tag{2.28}$$

and

$$\Psi^+(\boldsymbol{\varepsilon})=\frac{\lambda}{2}\left(\langle Tr(\boldsymbol{\varepsilon})\rangle_+\right)^2+\mu Tr\left\{\left(\boldsymbol{\varepsilon}^+\right)^2\right\}, \tag{2.29}$$

$$\Psi^-(\boldsymbol{\varepsilon})=\frac{\lambda}{2}\left(\langle Tr(\boldsymbol{\varepsilon})\rangle_-\right)^2+\mu Tr\left\{\left(\boldsymbol{\varepsilon}^-\right)^2\right\}, \tag{2.30}$$

where

$$\boldsymbol{\varepsilon}^+=\sum_{i=1}^{D}\langle\varepsilon^i\rangle_+\mathbf{n}^i\otimes\mathbf{n}^i,\quad \boldsymbol{\varepsilon}^-=\sum_{i=1}^{D}\langle\varepsilon^i\rangle_-\mathbf{n}^i\otimes\mathbf{n}^i. \tag{2.31}$$

where ε^i and $\mathbf{n}^i$ are the eigenvalues and eigenvectors of $\boldsymbol{\varepsilon}$, i.e. satisfying $\boldsymbol{\varepsilon}\mathbf{n}^i=\varepsilon^i\mathbf{n}^i$.

2.3.4 Thermodynamics and phase field equations

In what follows we derive the equation governing the evolution of the phase field $d(\mathbf{x})$, here used as a damage variable.

The degradation function $g(d)$ in (2.27) is assumed to have the simple form:

$$g(d)=(1-d)^2. \tag{2.32}$$

The function $g(d)$ has been chosen such that $g'(1)=0$ to guarantee that the strain energy density function takes a finite value as the domain is locally cracked (see e.g. [41]) and $g(0)=1$ to guarantee that the material is initially undamaged, $g(1)=0$ is limit for fully damaged. The quadratic function is chosen here $g(d)=(1-d)^2$, that is the simplest case to ensure the existence

of a solution regular in the sense of Carfagni. Alternatively the quartic function, and the cubic function are introduced in the work of Karma et al [103], Borden [30]. The small parameter $k << 1$ is introduced to maintain the well-posedness of the system for partially broken parts of the domain. It follows that if $\dot{d} > 0$ then the thermodynamic force F associated to $\dot{d}$ is given by:

$$F = 2(1-d)\Psi^+ - g_c Y_c(d). \tag{2.33}$$

As $2(1-d)\Psi^+ \geq 0$, then

$$Y_c(d) \geq 0, \quad \text{if } \dot{d} \geq 0. \tag{2.34}$$

Expressing the variation of crack length:

$$\frac{d}{dt}\Gamma_l = \int_\Omega Y_c(d)\dot{d}d\Omega, \tag{2.35}$$

we can check that due to (2.34)

$$\dot{\Gamma}_l \geq 0, \tag{2.36}$$

satisfying non-reversible evolution of cracks.

In addition, to handle loading and unloading histories, Miehe et al. [138] introduced the strain history functional:

$$\mathcal{H}(\mathbf{x},t) = \underset{\tau\in[0,t]}{max}\left\{\Psi^+(\mathbf{x},\tau)\right\} \tag{2.37}$$

which is substituted to Ψ^+ in (3.21). It yields the following phase field problem to be solved to evaluate the field $d(\mathbf{x},t)$ at time t, using (3.22):

$$\begin{cases} 2(1-d)\mathcal{H} - \frac{g_c}{l}\left\{d - l^2\Delta d\right\} = 0 \ \text{ in } \Omega, \\ d(\mathbf{x}) = 1 \ \text{ on } \Gamma, \\ \nabla d(\mathbf{x})\cdot\mathbf{n} = 0 \ \text{ on } \partial\Omega. \end{cases} \tag{2.38}$$

A viscous regularization was proposed in [138]. However, in the present work we have not used it.

2.4 Finite element discretization and simplified algorithm

In this section we derive the weak forms associated to mechanical and phase field problems and their Finite Element discretizations.

2.4.1 Phase field problem

2.4.1.1 Weak form

Starting from $(2.38)_1$, multiplying by a test function δd and integrating over Ω, we obtain:

$$\int_\Omega \left\{ 2(1-d)\mathcal{H}\delta d - \frac{g_c}{l}\left(d - l^2\Delta d\right)\delta d \right\} d\Omega = 0. \tag{2.39}$$

Using the property:

$$(\Delta d)\ \delta d = \nabla\cdot(\nabla d\delta d) - \nabla d\cdot\nabla(\delta d) \tag{2.40}$$

and the divergence theorem, Eq. (2.39) is rewritten as:

$$\int_\Omega \left\{ 2(1-d)\mathcal{H} - \frac{g_c\ d}{l} \right\} \delta d - \int_\Omega g_c l\nabla d\cdot\nabla(\delta d)\ d\Omega$$

$$+ \int_{\partial\Omega} g_c l\nabla d\cdot\mathbf{n}\delta d\ d\Gamma = 0 \tag{2.41}$$

Using (2.38_3), we finally obtain:

$$\int_\Omega \left\{ \left(2\mathcal{H} + \frac{g_c}{l}\right) d\delta d + g_c l\nabla d\cdot\nabla(\delta d) \right\} d\Omega = \int_\Omega 2\mathcal{H}\delta d d\Omega. \tag{2.42}$$

In the present work, the computations are performed in quasi-static conditions. Then, the time steps introduced in the following actually refer to load increments. Introducing a time stepping, the problem to be solved at time t^{n+1} is expressed by seeking $d(\mathbf{x}) \in \mathcal{S}_d$, such that:

$$\int_\Omega \left\{ \left(2\mathcal{H}_n + \frac{g_c}{l}\right) d_{n+1}\delta d + g_c l\nabla d_{n+1}\cdot\nabla(\delta d) \right\} d\Omega = \int_\Omega 2\mathcal{H}_n\delta d d\Omega.$$

$$\forall \delta d(\mathbf{x}) \in H_0^1(\Omega). \tag{2.43}$$

where $\mathcal{H}_n = \mathcal{H}(\mathbf{u}_n)$ is computed from the previous time step by:

$$\begin{cases} \mathcal{H}_{n+1}(\mathbf{x}) = \Psi_{n+1}^+(\mathbf{x}) & \text{if } \Psi_{n+1}^+(\mathbf{x}) > \Psi_n^+(\mathbf{x}), \\ \mathcal{H}_{n+1}(\mathbf{x}) = \Psi_n^+(\mathbf{x}) & \text{if } \Psi_{n+1}^+(\mathbf{x}) \le \Psi_n^+(\mathbf{x}). \end{cases} \tag{2.44}$$

Note that Eq. (2.44) is the algorithmic counterpart of Eq. (2.37).

2.4.1.2 FEM discretization of phase field problem

In this work, 2D and 3D problems are considered. For 2D problems, a mesh of linear 3-node triangles has been employed, while for 3D problems regular meshes with 8-node trilinear elements have been used. For the sake of clarity, only 2D FEM discretization is detailed. The phase field and phase field gradient are approximated in one element by

$$d(\mathbf{x}) = \mathbf{N}_d(\mathbf{x})\mathbf{d}_i \quad \text{and} \quad \nabla d(\mathbf{x}) = \mathbf{B}_d(\mathbf{x})\mathbf{d}_i, \tag{2.45}$$

where $\mathbf{d}_i$ are the nodal values of $\mathbf{d}_{n+1}$.

The same discretization is employed for the variations:

$$\delta d(\mathbf{x}) = \mathbf{N}_d(\mathbf{x})\delta\mathbf{d}_i \quad \text{and} \quad \nabla\delta\mathrm{d}(\mathbf{x}) = \mathbf{B}_\mathrm{d}(\mathbf{x})\delta\mathbf{d}_\mathrm{i} \tag{2.46}$$

where $\mathbf{N}_d(\mathbf{x})$ and $\mathbf{B}_d(\mathbf{x})$ are vectors and matrices of shape functions and of shape functions derivatives for scalar fields, respectively. Introducing the above FEM discretization in (2.4.1.1) results into a linear system of equations:

$$\mathbf{K}_d\mathbf{d} = \mathbf{F}_d \tag{2.47}$$

where $\mathbf{d}$ is the vector containing all nodal phase field variables,

$$\mathbf{K}_d = \int_\Omega \{(\frac{g_c}{l} + 2\mathcal{H}_n)\mathbf{N}_d^T\mathbf{N}_d + g_c l\mathbf{B}_d^T\mathbf{B}_d\}d\Omega \tag{2.48}$$

and

$$\mathbf{F}_d = \int_\Omega 2\mathbf{N}_d^T\mathcal{H}_n d\Omega. \tag{2.49}$$

In (2.48), $\mathcal{H}_n$ is evaluated at the Gauss points by (2.44).

2.4.2 Displacement problem

2.4.2.1 Weak form

The weak form associated with the displacement problem is found by solving the variational problem:

$$\mathbf{u}(\mathbf{x}) = Arg\left\{\inf_{\mathbf{u}\in\mathcal{S}_u}\left(E(\mathbf{u},d) - W^{ext}\right)\right\} \tag{2.50}$$

where $\mathcal{S}_u = \left\{\mathbf{u}|\mathbf{u}(\mathbf{x}) = \bar{\mathbf{u}} \text{ on } \partial\Omega_u, \ \ \mathbf{u}\in H^1(\Omega)\right\}$ and $W^{ext} = \int_\Omega \mathbf{f}\cdot\mathbf{u}d\Omega + \int_{\partial\Omega_F}\overline{\mathbf{F}}\cdot\mathbf{u}d\Gamma$ with $\mathbf{f}$ and $\overline{\mathbf{F}}$ body forces and prescribed traction over the boundary $\partial\Omega_F$. We obtain the classical weak form for $\mathbf{u}(\mathbf{x})\in\mathcal{S}_u$:

$$\int_\Omega \boldsymbol{\sigma} : \varepsilon(\delta\mathbf{u})d\Omega = \int_\Omega \mathbf{f}\cdot\delta\mathbf{u}d\Omega + \int_{\partial\Omega_F}\overline{\mathbf{F}}\cdot\delta\mathbf{u}d\Gamma \ \forall\delta\mathbf{u}\in H_0^1(\Omega), \tag{2.51}$$

where $\boldsymbol{\sigma} = \frac{\partial W_u}{\partial\boldsymbol{\varepsilon}}$ is given using (2.27) and (2.32), by:

$$\boldsymbol{\sigma} = \left((1-d)^2 + k\right)\left\{\lambda\left\langle Tr\boldsymbol{\varepsilon}\right\rangle_+\mathbf{1} + 2\mu\boldsymbol{\varepsilon}^+\right\} + \lambda\left\langle Tr\boldsymbol{\varepsilon}\right\rangle_-\mathbf{1} + 2\mu\boldsymbol{\varepsilon}^-. \tag{2.52}$$

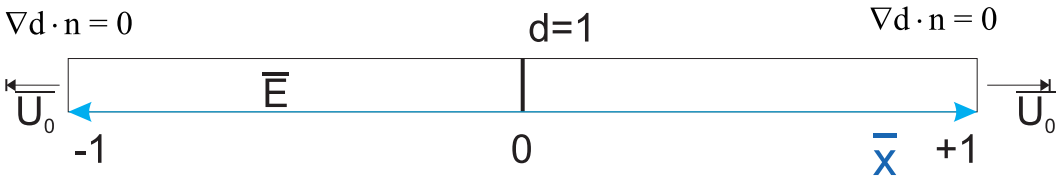

Figure 2.3: 1D problem to analyze the analytical solution: Geometry and boundary condition

2.5 Analytical solution of the one dimensional problem

In this section, we provide analytical solution for the phase field problem in one dimensional domain $\Omega = \mathbb{R}^1$ containing a crack in its middle section is considered, as depicted in Fig. 2.11. The material is assumed elastic and brittle, with Young's modulus E.

To arrive at the dimensionless formulation, we first setting the space variable x as well as the regularization length l are scaled by the macroscopic dimension L of the considered body, according to:

$$\overline{x} = \frac{x}{L}, \quad \overline{l} = \frac{l}{L} \tag{2.53}$$

the macroscopic dimension L is defined as:

$$L = \frac{g_c}{c_h E} \tag{2.54}$$

where the non-dimensional constant c_h is used to control the scaling of the problem (c_h is usually chosen such that the size of the elements in the mesh have an area equal to one yields good results [32]). The material parameter is chosen $\overline{E} = 1/c_h$ and $g_c = 1$. The displacement and the strain is here defined by

$$\overline{u} = \frac{u}{L} \quad \text{and} \quad \overline{\varepsilon} = \frac{d\overline{u}}{d\overline{x}}. \tag{2.55}$$

The boundary problem is defined by:

$$\begin{cases} \frac{d\sigma}{d\overline{x}} = 0 \\ \sigma = (g(d) + k)\overline{E}\overline{\varepsilon} \quad \text{with} \quad \overline{\mathrm{u}}(\pm 1) = \pm \overline{\mathrm{u}}_0 \\ 2(1-d)\Psi^+ - \frac{g_c}{\overline{l}}\left(\overline{l}^2 \frac{d^2 d}{d\overline{x}^2} - d\right) = 0 \quad \text{with} \quad \frac{dd}{d\overline{x}}(\pm 1) = 0. \end{cases} \tag{2.56}$$

In the case of monotonic traction load, $\Psi^+ = \Psi = \overline{E}\overline{\varepsilon}^2/2$ and from $(2.56)_3$ we have:

$$(1-d)\overline{\varepsilon}^2 + \frac{g_c}{\overline{l}}\left(\overline{l}^2 \frac{\partial^2 d}{\partial \overline{x}^2} - d\right) = 0. \tag{2.57}$$

2.5.1 Solution of initial state

At initial state the load is zero, so $\overline{\sigma} = 0$, $\overline{\varepsilon} = 0$. We assume the parameter k to be equal to zero, . Then, the problem (2.57) is reduced to:

$$\begin{cases} \bar{l}^2 \frac{d^2 d}{\partial \overline{x}^2} - d = 0 \\ \frac{dd}{d\overline{x}}(\pm 1) = 0 \\ d(\overline{x} = 0) = 1. \end{cases} \tag{2.58}$$

The solution of this problem is given by

$$d(\pm\overline{x}) = \cosh\left(\frac{\overline{\mathrm{x}}}{\bar{\mathrm{l}}}\right) \pm \coth\left(\frac{1}{\bar{\mathrm{l}}}\right) \sinh\left(\frac{\overline{\mathrm{x}}}{\bar{\mathrm{l}}}\right). \tag{2.59}$$

When $\bar{l} \to 0$ then

$$d \to e^{-|\overline{x}|/\bar{l}}. \tag{2.60}$$

The solution (2.60) only depends on $\overline{x}$ and on the regularization parameter $\bar{l}$. When $\bar{l} \to 0$, the discrete solution is recovered, i.e. $d(\overline{x} = 0) = 1$.

2.5.2 Monotonic tensile loading

The problem (2.57) is considered under monotonic tensile loading. We assume here that $\bar{l} \ll 1$. We consider only the positive part, the kinematic relation is defined by the following:

$$\begin{cases} \overline{\varepsilon} = \dfrac{\partial \overline{u}}{\partial x} \\ \int_0^1 \overline{\varepsilon} d\overline{x} = \overline{u}_0 \\ \overline{u}(1) = \overline{u}_0 \\ \overline{u}(0) = 0. \end{cases} \tag{2.61}$$

The stress $\sigma = (g(d) + k)\overline{E}\overline{\varepsilon}$ being constant, hence:

$$\overline{u}_0 = \frac{\overline{\sigma}}{\overline{E}} \int_0^1 \frac{1}{g(d) + k} d\overline{x}. \tag{2.62}$$

Using the solution of d in (2.60), we have:

$$\int_0^1 \frac{1}{g(d) + k} d\overline{x} = \int_0^1 \frac{1}{1 - 2\exp(-\frac{\overline{\mathrm{x}}}{\bar{\mathrm{l}}}) + \exp(-\frac{2\overline{\mathrm{x}}}{\bar{\mathrm{l}}}) + \mathrm{k}} d\overline{x}. \tag{2.63}$$

Defining

$$G(\overline{x}, k, \bar{l}) = \frac{\bar{l}}{1 + k} \left[\ln\left((1 + \mathrm{k}) \exp\left(\frac{2\overline{\mathrm{x}}}{\bar{\mathrm{l}}}\right) - 2\exp\left(\frac{\overline{\mathrm{x}}}{\bar{\mathrm{l}}}\right) + 1 \right) \right.$$

$$\left. + \frac{2}{\sqrt{k}} \arctan\left(\frac{(1 + \mathrm{k}) \exp\left(\frac{\overline{\mathrm{x}}}{\bar{\mathrm{l}}} - 1\right)}{\sqrt{\mathrm{k}}} \right) \right], \tag{2.64}$$

$$\int_0^1 \frac{1}{g(d) + k} d\overline{x} = G(\overline{x} = 1, k, \bar{l}) - G(\overline{x} = 0, k, \bar{l}), \tag{2.65}$$

the stress is provided by the expression:

$$\overline{\sigma} = \overline{E}\frac{\overline{u}_0}{G(\overline{x}, k, \bar{l})}. \tag{2.66}$$

Eq. (2.66) shows that the stress depends on the coefficient k and on the regularization length $\bar{l}$.

2.5.2.1 FEM discretization of displacement problem and shifted strain split algorithm

To avoid the nonlinearity related to the decomposition of the strain field (2.28)-(2.31) at time t^{n+1}, we introduce two shifted strain tensor split algorithms. Theses algorithms have been originally proposed in this PhD thesis and have been published in [158].

$$\text{Split algorithm 1}: \quad \boldsymbol{\varepsilon}^+_{n+1} \simeq \mathbb{P}^+_n : \boldsymbol{\varepsilon}_{n+1}, \quad \boldsymbol{\varepsilon}^-_{n+1} \simeq \mathbb{P}^-_n : \boldsymbol{\varepsilon}_{n+1}, \tag{2.67}$$

where $\mathbb{P}^{\pm}_n = \frac{\partial \boldsymbol{\varepsilon}^{\pm}_n}{\partial \boldsymbol{\varepsilon}_n}$ can be expressed thanks to the algorithm presented in Miehe and Lambrecht [139]. This algorithm seems to have been used in [138], although not explicitly described. Such a simplification might induce small time steps to maintain a good accuracy of the solution. To overcome this drawback, we propose a second algorithm, described as follows.

$$\text{Split algorithm 2}: \quad \boldsymbol{\varepsilon}^+_{n+1} \simeq \tilde{\mathbb{P}}^+_{n+1} : \boldsymbol{\varepsilon}_{n+1}, \quad \boldsymbol{\varepsilon}^-_{n+1} \simeq \tilde{\mathbb{P}}^-_{n+1} : \boldsymbol{\varepsilon}_{n+1}, \tag{2.68}$$

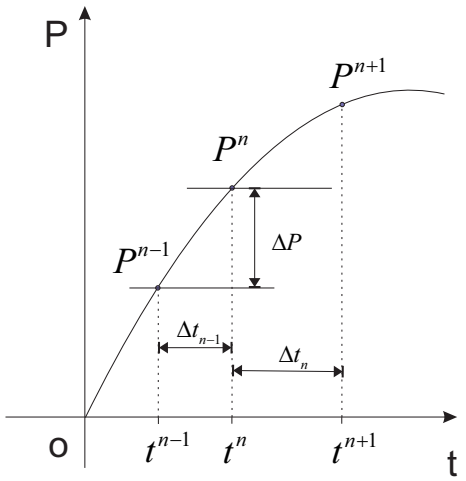

Figure 2.4: Evolution of the projection tensor between two time step t^n and t^{n+1}.

where

$$\begin{aligned} \tilde{\mathbb{P}}^+_{n+1} &\simeq \mathbb{P}^+_n + \Delta t_n \frac{\partial \mathbb{P}^+_n}{\partial t} \\ \tilde{\mathbb{P}}^-_{n+1} &= \mathbb{I} - \tilde{\mathbb{P}}^+_{n+1}; \end{aligned} \tag{2.69}$$

with $\Delta t_n = t^{n+1} - t^n$, and $\frac{\partial \mathbb{P}_n^+}{\partial t} \simeq \frac{\mathbb{P}_n^+ - \mathbb{P}_{n-1}^+}{\Delta t_{n-1}}$. We then allow time steps to be adapted, as when cracks begin nucleating and propagating, smaller time steps might be required. Furthermore, in the broken zone ($d \simeq 1$), the decomposition (2.31) might lead unphysical values of $\boldsymbol{\varepsilon}^{\pm}$. To alleviate this issue, we introduce a weight function $\beta(d)$ such that $\beta(d=0) = 0$, $\beta(d=1) = 0$, e.g. $\beta(d) = (1-d)^2$:

$$\mathbb{P}_{n+1}^+ \simeq \mathbb{P}_n^+ + \beta(d_n) \Delta t_n \frac{\partial \mathbb{P}_n^+}{\partial t}. \tag{2.70}$$

This ensures that for $\beta(d=0)$ behavior is linear and the projector tensor is well defined. For $d=1$, the property $\beta(d=1) = 0$ leads to compute the projector tensor as the projector from the previous load increment.

In addition, we propose the following approximations:

$$\langle Tr\boldsymbol{\varepsilon}_{n+1} \rangle_+ \simeq \mathcal{R}^+(\boldsymbol{\varepsilon}_n) Tr\boldsymbol{\varepsilon}_{n+1}, \quad \langle Tr\boldsymbol{\varepsilon}_{n+1} \rangle_- \simeq \mathcal{R}^-(\boldsymbol{\varepsilon}_n) Tr\boldsymbol{\varepsilon}_{n+1}, \tag{2.71}$$

with

$$\mathcal{R}^+(\boldsymbol{\varepsilon}_n) = \frac{1}{2}\left(\text{sign}\left(Tr\boldsymbol{\varepsilon}_n\right) + 1\right), \quad \mathcal{R}^-(\boldsymbol{\varepsilon}_n) = \frac{1}{2}\left(\text{sign}\left(-Tr\boldsymbol{\varepsilon}_n\right) + 1\right). \tag{2.72}$$

A FEM discretization and the vector form for second order tensors in 2D are introduced, namely: $[\boldsymbol{\varepsilon}] = \{\varepsilon_{11}; \varepsilon_{22}; 2\varepsilon_{12}\}^T$, $[\boldsymbol{\sigma}] = \{\sigma_{11}; \sigma_{22}; \sigma_{12}\}^T$, $[\mathbf{1}] = \{1; 1; 0\}^T$, as well as the FEM approximations $\mathbf{u} = \mathbf{N}\mathbf{u}_i$, $\delta\mathbf{u} = \mathbf{N}\delta\mathbf{u}_i$, $[\boldsymbol{\varepsilon}(\mathbf{u})] = \mathbf{B}\mathbf{u}_i$, $[\boldsymbol{\varepsilon}(\delta\mathbf{u})] = \mathbf{B}\mathbf{u}_i$; $\mathbf{u}_i$ denoting nodal displacements at time t_{n+1}. Setting $\mathcal{R}^{\pm}(\boldsymbol{\varepsilon}_n) \equiv \mathcal{R}_n^{\pm}$ and $\mathbf{P}^{\pm}(\boldsymbol{\varepsilon}_n) \equiv \mathbf{P}_n^{\pm}$, where $\mathbf{P}^{\pm}$ are the matrix forms associated with the fourth-order tensors $\mathbb{P}^{\pm}$, then the stress can be expressed at time t_{n+1} by:

$$\begin{aligned}[\boldsymbol{\sigma}_{n+1}] = \left((1-d_{n+1})^2 + k\right) \left\{\lambda \mathcal{R}_n^+ \left([\boldsymbol{\varepsilon}_{n+1}] \cdot [\mathbf{1}]\right)[\mathbf{1}] + 2\mu \mathbf{P}_n^+ [\boldsymbol{\varepsilon}_{n+1}]\right\} \\ + \lambda \mathcal{R}_n^- \left([\boldsymbol{\varepsilon}_{n+1}] \cdot [\mathbf{1}]\right)[\mathbf{1}] + 2\mu \mathbf{P}_n^- [\boldsymbol{\varepsilon}_{n+1}].\end{aligned} \tag{2.73}$$

Introducing the above FEM discretization and approximations (2.68)-(2.72) in (2.51), the linear system of equations is obtained:

$$\left\{\mathbf{K}_1(d_{n+1}, \mathbf{u}_n) + \mathbf{K}_2(\mathbf{u}_n)\right\} \mathbf{u}_{n+1} = \mathbf{F}_{n+1} \tag{2.74}$$

with

$$\mathbf{K}_1(d_{n+1}) = \int_\Omega \mathbf{B}^T \left\{\left((1-d_{n+1})^2 + k\right)\left(\lambda \mathcal{R}_n^+ [\mathbf{1}]^T [\mathbf{1}] + 2\mu \mathbf{P}_n^+\right)\right\} \mathbf{B} d\Omega, \tag{2.75}$$

$$\mathbf{K}_2 = \int_\Omega \mathbf{B}^T \left\{\lambda \mathcal{R}_n^- [\mathbf{1}]^T [\mathbf{1}] + 2\mu \mathbf{P}_n^-\right\} \mathbf{B} d\Omega, \tag{2.76}$$

$$\mathbf{F}_{n+1} = \int_\Omega \mathbf{N}^T \mathbf{f} d\Omega + \int_{\partial\Omega_F} \mathbf{N}^T \overline{\mathbf{F}}_{n+1} d\Gamma. \tag{2.77}$$

We can note that such algorithms then do not require Newton linearization for the displacement problem, as in each algorithm, the computation of $\mathbb{P}^{\pm}$ is performed at the previous time step. However, as pointed in [132], such staggered algorithm cannot handle snap-back-type instabilities. If such phenomena occur, a monolythic solving procedure with arc-length control may be required. We have assumed in this work that we do not encounter such phenomena.

2.5.3 Overall algorithm

The overall algorithm, involving the previously mentioned shifted strain decomposition algorithm (split algorithm 2), is described as follows.

Initialization. Initialize the displacement field $\mathbf{u}_0(\mathbf{x})$, the phase field $d_0(\mathbf{x})$, and the strain-history functional $\mathcal{H}_0 = 0$.

WHILE $t^{n+1} \leq T$, given $\mathbf{u}_n$, d_n and $\mathcal{H}_n$,

1. Compute $\tilde{\mathbb{P}}^{+}(\boldsymbol{\varepsilon}_n)$, $\tilde{\mathbb{P}}^{-}(\boldsymbol{\varepsilon}_n)$, $\mathcal{R}^{+}(\boldsymbol{\varepsilon}_n)$ and $\mathcal{R}_{-}(\boldsymbol{\varepsilon}_n)$ by (2.70)-(2.72).
2. Compute the strain history functional $\mathcal{H}_{n+1}$ by (2.44).
3. Compute $d_{n+1}(\mathbf{x})$ by solving the linear phase field problem (3.62).
4. Compute $\mathbf{u}_{n+1}(\mathbf{x})$ by solving the linear displacement problem problem (2.74).
5. $(.)_n \leftarrow (.)_{n+1}$ and go to (1).

All numerical examples studied in this thesis work have been implemented in a house-made code with Matlab. We have extensively optimized the code and parallelized many portions to allow the study of large examples in reasonable time. In addition, an iterative Biconjugate gradient stabilized solver [186] was used to solve the largest systems [59].

2.6 Discussion on the influence of input parameters in the phase field numerical simulations

In this section, we discuss the influence of the numerical parameters on the simulation results using the phase field method. More specifically, we study: the influence of (a) the mesh size, (b) the loading increments size, (c) the regularization parameter l in (2.38). For this purpose, we consider a benchmark problem with features similar to that of the experimental tests studied in Chapter 7. The benchmark described in Fig. 2.5 consists into a drilled sample subjected to compression. Compression tests are often preferred to tensile ones in civil engineering because of their better stability during crack propagation (see e.g. [190, 227]). More details about the real corresponding experimental test are provided in the following. The geometry of the sample and boundary conditions are depicted in Fig. 2.5. The material parameters have been chosen as $E = 12$ GPa, $\nu = 0.3$ and $g_c = 1.4$ N/m from the experimental values provided in [180]. Plane strain conditions are assumed. A part of this section has been submitted in [156].

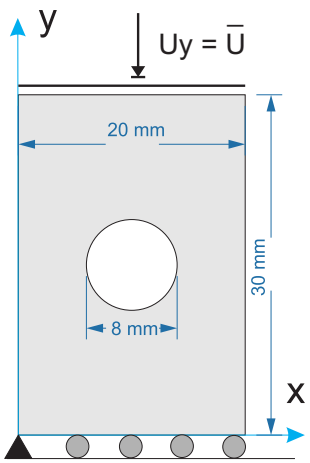

Figure 2.5: Benchmark problem for analyzing the influence of numerical parameters on the simulation results: geometry and boundary conditions.

2.6.1 Influence of the mesh size

In a first test, we investigate the convergence of the mechanical response with respect to mesh refinement. In all examples of this work, linear elements have been used, i.e. triangles in 2D and tetrahedra in 3D. Here, the regularization parameter is fixed to $l = 0.1$ mm. We discuss in the following how to choose this parameter. It has been shown in [138] that given l, the criterion

$$h \leq l/2 \tag{2.78}$$

must be fulfilled. Monotonic compressive displacement increments of $\overline{U} = -1 \times 10^{-4}$ mm have been prescribed for 250 load increments. Then we have performed several simulations using refined meshes, where the characteristic size of the elements varies between $h = 0.01$ mm and $h = 0.1$ mm. Let us define the overall critical axial stress σ^* as the ratio of the y-component of the resultant force prescribed at the top of the sample to the area of its upper face, when damage reaches the value $d = 1$ for the first load increment at some node in the mesh (i.e. stress associated to the onset of the first crack). We study in Fig. 2.6 the convergence of this quantity with respect to mesh size. A clear convergence is observed, with results becoming mesh independent when condition (2.78) is fulfilled. This confirms results of [138].

2.6.2 Influence of the load increment

Next, we analyze the influence of the load increment $\Delta\overline{U}$ in the numerical simulation on the mechanical response. We have used several load increments from $\Delta\overline{U} = 1.5 \times 10^{-3}$ mm to $\Delta\overline{U} = 3 \times 10^{-5}$ mm. Results are presented in Fig. 2.7. In Fig. 2.7(b), we study the evolution of σ^* with respect to $\Delta\overline{U}$ and can appreciate the related convergence: the evolution of σ^* is below 2% when the increment goes from 5.10^{-5} to 3.10^{-5}. This confirms the stability of the easy-to-implement staggered algorithm as soon as sufficiently small loading steps are used. Too

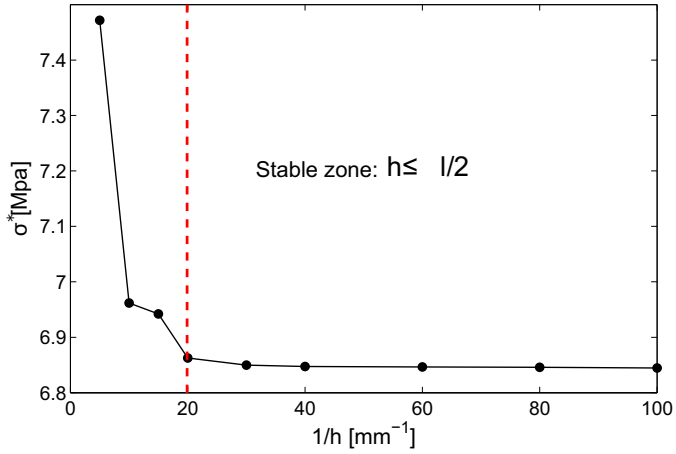

Figure 2.6: Convergence of the solution with respect to mesh size.

large steps tend to delay the initiation of damage and thus harden the overall response of the structure.

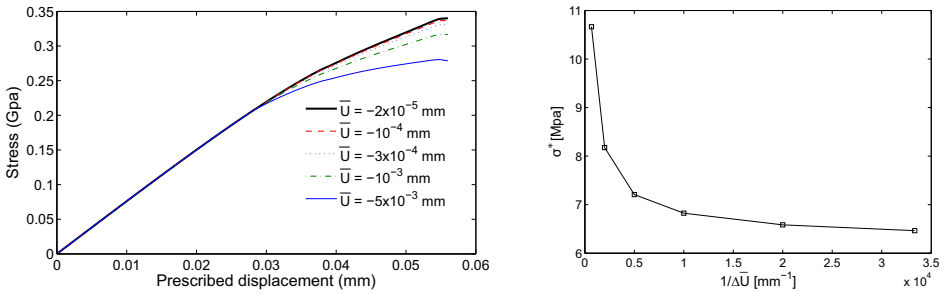

(a) (b)

Figure 2.7: Convergence of the solution with respect to the displacement increments in the numerical simulation: (a) Load - displacement curve; (b) σ^* for various displacement increments.

2.6.3 Choice of the regularization parameter l

In this section, following Amor et al. [16], we show that the regularization parameter l in (2.38) depends on material parameters. To illustrate this point, we consider a bar under uniaxial traction as depicted in Fig. 2.8. We assume that the Poisson ratio is zero. In this configuration and in the absence of initial defects, the damage distribution is assumed to be homogeneous, i.e. $\nabla d(\mathbf{x}) = 0$.

From section 2.3.2, we have:

$$F = 2(1-d)\Psi^+ - g_c Y_c = 0. \tag{2.79}$$

For a uniform damage parameter as in the considered 1D problem, Y_c reduces to $Y_c = d/l$.

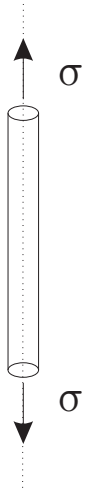

Figure 2.8: 1D problem for the analysis of the phase method in an initially homogeneous situation.

For uniaxial tension, and assuming $k \simeq 0$ we can write from (2.82):

$$\sigma = g(d)E\varepsilon, \qquad \Psi^+ = \frac{1}{2}E\varepsilon^2. \tag{2.80}$$

with $g(d) = (1-d)^2$. Then using (2.79), we obtain the relation:

$$(1-d)E\varepsilon^2 - \frac{g_c}{l}d = 0. \tag{2.81}$$

The strain and stress can then be expressed by:

$$\varepsilon(d,l) = \sqrt{\frac{g_c d}{lE(1-d)}}, \tag{2.82}$$

$$\sigma(d,l) = \sqrt{d(1-d)^3}\sqrt{\frac{Eg_c}{l}}. \tag{2.83}$$

The maximum value of the stress with respect to d is given by:

$$\sigma_c = \mathrm{Arg}\left\{\sup_{\mathrm{d=[0\ 1]}} \sigma(\mathrm{d,l})\right\} \tag{2.84}$$

which is reached for $d = 1/4$, corresponding to the critical value of the stress σ_c:

$$\sigma_c = \frac{9}{16}\sqrt{\frac{Eg_c}{3l}} \tag{2.85}$$

and of the strain:

$$\varepsilon_c = \sqrt{\frac{g_c}{3lE}} \tag{2.86}$$

These obtained formulations are similar with the result in the work of Amor et al [17]. From these expressions, it is clear that the critical stress will increase as l decreases. In the limit

of l tending to zero, i.e., when the phase-field formulation coincides with the discrete fracture formulation, the crack nucleation stress becomes infinite. This observation is consistent with the predictions of Griffith's theory, which only allows for crack nucleation at stress singularities. Eq. (2.86) gives a relationship between l and the material parameters, namely the Young modulus, E, the griffith critical surface energy, g_c, and σ_c, which now refers now to the critical stress leading to rupture in a uniaxial uniform tension test:

$$l = \frac{27 E g_c}{256 \sigma_c^2}. \tag{2.87}$$

Note that this relation only holds for uniaxial traction without damage gradient and only provides an estimation for l but clearly shows that l can be linked to material parameters. From the values of g_c and σ_c identified experimentally in [180] for a plaster material, i.e. $E = 12$ GPa, $\sigma_c = 3.9$ MPa and $g_c = 1.4$ N/m we obtain $l \simeq 0.1$ mm.

In the next test, we show numerically that the mechanical response does not converge with respect to the parameter l. An unstructured mesh with minimal element size $h_{min} = 0.01$ mm is employed around the hole where the cracks should initiate, and with maximal element size $h_{max} = 1$ mm away from the hole, such that mesh size ensures numerical convergence of the computations for all values of l considered hereafter. The displacement increment is chosen as $\Delta \overline{U} = 10^{-4}$ mm. In Fig. 2.9(a), the evolution of the solution with respect to the regularization parameter l is plotted for different values of l ranging from 0.025 mm to 0.5 mm. In Fig. 2.9(b), the stress required to onset the first crack σ^* is plotted versus l. While the force-displacement curve in Fig. 2.9(a) seems to converge when l decreases (indeed towards a purely elastic response), it is obvious that this is not the case for the value of σ^*. This test illustrates the fact that the regularization parameter l must be identified as a material parameter, i.e. each value of l will lead to a different response of the structure.

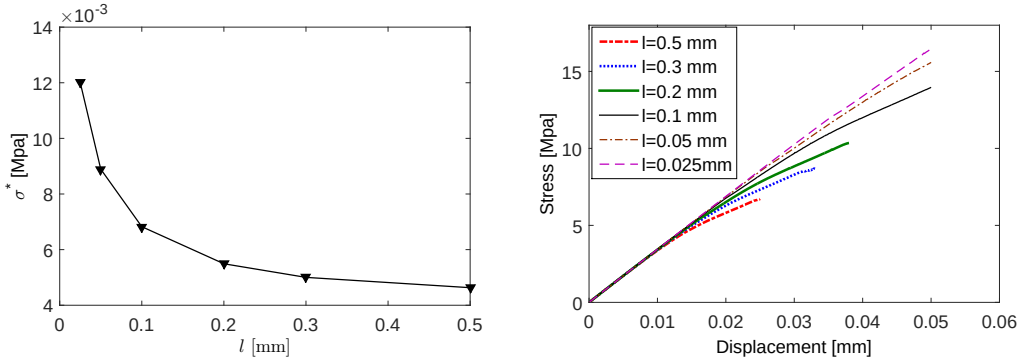

(a) (b)

Figure 2.9: Evolution of the solution with respect to the regularization parameter l: (a) Load - displacement curve; (b) σ^* versus l

2.7 Numerical examples

2.7.1 One-dimension solution

In this first example, we compare the analytical solution obtained in section 2.5 with a FEM numerical solution. The material parameters are chosen as $E = 2$ GPa, $\nu = 0$, $g_c = 10^{-4}$ kN/mm, the regularization length is taken $l = 0.05$ mm. The length of the bar is $L = 2$ mm. Then we obtain $\overline{l} = 0.025$, $\overline{E} = 1$ GPa. Results are provided in Fig. 2.10, showing a good agreement between the numerical solution and the analytical solution.

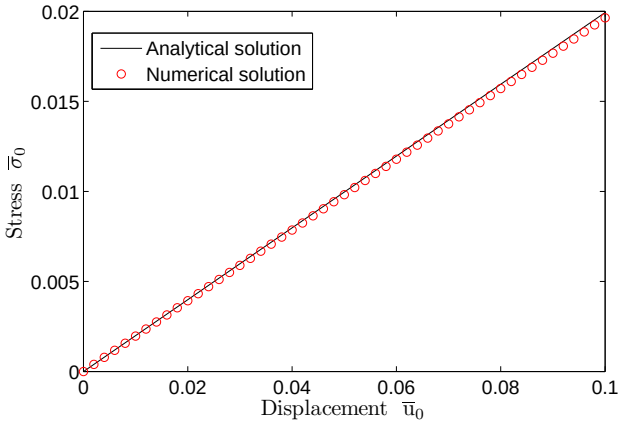

Figure 2.10: 1D problem: Comparison the stress response of analytical and numerical solution

2.7.2 Validation of the shifted tensor split algorithm: curved crack propagation in 2D

The main purpose of this first example is to validate the algorithm introduced in section 2.5.2.1. For this purpose, we consider the problem of curved crack propagation introduced in [138]. A square domain whose side length is $L = 1$mm contains an initial crack, as depicted in Fig. 2.11. The lower end ($y = 0$) of the domain is blocked along x- and y-directions. On the upper end ($y = L$), the displacement along y is fixed to zero, while the uniform $x-$displacement $\overline{U}$ is increased with time. Due to this shear loading, a curved crack initiates and propagates.

The initial cracked domain is meshed according to the initial geometry described in Fig. 2.11(a). The mesh is refined in the expected crack propagation zone, as shown in Fig. 2.11(b) and involves 74124 elements. The typical size of an element in the crack propagation zone is about $h_{min} \approx 6.10^{-4}$ mm and $h_{max} = 0.02$ mm in the rest of the domain.

Plane stress is assumed. The solid is supposed to be homogeneous isotropic solid (typical of a metal) with properties $\lambda = 121.15$ GPa and $\mu = 80.77$ GPa. The fracture toughness is $g_c = 2700$ N/m [138]. Two displacement increments $\overline{U} = 10^{-5}$ mm and $\overline{U} = 2.10^{-5}$ mm have been tested, and have been prescribed for 1500 load increments. The length scale parameter is chosen as $l = 0.0075$ mm. The evolution of the crack during the simulation is shown in Fig. 2.12.

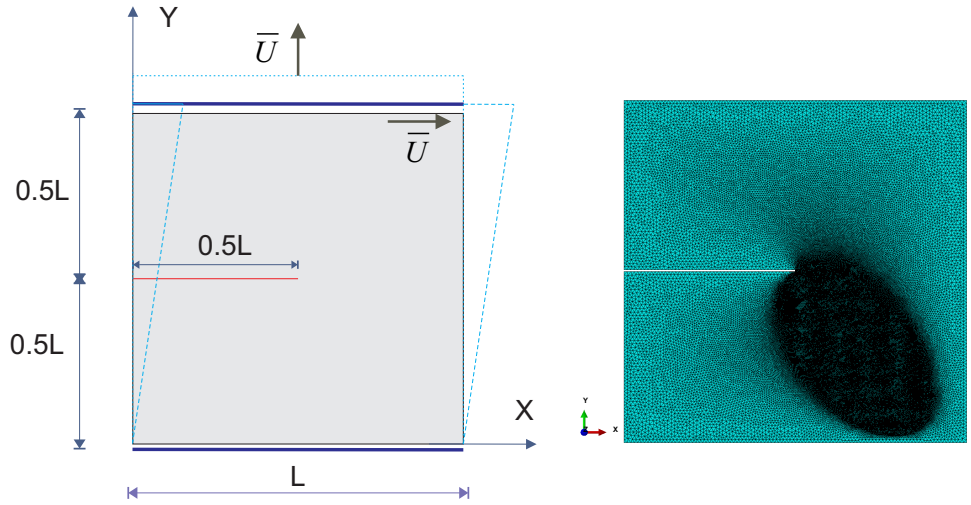

(a) (b)

Figure 2.11: Shear crack propagation problem: (a) geometry and boundary conditions; (b) FEM mesh.

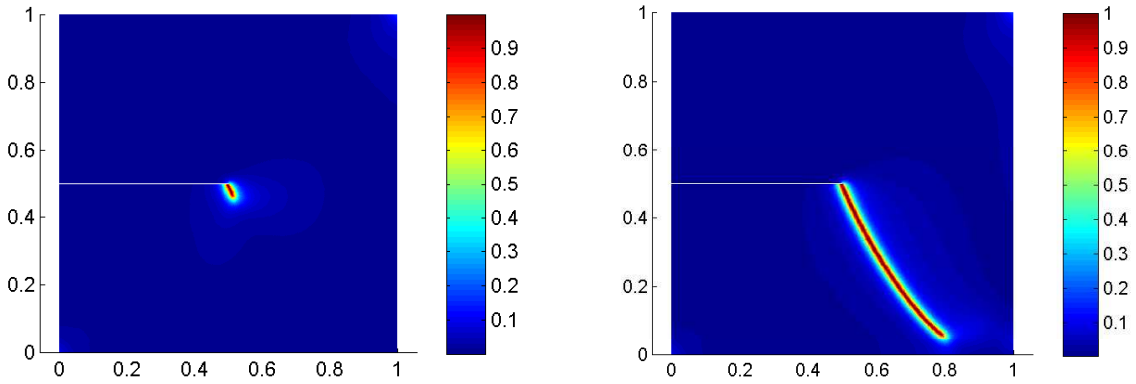

Figure 2.12: Phase field $d(\mathbf{x})$ distribution during crack evolution for the shear crack propagation problem for $\overline{U} = 10.10^{-3}$ mm and $\overline{U} = 13.10^{-3}$ mm.

To demonstrate the advantage of the proposed algorithm, we have compared the solutions provided by the two schemes defined in section 2.5.2.1 with the solution provided in [138], which involves viscous regularization. Then, we have computed the load-displacement curve for the two load increments mentioned above. The results are presented in Figs. 2.13. We can note in Fig. 2.13(a) that when small load increments are used, both algorithms provide accurate solutions with respect to the reference solution of [138]. However, when larger load increments are used, we can see that the algorithm 2 maintains a more accurate solution than algorithm 1. In Fig. 2.13(b), we have studied the convergence of the maximum load before failure with respect to the load increment. We can note that the convergence is increased with algorithm 2,

allowing larger load increments for computational saving.

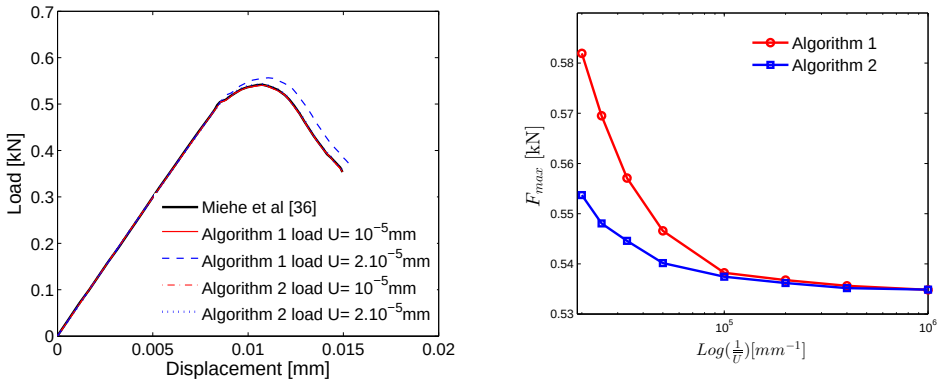

(a) (b)

Figure 2.13: (a) Comparison of force-displacement curve for two split algorithms; (b) convergence of the maximum load before failure with respect to the load increment for both algorithms.

Next, we investigate the convergence of the maximum load before failure with respect to the mesh size. In that case, a regular mesh has been employed on the geometry described in Fig. 2.11(a). The algorithm 2 has been used. The parameter $l = 0.01$ mm and the load increment is $\overline{U} = 10^{-5}$ mm. The results are provided in Fig. 2.14, demonstrating the convergence.

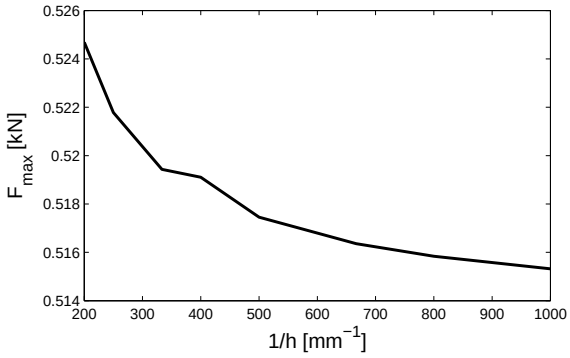

Figure 2.14: Convergence analysis of the maximum load before failure with respect to the mesh size.

Finally, we investigate the capability of the split algorithm to handle auto-contact in a fatigue crack propagation. For this purpose, the same initial domain as described in Fig. 2.11(a) is used, but traction conditions are prescribed, i.e. $y-$ displacements are prescribed while $x-$displacements are free. Here again, the algorithm 2 has been used. The evolution of the prescribed displacements is depicted in Fig. 2.15(a). In figure 2.15(b), the ε_{22} strain component in one element located just near the crack tip is plotted with respect to the resultant force on the upper end of the domain. We can note that the split algorithm is able to predict the progressive damage of the material in the case of cyclic loading.

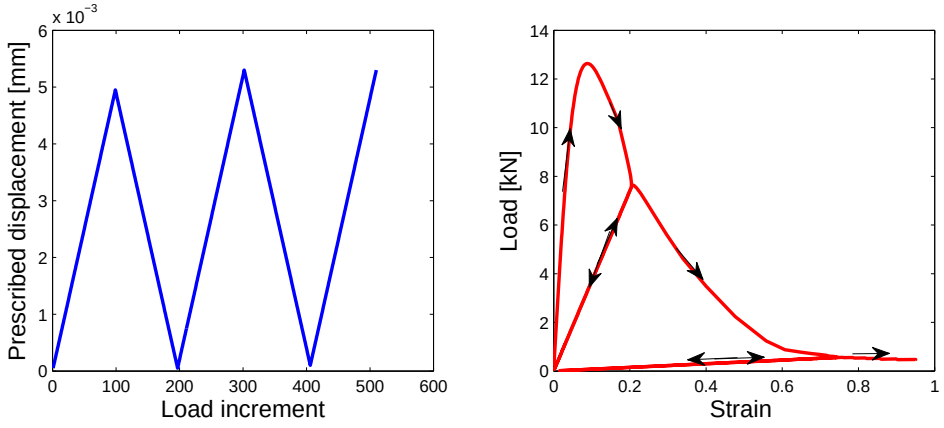

(a) (b)

Figure 2.15: (a) Prescribed loading for the cyclic traction test; (b) ε_{22} strain component in one element near the crack tip with respect to the load.

2.7.3 Traction test of a microtomography image-based mortar sample in 2D

The purpose of the next series of test is to demonstrate the potential of the phase field method to handle highly complex microstructures such as those arising from microtomography images of real materials. The different examples have then been selected as tough and challenging problems for crack propagation.

In this example, we consider a model of mortar made of cement paste and sand particles. The geometry of the microstructure has been obtained by segmentation of a microtomography image. The data were kindly provided by Assistant Professor Sylvain Meille and Dr. Ing. Jerome Adrien, MATEIS laboratory- UMR CNRS, INSA Lyon, University of Lyon, France. The geometry of the inclusions in the model is described in Fig. 2.16(a).

The domain contains an initial crack of length $a = 0.1L$, $L = 1$ mm, which is here defined by prescribing nodal values of the phase field $d(\mathbf{x}) = 1$ for the nodes on the crack. On the lower end ($y = 0$), the $y-$displacements are blocked, while the $x-$displacements are free. The node ($x = 0$), ($y = 0$) is blocked. On the upper end, the $x-$displacements are free, while the $y-$displacements are prescribed, with an increasing value of $\overline{U}$ during the simulation. Plane strain is assumed.

Three models are considered, each of them were obtained by segmenting the original image rescaled to three different resolutions. In each case, the voxel data are transferred into a regular grid of square domains associated with voxels, each divided into 2 3-nodes elements. The models contains 125×150, 250×300 and 500×600 elements, respectively. Fig. 2.16(a) shows the discretization associated with the last case. In this figure, white and black colors refer to matrix and inclusions, respectively. The material is a mortar composed of a cement paste (matrix) and sand (inclusions). The chosen material parameters of each phase are: $E_i = 30$ GPa, $\nu_i = 0.3$ (inclusions) and $E_m = 10$ GPa, $\nu_m = 0.2$ (matrix). The fracture toughness is $g_c = 250$ N/m.

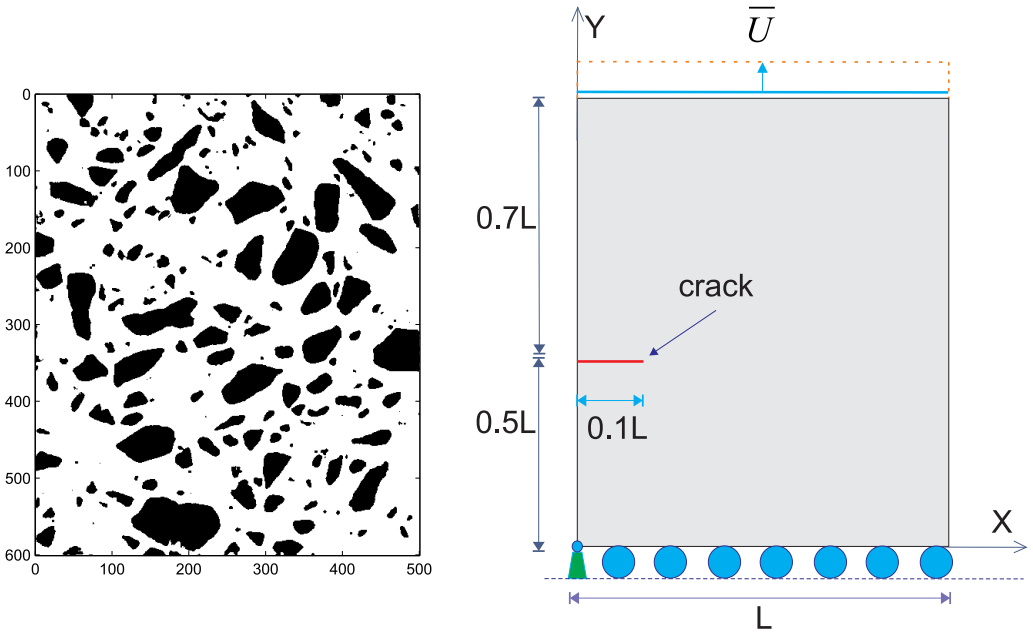

(a) (b)

Figure 2.16: Traction test of a microtomography image-based mortar sample in 2D: (a) geometry of the phases; (b) geometry of the domain and boundary conditions.

These numerical values have been chosen as the experimental ones described in [144], [97]. In all the examples of the present work, we have used the same g_c for all materials when two phases are involved in the microstructure. The computation is performed with monotonic displacement increments of $\overline{U} = 10^{-4}$ mm during the first 65 load increments and $\overline{U} = 5.10^{-6}$ mm during the last 500 increments corresponding to the softening part of the curve. The length scale parameter is chosen as $l = 0.016$ mm. The crack evolution for the different discretizations associated with different segmentations cases is depicted in Fig. 2.17.

We can note that the crack path is not much sensitive to the mesh refinement, despite of the highly heterogeneous nature of the microstructure and the large number of inclusions, with complex geometries and a wide span of sizes. A comparison of the load/displacement curves for the three cases is depicted in Fig. 2.18. A convergence of the different responses is observed for the different refined models. We can conclude that the phase field method is a promising tool for crack propagation in highly heterogeneous materials models obtained from microtomography images, mostly thanks to the weak dependency on the mesh refinement.

2.7.4 Shear test of a microtomography image-based mortar sample in 2D

In this example, we consider another slice taken from the same 3D microtomography image than in the previous example. The dimensions of the sample are the same as previously. However, the load here consists into shear conditions, as described in Fig. 2.19 (b). The geometry of the phases is described in Fig. 2.19(a). On the lower end ($y = 0$), the $y-$displacements and the

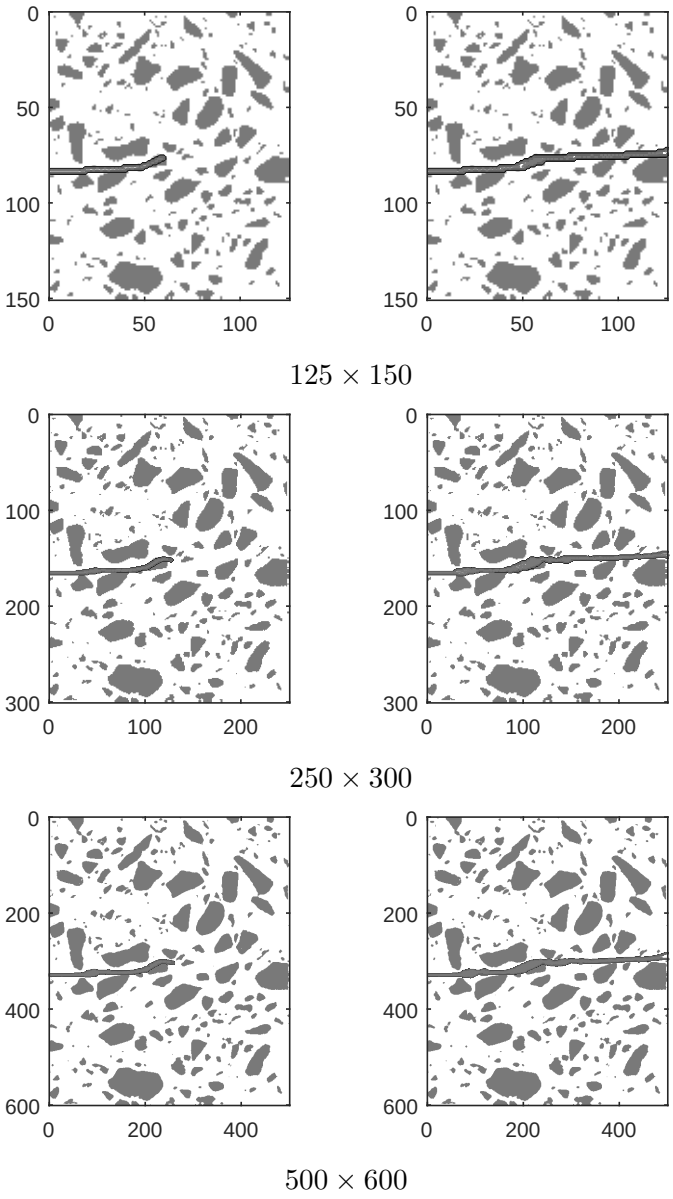

Figure 2.17: Traction test of a 2D microstructure defined by micro tomography image, crack propagation for lower end displacement $\overline{U} = 0.008$ mm (left) and $\overline{U} = 0.00845$ mm (right). From up to down: 125×150, 250×300 and 500×600 elements discretizations.

$x-$displacements are blocked. On the upper end, the y-displacements are blocked, while the x-displacements are prescribed, with an increasing value $\overline{U}$ during the simulation. The parameter $l = 0.016$ mm.

Here again, the same three resolutions as in the previous example are considered. The material parameters are the same as in the previous example. The crack evolution for the different segmentation cases is depicted in Fig. 2.20.

Due to the shear load, we can note that the crack path deviates from the original orientation of the crack, as in the example of Fig. 2.12. In this case, the microstructure has been chosen

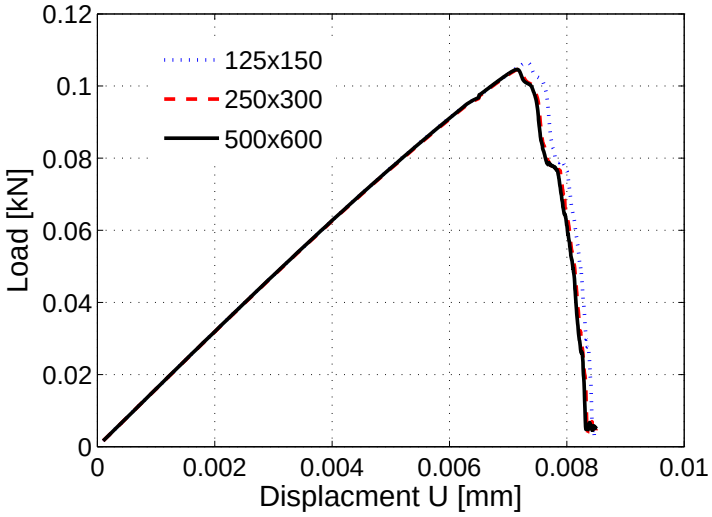

Figure 2.18: Load-deflection curve for the three segmentation of microtomography image-based models of mortar samples.

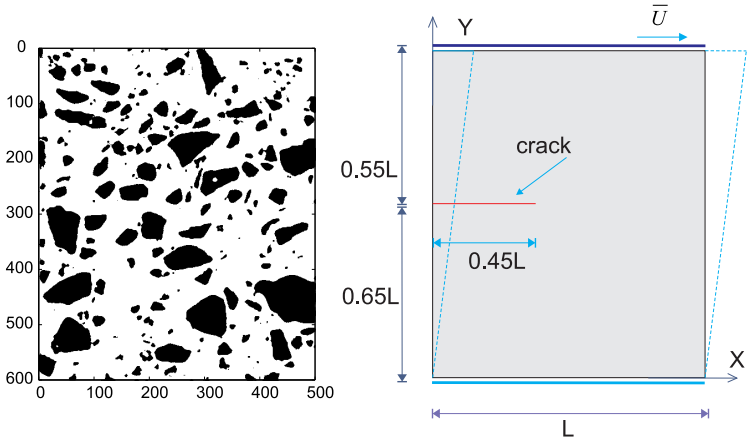

(a) (b)

Figure 2.19: Shear test of a microtomography image-based mortar sample in 2D: (a) geometry of the phases; (b) geometry of the domain and boundary conditions

such that one inclusion is in the path of the crack, to evidence the capability of the technique to propagate cracks in highly heterogeneous microstructures. No strong difference is noticed for the crack path with the different resolutions. The comparison of the load/displacement curves for the three cases is depicted in Fig. 2.21. The load curve is found to converge to the value of the finest resolution. The step-like look of the curve is due to the fact that the crack passes through some inclusions during the loading.

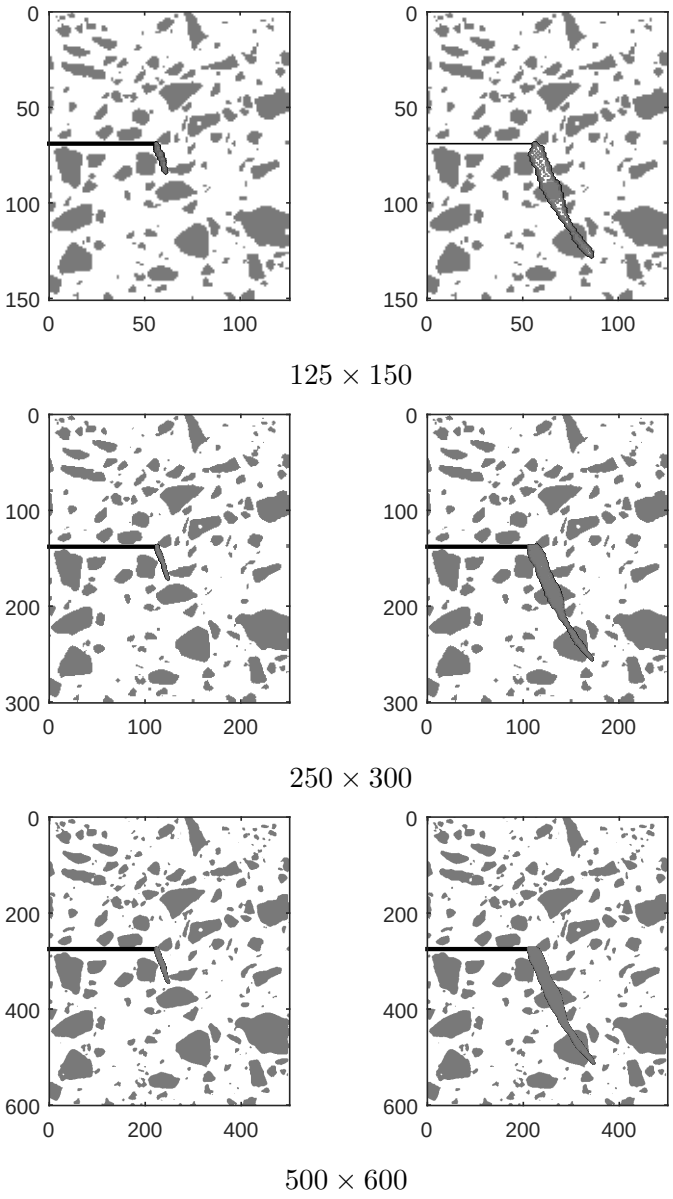

Figure 2.20: Shear test of a 2D microstructure, crack propagation for lower end displacement $\overline{U} = 0.0175$ mm (left) and $\overline{U} = 0.0235$ (right). From up to down: 125×150, 250×300 and 500×600 elements discretizations.

2.7.5 Compression test of a microstructure with uniformly distributed pores

In this next example, a microstructure made of plaster containing periodically distributed holes is considered. This example has been studied numerically and experimentally in [179, 209]. The domain, containing 23 holes with diameter $d = 0.2$ mm, as depicted in Fig. 2.22, is subjected to compression. The dimension of the sample is $L = 1$ mm (see figure 2.22).

The domain is meshed with elements whose characteristic size is $h \approx 6.10^{-3}$ mm, involving 299893 triangular elements. The properties of the matrix are $E = 12$ GPa, $\nu = 0.3$ and $g_c = 1.4$

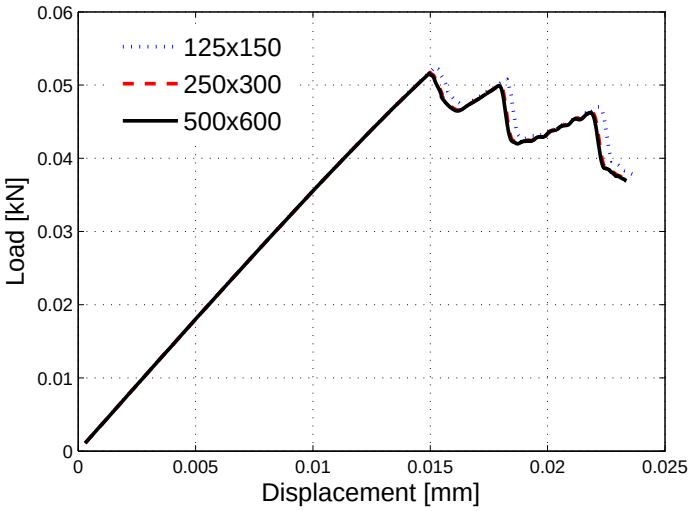

Figure 2.21: Shear test of a microtomography image-based mortar sample in 2D: load deflection curves for the three resolutions.

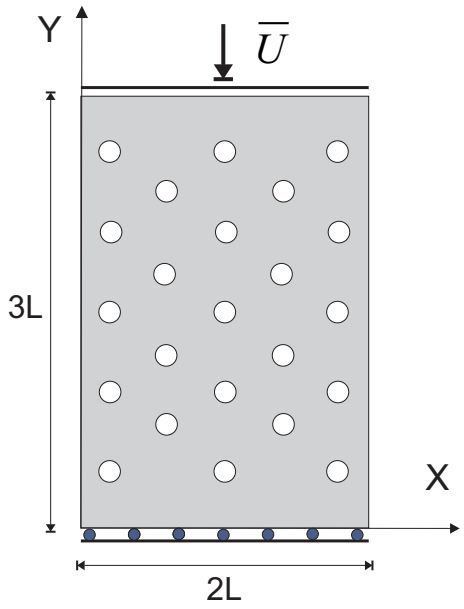

Figure 2.22: Compression test of a plate with regular distribution of holes: geometry of the domain and boundary conditions.

N/m. Monotonic compressive displacement increments of $\overline{U} = -1.5.10^{-4}$ mm is prescribed for the first 100 load increments and $\overline{U} = -3.10^{-5}$ mm in last 700 load increments. The length scale parameter is chosen as $l = 0.012$ mm. In Fig. 2.23, the evolution of the crack patterns with the a MFPA^{2D} simulation conducted in [209] are compared. The method captures the vertical crack propagation observed in the experiments performed in [179, 180] and in the simulations performed in [209]. The corresponding load curve is provided in Fig. 2.24. This example illustrates the capability of the method to nucleate cracks from undamaged microstructure, with

correct prediction of the crack path following the nucleation.

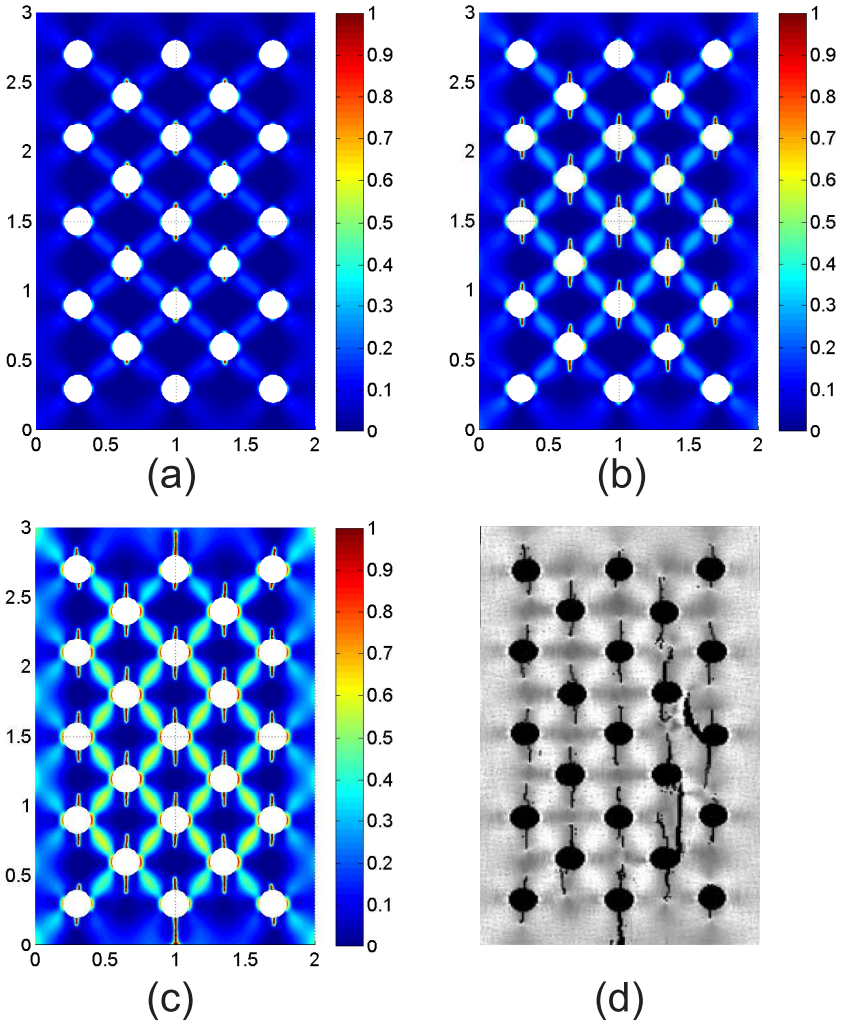

Figure 2.23: Compression test of a plate with regular distribution of holes: crack morphology field $d(\mathbf{x})$ at prescribed displacements: (a) $\overline{U} = 22.10^{-3}$ mm; (b) $\overline{U} = 26.10^{-3}$ mm; (c) and (d) $\overline{U} = 33.10^{-3}$ mm. The crack distribution depicted in (d) has been obtained by MFPA^{2D} simulation [209].

2.7.6 Compression test of a 3-phase microstructure without pre-existing cracks

In this example, a microtomography-based microstructure of a three-phases porous cementitious material is under consideration. The studied material is an EPS lightweight concrete [146], made from quartz sand and EPS beads embedded in a cement matrix. A microtomography image was recorded in about 45 min using an XR-CT laboratory scanner available at Laboratoire Navier, with a voxel size of 15 μm. The grey level image was segmented in order to separate the three phases of the microstructure. The dimension of the sample is $L = 1$ mm (see figure 2.25)(b). As

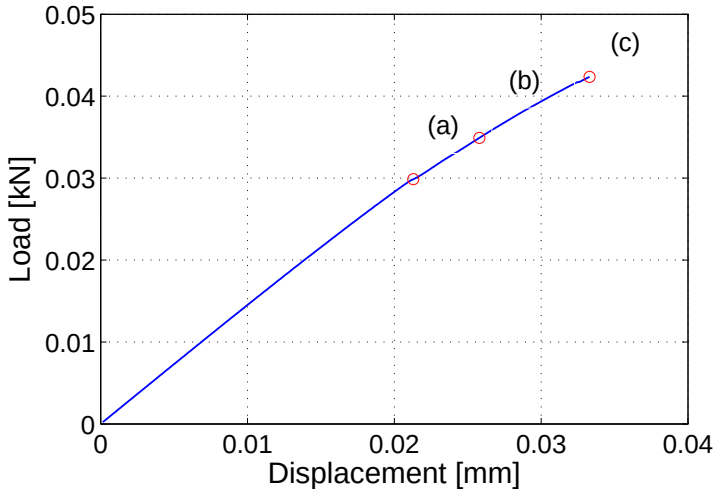

Figure 2.24: Compression test of a plate with regular distribution of holes: load-deflection curve.

depicted in the same figure, the white, grey and black phases correspond to matrix, inclusions and pores, respectively.

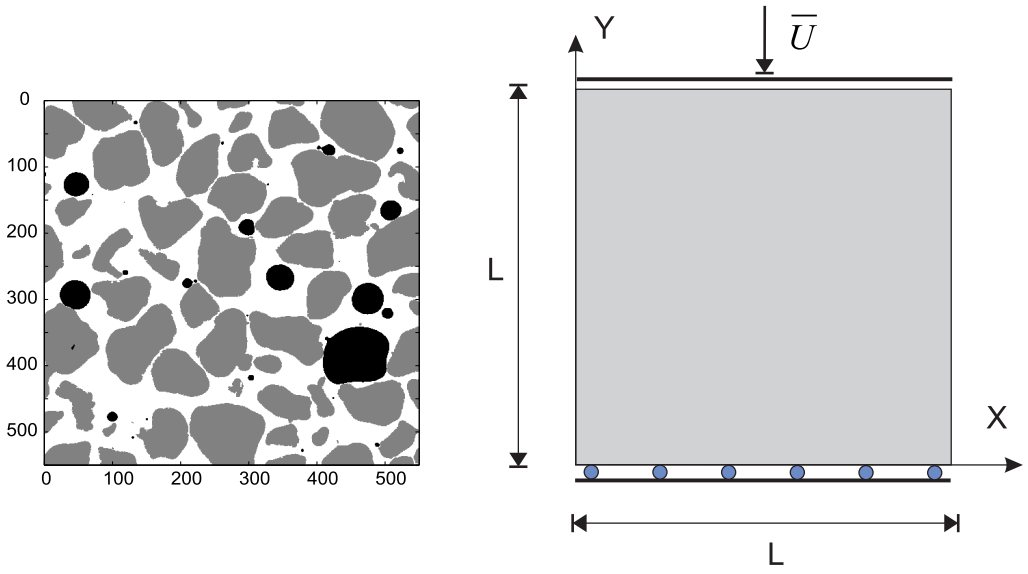

Figure 2.25: Compression test of a microtomography image-based model of porous cement based material: (a) microstructure: the white, grey and black phases correspond to matrix, inclusions and pores, respectively; (b) geometry of the domain and boundary conditions.

On the lower end, the $y-$displacements are blocked while the $x-$displacements are free. On the upper end, the $x-$displacements are free, while the y-displacements are prescribed at value of $\overline{U}$ which increases during the simulation. Plane strain is assumed. The model consists of 550×550 pixels, each associated with a material property of matrix, inclusion or holes,

according to the data obtained from the microtomography image segmentation. The voxel data are transferred into a regular grid of square domains associated with voxels, each divided into 2 3-nodes elements. The material parameters of inclusions and matrix are, respectively: $E_i = 30$ GPa, $\nu_i = 0.3$, and $E_m = 10$ GPa, $\nu_m = 0.2$. The pores are meshed and have elastic properties $E_p = 10^{-10}$ GPa, $\nu_p = 10^{-10}$. The fracture toughness is $g_c = 250$ N/m, and assumed to be identical for the different phases. This assumption is made for all further examples. The simulation is performed with monotonic displacement increments of $\overline{U} = -10^{-4}$ mm during the first 110 load increments and $\overline{U} = -10^{-6}$ mm during the last 240 load increments which correspond to the propagation of the micro cracks. The length scale parameter is chosen as $l = 7.5.10^{-3}$ mm. In this example, the domain does not contain pre-existing cracks, and the cracks first nucleate and then propagate with increase of the compressive load. The crack distribution evolution for different load increments is depicted in Fig. 2.26. The load-displacement curve is provided in Fig. 2.27. We can observe that several cracks are nucleated from the pores and can propagate either in the matrix or in the inclusions, with complex paths. When the microcracks start nucleating, the materials strength quickly drops. This examples shows the potential of the method for describing microcracking, involving nucleation and complex crack patterns in real microstructures.

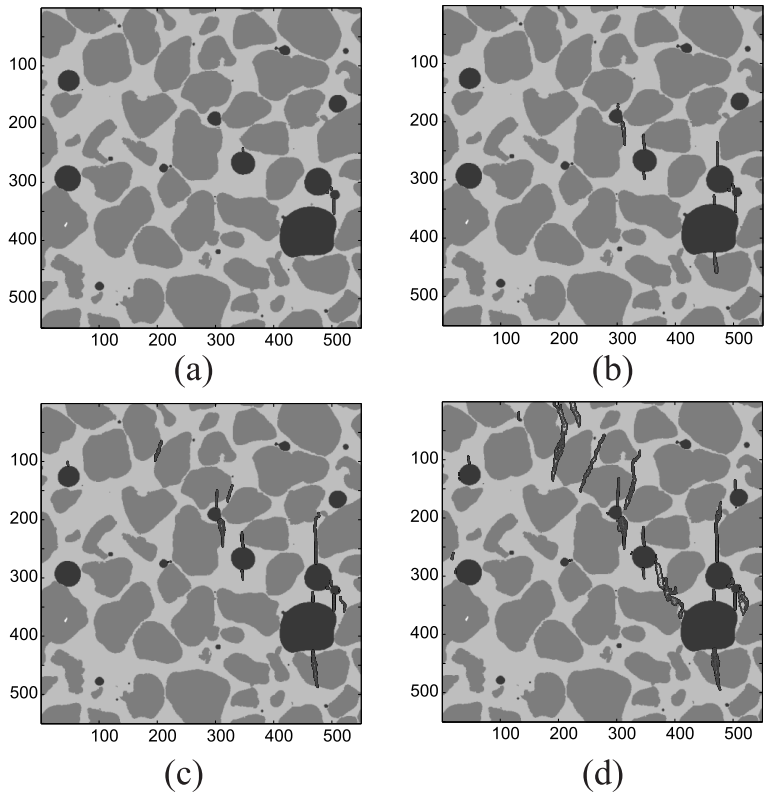

Figure 2.26: Compression test of a microtomography image-based model of cementitious material: crack propagation for (a) $\overline{U} = 20.5{\times}10^{-3}$ mm, (b) $\overline{U} = 23.5{\times}10^{-3}$ mm, (c) $\overline{U} = 24{\times}10^{-3}$ mm and (d) $\overline{U} = 25 \times 10^{-3}$ mm.

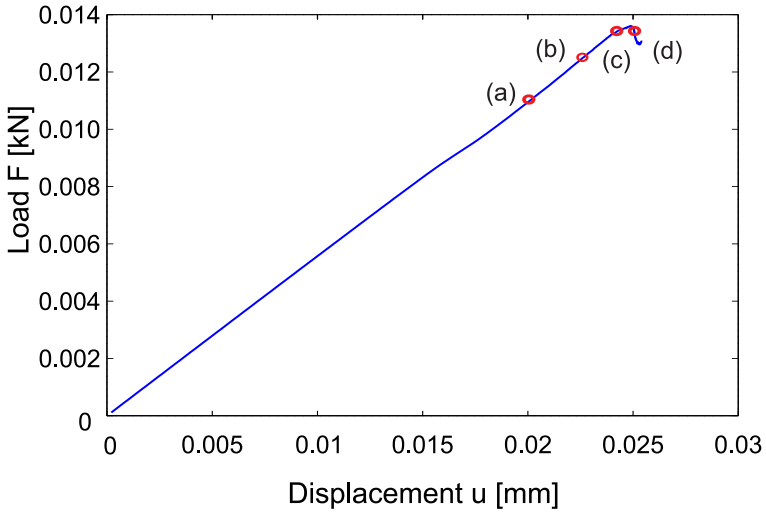

Figure 2.27: Compression problem: stress-deflection curve.

2.7.7 Traction test of a 3D microtomography image-based microstructure

In this last example, we consider the same microtomography-based image model as in section 2.7.6. However, we here use a fully 3D model. The geometry of inclusions in the model is described in Fig. 2.28(a). The dimension of the sample is $L = 1$ mm.

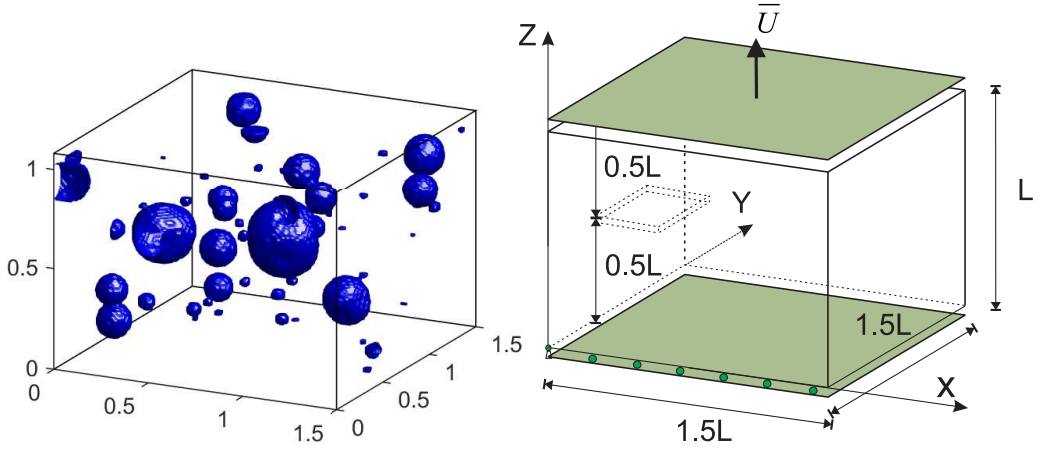

(a) (b)

Figure 2.28: Traction test of a microtomography image-based concrete sample in 3D: (a) geometry of the phases; (b) geometry of the domain and boundary conditions.

The domain contains an initial crack of size $0.35 \times 0.3 \times 0.01$ mm^3 which is here defined by prescribing nodal values of the phase field $d(\mathbf{x}) = 1$ for the nodes on the crack. On the lower end ($z = 0$), the $z-$displacements are blocked, while the $x-$displacements and $y-$displacements are free. The node ($x = 0$), ($y = 0$), ($z = 0$) is blocked. On the upper end, the $x-$displacements and $y-$displacements are free, while the $z-$displacements are prescribed, with an increasing value of $\overline{U}$ during the simulation.

The model is directly obtained from segmentation of the original image. The voxel data are transferred into a regular grid of 8-node elements. The model contains $300 \times 300 \times 200 = 18$ million elements. Fig. 2.28(a) shows the discretization. In this figure, white and blue colors refer to cement paste matrix and sand inclusions, respectively. We have here replaced the pores in the previous image by sand inclusions using the same geometry. The material parameters of each phase are: $E_i = 30$ GPa, $\nu_i = 0.3$, $E_m = 10$ GPa, $\nu_m = 0.2$. The fracture toughness is $g_c = 50$ N/m for both materials. The computation is performed with monotonic displacement increments of $\overline{U} = 10^{-4}$ mm during the 105 load increments and $\overline{U} = 10^{-5}$ mm during the last 90 load increments corresponding to the softening part of the curve. The length scale parameter is chosen as $l = 7.5.10^{-2}$ mm. The crack evolution is depicted in Fig. 2.29 and the stress-deflection curve is depicted in Fig. 2.30. Here, we demonstrate the capability of the method to describe 3D, multiple cracks propagation and interaction in image-based microstructure, up to the failure of the sample.

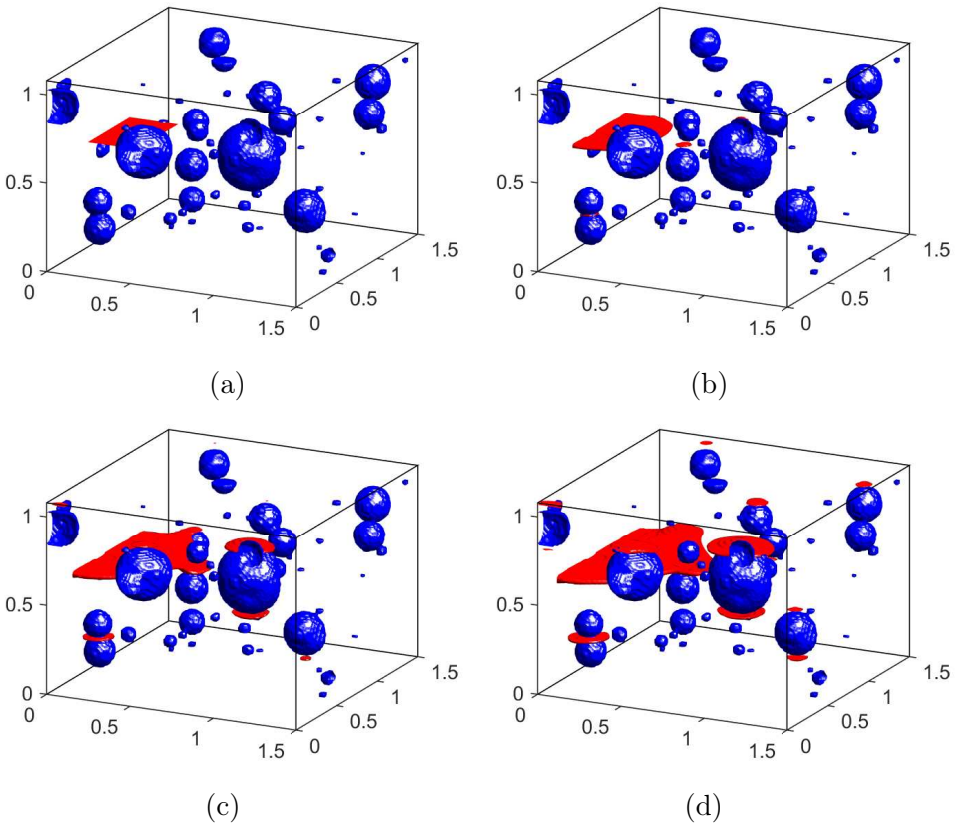

Figure 2.29: Traction test of a 3D microstructure defined from microtomography image, crack propagation for lower end displacement (a) : $\overline{U} = 0$ mm , (b) : $\overline{U} = 11 \times 10^{-3}$ mm, (c) : $\overline{U} = 11.2 \times 10^{-3}$ mm and (d) : $\overline{U} = 11.3 \times 10^{-3}$ mm.

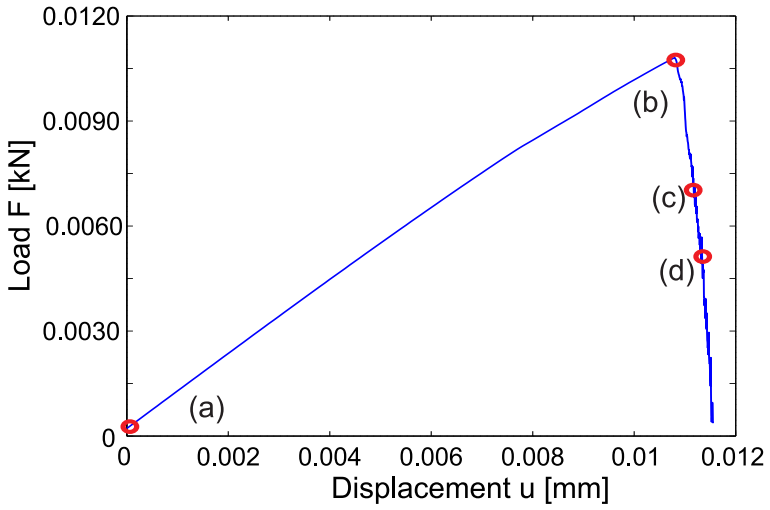

Figure 2.30: Tension test of a 3D microstructure defined from microtomography image: stress-deflection curve.

2.7.8 Traction test of a real 3 phase microtomography image-based microstructure in 3D

In this last example, we show the capability of the phase field method to handle very large, complex and realistic models of microstructures in 3D. A 3-phase microstructure model of cementitious material obtained from XR-CT is considered. Here, we first obtain the geometry from the segmentation of a sub-volume of a full $294 \times 327 \times 399$ voxels image of the sample, which is depicted in Fig. 2.31(c). Each voxel is $15 \times 15 \times 15$ μm^3. The detailed procedure to obtain the image is detailed in Chapter 6. The geometry of the phases is depicted in Fig. 2.31.

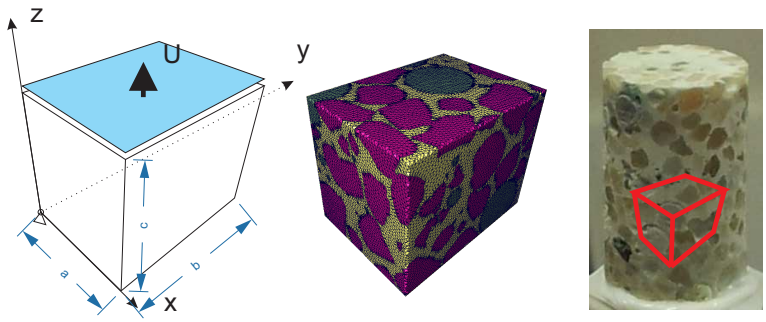

Figure 2.31: Traction test of a microtomography image-based concrete sample in 3D: (a) Geometry of the sub-volume extracted from the sample and boundary conditions (b) geometry of the phases and mesh; (c) Original sample.

Direct mapping of voxels to regular elements can lead to very large FEM meshes. One possibility to reduce the FEM mesh is to use the initial segmented geometry to construct a mesh of unstructured tetrahedral elements conformed to the interfaces. This can be achieved by available softwares. Through a collaboration with F. Bilteryst and E. Steib at LEMTA Laboratory, Saint-Die, France, the AVIZO software has been employed and a mesh of 6914199 elements has been constructed. The dimensions of the subvolume are $a = 4.41$ mm, $b = 4.91$ mm, and $c = 5.992$ mm. The material parameters are the same as in the previous example 2.7.6. The regularization length is taken as $l = 0.05$ mm (this value satisfies the condition $l/h_e = 0.05/0.015 > 2$). The computation is performed with monotonic displacement increments of $U = 5 \times 10^{-5}$ mm during the 200 time steps. The crack front at $U = 0.008$ mm is depicted in Fig. 2.32.

We test also second example, with size $5.24 \times 5.99.02$ mm^3. The mesh is about 17 millions elements. The material parameters is taken the same as previous example, in the simulation, monotonic compressive displacement increments $U = 5 \times 10^{-5}$ mm have been prescribed while $d_{\max} < 0.9$, then decreased to $U = 2 \times 10^{-5}$ mm. The crack front at $U = 0.01$ mm is depicted in Fig. 2.33.

For the sake of clarity, we plot the crack path within several planes. The results are depicted in Fig. 2.34

This example demonstrates well the robustness of the method and its capability to handle:

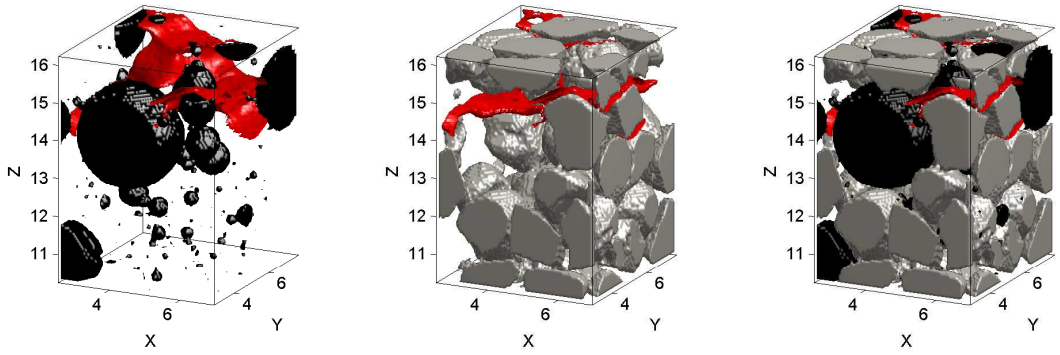

Figure 2.32: Traction test of a microtomography image-based concrete sample in 3D. The black, grey and red colors refer to the pores, the sand and the crack, respectively. The white color refers to the matrix (mortar); (a) Pores and cracks; (b) inclusions and crack; (c) Pores, inclusions and cracks.

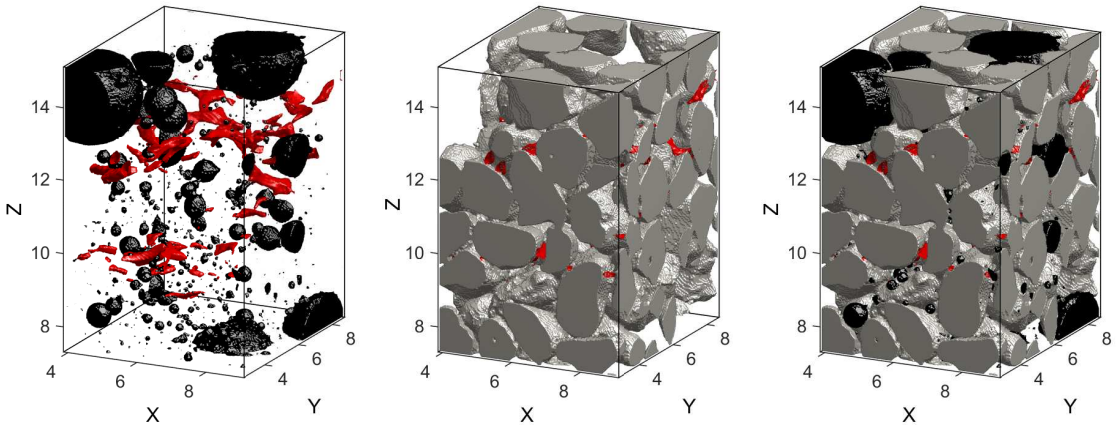

Figure 2.33: Second traction test: (a) Pores and cracks; (b) inclusions and crack; (c) Pores, inclusions and cracks.

(a) initiation of complex, 3D, multiple cracks; (b) interaction of multiple crack fronts; (c) softening associated to damage. No remeshing was necessary here and the simulation was not stopped by any convergence issue, as in the proposed framework we only solve linear problems at each load increment. We remind that these large examples, involving up to 18 million of elements, has been run on a Matlab code and in a workstation with only 8 cores. Then, we believe that much larger models could be investigated on compiled codes run on high performances machines. We observe that the crack initiates from the boundaries of the pores, and then propagates into the matrix, surrounding the inclusions. The corresponding load - displacement curve is depicted in Fig. 2.35, the red circle corresponding to the figure 2.32.

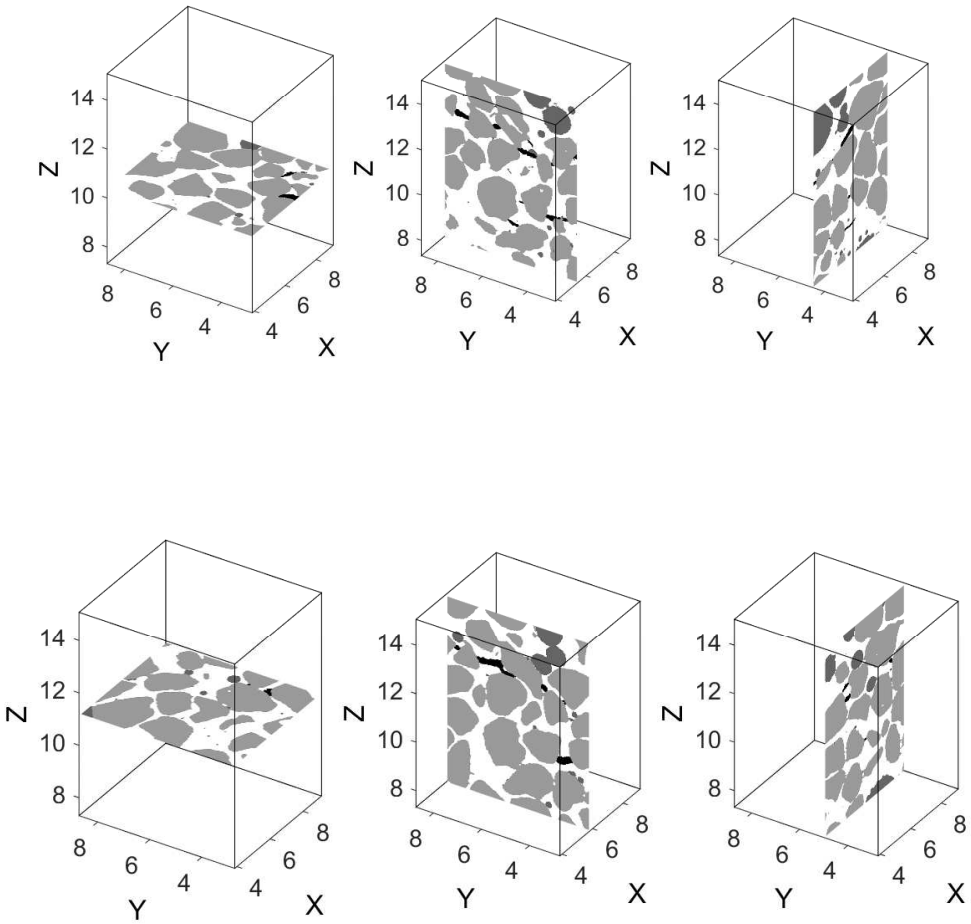

Figure 2.34: Second test: illustration of crack paths in several planes of investigation

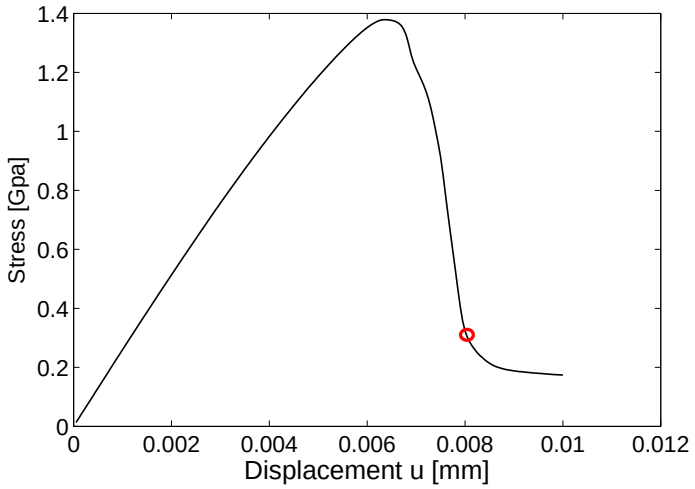

Figure 2.35: Stress-diplacement curve for the 3D microstructure problem in tension.

2.7.9 Computational times

Finally, a summary of the computational times for the different examples is reported in Table 2.1. For all cases, a workstation with 8 cores, 144 Go Ram and 3.47 GHz processor was used. The present code has been implemented in Matlab ®.

Problem	Nb. elements	Nb. time steps (increments)	CPU time for one time step (s)	Total simulation time (h)
2D shear crack	74418	1200	10	3.34
2D tensile crack				
125×150	38052	350	4	0.4
2D tensile crack				
250×300	151102	350	18	1.75
2D tensile crack				
500×600	602202	350	80	7.78
2D shear crack				
125×150	38052	600	4.5	0.75
2D shear crack				
250×300	151102	600	19	3.17
2D shear crack				
500×600	602202	600	82	13.67
3 phases	607202	410	93	10.6
23 holes	303930	800	53	11.78
3D two phases	18.10^6	195	4131	224
3D three phases	17.10^6	400	3761	417

Table 2.1: Computational times for the different examples

2.8 Conclusion

In this chapter, we have reviewed the phase field method and the computational framework proposed in Miehe et al. [138] and investigated the capabilities of the phase field method for simulating crack propagation in microstructural models of brittle materials like concrete obtain from direct imaging of their microstructure by microtomography. We have introduced the following contributions: (a) first, we have introduced a new shifted algorithm for the treatment of unilateral contact, to avoid the nonlinearities associated to the polar decomposition of the strain tensor to handle damage due to the traction part only. As a result, only linear problems have to be solved at each loading step, and larger load increments could be used to reduce the computational times. Secondly (b), we have applied the phase field method for the first time to our knowledge to realistic models of microstructures directly obtained from segmented (voxel-based) images obtained from microtomography. We have conducted both 2D and 3D applications on cement-based microstructure models to obtain both microstructural crack networks morphologies and strength prediction. In particular, we have conducted a very large 3D example involving 18 M elements. Finally (c) we have conducted an analysis of the influence of the numerical parameters of the phase field method with respect to the obtained solution. More specifically, we have shown, following the work of Amor et al. [16], that the regularization length is related to material parameters. In Chapter 7, we will provide experimental evidences of this important result.

Chapter 3

A phase-field method for computational modeling of interfacial damage interacting with crack propagation in complex microstructures

---

Contents

The main content of this chapter is adapted from our submitted paper in [157].

3.1 Introduction

Experimental results show that in highly heterogeneous materials like concrete, cracks can initiate at the interfaces due to decohesion, and propagate within the matrix, or reversely (see Fig. 3.1). For example, it has been suggested that the strength of concrete is largely attributed to the properties of mortar-aggregate interfaces [80, 118]. Interfacial cracking has a physically different origin from matrix cracking and involves and can involve a specific behavior. In this chapter, we develop a phase field framework for modelling cracking of the matrix in a microstructure as well as possible interfacial cracking, occuring between the matrix and the inclusions.

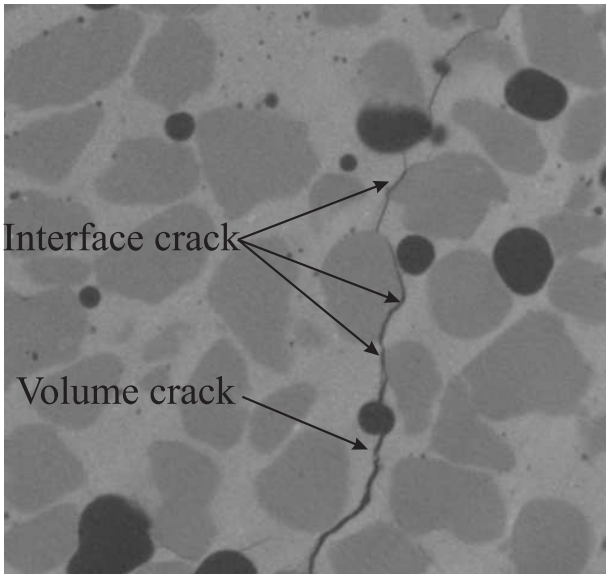

Figure 3.1: Matrix and interfacial cracking in an EPS lightwight concrete specimen loaded in compression, experimentally observed by microtomography.

The interaction of an interphase and matrix crack has been studied in ceramic matrix composites [51]. Damage by fiber cracking or decohesion in metallic composites reinforced by brittle fibers has been studied in [213].

Many numerical methods have been developed to investigate interface damage, including thin interphases with graded properties [223], or cohesive zone models, which has been reviewed in Chapter 1.

Simulating interfacial damage and its interaction with matrix cracking in voxel-based models of complex microstructures of real materials is highly challenging. Indeed, in voxel models consisting of regular meshes, the interfaces are not explicitly described and normal vectors are not defined. Furthermore, due to the highly heterogeneous nature of real microstructures like concrete, a very complex network of cracks can nucleate, propagate and interact, either from the interfaces and then through the solid phases, or the opposite. Simulating such complex networks of cracks is a well-known issue for meshing algorithms and remeshing techniques are not suited to regular meshes based on voxels, where maintaining the same mesh during the simulation is favorable for robustness and parallel computing purpose.

Apart from cohesive elements, the eXtended Finite Element Method (XFEM) [149, 204] can alleviate the issue of describing arbitrary cracks in regular meshes by using an enriched FEM discretization scheme with additional nodal variables for describing displacement jump over arbitrary surfaces not matching the mesh. However, this technique has shown difficulties to describe crack nucleation and requires level-set function construction to describe the crack, which can be cumbersome when multiple cracks interact. We also mention a related method, called Thick Level-Set method (TLS) [27, 53] in which a level-set function is employed to separate the undamaged zone from the damaged one, and where the crack is a consequence of the damage front motion, allowing crack initiation.

In Chapter 2, the Phase Field Method has been presented and has proved to be very well suited to the simulation of microcracking in complex voxel-based models of concrete microstructures. The technique has been recently adapted to cohesive cracks in [218].

In this chapter, we investigate several models to take into account interfacial damage within the phase field method. First, a simple technique using a volumic damageable interphase is studied. Then, we propose a new phase field formulation modelling interfaces as smeared surfaces. The introduced methodology shares some features with the one proposed by Verhoosel and de Borst [218] but differs by the following points. First, we introduce a new energetic formulation mixing bulk damageable energy and cohesive surface energy such that the interfaces do not initially involve discontinuities and thus no damage in the phase field sense. In this formulation, the phase field describes the bulk crack surface density, as well as the interface crack density, allowing interaction between both crack types in a simple manner. Second, we have investigated two models, one involving internal variables to describe interfacial damage within cohesive traction law, and the other without internal variable. We show that in our formulation, the phase field is sufficient to model crack opening and re-closure without internal variables for interfaces. Third, to describe the diffuse displacement jump at the interface, we use a level-set method without additional variables, unlike in [218]. A special algorithm dedicated to the construction of the level-set functions in voxel-based models of complex microstructures is introduced. The features of the proposed method are summarized as follows:

- The technique allows simulating interfacial cracking in voxel-based regular FEM models of real microstructures, and their interaction with matrix cracks.

- No additional variables are needed to describe the jump at the interface.
- The solution is convergent with respect to the mesh and the crack path is mesh-independent.
- There is no dependence to the mesh structure.
- The phase field describes both the crack density in the matrix and the interface crack density; it can be used as an internal variable to model irreversible damage of the interface.

The content of this chapter is as follows. First, we study in section 3.2 a simple model for interfacial cracking using thick damageable interphases. Then, the proposed method using smeared interfaces is developed in sections 3.3.1 and 3.3.2, where a level-set method is employed to describe the interfaces. A method for the construction of the level-set functions in complex, voxel-based microstructures is proposed in section 3.5. The FEM discretization of the method is developed in section 3.6. Finally, several numerical example involving both interfacial and matrix microcracking in realistic models of microstructures are presented in section 3.7.

3.2 Interphase model

In this section, we investigate a simple model for interfacial damage using a damageable layer of finite thickness with its own mechanical properties (see Fig. 3.2). The classical phase field framework of Chapter 2 is used.

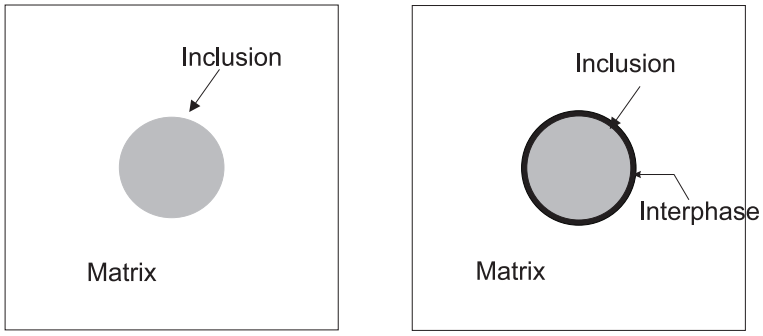

(a) (b)

Figure 3.2: The white color and grey color correspond to the matrix phase and inclusion phase, respectively; (a) microstructure without interphase; (b) microstructure with interphase.

In order to apply this technique to voxel-based models obtained from XR-CT, we define the interphase as a 1 pixel (voxel in 3D)-thick interphase. The associated elements have their own mechanical properties and can damage through the phase field method. To analyze the solutions obtained by such technique, an example is studied in the following. A 2D microstructure obtained from a microtomography image of a real cementitious material is considered (see Fig. 3.3 (a)). In this figure, the white, grey and black colors refer to matrix (cement paste), inclusions (sand) and pores (EPS beads, or air), respectively.

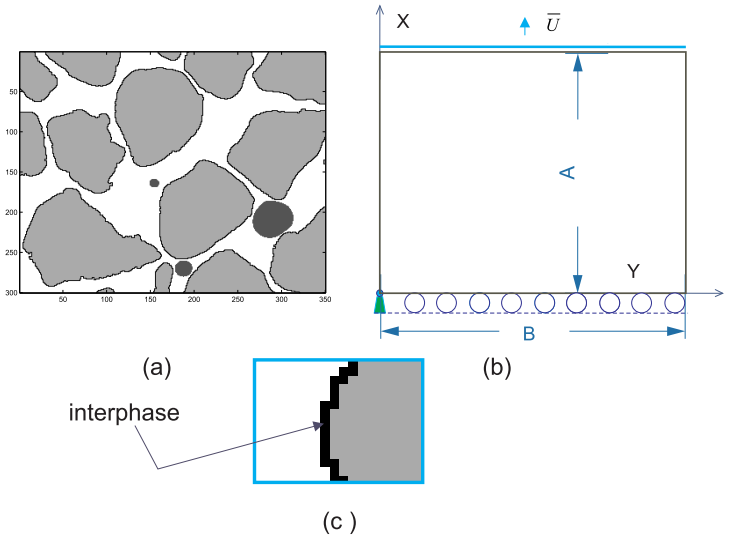

Figure 3.3: Interfacial damage simulation in cement-based material: (a) geometry of the microstructure obtained from segemented microtomography image; (b) domain geometry and loading conditions; (c) zoom on the interphase: the black voxels correspond to interphase voxels.

The boundary conditions are described in Fig. 3.2(b). The image resolution is 350×300 pixels. the interphase is depicted in Fig. 3.3(c). The material properties of the matrix, inclusion or pores, are mapped on a regular grid of square domains associated with finite elements. The material parameters of inclusions and matrix are, respectively: $E_i = 60$ Gpa, $\nu_i = 0.3$, $E_m = 18$ Gpa, and $\nu_m = 0.2$. We have chosen very compliant properties for the pores, $E_p = 10^{-6}$ Gpa, $\nu_p = 10^{-6}$. We study 4 cases:

1. No interphase is considered and the toughness is the same for the matrix and the inclusions, $g_c = 59.3$ N/m. We refer to this model by "No interphase, homogenenous g_c".

2. No interphase is considered and the toughness is here different in the matric and the inclusions, $g_c^m = 59.3$ N/m for matrix and $g_c^{inc} = 200$ N/m for inclusion. We refer to this model by "No interphase, heterogeneous g_c".

3. An interphase is considered and the toughness is here different in the matric and the inclusions, $g_c^m = 59.3$ N/m for matrix and $g_c^{inc} = 200$ N/m for inclusion. the properties of the interfaces are taken as $E_{inter} = E_i \times f_i$, $g_c^{inter} = g_c^m \times f_i$, $f_i = 0.2$. We refer to this model by "Interphase, $f_i = 0.2$".

4. An interphase is considered and the toughness is here different in the matric and the inclusions, $g_c^m = 59.3$ N/m for matrix and $g_c^{inc} = 200$ N/m for inclusion. the properties of the interfaces are taken as $E_{inter} = E_i \times f_i$, $g_c^{inter} = g_c^m \times f_i$, $f_i = 2$. We refer to this model by "Interphase, $f_i = 2$".

These simulation are performed with monotonic displacement increments $\overline{U} = 3.10^{-5}$ mm for the first time steps. When $d_{\max} > 0.5$ we reduce them to $\overline{U} = 3.10^{-6}$ mm for accuracy

purpose. The regularization parameter is chosen as $l = 5$ μm. The crack network in the domain for each model is depiceted in Figs. 3.4 and 3.5.

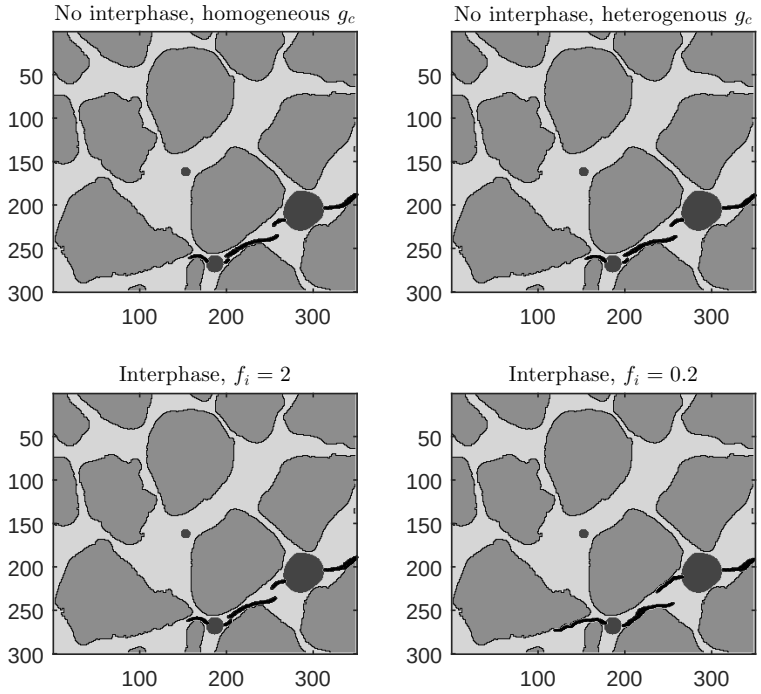

Figure 3.4: Comparison of cracks networks obtained by 4 models. The cracks are depicted in black.

The cracks nucleate in the pores and then propagate roughly horizontally. The stress-displacement curve for the 4 models is depicted in Fig. 3.6. Results are quite similar for the three first models, the crack do not propagate through the interfaces. The model of interphase with $f_i = 2$ leads to crack propagation through the interface, even though the interphase properties are higher in this case than the matrix. This shows that even usable, such model leads to parameters related to the interfaces which do not have a physical meaning. Another issue comes from the definition of the artificial thickness of the interphase. For this reason, we investigate in the next sections interfacial damage models based on a smeared description of interfaces.

3.3 Diffuse approximation of discontinuous fields

For the purpose of the next sections, we introduce here the notion of smeared, or diffuse approximations for discontinuous fields, which will be used in the sequel.

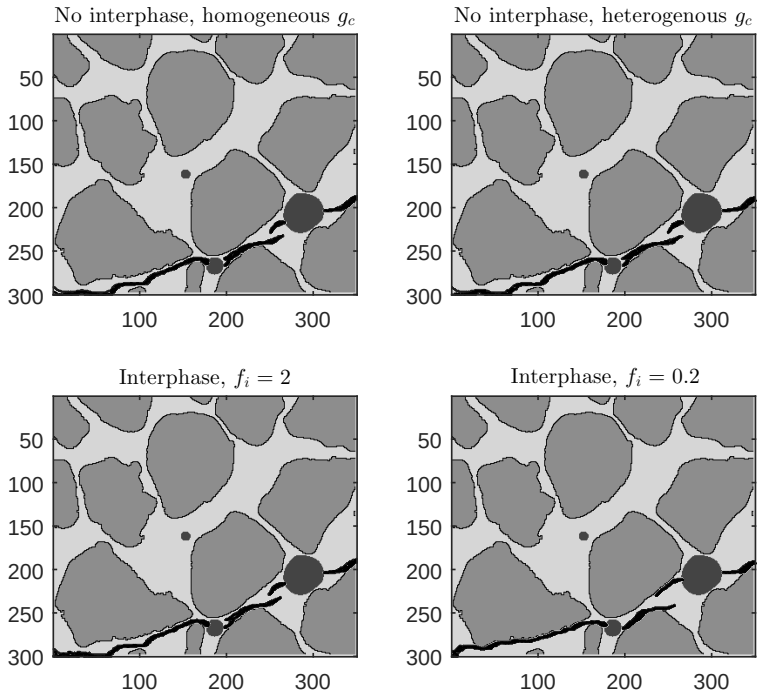

Figure 3.5: Comparison of cracks networks obtained by 4 models: fully broken state.

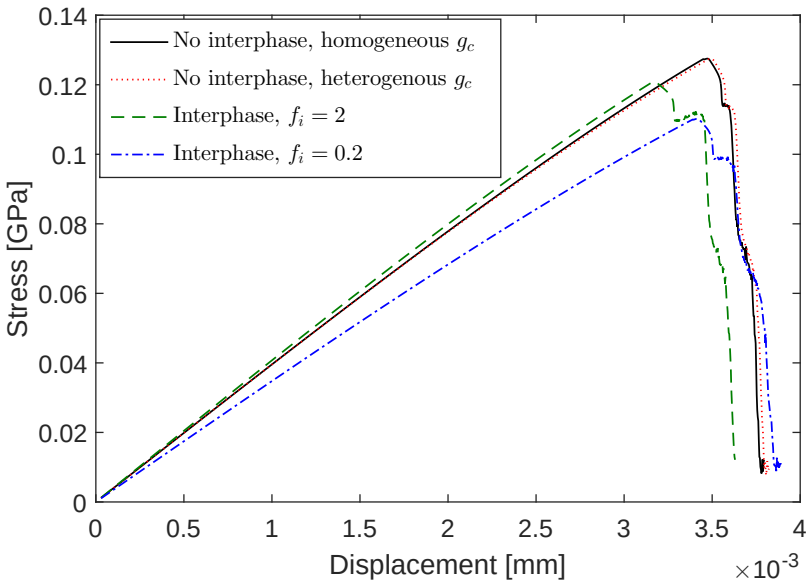

Figure 3.6: Comparison of the 4 models of interphase damage models: load-deflection curve.

3.3.1 Smeared approximation of cracks and interfaces

Let $\Omega \in \mathbb{R}^d$ be an open domain describing a solid with external boundary $\partial\Omega$. The solid is heterogeneous, and contains internal interfaces between the phases, collectively denoted by Γ^I.

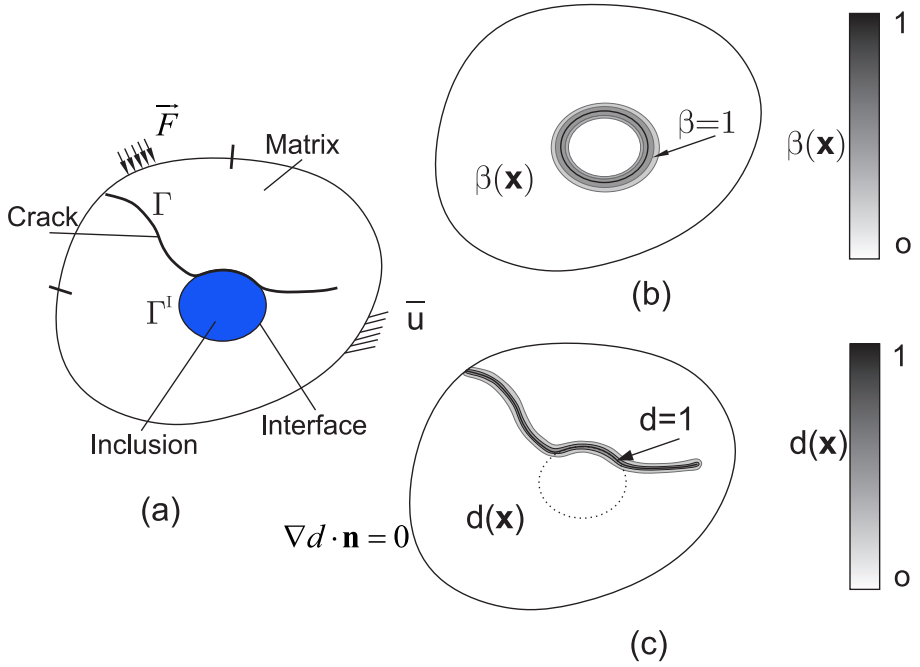

Figure 3.7: Regularized representation of a crack and smeared crack: (a) a body containing an interface and a crack possibly passing through the interface; (b) smeared representation of the interface; (c) smeared representation of the crack.

During the loading, cracks may propagate in the solid phases and can pass through the interfaces as depicted in Fig. 3.7(a). The crack surfaces are collectively denoted by Γ. In the present work, we adopt the regularized framework proposed in [49, 152, 12] for replacing cracks and interfaces surfaces by regularized approximation functions. Cracks are associated with an evoluting phase field $d(\mathbf{x}, t)$ (see Fig. 3.7(c)), while interfaces between phases are associated with a fixed scalar field $\beta(\mathbf{x})$ (see Fig. 3.7(b)). The definition of phase field $d(\mathbf{x}, t)$ was been presented in Chapter 2.

The interfaces are here described in the same manner. The field $\beta(\mathbf{x})$ satisfies:

$$\begin{cases} \beta(\mathbf{x}) - l_\beta^2(\mathbf{x}) \triangle \beta(\mathbf{x}) = 0 \ \text{ in } \Omega, \\ \beta(\mathbf{x}) = 1 \ \text{ on } \Gamma^I, \\ \nabla \beta(\mathbf{x}) \cdot \mathbf{n} = 0 \ \text{ on } \partial\Omega, \end{cases} \tag{3.1}$$

where l_β is the regularization parameter describing the width of the regularized interfaces. Similarly, (3.1) is the Euler-Lagrange equation associated with the variational problem:

$$\beta(\mathbf{x}) = Arg \left\{ \inf_{\beta \in \mathcal{S}_\beta} \Gamma_\beta(\beta) \right\}, \tag{3.2}$$

where $\mathcal{S}_\beta = \left\{ \beta | \beta(\mathbf{x}) = 1 \ \forall \mathbf{x} \in \Gamma^I \right\}$ and $\Gamma_\beta(\beta) = \int_\Omega \gamma_\beta(\beta) d\Omega$, where Γ_β represents the total interface length and γ_β is defined by

$$\gamma_\beta(\beta) = \frac{1}{2 l_\beta} \beta(\mathbf{x})^2 + \frac{l_\beta}{2} \nabla \beta(\mathbf{x}) \cdot \nabla \beta(\mathbf{x}). \tag{3.3}$$

For $l_\beta \to 0$ the above variational principle leads to the exact description of the sharp interface Γ^I. In the following, we will choose identical regularization lengths for cracks and interfaces, i.e. $l_\beta = l$ and that $\beta(\mathbf{x})$ does not change throughout the simulation (the interfaces do not evolve).

3.3.2 Smeared displacement jump approximation

In the present work, the displacement jump $[\![\mathbf{u}(\mathbf{x})]\!]$ created by interface decohesion is approximated as a smooth transition, and defined as follows. Let Γ^I be the interface. We define Γ^I as the zero level-set of a function $\phi(\mathbf{x})$, such that:

$$\begin{cases} \phi(\mathbf{x}) > 0 \text{ for } \mathrm{x} \in \Omega^{\mathrm{i}} \\ \phi(\mathbf{x}) < 0 \text{ for } \mathrm{x} \in \Omega/\Omega^{\mathrm{i}} \\ \phi(\mathbf{x}) = 0 \text{ for } \mathrm{x} \in \Gamma^{\mathrm{I}} \end{cases} \tag{3.4}$$

where Ω^i denotes the set of inclusions, and Ω/Ω^i the matrix[1]. Let h be a small scalar parameter, $\mathbf{x} \in \Gamma^I$ and $\mathbf{n}^I$ the normal vector to Γ^I at the point $\mathbf{x}$. If the function $\phi(\mathbf{x})$ is known, the normal vector to Γ^I is found through:

$$\mathbf{n}^I(\mathbf{x}) = \frac{\nabla\phi(\mathbf{x})}{\|\nabla\phi(\mathbf{x})\|}. \tag{3.5}$$

Using a Taylor expansion at first order of the assumed smoothed regularized displacement fields $\mathbf{u}(\mathbf{x})$, we can express (see Fig. 3.8):

$$\mathbf{u}\left(\mathbf{x} + \frac{h}{2}\mathbf{n}^I\right) \simeq \mathbf{u}(\mathbf{x}) + \frac{h}{2}\nabla\mathbf{u}(\mathbf{x})\mathbf{n}^I, \tag{3.6}$$

$$\mathbf{u}\left(\mathbf{x} - \frac{h}{2}\mathbf{n}^I\right) \simeq \mathbf{u}(\mathbf{x}) - \frac{h}{2}\nabla\mathbf{u}(\mathbf{x})\mathbf{n}^I. \tag{3.7}$$

Then in a regularized context, the displacement jump is not only defined on the interface but over all the domain, and its expression at any point $\mathbf{x} \in \Omega$ is given by:

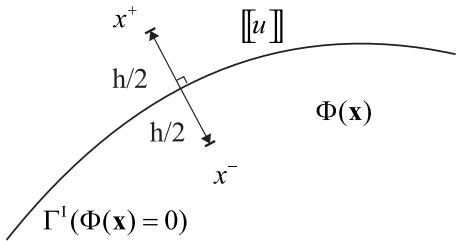

Figure 3.8: Approximation of the displacement jump across the interface.

[1]Note that even though presented here for bi-material interfaces, P interfaces could be considered if P couples of nodes with different materials are involved. In that case, the P interfaces would each have their own geometrical definition through P fields $\beta_i(\mathbf{x})$, $i = 1, ..., P$ and P coefficients g_c^i, $i = 1, ..., P$.

$$[\![\mathbf{u}(\mathbf{x})]\!] \simeq \mathbf{w}(\mathbf{x}) = \mathbf{u}\left(\mathbf{x} + \frac{h}{2}\mathbf{n}^I\right) - \mathbf{u}\left(\mathbf{x} - \frac{h}{2}\mathbf{n}^I\right)$$

$$= h\nabla\mathbf{u}(\mathbf{x})\frac{\nabla\phi(\mathbf{x})}{\|\nabla\phi(\mathbf{x})\|}. \tag{3.8}$$

where $\mathbf{w}(\mathbf{x})$ denotes the smoothed displacement jump approximation.

A detailed description for the numerical computation of $\phi(\mathbf{x})$ for an arbitrary morphology of microstructure described by a regular grid of voxels is provided in section 3.5.

3.4 Phase field incorporating bulk brittle fracture and cohesive interfaces

3.4.1 Energy functional

Let us consider a two-phase solid as described in section 3.3.1. The solid contains both cracks and interfaces, implying strong displacement discontinuities. In a standard framework of sharp discontinuity description, the total energy is given by:

$$E = \int_\Omega W_u\left(\boldsymbol{\varepsilon}(\mathbf{u})\right) d\Omega + \int_\Gamma g_c d\Gamma + \int_{\Gamma^I} \Psi^I([\![\mathbf{u}]\!], \boldsymbol{\alpha}) d\Gamma. \tag{3.9}$$

In (3.9), dS is a density of crack surface, g_c the toughness, Ψ^I is a strain density function depending on the displacement jump across the interface Γ^I and $\boldsymbol{\alpha}$ is a history parameter. If a regularized description for strong discontinuities related to both cracks and interfaces is adopted (substituting $[\![\mathbf{u}]\!]$ by $\mathbf{w}(\mathbf{x})$), then propose to split the infinitesimal strain tensor into a part related to the bulk and a part induced by the smoothed jump at the interfaces, denoted by $\boldsymbol{\varepsilon}^e$ and $\tilde{\boldsymbol{\varepsilon}}$, respectively:

$$\boldsymbol{\varepsilon} = \boldsymbol{\varepsilon}^e + \tilde{\boldsymbol{\varepsilon}}. \tag{3.10}$$

This decomposition is proposed here such that $\tilde{\boldsymbol{\varepsilon}} \to 0$ away from the interfaces, i.e. when $\beta(\mathbf{x}) \to 0$. Then, we propose to replace the above functional by the following one:

$$E = \int_\Omega W_u^e\left(\boldsymbol{\varepsilon}^e(\mathbf{u}, \beta), d\right) d\Omega + \int_\Omega [1 - \beta(\mathbf{x})] g_c \gamma_d(d) d\Omega,$$

$$+ \int_\Omega \Psi^I(\mathbf{w}, \boldsymbol{\alpha}) \gamma_\beta(\beta) d\Omega. \tag{3.11}$$

where γ_d and γ_β have been defined in section (3.3.1).

The factor $[1-\beta(\mathbf{x})]$ is introduced so as to verify that for $\beta(\mathbf{x}) \to 0$ (away from the interface) which includes $\gamma_\beta \to 0$ and $\boldsymbol{\varepsilon}^e \to \boldsymbol{\varepsilon}$. As a consequence of these definitions, we recover the regularized energy functional for brittle fracture without interfaces [79, 49]:

$$E = \int_{\Omega} W_u\left(\boldsymbol{\varepsilon}(\mathbf{u}), d\right) d\Omega + \int_{\Omega} g_c \gamma_d(d) d\Omega. \tag{3.12}$$

In (3.11), we identify

$$W = W_u^e\left(\boldsymbol{\varepsilon}^e(\mathbf{u}, \beta), d\right) + [1 - \beta(\mathbf{x})] g_c \gamma_d(d) + \Psi^I(\mathbf{w}, \boldsymbol{\alpha}) \gamma_\beta(\beta) \tag{3.13}$$

as the free energy. Using the variational principle for minimizing E with respect to displacements, i.e.

$$\mathbf{u}(\mathbf{x}) = Arg\left\{ \inf_{\mathbf{u} \in \mathcal{S}_u} \left(E(\mathbf{u}, d, \beta, \alpha) - W^{ext} \right) \right\} \tag{3.14}$$

where $\mathcal{S}_u = \left\{ \mathbf{u} | \mathbf{u}(\mathbf{x}) = \bar{\mathbf{u}} \text{ on } \partial\Omega_u, \ \ \mathbf{u} \in H^1(\Omega) \right\}$ and $W^{ext} = \int_\Omega \mathbf{f} \cdot \mathbf{u} d\Omega + \int_{\partial\Omega_F} \overline{\mathbf{F}} \cdot \mathbf{u} d\Gamma$ with $\mathbf{f}$ and $\overline{\mathbf{F}}$ being body forces and prescribed traction over the boundary $\partial\Omega_F$, we obtain the weak form for $\mathbf{u}(\mathbf{x}) \in \mathcal{S}_u$:

$$\begin{aligned} \int_{\Omega} \frac{\partial W_u^e}{\partial \boldsymbol{\varepsilon}^e} : \boldsymbol{\varepsilon}^e(\delta\mathbf{u}) d\Omega + \int_{\Omega} \frac{\partial \Psi^I(\mathbf{w}, \boldsymbol{\alpha})}{\partial \mathbf{w}} \cdot \delta\mathbf{w} \gamma_\beta(\beta) d\Omega, \\ = \int_{\Omega} \mathbf{f} \cdot \delta\mathbf{u} d\Omega + \int_{\partial\Omega_F} \overline{\mathbf{F}} \cdot \delta\mathbf{u} d\Gamma = \delta W^{ext} \end{aligned} \tag{3.15}$$

In the absence of body forces ($\mathbf{f} = \mathbf{0}$), invoking the local balance of stress and global balance of power (i.e. $\int_\Omega \boldsymbol{\sigma}^e : \boldsymbol{\varepsilon}^e d\Omega = \delta W^{ext}$) and using the divergence theorem we can re-write (3.15) as:

$$\int_{\Omega} \boldsymbol{\sigma}^e : \boldsymbol{\varepsilon}^e(\delta\mathbf{u}) d\Omega + \mathbf{t}(\mathbf{w}, \boldsymbol{\alpha}) \cdot \delta\mathbf{w} \gamma_\beta(\beta) d\Omega - \int_{\Omega} \boldsymbol{\sigma}^e : \nabla^s \delta\mathbf{u} d\Omega = 0 \tag{3.16}$$

where $\boldsymbol{\sigma}^e = \frac{\partial W_e}{\partial \boldsymbol{\varepsilon}^e}$ is the Cauchy stress and $\mathbf{t}(\mathbf{w}, \boldsymbol{\alpha}) = \frac{\partial \Psi^I(\mathbf{w}, \boldsymbol{\alpha})}{\partial \mathbf{w}}$ is the traction vector acting on the interface oriented by $\mathbf{n}^I$ and associated with the displacement jump at the interface, as a consequence of the assumptions on the elastic behaviour of the bulk material and the partitioning of the local strain near the interface. In (3.16), $\delta\mathbf{w}$ is obtained using (3.8) as:

$$\delta\mathbf{w}(\mathbf{x}) = h \nabla \delta\mathbf{u}(\mathbf{x}) \frac{\nabla\phi(\mathbf{x})}{\|\nabla\phi(\mathbf{x})\|}. \tag{3.17}$$

Using $\boldsymbol{\sigma}^e \mathbf{n} = \mathbf{t}$, Eq. (3.16) can be further re-written as:

$$\int_{\Omega} \boldsymbol{\sigma}^e : \left\{ \boldsymbol{\varepsilon}^e(\delta\mathbf{u}) + \mathbf{n} \otimes \delta\mathbf{w} \gamma_\beta(\beta) - \nabla^s \delta\mathbf{u} \right\} d\Omega = 0 \tag{3.18}$$

which is satisfied for an admissible strain field in the form:

$$\boldsymbol{\varepsilon}^e = \nabla^s \mathbf{u} - \mathbf{n} \otimes^s \mathbf{w} \gamma_\beta, \tag{3.19}$$

where $\left(\nabla^s \mathbf{u}\right)_{ij} = \frac{1}{2}\left(u_{i,j} + u_{j,i}\right)$ and $\left(\mathbf{n} \otimes^s \mathbf{w}\right)_{ij} = \frac{1}{2}\left(n_i w_j + w_i n_j\right)$. From (3.10) we identify $\tilde{\boldsymbol{\varepsilon}}$ as:

$$\tilde{\boldsymbol{\varepsilon}} = \mathbf{n} \otimes^s \mathbf{w} \gamma_\beta. \tag{3.20}$$

3.4.2 Phase field problem

The reduced Clausius-Duhem inequality relative to the evolution of the damage parameter d has been defined in (2.16). According to the local normality law (2.23), it yields that for $\dot{d} > 0$, $F = 0$ which gives (see more details in Chapter 2):

$$F = -\frac{\partial W}{\partial d} = -\left\{ \frac{\partial W_u^e}{\partial d} + [1-\beta] g_c Y_c(d) \right\} = 0, \tag{3.21}$$

where:

$$Y_c(d) = \frac{d}{l_d} - l_d \Delta d. \tag{3.22}$$

We assumed an isotropic elastic behavior of he phases in both the initial and damaged state, with initial Lamés's coefficients λ and μ. To take into account unilateral contact, damage is assumed to modify the sole tensile part of the elastic energy, which is defined as

$$W_u^e = \Psi_e^+(\boldsymbol{\varepsilon}^e) \{g(d) + k\} + \Psi_e^-(\boldsymbol{\varepsilon}^e) \tag{3.23}$$

where

$$\boldsymbol{\varepsilon}^e = \boldsymbol{\varepsilon}^{e+} + \boldsymbol{\varepsilon}^{e-} \tag{3.24}$$

and

$$\Psi_e^{\pm}(\boldsymbol{\varepsilon}) = \frac{\lambda}{2} \left(\langle Tr(\boldsymbol{\varepsilon}^e) \rangle_{\pm} \right)^2 + \mu Tr \left\{ \left(\boldsymbol{\varepsilon}^{e\pm} \right)^2 \right\}. \tag{3.25}$$

These two contributions to the strain energy are then defined as:

$$\boldsymbol{\varepsilon}^{e\pm} = \sum_{i=1}^{D} \left\langle \varepsilon^i \right\rangle_{\pm} \mathbf{n}^i \otimes \mathbf{n}^i, \tag{3.26}$$

and ε^i and $\mathbf{n}^i$ are the eigenvalues and eigenvectors of $\boldsymbol{\varepsilon}^e$, i.e. satisfying $\boldsymbol{\varepsilon}^e \mathbf{n}^i = \varepsilon^i \mathbf{n}^i$. In (3.25) - (3.26), $\langle x \rangle_{\pm} = (x \pm |x|)/2$. The degradation function $g(d)$ is assumed to have the simple form $g(d) = (1-d)^2$. The small parameter $k << 1$ is introduced to maintain the well-posedness of the system for partially broken parts of the domain while perturbating the strain energy in non damaged parts to a negligible level. It follows that when $\dot{d} > 0$ then:

$$-2(1-d)\Psi_e^+ + [1-\beta] g_c Y_c(d) = 0. \tag{3.27}$$

It is worth noting that as $2(1-d)\Psi_e^+ \geq 0$, then $Y_c(d) \geq 0$, yielding $\dot{\Gamma}^d \geq 0$. To handle loading and unloading history, we follow Miehe et al. [49] and introduce the strain history function

$$\mathcal{H}(\mathbf{x}, t) = \max_{\tau \in [0,t]} \left\{ \Psi_e^+(\mathbf{x}, \tau) \right\} \tag{3.28}$$

which is substituted to Ψ_e^+ in (3.28). It yields the following phase field problem to be solved to evaluate the field $d(\mathbf{x}, t)$ at time t, using (3.22):

$$\begin{cases} 2(1-d)\mathcal{H} - (1-\beta)\frac{g_c}{l_d}\left\{d - l_d^2\Delta d\right\} = 0 \ \text{ in } \Omega, \\ d(\mathbf{x}) = 1 \ \text{ on } \Gamma, \\ \nabla d(\mathbf{x}) \cdot \mathbf{n} = 0 \ \text{ on } \partial\Omega. \end{cases} \tag{3.29}$$

The associated weak form is obtained as:

$$\int_\Omega \left\{ \left(2\mathcal{H} + [1-\beta]\frac{g_c}{l_d} \right) d\delta d + [1-\beta] g_c l_d \nabla d \cdot \nabla(\delta d) \right\} d\Omega = \int_\Omega 2\mathcal{H}\delta d d\Omega. \tag{3.30}$$

3.4.3 Displacement problem

3.4.3.1 Governing equations

The weak form associated with the displacement problem has been defined in (3.15), with the above described strain energy, the Cauchy stress now reads:

$$\boldsymbol{\sigma}^e = \frac{\partial \Psi_e^+}{\partial \boldsymbol{\varepsilon}^e}\left\{g(d) + k\right\} + \frac{\partial \Psi_e^-}{\partial \boldsymbol{\varepsilon}^e}$$

$$= \left((1-d)^2 + k\right)\left\{\lambda \left\langle Tr\boldsymbol{\varepsilon}^e \right\rangle_+ \mathbf{1} + 2\mu\boldsymbol{\varepsilon}^{e+}\right\} + \lambda \left\langle Tr\boldsymbol{\varepsilon}^e \right\rangle_- \mathbf{1} + 2\mu\boldsymbol{\varepsilon}^{e-}. \tag{3.31}$$

In the applications of the following work, we have used the numerical value $k = 10^{-8}$.

3.4.3.2 Cohesive model

Regarding the constitutive relation of the interface, two models are investigated in the present paper. The general form in 2D is given by

$$\mathbf{t}(\mathbf{w}, \boldsymbol{\alpha}) = [t^n, \ t^t]^{\mathrm{T}} \tag{3.32}$$

where t^n and t^t denote normal and tangential parts of the traction vector $\mathbf{t}$ across the interface Γ^I oriented by its normal $\mathbf{n}^I$. In a first model (called M1), a nonlinear elastic cohesive model without dependence on history is used [66, 218]:

$$t^n = g_c^I \frac{\mathrm{w^n}}{\delta^n} \exp(-\frac{\mathrm{w^n}}{\delta^{\mathrm{n}}}) \exp(-\frac{\left(\mathrm{w^t}\right)^2}{(\delta^{\mathrm{t}})^2}), \tag{3.33}$$

where $\mathrm{w^n} = \mathbf{w} \cdot \mathbf{n}^{\mathrm{I}}$ and $\mathrm{w^t} = \mathbf{w} \cdot \mathbf{m}^{\mathrm{I}}$, $\mathbf{m}^I$ being a tangent vector to Γ^I, g_c^I is the toughness associated with the interface, and

$$t^t = 2g_c^I \frac{\mathrm{w^t}}{\delta^t}(1 + \frac{\mathrm{w^n}}{\delta^n}) \exp(-\frac{\mathrm{w^n}}{\delta^{\mathrm{n}}}) \exp(-\frac{\left(\mathrm{w^t}\right)^2}{(\delta^{\mathrm{t}})^2}). \tag{3.34}$$

The relation between δ^n, the toughness g_c^I (which corresponds to the total area under the traction-opening curve) and the fracture strength t_u is given by $\delta^n = g_c^I/(t_u e)$, $e = \exp(1)$ (see Fig. 3.9).

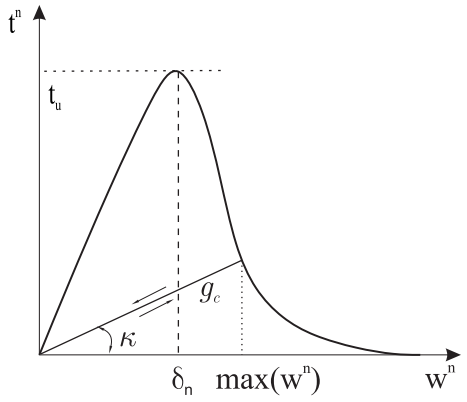

Figure 3.9: Cohesive model for the interfaces.

Another possible model, denoted by (M2), introduces a history parameter to describe the irreversible damage in the interface (see Fig. 3.9). In that case, the expression of the traction at the interface is given e.g. for the normal traction by

$$t^n(\mathbf{w},\boldsymbol{\alpha}) = \begin{cases} \text{Eqs. (3.33)} & \text{if } \mathrm{w^n}(\mathbf{x},\mathrm{t}) \geq \alpha^{\mathrm{n}}(\mathrm{t}) \\ \mathcal{K}^n \mathrm{w^n} & \text{if } \mathrm{w^n}(\mathbf{x},\mathrm{t}) < \alpha^{\mathrm{n}}(\mathrm{t}) \end{cases} \tag{3.35}$$

with:

$$\alpha^n(\mathbf{x},t) = \underset{\tau\in[0,t]}{max} \left\{\mathrm{w^n}(\mathbf{x},\tau)\right\}, \tag{3.36}$$

and

$$\mathcal{K}^n = \frac{t^n(\alpha(\mathbf{x},\mathrm{t}))}{\alpha^n(\mathbf{x},\mathrm{t})}. \tag{3.37}$$

Similarly,

$$t^t(\mathbf{w},\boldsymbol{\alpha}) = \begin{cases} \text{Eqs. (3.34)} & \text{if } \mathrm{w^t}(\mathbf{x},\mathrm{t}) \geq \alpha^{\mathrm{t}}(\mathrm{t}) \\ \mathcal{K}^t \mathrm{w^t} & \text{if } \mathrm{w^t}(\mathbf{x},\mathrm{t}) < \alpha^{\mathrm{t}}(\mathrm{t}) \end{cases} \tag{3.38}$$

with:

$$\alpha^t(\mathbf{x},t) = \underset{\tau\in[0,t]}{max} \left\{\mathrm{w^t}(\mathbf{x},\tau)\right\}, \tag{3.39}$$

and

$$\mathcal{K}^t = \frac{t^t(\alpha^t(\mathbf{x},\mathrm{t}))}{\alpha^t(\mathbf{x},\mathrm{t})}. \tag{3.40}$$

Note that in the model M1, no internal variable is involved. In the model M2, we introduce only one internal variable α^n for the normal traction component in the cohesive model for the sake of simplicity, the tangential part of the traction was assumed to be zero.

3.4.4 Linearization of the displacement problem

We note that for a fixed value of d, the mechanical problem (3.15) is nonlinear, because of the decomposition (3.24) which requires computing the eigenvalues of $\boldsymbol{\varepsilon}^e$ and the nonlinear interfacial law (3.33)-(3.34). In what follows, we introduce a linearization procedure to solve the problem by the Newton method.

From (3.15) and (3.31) can we rewrite the balance equation as

$$\mathcal{R} = \int_\Omega \boldsymbol{\sigma}^e : \varepsilon^e(\delta\mathbf{u}) d\Omega + \int_\Omega \gamma_\beta(\mathbf{x})\mathbf{t}(\mathbf{w},\alpha)\cdot\delta\mathbf{w} d\Omega - \int_\Omega \mathbf{f}\cdot\delta\mathbf{u} d\Omega - \int_{\partial\Omega_F} \overline{\mathbf{F}}\cdot\delta\mathbf{u} d\Gamma = 0. \tag{3.41}$$

where $\varepsilon^e(\delta\mathbf{u}) = \nabla^s(\delta\mathbf{u}) - \mathbf{n}\otimes^s \delta\mathbf{w}\gamma_\beta$. In a standard Newton method, the displacements are updated for each loading increment by solving the tangent problem:

$$D_{\Delta u}\mathcal{R}(\mathbf{u}^k, d) = -\mathcal{R}(\mathbf{u}^k, d) = 0, \tag{3.42}$$

where $\mathbf{u}^k$ is the displacement solution known from the previous iteration. The displacement corrections are obtained as

$$\mathbf{u}^{k+1} = \mathbf{u}^k + \Delta\mathbf{u}. \tag{3.43}$$

In (3.42),

$$D_{\Delta\mathbf{u}}\mathcal{R}(\mathbf{u}^k) = \int_\Omega \frac{\partial\boldsymbol{\sigma}^e}{\partial\boldsymbol{\varepsilon}^e} : \varepsilon^e(\Delta\boldsymbol{\varepsilon}) : \varepsilon^e(\delta\boldsymbol{\varepsilon}) + \int_\Omega \frac{\partial\mathbf{t}(\mathbf{w})}{\partial\mathbf{w}} : \Delta\mathbf{w} : \delta\mathbf{w} d\Omega$$

with

$$\Delta\mathbf{w}(\mathbf{x}) = h\nabla\Delta\mathbf{u}(\mathbf{x})\frac{\nabla\phi(\mathbf{x})}{\|\nabla\phi(\mathbf{x})\|} \tag{3.44}$$

and

$$\frac{\partial\boldsymbol{\sigma}^e}{\partial\boldsymbol{\varepsilon}^e} = \mathbb{C}(\mathbf{u}, d)$$

$$= ((1-d)^2 + k)\left\{\lambda R^+[\mathbf{1}]^T[\mathbf{1}] + 2\mu\mathbf{P}^+\right\} + \left\{\lambda R^-[\mathbf{1}]^T[\mathbf{1}] + 2\mu\mathbf{P}^-\right\} \tag{3.45}$$

where the operators $R^\pm$ and $\mathbf{P}^\pm$ have been defined in [158], and λ , μ are the material parameters.

For the model M1, we obtain:

$$\frac{\partial\mathbf{t}(\mathbf{w})}{\partial\mathbf{w}} = \mathbf{K}_I = \begin{bmatrix} D_{nn} & D_{nt} \\ D_{tn} & D_{tt} \end{bmatrix} \tag{3.46}$$

with

$$D_{nn} = \frac{\partial \mathrm{t}^{\mathrm{n}}}{\partial w^n},\ D_{nt} = \frac{\partial \mathrm{t}^{\mathrm{n}}}{\partial w^t},\ D_{tn} = \frac{\partial \mathrm{t}^{\mathrm{t}}}{\partial w^n},\ D_{tt} = \frac{\partial \mathrm{t}^{\mathrm{t}}}{\partial w^t}. \tag{3.47}$$

The expressions of D_{nn}, D_{nt}, D_{tn} and D_{tt} are provided in Appendix A.2. For the model M2, we obtain:

$$\frac{\partial \mathbf{t}(\mathbf{w}, \boldsymbol{\alpha})}{\partial \mathbf{w}} = \begin{cases} (3.47) & \text{if } \mathrm{w}(\mathbf{x}, \mathrm{t}) \geq \alpha(\mathrm{t}) \\ \mathcal{K}\mathbf{1} & \text{if } \mathrm{w}(\mathbf{x}, \mathrm{t}) < \alpha(\mathrm{t}), \end{cases} \tag{3.48}$$

where $\mathcal{K}$ has been defined in (3.37).

3.5 A simple method for constructing the level-set function for arbitrary shaped inclusions in regular meshes

A major difficulty when dealing with complex morphologies provided by voxel-based models (i.e. where each voxel is associated with a square element in 2D and to a cubic element in 3D) is to construct the level-set function $\phi(\mathbf{x})$. For example, Hamilton-Jacobi methods and upwind schemes [160] are very complex to implement and can fail for non-convex inclusions. To overcome these limitations, we propose in this thesis work a simple technique for constructing the level-set function for arbitrary shaped inclusions in regular meshes as provided in voxel-based models[2]. Let Ω^i a domain associated with inclusions such that $\Omega^i \subset \Omega$. We first solve the following problem:

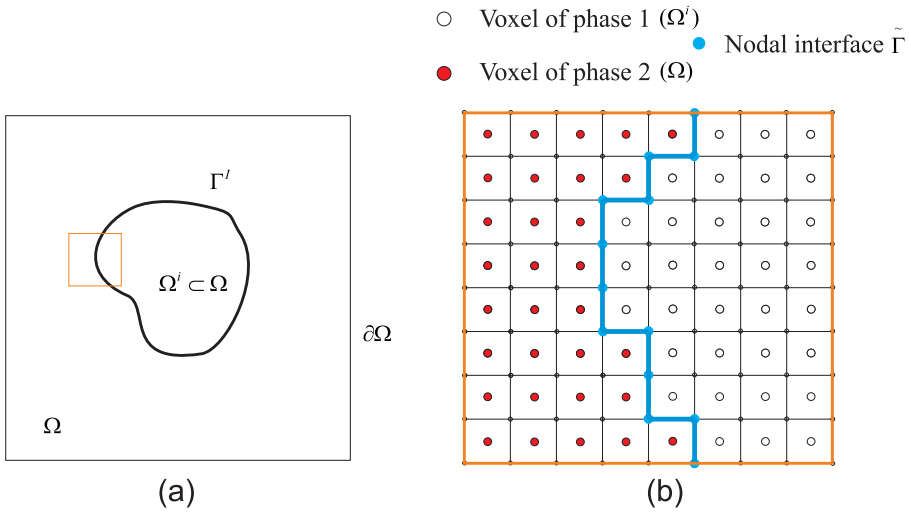

Figure 3.10: (a) Schematic of the geometrical interfaces separating an inclusion Ω^i and the matrix; (b) interface nodes.

$$\begin{cases} \Delta\phi^0(\mathbf{x}) + f(\mathbf{x}) = 0 \ \text{ in } \Omega \\ \phi^0(x) = 0 \ \text{ in } \tilde{\Gamma}, \\ \nabla\phi^0(\mathbf{x}) \cdot \mathbf{n} = 0 \ \text{ on } \partial\Omega, \end{cases} \tag{3.49}$$

[2]Note that we use abusively the term voxel, even though in 2D the term pixel would be more appropriate.

where $\tilde{\Gamma}$ is the interface composed by the set of nodes defined as follows (blue curve in Fig. 3.10(b)). We detect the nodes which are at the corners of voxels on the interface by a simple algorithm (see Fig. 3.10): first, indices are assigned to each element, to indicate its belonging to the different phases. Second, for each node, we loop over the elements connected to the node. If at least two indices are different, then the node is defined as an interface node. In Fig. 3.11 we depict an inclusion defined in a voxel grid. In Fig. 3.11 (a), the nodes belonging to the interface are depicted in black. The source function $f(\mathbf{x})$ is defined as

$$f(\mathbf{x}) = \chi(\mathbf{x}) f_1 + (1 - \chi(\mathbf{x})) f_2, \tag{3.50}$$

$\chi(\mathbf{x})$ is a characteristic function such that $\chi(\mathbf{x}) = 1$ in Ω^i and zero elsewhere, and f_1 and f_2 are scalar parameters. The problem (3.49) is solved by finite elements. In the present test, we have used the following parameters $f_1 = 5$ and $f_2 = -5$. In Fig. 3.11(b), we show the obtained zero level of $\phi^0(\mathbf{x})$. We note that the obtained interface is not smooth, which can induce high local values of the gradient of $\phi(\mathbf{x})$ and numerical errors when evaluating the normal $\mathbf{n}^I$ and the displacement jump $[\![\mathbf{u}(\mathbf{x})]\!] \simeq \mathbf{w}(\mathbf{x})$. We then propose the following correction step: for the nodes of the interface, we solve a second problem defined by:

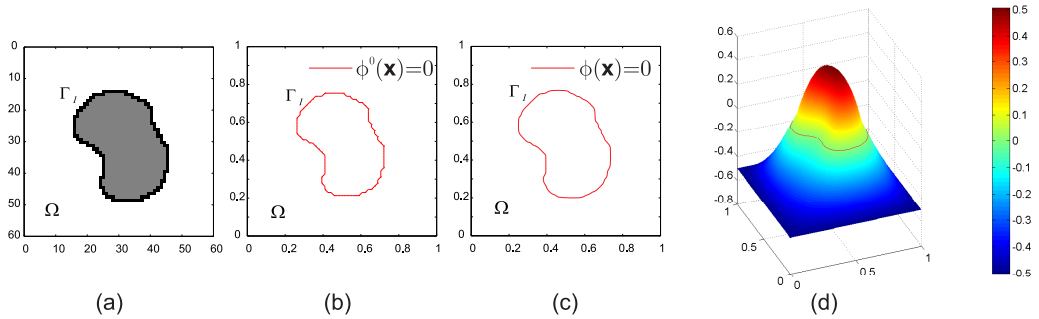

Figure 3.11: Construction of the level-set function for an arbitrary geometry of inclusion: (a) nodes of the interface; (b) zero-level set obtained from the first step of the proposed algorithm; (c) zero-level set obtained from the second step of the proposed algorithm; (d) corresponding level-set function.

$$\begin{cases} \Delta\phi(\mathbf{x}) + f(\mathbf{x}) = 0 \ \text{ in } \Omega \\ \phi(x) = \phi^0(x) \ \text{ in } \Omega/\tilde{\Gamma}, \end{cases} \tag{3.51}$$

In practice, all nodes but the interface nodes are set with the values obtained in the problem (3.49). The only unknowns are the nodal values of the interface nodes. Then this step only requires to solve a small linear problem. In Fig. 3.11(c), we show the zero level of the obtained level-set function $\phi(\mathbf{x})$, which presents a nice smooth boundary. Note that the choice of the ratio f_1/f_2 relies on the microstructural morphology, and more specifically on the number of voxels between two inclusions.

3.6 Discretization and numerical implementation

3.6.1 FEM discretization of displacement problem

A 2D plane strain FEM discretization is described in the following, even though extension to 3D is straightforward. The vector form of second-order tensors are introduced as $[\boldsymbol{\varepsilon}] = \left\{\varepsilon_{11}; \varepsilon_{22}; \sqrt{2}\varepsilon_{12}\right\}^{\mathrm{T}}$, $[\boldsymbol{\sigma}] = \left\{\sigma_{11}; \sigma_{22}; \sqrt{2}\sigma_{12}\right\}^{\mathrm{T}}$, as well as the FEM approximations $\mathbf{u} = \mathbf{N}\mathbf{u}^e$, $\delta\mathbf{u} = \mathbf{N}\delta\mathbf{u}^e$, and $\Delta\mathbf{u} = \mathbf{N}\Delta\mathbf{u}^e$ where $\mathbf{u}^e$, $\delta\mathbf{u}^e$ and $\Delta\mathbf{u}^e$ are nodal displacement components in one element, nodal trial function components and nodal incremental displacement components, respectively. Furthermore, we have:

$$[\boldsymbol{\varepsilon}](\Delta\mathbf{u}) = \mathbf{B}_u\Delta\mathbf{u}^e, \quad [\boldsymbol{\varepsilon}](\delta\mathbf{u}) = \mathbf{B}_u\delta\mathbf{u}^e \tag{3.52}$$

where $\mathbf{B}_u$ is a matrix of shape function derivatives. From (3.8) the diffuse jump approximation vector $\mathbf{w}$ and its incremental counterparts can be discretized as:

$$\mathbf{w} = h\mathbf{N}\tilde{\mathbf{B}}_u\mathbf{u}^e, \quad \Delta\mathbf{w} = h\mathbf{N}\tilde{\mathbf{B}}_u\Delta\mathbf{u}^e, \quad \delta\mathbf{w} = h\mathbf{N}\tilde{\mathbf{B}}_u\delta\mathbf{u}^e, \tag{3.53}$$

where

$$\mathbf{N} = \begin{bmatrix} n_1 & n_2 & 0 & 0 \\ 0 & 0 & n_1 & n_2 \end{bmatrix}, \tag{3.54}$$

and n_1 and n_2 are the $x-$ and $y-$ components of the normal vector $\mathbf{n}^I$ computed from (3.5), and based on the level-set function ϕ constructed as described in the previous section, and $\tilde{\mathbf{B}}_u$ is a matrix of shape functions derivatives such that

$$\begin{bmatrix} \frac{\partial u_1}{\partial x_1} \\ \frac{\partial u_1}{\partial x_2} \\ \frac{\partial u_2}{\partial x_1} \\ \frac{\partial u_2}{\partial x_2} \end{bmatrix} = \tilde{\mathbf{B}}_u\mathbf{u}^e. \tag{3.55}$$

We define the vector associated with $\tilde{\boldsymbol{\varepsilon}}$ by:

$$[\tilde{\boldsymbol{\varepsilon}}] = \begin{bmatrix} \tilde{\varepsilon}_{11} \\ \tilde{\varepsilon}_{22} \\ \sqrt{2}\tilde{\varepsilon}_{12} \end{bmatrix} = \gamma_\beta(\mathbf{x}) \begin{bmatrix} w_1 n_1 \\ w_2 n_2 \\ \frac{1}{\sqrt{2}}(w_1 n_2 + w_2 n_1) \end{bmatrix}. \tag{3.56}$$

Then we have:

$$[\tilde{\boldsymbol{\varepsilon}}(\Delta\mathbf{u})] = h\gamma_\beta(\mathbf{x})\mathbf{M}\tilde{\mathbf{B}}_u\Delta\mathbf{u}^e \tag{3.57}$$

where

$$\mathbf{M} = \begin{bmatrix} n_1^2 & n_1 n_2 & 0 & 0 \\ 0 & 0 & n_1 n_2 & n_2^2 \\ \frac{1}{\sqrt{2}}n_1 n_2 & \frac{1}{\sqrt{2}}n_2^2 & \frac{1}{\sqrt{2}}n_1^2 & \frac{1}{\sqrt{2}}n_1 n_2 \end{bmatrix}. \tag{3.58}$$

After discretization, the linear system (3.42) reduces to the set of linear algebraic equations:

$$\mathbf{K}_{tan}\Delta\tilde{\mathbf{u}} = -\mathbf{R}(\tilde{\mathbf{u}}^k) \tag{3.59}$$

where $\tilde{\mathbf{u}}$ is a column vector containing the nodal values of $\mathbf{u}$ and

$$\mathbf{K}_{tan} = \int_\Omega \left[\mathbf{B}_u^T - h\gamma_\beta(\mathbf{x})\tilde{\mathbf{B}}_u^T\mathbf{M}^T\right]\mathbf{C}(\mathbf{x})\left[\mathbf{B}_u - h\gamma_\beta(\mathbf{x})\mathbf{M}\tilde{\mathbf{B}}_u\right]d\Omega$$

$$+\int_\Omega h^2\gamma_\beta(\mathbf{x})\tilde{\mathbf{B}}_u^T\mathbf{N}^T\mathbf{K}_I\mathbf{N}\tilde{\mathbf{B}}_u d\Omega, \tag{3.60}$$

and

$$\mathbf{R} = \int_\Omega \left[\mathbf{B}_u^T - h\gamma_\beta(\mathbf{x})\tilde{\mathbf{B}}_u^T\mathbf{M}^T\right]\mathbf{C}(\mathbf{x})\left[\mathbf{B}_u - h\gamma_\beta(\mathbf{x})\mathbf{M}\tilde{\mathbf{B}}_u\right](\mathbf{u}^e)^k\, d\Omega$$

$$+\int_\Omega h\gamma_\beta(\mathbf{x})\tilde{\mathbf{B}}_u^T\mathbf{N}^T\mathbf{t}(\mathbf{w}^k)d\Omega + \int_\Omega \mathbf{f}\mathbf{N}^T d\Omega + \int_{\Omega_F}\overline{\mathbf{F}}\mathbf{N}^T d\Gamma. \tag{3.61}$$

In Eq. (3.60), $\mathbf{C}$ is the matrix form corresponding to the fourth-order tensor $\mathbb{C}$ in Eq. (3.45).

3.6.2 FEM discretization of the phase field problem

As we employ a staggered procedure, we solve alternatively the phase field problem and then the mechanical problem. Given displacements from the mechanical problem, the phase field problem is linear. Introducing the phase field discretization provided in section 3.4.2 to the above equations leads to the discrete system:

$$\mathbf{K}_d\tilde{\mathbf{d}} = \mathbf{F}_d \tag{3.62}$$

where $\tilde{\mathbf{d}}$ is a column vector containing the nodal values of $\mathbf{d}$ and

$$\mathbf{K}_d = \int_\Omega \left\{\left(\frac{g_c}{l}(1-\beta) + 2\mathcal{H}\right)\mathbf{N}_\mathbf{d}^\mathbf{T}\mathbf{N}_\mathbf{d} + (1-\beta)g_c l\mathbf{B}_d^T\mathbf{B}_d\right\}d\Omega \tag{3.63}$$

and

$$\mathbf{F}_d = \int_\Omega 2\mathbf{N}_d^T\mathcal{H}(\mathbf{u}_n)d\Omega. \tag{3.64}$$

3.6.3 Overall algorithm

The overall algorithm is described in the following.

- **Initialization**

  1.1 Initialize the displacement field $\mathbf{u}_0(\mathbf{x})$, the phase field $d_0(\mathbf{x})$, and the strain-history functional $\mathcal{H}_0 = 0$.

1.2 Compute the level-set function $\phi(\mathbf{x})$ by means of the algorithm described in section 3.5.

1.3 Compute the phase field $\beta(\mathbf{x})$ by solving (3.1).

- **FOR** all loading increment (pseudo time t^{n+1}):
  Given $\mathbf{u}_n$, d_n and $\mathcal{H}_n(\mathbf{x})$:

2.1 Compute the strain history functional $\mathcal{H}_{n+1}(\mathbf{x})$ by (3.28).

2.2 Compute $d_{n+1}(\mathbf{x})$ by solving the linear phase field problem (3.62).

2.3 Compute $\mathbf{u}_{n+1}(\mathbf{x})$:
Initialize $\mathbf{u}_k = \mathbf{u}_n$ (displacement of time t_n)
WHILE $\parallel \Delta\mathbf{u}_{k+1} \parallel > \epsilon$, $\epsilon << 1$:

2.3.1 Compute $\Delta\mathbf{u}^e_{k+1}$ from (3.59).

2.3.2 Update $\mathbf{u}_{k+1} = \mathbf{u}_k + \Delta\mathbf{u}^e_{k+1}$.

2.3.3 $(.)_n \leftarrow (.)_{n+1}$ and go to 2.3.1.
END

END

3.7 Numerical examples

For all of the following numerical examples, a regular mesh of bilinear 4-node elements and plane strain assumption has been used. We assume a simplified cohesive model for the interface by taking into account the normal traction only, $\mathbf{t}(w) \cdot \mathbf{n}^I = t^n$. Then, the cohesive law can be rewritten as:

$$t^n = g_c^I(\frac{\mathrm{w^n}}{\delta^n})\exp(-\frac{\mathrm{w^n}}{\delta^n}). \tag{3.65}$$

3.7.1 Discontinuous benchmark

In this first example, we analyze the accuracy of the diffuse displacement jump approximation introduced in section 3.3.2. For this purpose, a benchmark with analytical solution is studied. A bi-material square domain including a cohesive zone is depicted in Fig. 3.12. The length of the square domain is $L = 1$ mm.

We consider small strains, and zero Poisson's coefficient $\nu = 0$ in both parts of the domain. For both (left and right) parts, isotropic elastic behavior is assumed, with Young's coefficients $E_1 = 100$ Mpa and $E_2 = 200$ Mpa for the respective domains. With the boundary conditions described in Fig. 3.12 the problem is unidimensional with a solution independent on the y-component (the displacements are prescribed along the $x-$direction only, the displacement along y are free). We use here a linear cohesive law to consider the first step of interface opening:

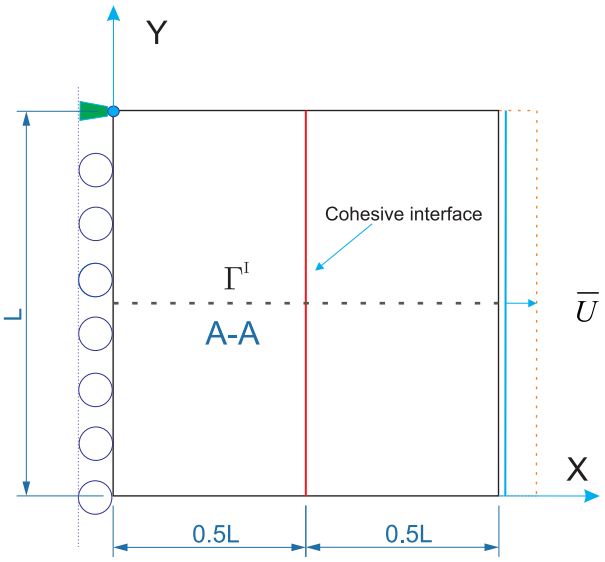

Figure 3.12: Discontinuous benchmark, geometry and boundary conditions.

$$t_n = \frac{g_c^I}{(\delta^n)^2} \times [\![u_1]\!] \,. \tag{3.66}$$

The analytical solution for this problem can be simply obtained by considering the displacement boundary conditions and the continuity condition at the interface, and is provided in Appendix A.1.

First, we evaluate the error of the displacement jump approximation introduced in Eq. (3.8). A 500×500 mesh was chosen, and the jump approximation parameter h in Eq. (3.8) varies between $0.25 \leq h_e/h \leq 10$. We define the relative jump error with respect to the analytical solution as:

$$ERR_1 = \sqrt{\frac{\int_\Gamma \left([\![\mathbf{u}^h(\mathbf{x})]\!] - [\![\mathbf{u}^{ex}(\mathbf{x})]\!]\right) \cdot \left([\![\mathbf{u}^h(\mathbf{x})]\!] - [\![\mathbf{u}^{ex}(\mathbf{x})]\!]\right) d\Gamma}{\int_\Gamma \left([\![\mathbf{u}^{ex}(\mathbf{x})]\!]\right) d\Gamma}}. \tag{3.67}$$

with $\left[\left[\mathbf{u}^h(\mathbf{x})\right]\right] = \mathbf{w}(\mathbf{x})$ is given by Eq. (3.8). We consider here undamaged bulk materials ($d(\mathbf{x}) = 0$) everywhere. Numerical parameters of the constitutive relation of the interface are: $t_u = 1$ MPa and $g_c^I = 0.1$ N/mm. Results are depicted in Fig. 3.13. We note minimal error for the ratio $h_e/h = 1$.

Next, we analyze more specifically the influence of the regularization parameter l. A 1000×1000 mesh with an element size he was chosen to ensure that $l/h_e \geq 1$, and the approximation jump in (3.8) parameter is chosen $h = h_e$ for all tested values of l_β. The regularization parameter l takes values between 0.002 and 0.02. We remind that in this test, the phase-field is set to zero $d(\mathbf{x}) = 0$ and the discontinuity only occurs from the cohesive laws at the interface. Comparisons of the displacement solution for several values of l is provided in Fig. 3.14.

We define the relative regularization error by:

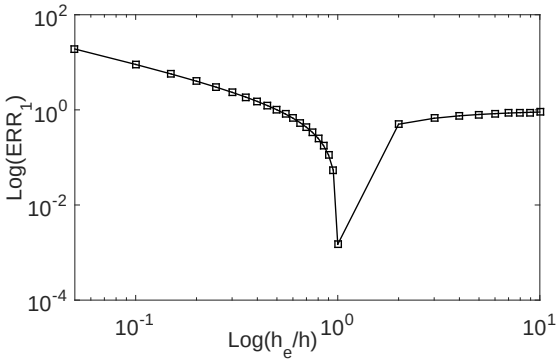

Figure 3.13: Displacement jump error: influence of the parameter h in Eq. (3.8) with respect to the mesh size h_e.

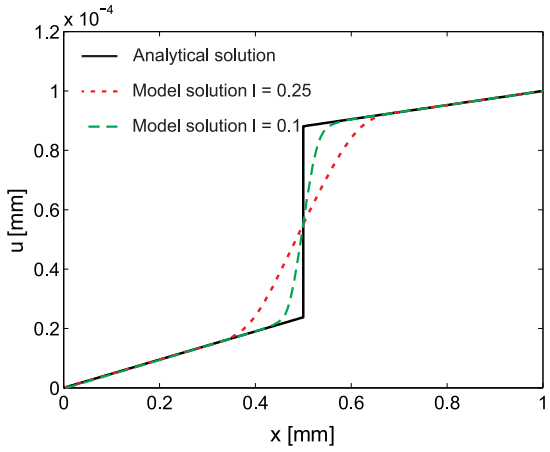

Figure 3.14: Discontinuous benchmark problem: comparison between the analytical solution and the approximated one for two values of the regularization parameter l.

$$ERR_2 = \frac{\left\|\mathbf{u}^h(\mathbf{x}) - \mathbf{u}^{ex}(\mathbf{x})\right\|_{L^2}}{\|\mathbf{u}^{ex}(\mathbf{x})\|_{L^2}} = \sqrt{\frac{\int_\Omega \left(\mathbf{u}^h(\mathbf{x}) - \mathbf{u}_{\text{ex}}(\mathbf{x})\right) \cdot \left(\mathbf{u}^h(\mathbf{x}) - \mathbf{u}_{\text{ex}}(\mathbf{x})\right) d\Omega}{\int_\Omega \left(\mathbf{u}_{\text{ex}}(\mathbf{x})\right) \cdot \left(\mathbf{u}_{\text{ex}}(\mathbf{x})\right) d\Omega}}. \tag{3.68}$$

The global L_2 error norm of the regularized solutio for the benchmark problem is plotted in Fig. 3.15.

Finally, we consider the error of mesh. The error is here computed by the following:

$$ERR_3 = \frac{\left\|\mathbf{u}^{h_e}(\mathbf{x}) - \mathbf{u}^{ex}(\mathbf{x})\right\|_{L^2}}{\|\mathbf{u}^{ex}(\mathbf{x})\|_{L^2}} = \sqrt{\frac{\int_\Omega \left(\mathbf{u}^{h_e}(\mathbf{x}) - \mathbf{u}_{\text{ex}}(\mathbf{x})\right) \cdot \left(\mathbf{u}^{h_e}(\mathbf{x}) - \mathbf{u}_{\text{ex}}(\mathbf{x})\right) d\Omega}{\int_\Omega \left(\mathbf{u}_{\text{ex}}(\mathbf{x})\right) \cdot \left(\mathbf{u}_{\text{ex}}(\mathbf{x})\right) d\Omega}}. \tag{3.69}$$

The obtained results, with respect to the element mesh size h_e is described in Fig. 3.16

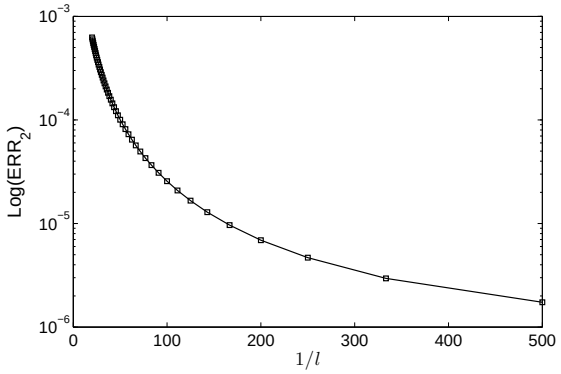

Figure 3.15: L_2 error norm for the discontinuous benchmark problem.

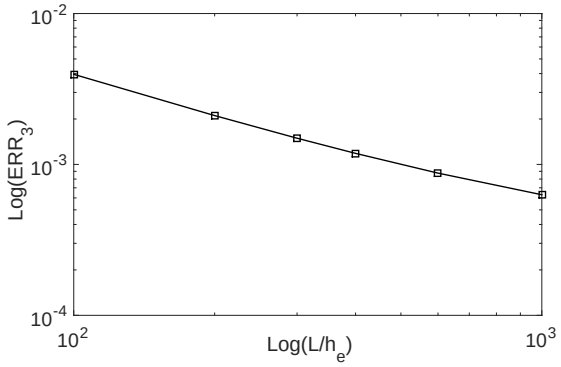

Figure 3.16: L_2 error norm for the mesh influence.

3.7.2 Crack propagation under cyclic loading

In this next example, we investigate the capability of the present method for handling cracking under cyclic loading. A square domain of length $L = 1$ mm is considered. The domain contains a cohesive interface, whose geometry is depicted in Fig. 3.17.

The material is described by the model described in section 3.4.1 with parameters $E = 100$ MPa and $\nu = 0$, fracture strength and toughness $t_u = 10$ MPa and $g_c = g_c^I = 0.1$ N/mm, respectively. Note that from now on, we will assume that $t^n = 0$. In addition, small strain an local isotropic behavior of the phases is assumed. The regularization parameter l is chosen as $l = 0.02$ mm. Plane-strain condition is assumed. The two models M1 and M2 have been used for comparison. A cyclic displacement $\overline{U}$ whose evolution is described in Fig. 3.18(a) is prescribed on a portion of the upper end, as depicted in Fig. 3.17. The displacements are prescribed along the $y-$direction while the displacement along x are free. The evolution of the computed displacement jump along y in the element A near the crack tip is depicted in Fig. 3.18(b) for both models M1 and M2.

The normal traction force in the element located near the crack tip is depicted in Fig. 3.19(a) versus displacement jump and (b) versus the prescribed vertical displacement. We can note

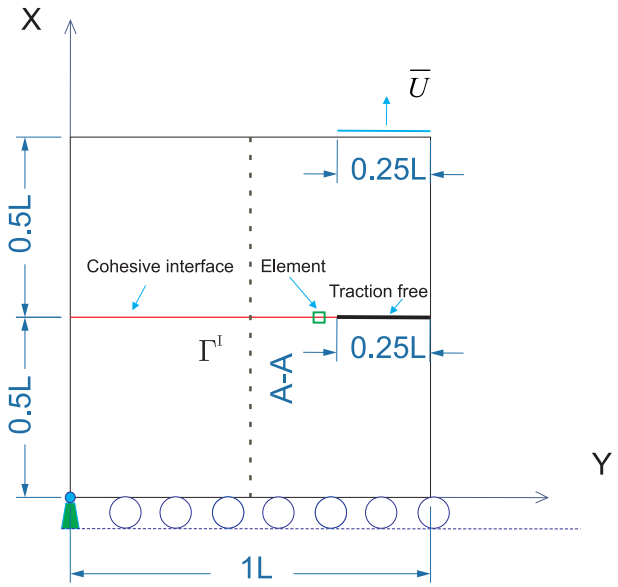

Figure 3.17: Geometry of the sample for the fatigue crack test: geometry and boundary conditions.

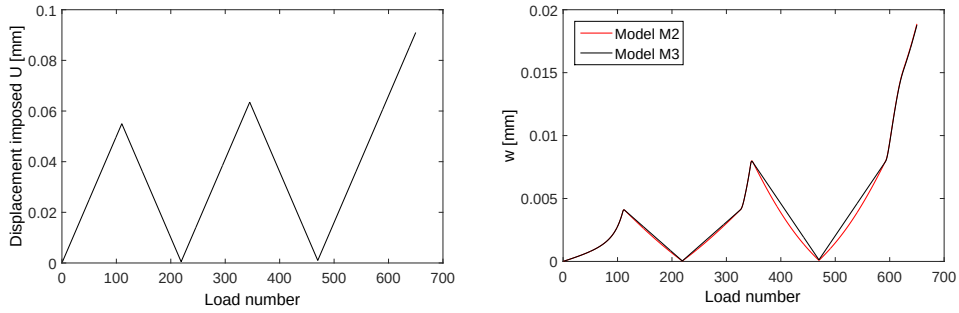

(a) (b)

Figure 3.18: Cyclic loading test: (a) evolution of the load; (b) Computed displacement jump along y.

that simplest model M1 is able to capture the interfacial damage, even without using internal variables. The response is very similar to the response obtained by model M2.

3.7.3 Crack propagation in symmetric three-point bending test

The purpose of this example is to validate the solution provided by our new formulation. We consider the three-point bending problem studied e.g. in [224] and described Fig. 3.20. The dimensions of the beam are $L = 10$ mm, and $H = 3$ mm. The load consists into a prescribed displacement at the center of the beam on the top edge. The node at $(x = 0), (y = 0)$ is fixed, while the node at $(x = L)$, $(y = 0)$ the y-displacement is fixed and the x-displacement is free. For this case, an initial cohesive interface has been inserted as described in Fig. 3.20, to validate the cohesive model only. Materials on either sides of the interface are identical.

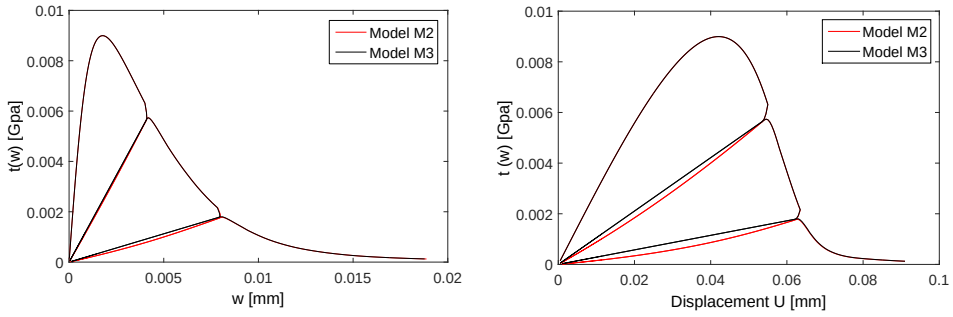

(a) (b)

Figure 3.19: Cyclic loading test: (a) cohesive traction with respect to the displacement jump within the interface; (b) cohesive traction within the interface with respect to the prescribed displacement.

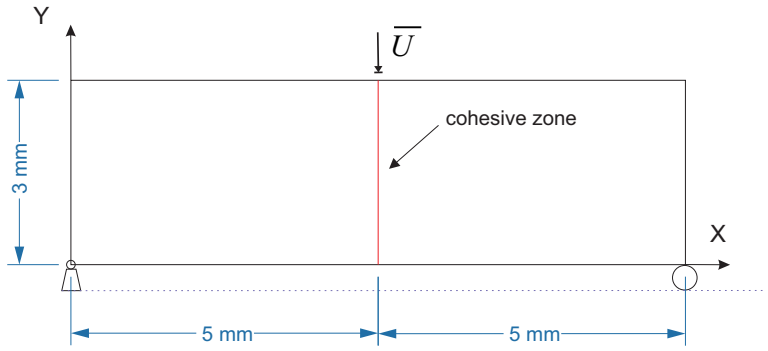

Figure 3.20: Symmetric three-point bending test problem: Geometry and boundary conditions.

A regular mesh of 60×200 quadrilateral elements is employed. The material parameters are chosen as follows: $E = 100$ MPa, $\nu = 0.0$, the fracture strength is $t_u = 1.0$ MPa, and the toughness is $g_c = g_c^I = 0.1$ N/mm. The computation is performed with monotonic displacement increments of $\overline{U} = 5.10^{-3}$ mm for 120 load increments. The displacements are prescribed along the $y-$direction while the displacement along x are free. The regularization parameter l is chosen as $l = 0.15$ mm. Plane strain condition is assumed. The damage evolution (phase field $d(\mathbf{x})$) for the different values of the load is depicted in figure 3.21. In contrast to the approach developed in [64] where interfaces are initially damaged in the phase field sense, here the phase field can be used to follow the interfacial damage directly.

To validate the results, we compare in Fig. 3.22 the curve obtained with the present method to the solution provided in [224]. We can note a good agreement between both simulations which validates the present method for the damage of interfaces.

3.7.4 Delamination peel test

In this next test, another validation is performed through the so-called peeling test, described in Fig. 3.23: two cantilever elastic beams are connected over 90% of their length by means of an

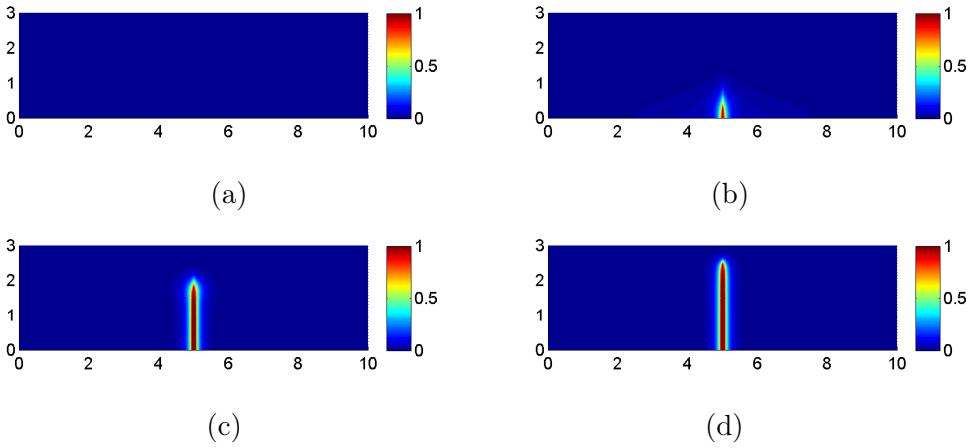

Figure 3.21: Symmetric three-point bending test problem: Damage evolution for: $\overline{U} = 0$ mm; $\overline{U} = 0.2$ mm; $\overline{U} = 0.25$ mm and $\overline{U} = 0.35$ mm

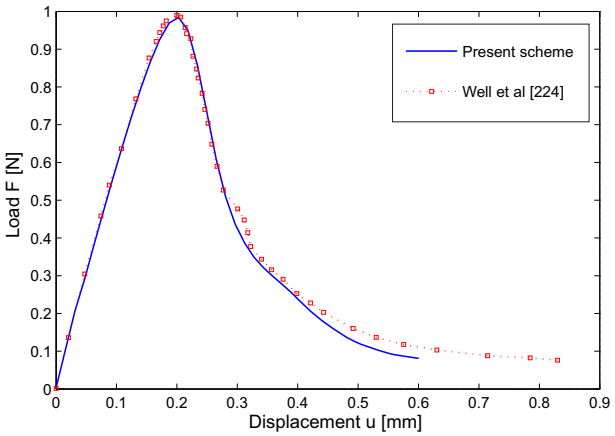

Figure 3.22: Force-displacement curve for the crack propagation problem with symmetric three-point bending test problem: comparison between the present approach and the results obtained in [224]

adhesive layer. The structure is 10 mm in length and 0.5 mm in height (see Fig. 3.23).

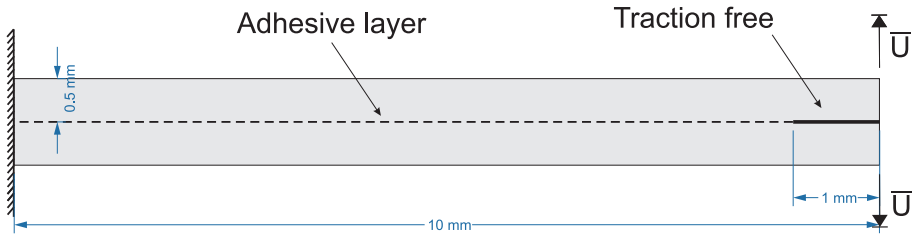

Figure 3.23: Delamination peel test problem: geometry and boundary conditions

The points located at the top and bottom right ends of the structure are subjected to a prescribed vertical displacement $\overline{U}$. The bulk material is modeled as linear elastic and isotropic

with Young's modulus $E = 1000$ MPa and Poisson's ratio $\nu = 0.3$. The fracture strength and fracture energy are taken as $t_u = 1$ MPa and $g_c = g_c^I = 0.1$ N/mm, respectively. The length scale parameter l is chosen $l = 0.05$ mm. Plane strain conditions are assumed. In Fig. 3.24, the evolution of the interfacial damage is depicted. In the present framework, this damage coincides with the phase field distribution, which is initially zero in the interface, in contrast to the approach proposed in [218].

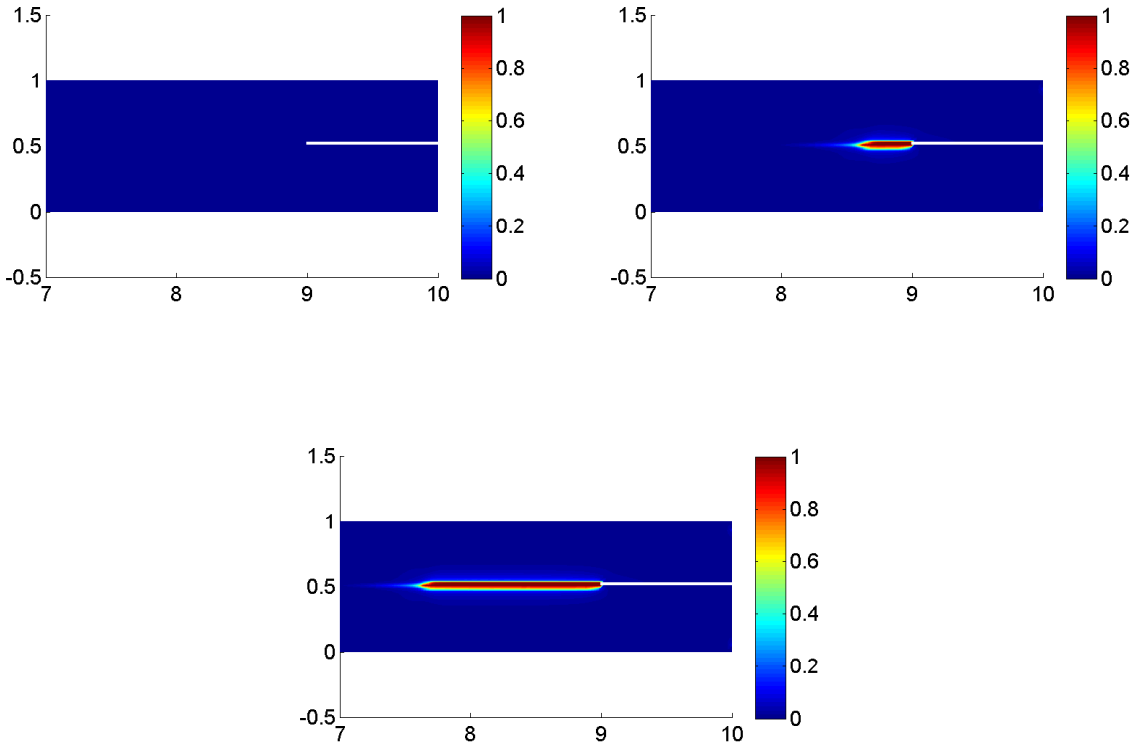

Figure 3.24: Delamination peel test problem: phase field evolution $d(\mathbf{x})$ for: $u = 0$ mm, $u = 0.4$ mm and $u = 1$ mm

To validate the results, we compare in Fig. 3.25 the obtained response with the solution in [218] for both models M1 and M2. We can note that both models provide a very good agreement with the reference solution.

3.7.5 Traction test of a microstructure with circular inclusion

In this example, we test the influence of the mesh on the predicted crack path, when an interfacial crack interact with a bulk crack. The problem geometry is depicted in Fig. 3.26. A square domain of length $L = 1$ mm contains a centered circular inclusion of diameter $D = 0.3L$.

The boundary conditions are as follows: on the lower end ($y = 0$), the $y-$ displacements are fixed, while the $x-$displacements are free and the node ($x = 0, y = 0$) is fixed. On the upper

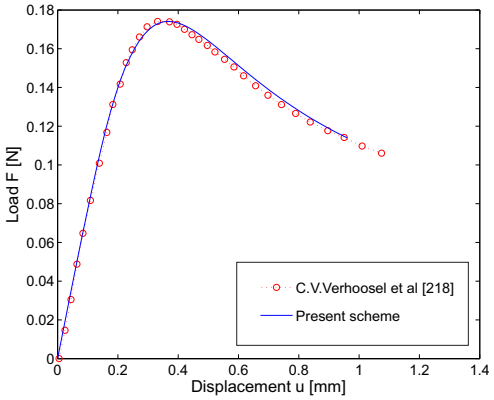

Figure 3.25: Force-displacement curve for the peel-test problem: comparison between the present approach and the results obtained in [218].

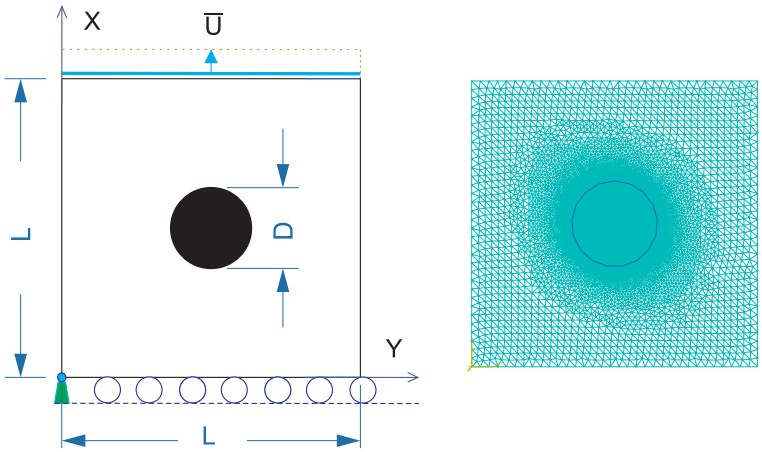

(a) (b)

Figure 3.26: Traction test of a microstructure containing a single inclusion with damageable interface: (a) geometry of the phases; (b) unstructured mesh of triangles.

end, the $x-$displacements are free, while the $y-$displacements are prescribed to an increasing uniform value of $\overline{U}$ during the simulation. Plane strain is assumed.

The material parameters of each phase are taken as: $E_i = 52$ GPa, $\nu_i = 0.3$, $E_m = 10.4$ GPa, $\nu_m = 0.3$, where the indices i and m correspond to the matrix and inclusion, respectively. These parameters are those of a mortar composed of a cement paste (matrix) and sand (inclusions) [97]. The toughness is $g_c = g_c^I = 1 \times 10^{-4}$ kN/mm and $t_u = 10^{-2}$ GPa. Computations are performed with monotonic displacement increments of $\overline{U} = 5.10^{-5}$ mm during 260 load increments for interfacial model, and 320 load increments for the classical phase field method.

To investigate the effects of the mesh on the crack path and load response, 4 different meshes have been used for comparison: 3 regular meshes wit 4-node elements on regular grids of

200×200, 300×300 and 400×400 element, and a mesh of 30488 elements with $h_e^{max} = 0.03$ mm and $h_e^{min} = 0.003$ mm. The obtained crack paths are depicted in Fig. 3.27 for the regular mesh of 200×200 elements and the unstructured mesh, which have roughly the same number of elements. The comparison has been made for the same load: $\overline{U} = 0.01175$ mm. We can note a similar crack path for both meshes. Finally, the response for the 4 meshes are compared in Fig. 3.28, which shows the convergence of the solution with mesh refinement. Note that the unstructured mesh solution corresponds to the element size of the 200×200 regular mesh. Here, we have chosen $h = h_e$. We can see from Fig. 3.28 that as the mesh is being refined, the solution converges also with respect to the value of h.

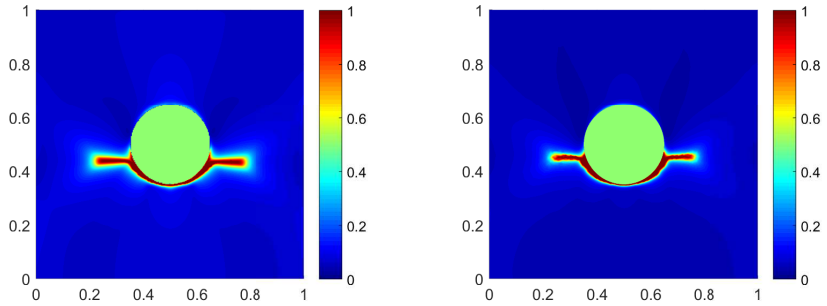

(a) (b)

Figure 3.27: (a) Crack path obtained for a regular mesh. (b) Crack path obtained for an unstructured mesh. The load is $\overline{U} = 0.0107$ mm.

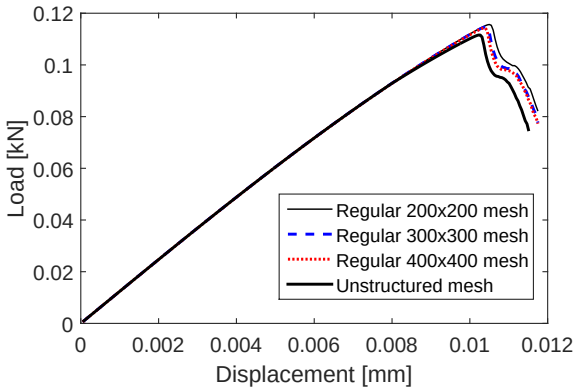

Figure 3.28: Comparison of solutions obtained with different meshes for the single inclusion problem with damageable interface.

Next, we investigate the influence of the parameter l_β in (3.1). We chose the following values: $l_d/l_\beta = 1/3$, $l_d/l_\beta = 1$ and $l_d/l_\beta = 2$ for $l = 0.01$ mm. Results are presented in Figs. 3.29 and 3.30 for the same load $\overline{U} = 0.0107$ mm, showing that a modification of l_β has a strong influence on the crack path and on the overall response. This suggests that like l_d, this parameter should be identified through experimental data. However, as the purpose of this work is to demonstrate

the capabilities of the numerical scheme, we will assume in the following that $l_d = l_\beta = l$.

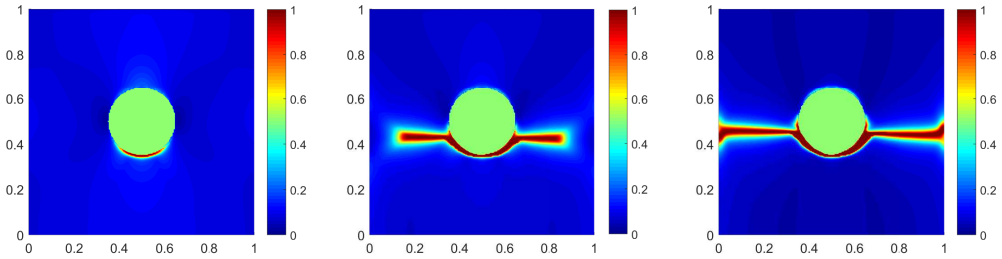

(a) (b) (c)

Figure 3.29: Crack paths obtained with different length parameter l_β for the same load $\overline{U} = 0.013$ mm: (a) $l_d/l_\beta = 2$; (b) $l_d/l_\beta = 1$; (c) $l_d/l_\beta = 1/3$, $l_d = 0.01$ mm.

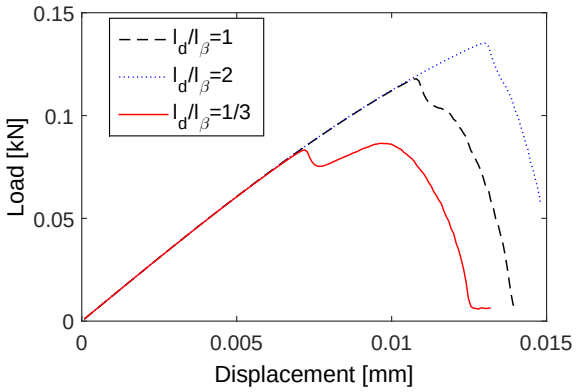

Figure 3.30: Comparison of solutions obtained with different length parameters l_β.

3.7.6 Traction test of a microstructure with non convex inclusion

In this next test, we evaluate the capability of the method to describe interfacial damage in a microstructure containing an inclusion with complex, non-convex geometry. In addition, the initial data of local properties are provided on a regular grid of voxels. We then test the procedure described in section 3.5 to construct the level-set function used to evaluate the normal vector to the interface and construct the smeared discontinuous field $[\![\mathbf{u}(\mathbf{x})]\!]$. The geometry of the microstructure is described in Fig. 3.31(a). A non-convex inclusion composed of the union of two discs is embedded into a square domain of length $L = 1$ mm. This non convex geometry has been chosen to test the capability of the level-set construction method described in section 3.5 for this difficult case. The obtained level-set is plotted in Fig. 3.31(b) and its zero iso-contour, corresponding to the interface geometry, is depicted in Fig. 3.31(c). The geometrical parameters are: $A = 0.43L$, $D = 0.2L$. A small dissymmetry is introduced through the parameter $\epsilon = 0.01L$.

The boundary conditions are as follows: on the lower end ($y = 0$), the $y-$ displacements are fixed, while the $x-$displacements are free and the node ($x = 0, y = 0$) is fixed. On the upper

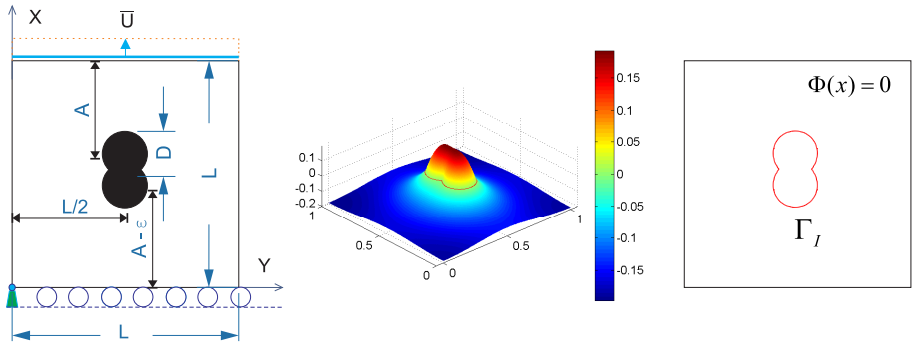

(a) (b) (c)

Figure 3.31: Traction test of a complex microstructure in 2D: (a) geometry of the phases; (b) and (c) level-set function

end, the $x-$displacements are free, while the $y-$displacements are prescribed to an increasing uniform value of $\overline{U}$ during the simulation. Plane strain is assumed.

The material parameters of each phase are taken as: $E_i = 52$ GPa, $\nu_i = 0.3$, $E_m = 10.4$ GPa, $\nu_m = 0.3$, where the indices i and m correspond to the matrix and inclusion, respectively. These parameters are those of a mortar composed of a cement paste (matrix) and sand (inclusions) [97]. The toughness is $g_c = g_c^I = 1 \times 10^{-4}$ kN/mm and $t_u = 10^{-2}$ GPa. Computations are performed with monotonic displacement increments of $\overline{U} = 5.10^{-5}$ mm during 260 load increments for interfacial model, and 320 load increments for the classical phase field method. A regular mesh of 400×400 elements is used. The regularization parameter l is chosen as $l = 0.005$ mm. We perform two simulations: one with the whole formulation, able to take into account both interfacial damage and matrix damage, and another which only takes into account damage of the bulk (basic phase field method). Damage evolution for each model is depicted in figure 3.32.

In this example and in all following ones, the domain does not contain pre-existing cracks, and the cracks first nucleate and then propagate as the load is increased. We can note that in the case of the classical phase field method (damage only occurring in the phases), two cracks initiate on the top and at the bottom of the inclusion, where stress concentration occurs, and then propagate. In the case where interfacial damage is included, the damage clearly initiates in the interface and then propagates into the matrix. We note that in this case, only one crack propagates. The general dissymmetry is induced by the perturbation parameter ϵ (see Fig. 3.31(a)) and due to the way the mesh cuts the exact disc and the assignment of material properties to the elements. The load-displacement curves are plotted for each case in Fig. 3.33.

We can note that both models M1 and M2 provide similar behaviors. The slight local minimum observed for the model with interfacial damage might be due to local relaxation associated to the damage near the interface. We can conclude that in the present framework, the use of additional internal variables (as in the M2 model) is unnecessary.

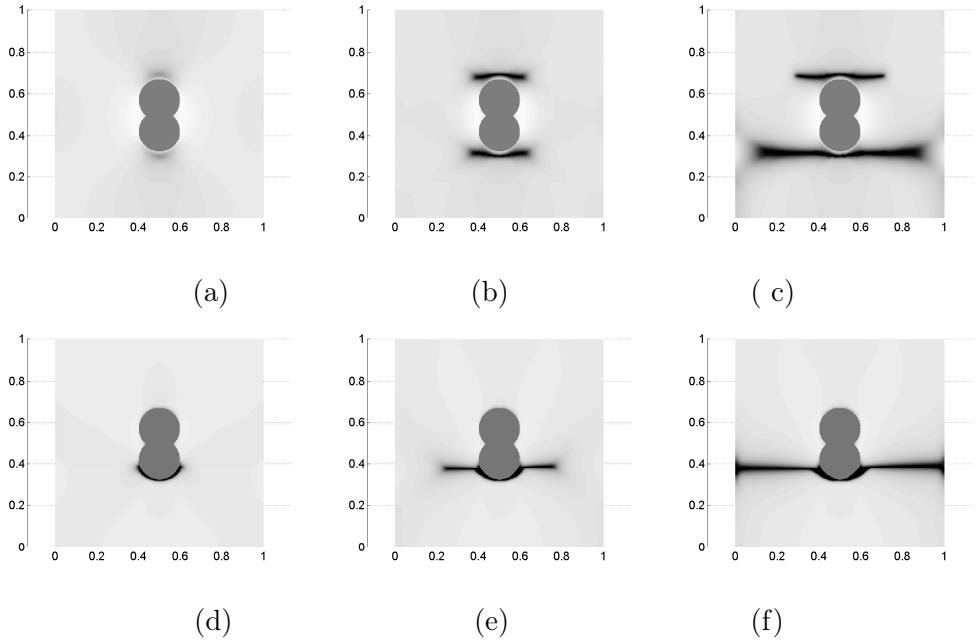

Figure 3.32: Tensile test of a heterogeneous sample with complex inclusion: crack propagation. The phase field $d(\mathbf{x})$ is plotted. Figures (a), (b) and (c) depict the cracks initiation and propagation by using the classical phase field method and correspond to $\overline{U} = 0.014$ mm, $\overline{U} = 0.015$ mm, and $\overline{U} = 0.016$ mm, respectively. Figs. (d), (e) and (f) depict crack propagation and initiation for the model including both phases and interfacial damage and correspond to $\overline{U} = 0.008$ mm, $\overline{U} = 0.01$ mm, and $\overline{U} = 0.012$ mm, respectively.

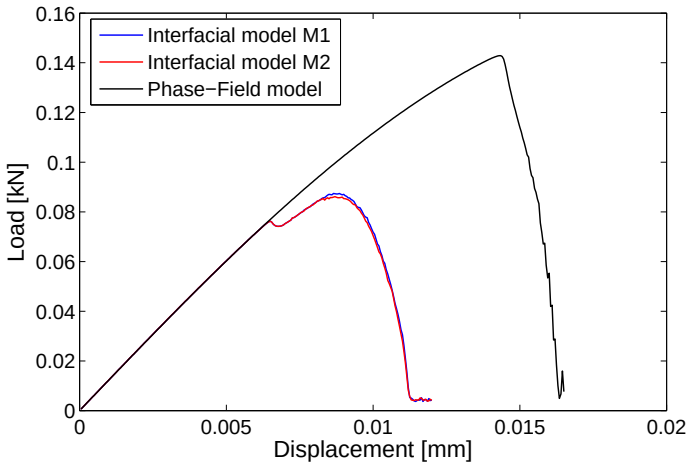

Figure 3.33: Traction test of a complex microstructure: load-displacement curve.

3.7.7 Microcracking in a microstructure containing randomly distributed inclusions

A microstructure containing 9 randomly distributed circular inclusions is considered, as depicted in Fig. 3.34 (a)-(b).

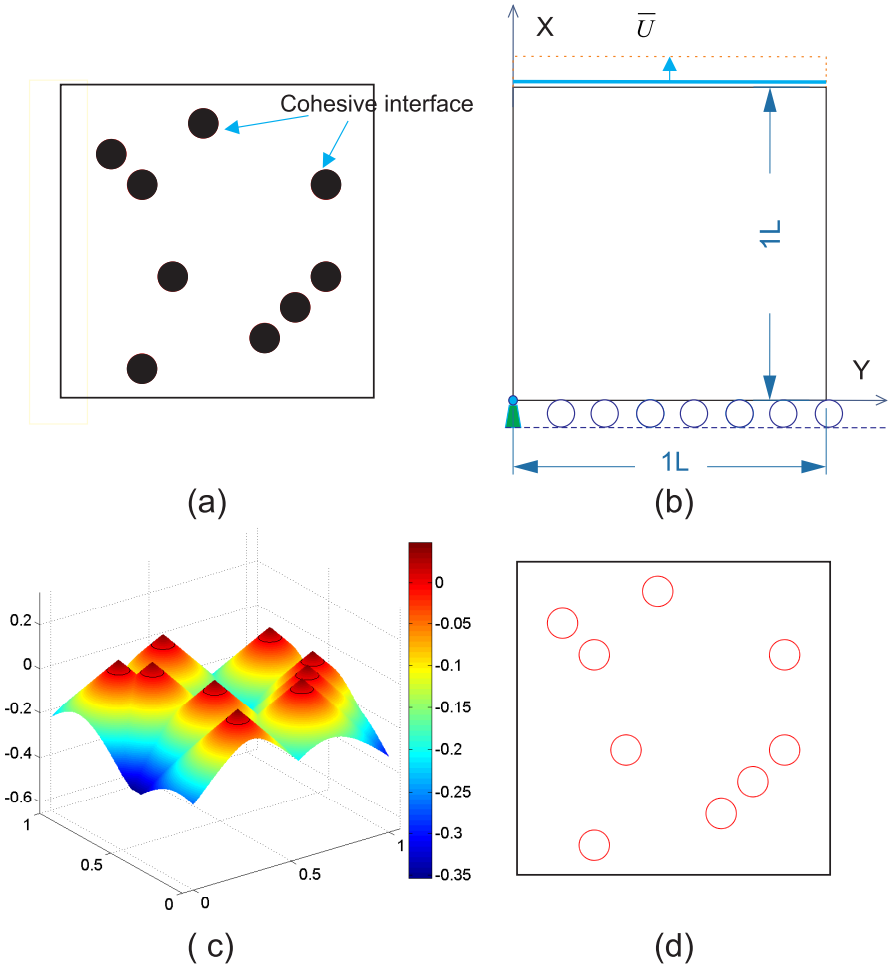

Figure 3.34: Traction test of a microstructure containing randomly distributed inclusions: (a) geometry of the phases; (b) geometry of the domain and boundary conditions; (c) level-set function; (d) zero isocontour of the associated level-set

The microstructure is modeled as a square domain whose length is $L = 1$ mm. The radius of the inclusions is computed such that the volume fraction f is equal to 0.07. The elasticity parameters of each phase are the same as in the previous example: $E_i = 52$ GPa, $\nu_i = 0.3$, $E_m = 10.4$ GPa, $\nu_m = 0.3$. The interfaces can be damaged through the model proposed in section 3.4.3.2, with again $t_u = 10^{-2}$ GPa. The toughness of both phases is taken as $g_c = 2.7 \times 10^{-4}$ kN/mm and $g_c^I = g_c$. The boundary conditions are as follows: on the lower end ($y = 0$, the y-displacements are fixed, while the x-displacements are free. The node at ($x = 0$), ($y = 0$) is fixed. On the upper end, the x-displacements are free, while the y-displacements are prescribed, with a uniform increasing value of $\overline{U}$ during the simulation. Lateral boundaries

are free. Plane strain is assumed. The computation is performed with monotonic displacement increments of $\overline{U} = 5 \times 10^{-5}$ mm during 200 increments. A regular mesh of 300×300 quadrilateral elements is used. The regularization parameter is chosen as $l = 0.0075$ mm.

The microcracking distribution (damage variable $d(\mathbf{x})$) is depicted in Fig. 3.35 for several realizations of microstructures at a stage close to the peak stress.

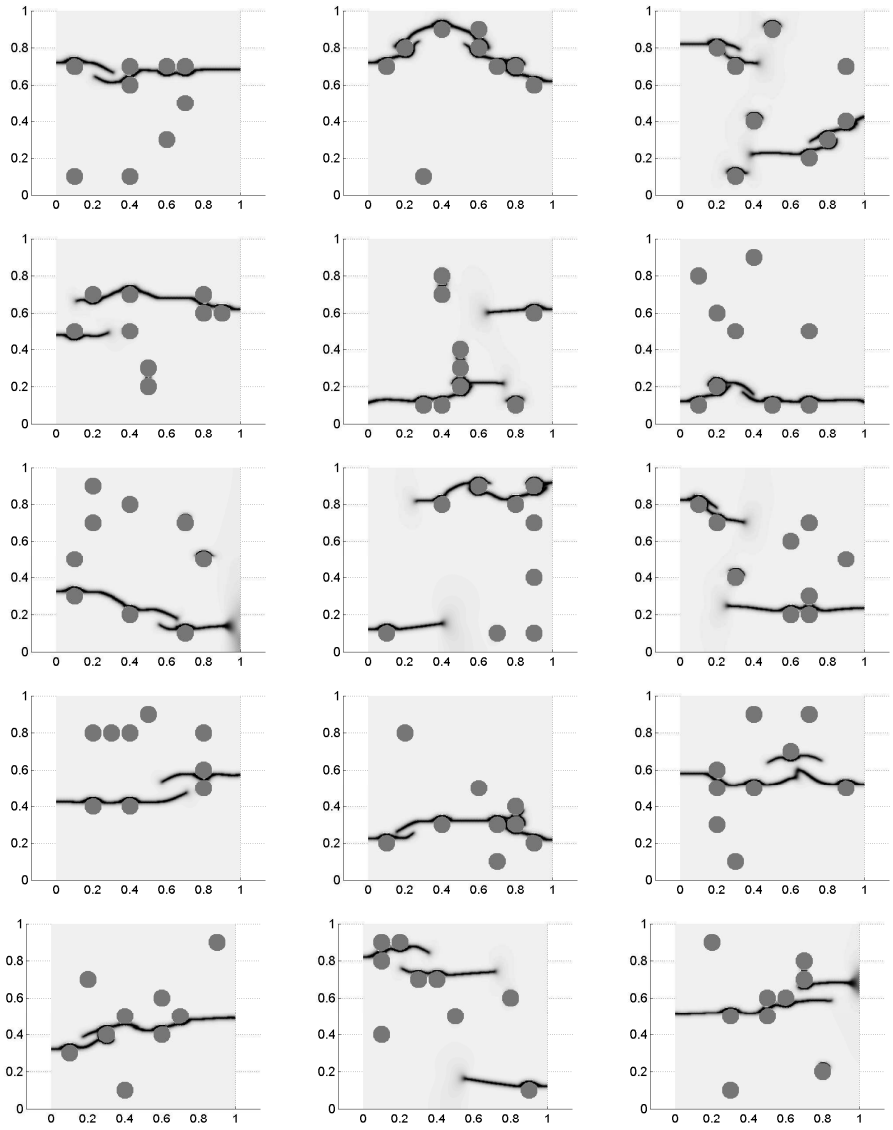

Figure 3.35: Microcrocracking evolution for 15 realizations of microstructures in traction.

In the different figures of Fig. 3.35, we can note that in each case, the cracks initiate at the interface between the matrix and the inclusions, and then propagate into the matrix. For most cases, a crack path is created between the inclusions passing through the interfaces and then leading to the rupture of the specimen. This example illustrates well the capability and robustness of the technique to handle: (a) interaction between many cracks and (b) crack propagation from interfaces to the bulk. We note that the same regular mesh was used for each simulation,

by only changing the level-set construction through the procedure described in section 3.5.

The corresponding force-displacement curves are depicted in figure 3.36 for the set of 15 realizations. We note a relatively large dispersion of the individual results, with possibly non monotonous evolutions of the force/displacement curves. This shows on the one hand the strong sensitivity of the overall quasi-brittle response to the local morphology of microstructure as well as the capability of the proposed method to capture these effect. This variability is as expected much larger in the damaged part of the force displacement curve than in its initial linear part. On the other hand, the average of this individual responses, shown in red, exhibits a much more regular shape, which might be considered as a first evaluation of the overall softening response of a damaging composite containing much more inclusions. The convergence of individual simulations with increasing window sizes, or of their statistical averages, towards the effective behavior of such a composites remains a stringent open question. These preliminary results suggest that the proposed numerical tools might provide an efficient tool to make a big step for its investigation. More precisely, the concept of "representative volume element" for a quasi-brittle material might be clarified this way, following earlier ideas used for simpler linear elastic behaviours (e.g. [102]).

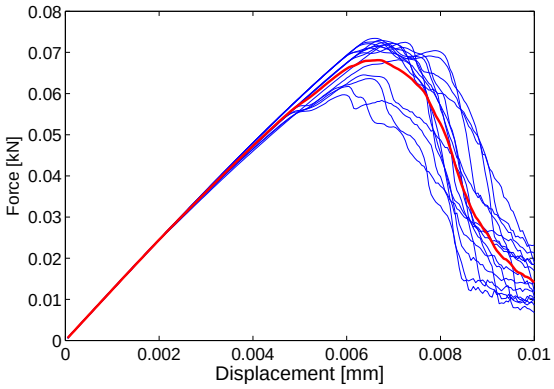

Figure 3.36: Traction test of a microstructure containing randomly distributed inclusions with interfacial damage: load-deflection curve for 15 realizations. The red curve denotes the average response.

3.7.8 Compression test of a realistic microstructure extracted from micro-tomography image of an EPS lightweight concrete

This last example illustrates the capability of the technique to solve problems of microcrack propagation in voxel-based models obtained from microtomography of real materials with both interfacial and bulk damage.

The considered 2D microstructure is a cross-section of a microtomography image of a real cementitious material obtained with the XR-CT, the detail of this procedure is presented in chapter 4. We use the real geometry by meshing the segmented image (see chapter 6). The

grey level image was filtered and thresholded to separate the three phases of the microstructure. The results are presented in Fig. 3.37(a), where the white, grey and black phases correspond to matrix (cement paste), inclusions (sand grains) and pores (EPS beads), respectively. The obtained level-set for this complex geometry described in section 3.5 is shown in Fig. 3.37(c), and its zero isovalue, corresponding to the interface between the matrix and the rigid inclusions, is depicted in 3.37 (d). Note that the construction of a level-set function for such complex geometry is not trivial and proves the robustness of the original algorithm proposed in this work. Note that no level-set is used here to describe the matrix-pores interface, as it would make no sense to propagate cracks along such interfaces.

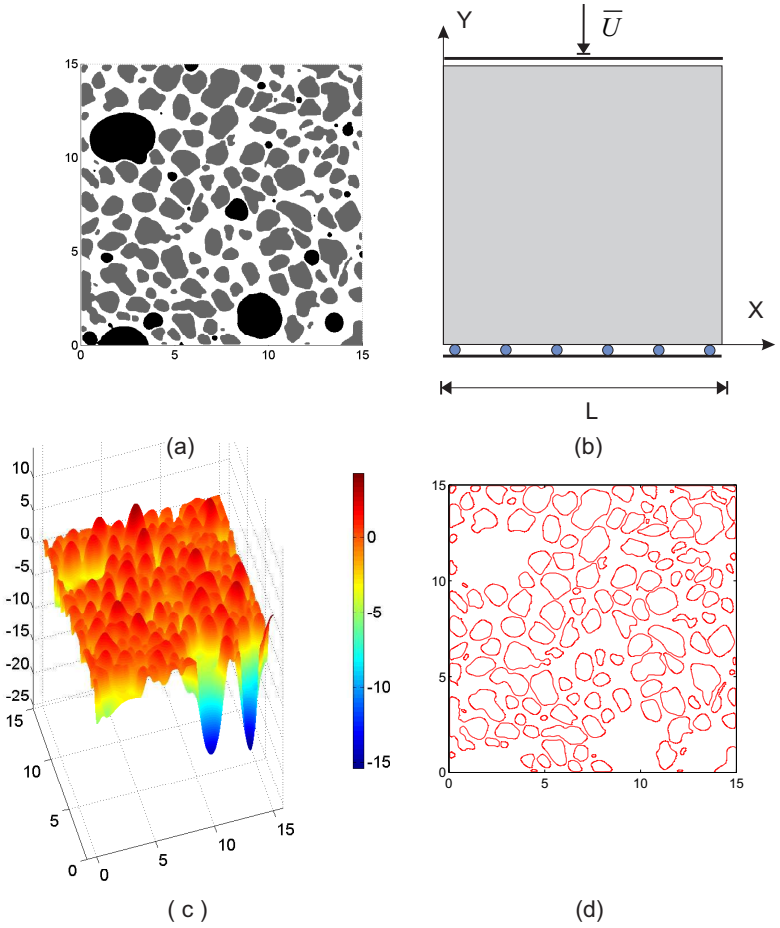

Figure 3.37: Compression test of a microtomography image-based model of EPS lightweight concrete: (a) microstructure obtained from segmented image: the white, grey and black phases correspond to matrix, inclusions and pores, respectively; (b) geometry of the domain and boundary conditions; (c) level-set function and (d) zero isovalue of the constructed level-set.

The boundary conditions and geometry of the sample are described in Fig. 3.37(b) and are similar to the previous examples. From the 1000×1000 pixels, a mesh of 1000×1000 quadrilateral elements is generated, where the material property of matrix, inclusion or holes, are transferred into a regular grid of square domains associated with elements. The material

parameters of inclusions and matrix are, respectively: $E_i = 60$ GPa, $\nu_i = 0.3$, $E_m = 18$ GPa, and $\nu_m = 0.2$. The pores are covered with elements of the regular mesh. We have chosen very compliant properties for these elements, $E_p = 10^{-6}$ GPa, $\nu_p = 0$. The toughness $g_c = 59.3$ N/m is assumed to be identical for the different phases and $g_c^I = g_c$. Note that in this example we have considered both normal and tangential components for the cohesive law, with $t_u = 3.4$ MPa for both components [182]. The simulation is performed with monotonic displacement increments $\overline{U} = -6.10^{-4}$ mm during 250 load increments. The regularization parameter is chosen as $l = 30$ μm. The microcracking evolution in the domain is presented in Fig. 3.38.

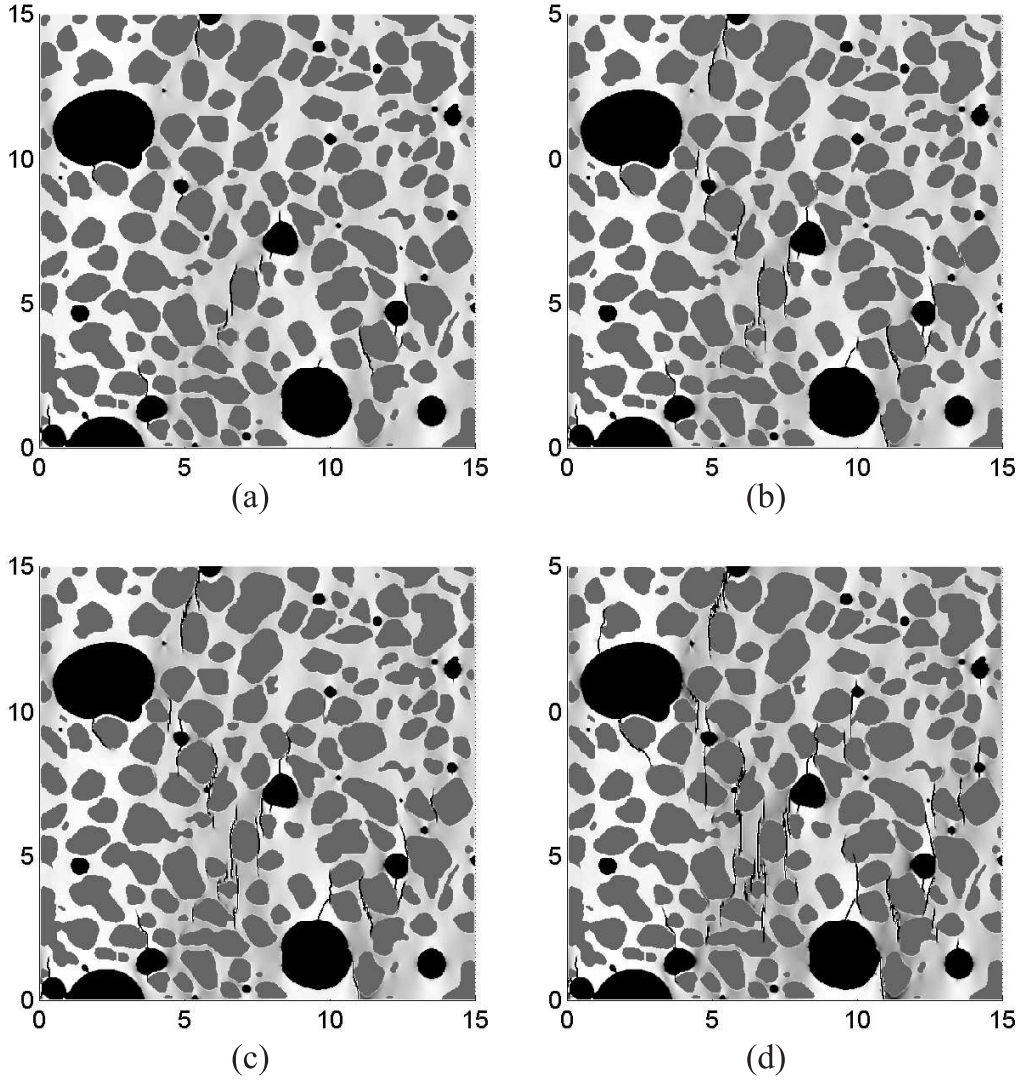

Figure 3.38: Compression test on a microtomography image-based model of EPS lightweight concrete: microcracking evolution for: $u_a = 0.12$ mm, $u_b = 0.15$ mm, $u_c = 0.162$ mm and $u_d = 0.18$ mm (see Fig. 3.39 for corresponding force-displacement curve).

We can observe several microcracks nucleation modes. In the vicinity of pores, cracks nucleate vertically, which is consistent with some recent experimental observations of plaster materials

containing holes subjected to compression [180]. Other cracks nucleate from interfaces between inclusions and the matrix, and then propagate into the matrix. A few cracks propagate through inclusions. In all cases, the crack paths are very complex and show the potential of the method to describe microcracking with interfacial damage in very complex, heterogeneous microstructures such as obtained by experimental imaging. The load-displacement curve is provided in Fig. 3.39. When microcracks start nucleating, the material strength quickly drops. We can note that both M1 and M2 models provide comparable solutions, which shows that the present framework can be employed with the simplest cohesive model and without internal interface variables, at least for monotonous loading conditions.

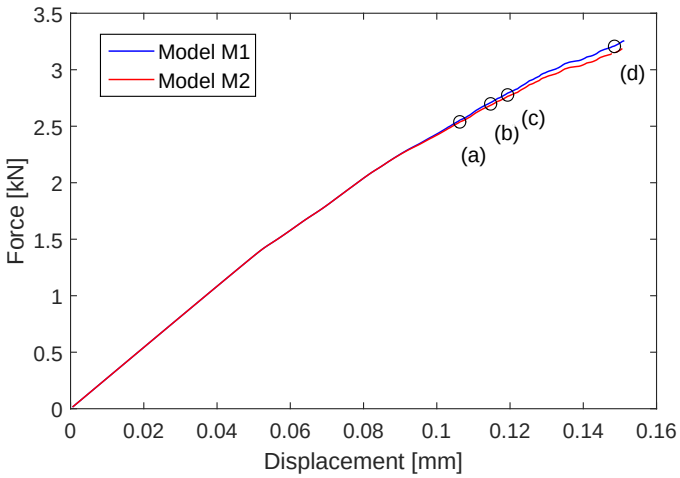

Figure 3.39: Compression test of a microtomography image-based model of EPS lightweight concrete: load-deflection curve.

3.8 Conclusion

In this chapter, we have proposed different methodologies to model the interfacial damage in the context of the phase field method. First, a simple interphase model has been investigated. Such model suffers form an inherent drawback related to the definition of the thickness of the interphase and the non physical interpretation of the parameters related to the interphase. Secondly, a new phase field framework capable of describing interactions between bulk brittle fracture and interfacial damage has been introduced. The method shares some features with the method of Verhoosel and al. [218] but differs in the following points: (a) no additional variable is used to described the displacement jump at the interface. Instead, a smeared approximation of the jump based on a level-set method is introduced. An original and simple technique has been introduced to construct the level-set function in voxel-based models, to allow applications of the method to image-based models of microstructures. Further, our new formulation allows describing opening and re-closure of cracks by using directly the phase field as an internal

variable, which removes the need for internal variables related to cohesive interfaces. Then, the sole and unique phase field is employed to describe both bulk brittle fracture and interface cracking, and thus allows interaction between the two type of cracks. More specifically, we have simulated crack nucleation from interfaces and their propagation into the bulk. The accuracy of the method has been proved through several well-known benchmarks (peeling test, crack propagation in 3-point bending of a beam). In addition, we have demonstrated the capability of the method to simulate interactions between interfacial damage and bulk brittle fractures for complex geometries arising from voxel-based model of microtomography images, which has been done for the first time in this work to our knowledge. The method then constitutes a very promising modeling and simulation tool for studying microcracking in a wide class of composite materials where both interfacial damage and matrix crack propagation occur.

Part II

Experimental methods for microcrack observation

Chapter 4

Experimental procedure

Contents

4.1 Introduction

This chapter aims at describing the experimental procedures developed in order to observe 3D cracking in heterogeneous brittle materials at micro scale. In fact, an experimental characterization of the evolutive damage is needed for a better understanding of the cracking and to validate the numerical tools presented in Part I. The objective of this chapter is to present the sample manufacturing and mechanical testing procedures specifically developed to observe the propagation and the morphology of cracks in 3D. Additional tests have been conducted to evaluate elastic properties of the studied material. The results will be used to feed and validate the numerical model developed in Part I.

Various experimental methods have been proposed in the literature to study damage phenomena in civil engineering materials. In this study, in-situ compression tests are performed under X-ray Computed Tomography (XR-CT), a prevalent tool to observe and characterize microstructure and/or damage phenomena inside specimens. The potential of this technique has been demonstrated in former studies for several materials. In particular, damage in cement based material was successfully observed using in-situ loading and tomography [113, 221, 65]. Landis et al [112] measured the crack growth in a mortar specimen in compression from XR-CT images. However, such experimental results are rare drirectly compared with numerical modeling, especially in three dimensions. A reason for that is probably that: it is hard to reproduce perfect loading conditions used for numerical tests, as those launched to the fact into for numerical models on a real experiment, or conversely, it is hard to reproduce on a numerical model the details of a real experiment (imperfections of machine loading, imperfect boundary conditions or of geometry of sample). Moreover, the local features of a crack network might be very sensitive to such imperfections, especially for brittle materials, so that the exact reproduction of a real network by numerical simulation might seem out of reach.

We are interested here in civil engineering materials, which often exhibit a brittle behaviour. In order to observe cracks using tomography, their propagation within the chosen materials must be slow and stable enough to make it possible to acquire several successive CT images (a few hours each). Quasi-brittle materials can ensure these conditions since they do not exhibit the problem of brutal rupture as brittle materials do (see Fig. 4.1(a)). Indeed, they show a damage domain where crack propagation is stable, corresponding to a loss of linearity on the macroscopic response curve as depicted in Fig. 4.1(b).

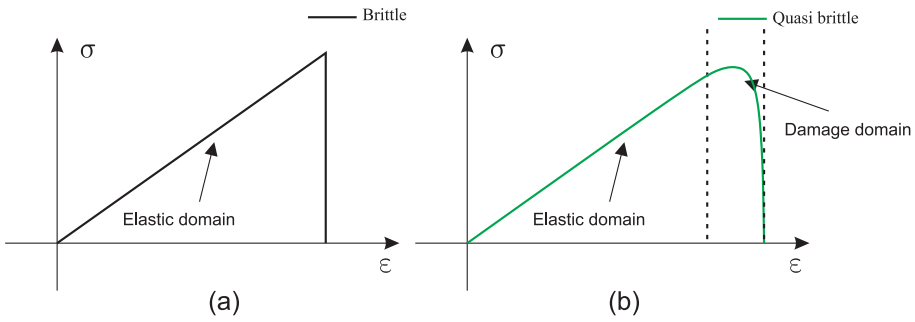

Figure 4.1: Comparison of behaviours of (a) a brittle and (b) a quasi-brittle material

The studied material should also be adapted to XR-CT and DVC : it must be transparent to X-rays and show a natural contrast at a suitable scale to perform the DVC analysis. Indeed, the quality of obtained images will strongly affect the crack detection. Finally, if the wanted material does not exist in its final form, it will have to be manufactured in the laboratory.

The first material of interest, which satisfies a priori those requests, is expanded polystyrene (EPS) light-weight concrete. Widely used in civil engineering construction, this material is strongly heterogeneous and exhibits a quasi-brittle behavior under compressive loading as a

consequence of the development of a complex microcrack network. This material is appropriate to develop and validate specific experimental and modelling tools devoted to heterogeneous microstructures.

However, as discussed in this chapter, a preliminary test on such EPS concrete material brought out some experimental issues that were difficult with such a material. Moreover, the complex microstructure and crack network turned out to be too complex for a robust validation of the numerical model in a first approach. Hence, a second material, made from EPS beads embedded in a plaster matrix (EPS plaster), has been elaborated. A procedure has been developed to manufacture specimens with a controlled structure to get a stable crack propagation through a much simpler microstructure. In fact, particular attention should be paid to overcome boundary effects on crack initiation. We will present here the method to manufacture the specimens together with the in-situ compression test procedure. Finally, in order to model the crack propagation through the EPS plaster samples, elastic properties of plaster have been determined using compression tests combined with digital image correlation (DIC) method.

4.2 Preliminary test on an EPS concrete sample

A preliminary test was performed on an EPS concrete sample using the tools available at Laboratoire Navier. An in-situ compression device was used on the XR-CT laboratory scanner to observe cracks in the sample under load. The details of these tools will be presented in this section. This experiment confirms the quasi-brittle nature of the material and the ability to detect progressive cracking in this material. Nevertheless, it also highlighted issues relative to sample and to experimental loading conditions.

4.2.1 EPS concrete sample

The expanded polystyrene (EPS) concrete is made from quartz sand and EPS beads embedded in a cement matrix. This material is a multi-purpose material for construction, which offers a range of technical, economical and environment-enhancing features. EPS concrete has some distinguished advantages like higher strength to weight ratio, better tensile strain capacity with respect to classical concrete, and superior heat and sound insulation characteristics due to inclusion of air voids in the lightweight aggregate. It is has been studied in many researches. For example, the size effect of polystyrene aggregates on strength and moisture migration characteristics of lightweight concrete was analyzed by [19] and on the compressive strength in [124]. The fracture phenomena of this typical material at macro scale are mainly studied under compression [145, 144]. The XR-CT technique has been applied to study such material in [198, 126]. The obtained image were of good quality.

The complex microstructure of this material ensures a heterogeneous behaviour at micro scale, making it an interesting candidate for comparisons with multiscale numerical simulations. Moreover, the high porosity of this concrete is suitable for crack initiation at relatively low

compressive loads and for stable crack propagation.

Several samples of EPS concrete were provided by Prof K.Miled (ENIT, Tunis) [144]. For the preliminary test, a cylindrical specimen (11.6 mm in diameter and 18.2 mm long, see 4.2(a)) was machined using diamond core drilling and cutting from a cubic sample. A slice of a CT image shows the microstructure in Fig. 4.2(b). The typical sizes of the components are about 1 mm for sand grains and 2 mm for EPS beads. Using a segmentation of the CT image of the whole specimen, the volumes fractions have been estimated to 18% for porosity and 57% for quartz sand. Finally, Fig. 4.2 shows that the local contrast of grey levels seems good in cement matrix and at interfaces with sand grains, which is promising for DVC.

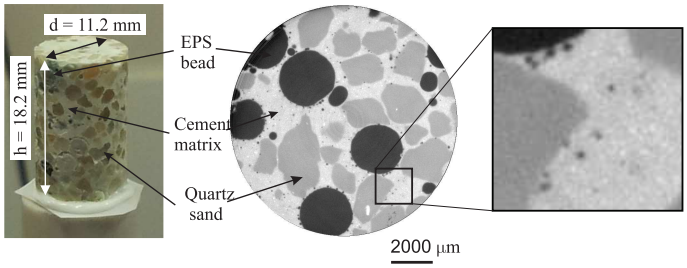

(a) (b) (c)

Figure 4.2: Geometry and composition of the EPS concrete specimen: (a) global view, (b) cross section (XR-CT image), (c) local contrast

4.2.2 Tomography

X-ray Computed Tomography was first used in the medical field 40 years ago. Nowadays it is widely developed for material science. This nondestructive technique is used for visualizing interior features within solid objects, and for obtaining information on their 3D geometries and properties. The XR-CT is based on X-ray radiography: an X-ray beam is sent on the sample and the transmitted beam is recorded on a detector. The ratio of the number of transmitted to incident photons, according to Beer-Lambert law, is related to the integral of the absorption coefficient of the material μ along the path that the photons follow through the sample:

$$I = I_0 \exp(-\mu x), \tag{4.1}$$

where I_0 and I are, respectively, the initial intensity of X-rays and the X-ray intensity measured after passing the object, x is the path length of the X-rays through the object and μ is the linear attenuation coefficient. X-ray absorption is a function of the nature of the atoms constitutive of the material and their number as well as the energy of the rays. Using the detector which is generally a combination of a scintillator (i.e. a material that converts X-ray energy to visible light) and a CCD sensor in modern tomographs, a series of radiographs (so-called projections) is recorded corresponding to various angular positions of the sample in the

beam. Those radios are used by a reconstruction software to obtain a three dimensional image, which represents the heterogeneous distribution of μ. A schematic illustration of an XR-CT experiment setup is depicted in Fig. 4.3.

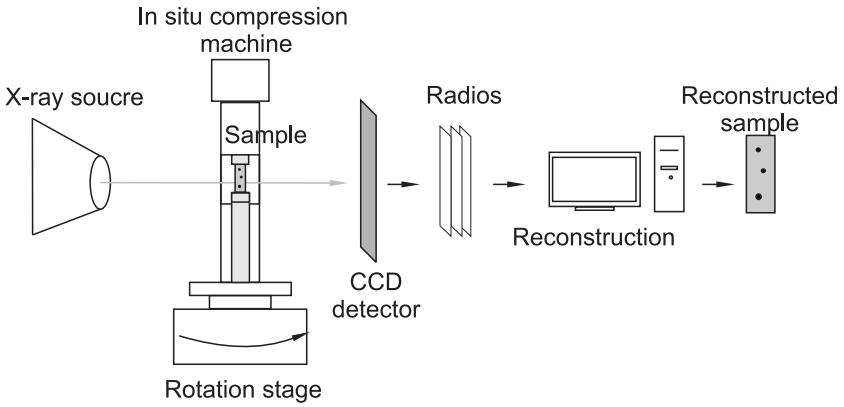

Figure 4.3: Schematic illustration of the in-situ compression test in a XR-CT device

The CT images of this work were captured on the XR-CT laboratory scanner available at Laboratoire Navier (Ultratom from RX-Solution) using a micro-focus source Hamamatsu L10801 (230 kV, 200 W, 5 μm) and a “flat-panel" imager Paxscan Varian 2520 V (1920x1560 pixels, pixel size 127 μm). The hollow rotation stage is able to support heavy samples (up to 100 kg) and was designed to receive in-situ experiments. A view of the in-situ experiments realized on the laboratory tomograph is depicted in Fig. 4.4.

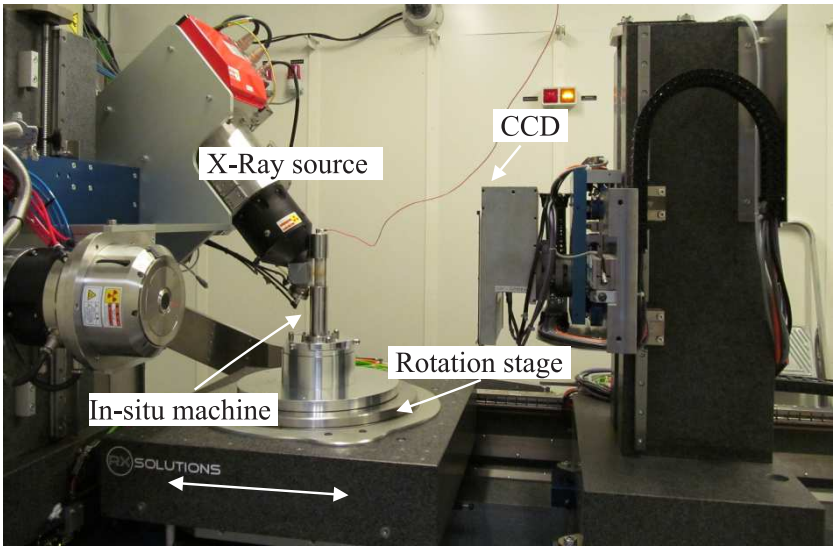

Figure 4.4: Global view of in-situ compression test combined with XR-CT at Laboratoire Navier

The XR-CT images are reconstructed by using the GPU-based reconstruction software Xact developped by the RX solutions. Some filters may be used to correct some artifacts as ring artifacts.

For the preliminary test on EPS concrete, tube voltage and current were respectively set to 120 kV and 125 μA, and the voxel size to 15 μm. The CT images of the whole specimen ($800 \times 800 \times 1200$ voxel^3) was created from 1120 projections, resulting from a scan lasting about 80 minutes.

4.2.3 Description of in-situ compression test

We are interested in the evolution of the crack network under compressive loading. Several CT images at several damage levels are required. In order to avoid crack closure after releasing the load to scan the specimen after each loading step (as would be done in an "ex-situ" experiment), a specific in-situ compression device has been used to hold the loading state during each scan.

The compression in-situ machine used for this study was developed by LMS (Ecole polytechnique). The device is mainly made of steel to ensure the mechanical strength. The transparency to X-rays is provided by a polycarbonate tube around the specimen (see Fig. 4.5). The specimen is centered in the beam with alignment screws at the bottom of the machine. The loading capacity of 10 kN is sufficient to load the EPS concrete specimen until rupture (up to 3.5 kN). Very low displacement rates (down to 0.1 μm/s) can be applied to ensure a slow propagation of cracks.

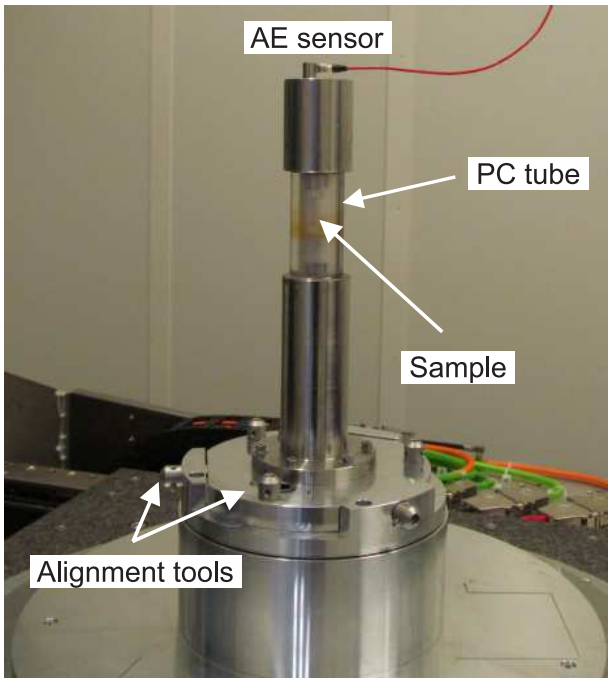

Figure 4.5: Description and installation of in-situ machine and acoustic emission

The load is applied to the specimen through ceramic tabs (made of Macor) with low X-ray attenuation in order to limit imaging artifacts at its boundaries. As described in Fig. 4.6, silicon mastic was added between the ceramic tabs and the specimen to compensate potential surface irregularities and plastic sheets were added to limit friction. In order to detect crack initiation or

propagation during loading, acoustic emission (AE) was acquired during loading using ab USB AE Node system (Mistras). A miniature sensor (Micro80) was stuck at the upper end of the machine (see Fig. 4.5). The sensor cable had to be unplugged during scanning to avoid collision with the source.

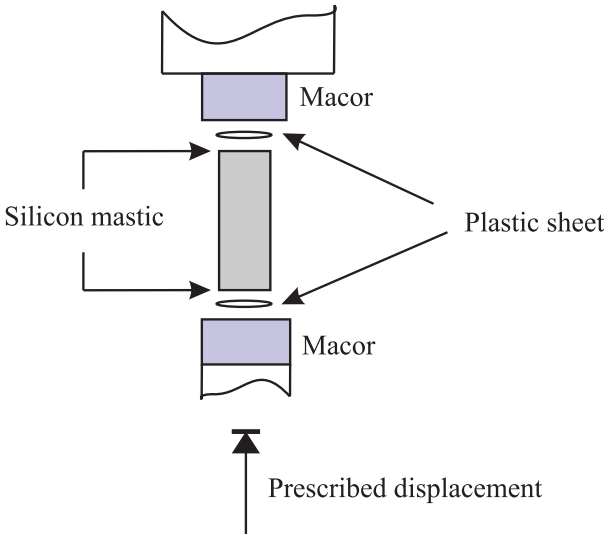

Figure 4.6: Set-up of the EPS concrete sample for the in-situ compression test

A first image, called “reference image", has been acquired once the specimen had touched the ceramic tabs (preload of a few Newtons). A second image, called “zoom image", has been acquired after a slight magnification change obtained with a little move of the detector. This image will be used to quantify the image correlation accuracy. Then, eleven successive loading steps have been applied to the specimen up to 1.381 kN. The displacement rate was 0.002 mm/s, except for the last 3 steps when it was decreased down to 0.0005 mm/s. Loading duration is a few minutes. After each loading step, the displacement was kept constant until the next loading and a CT image was acquired after a 10 min relaxation time. Finally, note that the specimen was unloaded during nights (i.e. between steps 2-3; 6-7; 8-9) to avoid brutal rupture after a too long loading at high stress.

4.2.4 Result and discussion

The macroscopic load - axial strain curve is plotted in Fig. 4.7. The global axial strain is here computed from DVC data (two planes of correlation points, near the lower end and upper end are chosen to compute strain). First cracks have been observed at the upper end of the sample (see Fig. 4.8) at the eighth loading step, corresponding a load $F = 1221$ N (stress $\overline{\sigma} = 10.8$ MPa) and a strain $\overline{\varepsilon} = 0.06\%$. This step matches the loss of linearity of the macroscopic curve. Then the cracks slowly propagate and have been observed in the next three images (steps 9 to 11). The mechanical response and the slow crack propagation confirm the expected quasi-brittle behaviour of the material.

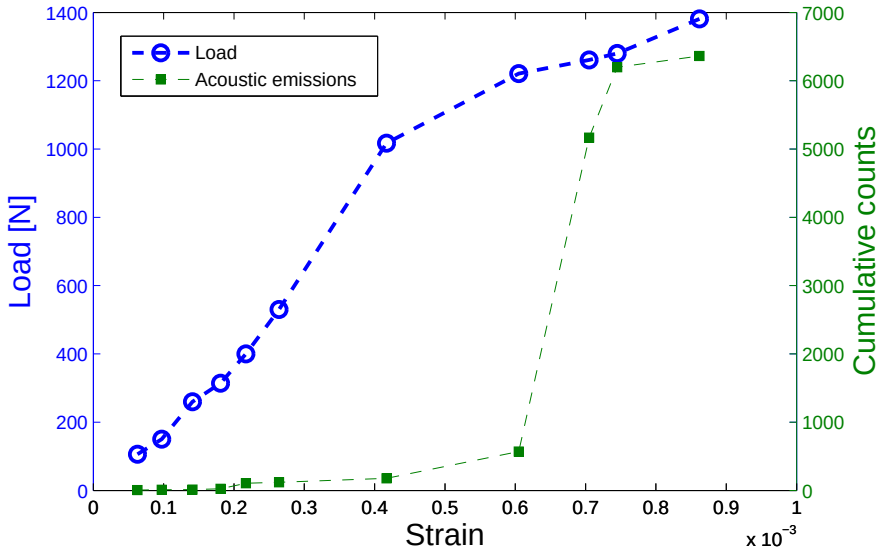

Figure 4.7: Macroscopic load - axial strain response under compression test of EPS concrete specimen

The initiation of cracking corresponds to a clear rise in AE counts as presented in Fig. 4.7. The high jump between steps 8 (1.221 kN) and 9 (1.261 kN) is due to the major propagation of the cracks. AE activity remained important during slight propagation and crack opening until the last loading level. This shows the ability of acoustic emission recording to detect crack initiation and propagation while loading the EPS concrete. Thus, the number of loading steps in the elastic part may be reduced for next tests, and more scan time could be dedicated to damage propagation analysis.

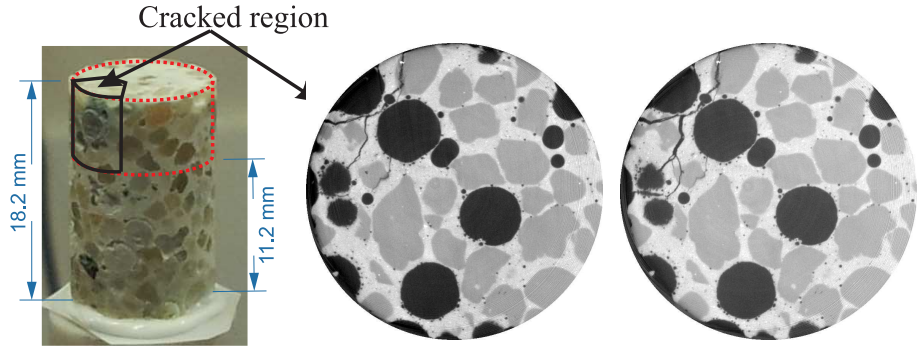

Figure 4.8: Crack localization and propagation observed in the EPS concrete sample under compression: (a) global view; CT cross-section of cracked region at load (b) F = 1.261 kN and (c) F = 1.381 kN

However, the crack localization is not satisfactory and reveals issues with boundary conditions

of the sample : the cracks initialize in the upper boundary region before appearing in the most porous region. This phenomenon may be due to stress concentration at the upper bearing surface and indicates a possible parallelism defect. Friction effect could also worse this phenomenon. Thus, the precautions taken were not sufficient to correct the defects of the sample. Detained boundary conditions are eventually not known and will be impossible to reproduce exactly in the numerical simulation. So procedures to prepare the sample need to be improved together with the sample set-up in the in-situ testing device.

Several phenomena interfere and the microstructure heterogeneity make them harder to understand and to correct. Moreover, the damage response of EPS concrete is complex to model and several difficulties are raised to validate modeling:

- The complex behavior of three phases containing interfacial phenomena requires more elaborate constitutive relations and too many parameters to be identified for the numerical validation.
- The interactions between the different phases of concrete, i.e. coarse aggregate, interfacial transition zone, and cement matrix are still open issues in both experiments and modeling.
- The geometry input for the numerical simulation requires a segmentation of the CT images to define the spatial distribution of the three constituents. Such a segmentation might not be straightforward in a three-phase material with complex shaped inclusions and similar gray levels of the phases, or even fluctuating gray levels (as in cement). Imperfect segmentation might have a strong influence on the local response of the material and the paths of the microcracks.

Therefore, a simpler material has been chosen to enhance the experimental protocol and validate the numerical model. However, beyond the mechanical questions, this preliminary test provided CT images of a heterogeneous cracked microstructure that turned out to be useful to develop specific DVC-based tools to detect and extract damage as described in Chapter 5.

4.3 Improved experimental procedure

4.3.1 EPS plaster

In this section, we introduce the material chosen for addressing issues raised by the preliminary test. The latter should satisfy the following conditions:

- It should be composed of two phases only: matrix and porosity, for an easier comparison and validation to the numerical method.
- The geometry of the constituent should be simplest, to be easy to model in the numerical simulation.

- The localization of damage should be controllable, and not sensitive to non predictable imperfections of the boundary conditions.
- The matrix phase should exhibit a sufficient local contrast for the application of DVC, at least for overall strain measurements.
- The constitutive relation of the matrix phase should be simple, isotropic and homogeneous.
- Samples should be easy to manufacture with as perfect as possible geometries

A good candidate for these requirement is Plaster material. It is wide spread in civil engineering. Its manufacturing is easy and fast. Significant research activity on this material has been reported in literature, especially on its mechanical properties and its damage mechanisms [187, 134, 98]. In particular, thanks to a recent study by Romani et al [179, 180], there is some knowledge on this material at laboratory Navier. Moreover, at our scale of analysis, plaster can be considered as a homogeneous material.

Plaster exhibits a brittle behavior. In order to develop a stable crack network, and localize it in a specific region of the sample, EPS beads have been added within the plaster matrix. EPS stiffness is very low (4-8 MPa) so they can be assimilated to air only. This material is thus composed of two phases: the assumed homogeneous plaster matrix and porosity (EPS beads and residual porosity), with a controllable spatial phase distribution through EPS beads number, size and position. In addition, it is suitable for an easy data input in the numerical model. Indeed, the segmentation of porosity is very easy and the beads are quasi-spherical, making possible the generation of similar virtual microstructure (see Chapter 6).

Specific experimental procedures have been developed to manufacture small EPS plaster samples adapted to the in-situ compression test. They will be presented thereafter, together with the enhancement of the in-situ set-up.

4.3.2 Description of the improved set-up for in-situ compression testing

The result of the preliminary test has indicated that: the problem of friction, roughness and non parallelism of the bearing surfaces need to be addressed specifically. Several enhancements have been proposed to improve the conditions of the compression test.

(1) In-situ machine: Two Macor tabs are replaced by aluminum tabs. Special care is in addition taken to center the specimen on these tabs.

(2) As the work of Romani [179], two PMMA plates are added on top and bottom of sample. At the contact region (PMMA - sample) we also add silicon grease to reduce friction.

(3) As described in more details in Chapter 6, the transverse strain prescribed by the tabs to the sample at its ends plays a central role on the initiation of damage. It depends on the discrepancy of the Poisson's ratio / Young's modulus ratios of the materials in contact and on the friction coefficient. Three solutions have been tested to reduce this effect: (3a) the PMMA plates are machined with the same cylindrical shape and same diameter as the sample, in order

to avoid the punching effet; (3b) the PMMA plates are carefully polished at their interface with the sample (3c) aluminium plates with same shape and size and similarly polished have also been used in place of the PMMA plates.

(4) Loading: Rate of prescribed displacement is reduced in damaged domain.

The detail of the new set-up for the in-situ compression test is described in Fig. 4.9

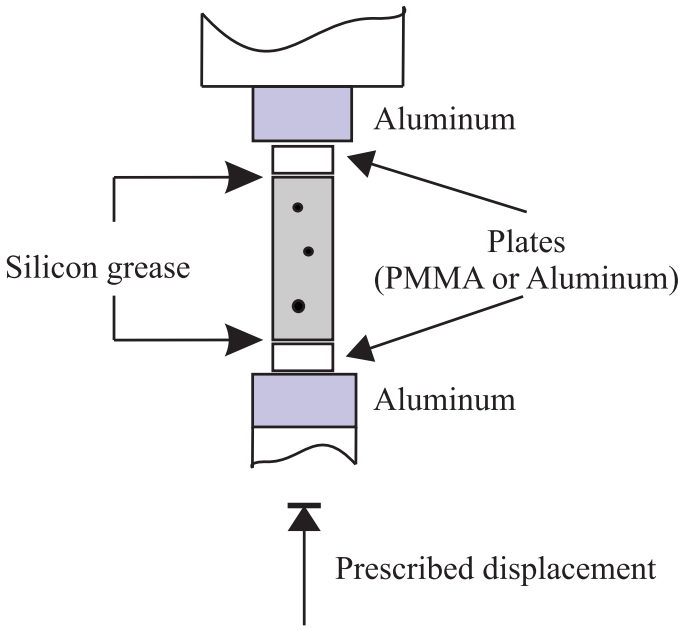

Figure 4.9: Description of the new set-up for in-situ compression test

4.3.3 Plaster samples preparation

4.3.3.1 Issues to be addressed

The obtained samples are used to observe the 3D crack phenomena at micro scale. Therefore the specimen manufacturing process has to satisfy the following conditions:

- Reproducible behavior, so that the load levels at which damage occurs in the samples can be reasonably well evaluated by preliminary ex-situ tests.
- Control of microstructure (position and volume fraction of EPS beads)
- Satisfactory conditions of uniaxial compression test (parallelism, friction,...)
- Small sample for a better resolution of CT images.

Note that because of the simple geometry of the almost spherical EPS beads and the homogeneity of the plaster matrix, this material is a priori a good candidate for comparisons with the numerical model. However we want to manufacture samples with simple geometries and limited numbers of beads, ideally placed far away from the ends of the sample where mechanical

conditions are more difficult to control. That's why a direct mixing of EPS beads into the plaster paste is not the right way to manufacture this two-phase material, because such a procedure does not allow to control the positions of the beads. Even the local volume fraction would be hard to control because of aggregation and buoyancy effects.

That's why a more original manufacturing route has been preferred, based on the use of medical syringes in which the plaster paste is sucked, together with individual EPS beads in selected number and sizes. This protocol has also the advantage to limit the presence of other porosities in the samples, and produces directly cylindrical samples with almost perfect lateral surfaces. After unmolding, there is no need to machine the latter. Several syringe sizes can be used to manufacture samples with different sizes.

The final protocol is described in Fig.4.10. It involves four major preparation steps : mixing, drying, cutting and polishing. The protocol is fully detailed in Appendix A.3. Specific issues of each step and their impact on the sample are discussed below.

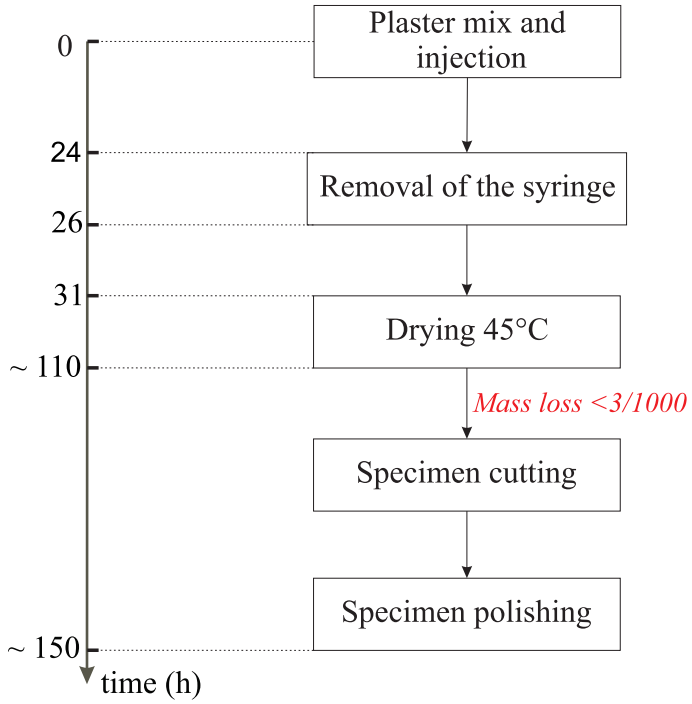

Figure 4.10: EPS plaster preparation process and corresponding time for about 10 specimens

4.3.3.2 Specimen molding in syringe

The used plaster (Prestia Profilia 35) is the same as in the work of Romani [179], where, its mechanical properties (elastic moduli, fracture parameters) have been determined experimentally and some damage phenomena on samples with a particular 2D shape (rectangular plate with one or several regularly spaced cylindrial holes) have been studied. The plaster is first mixed with water using the same mixing rate (water/plaster=0.33) as in the work of Romani [179]. Syringes are immediately filled with plaster and the chosen number of EPS beads. Used tools

and materials are detailed in Appendix A.3. The syringes are removed after about 24 hours to facilitate the drying process. Moreover, it will be easier to cut the specimens without them (better clamping). Since mechanical properties of plaster are very sensitive to hydration time [179], the specimens are placed in an oven until complete drying.

In order to ensure a reproducible behaviour of the plaster matrix, this protocol must be strictly performed in the same conditions that are:

- the time between mixing and drying (31h);
- the drying temperature in the oven (45°C, to speed up drying without altering plaster properties);
- the mass loss criterion to stop drying (the drying is stopped when the mass change is less than 3/1000 after a 24h period)

4.3.3.3 Selection of region of interest

The behavior of the specimens and the cracks location are strongly influenced by the position of the EPS beads. To avoid cracking near the boundaries and to ensure crack initiation near EPS beads, they should ideally be placed at the center of the specimen (longitudinally). The porosity volume fraction should also be high enough to ensure a sufficient stress concentration in the beads region. In order to control the positions of the beads, the following precaution need to be taken.

First, during the molding, EPS beads must be suck in a sequence taking into account the fact they will go up by buoyancy as long as the plaster is not dry; during this time, and the syringe must stay vertical so that beads don't migrate towards the lateral surfaces (see details in Appendix A.3). Then, the actual position of the beads in the sample is detected within the syringe from two radiographs recorded at two orthogonal angular positions. Finally, satisfactory specimens are selected and cutting marks are positioned to center the EPS beads as orthogonal as possible in the sample. The diameter of specimens being about 9 mm, the height is chosen to be at least 18 mm (about 18-20 mm in practice).

An example of radiographs is depicted in Fig. 4.11. Here, the sample 02 and 03 are selected and cutting marks are depicted in Fig. 4.11(b). The other ones shows cracks resulting from drying near the EPS beads and has been discarded.

4.3.3.4 Enhancement of parallelism, flatness and friction conditions

The errors of the parallelism of end surfaces have been estimated with a comparator by measuring level differences on a flat end of the specimen while the other end stays on a flat reference plane (see Fig. 4.12). This quantification of parallelism has been used to analyze effects of cutting and polishing on parallelism. Note that both latter elaboration steps have been performed without water to avoid uncontrolled changes in mechanical properties of plaster.

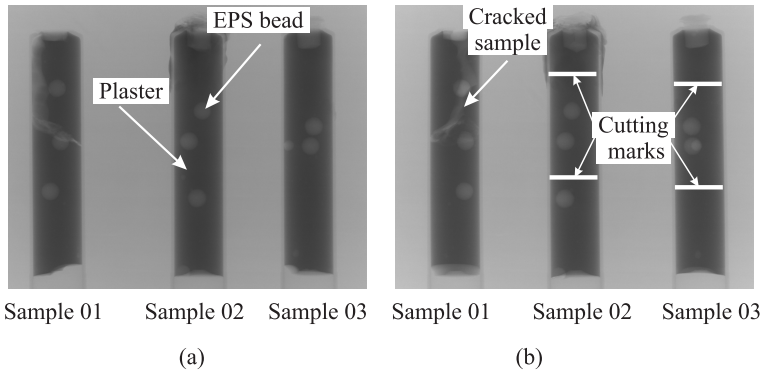

Figure 4.11: Radiographs of three typical EPS plaster specimens before cutting, at two orthogonal positions: (a) 0°; (b) 90°

First, both ends of each specimens have been cut with a precision table-top cut-off machine (using a ⊘125 mm cut-off wheel). It has been noticed that the parallelism error is related to the feed speed of the sample. Indeed, a low feed speed gives a low parallelism error, but it requires more working time. An reasonable value V = 0.02 mm/s has been chosen after detailed analyzes which are presented in Appendix A.4, is feed speed leads to parallelism errors between $20 - 40$ μm. A few specimen were tested for compression test right after cutting. It turned out that, cracks still initiated at the boundaries. That's why a polishing step has then been added to reduce parallelism errors and to decrease the roughness of bearing faces. In fact, as it will be demonstrated in Chapter 6, friction at the contact area is the main reason of crack initiation at the boundary. Hence, both ends of each specimen have been polished using an automatic polisher (1200 and 2000 SiC grind paper) equipped with a specifically designed holder to ensure accurate orthogonality of sample end surfaces and lateral surface. The detailed description of this processing is also presented in Appendix A.4. After polishing, the parallelism errors have been quantified to be below 30 μm. Note that results are better for specimens already showing a low parallelism error after cutting.

4.4 Summary of results of in-situ compression tests

Finally, one week is required to manufacture a group (dozen) EPS plaster specimens. In fact, some samples were discarded during the ROI selection step. If the manufacturing process is respected, each final sample satisfies the following conditions:

. The porosity is controlled through the number of beads and their position.

. The bearing surfaces are very smooth.

. The parallelism error is acceptable (about 10-20 μm).

. The flatness error is negligible.

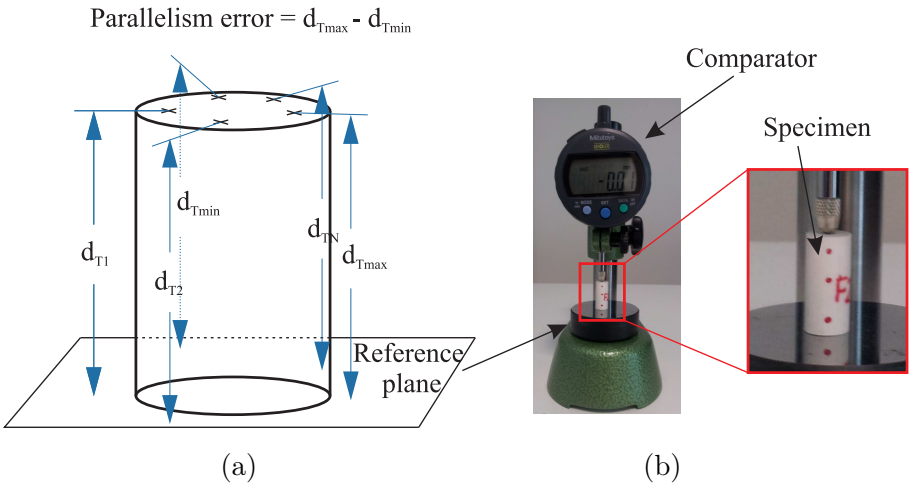

Figure 4.12: Parallelism error quantification: (a) main principle; (b) real measurement

. The elastic behavior is reproducible (see section 4.5).

In the end, six EPS plaster specimens were tested in-situ under XR-CT, whose settings are reported in Table 4.1. The detail of the tomography parameters is reported in Table 4.1. Two groups of settings were used, both leading to a 3 hours helical scan (two turns to scan the whole specimen) with a 8.00μm voxel size. The second settings group, used for PlasterF1 and F3, leads to slightly better images with a higher signal to noise ratio.

Name	Current (μA)	Voltage (kV)	Frame rate (proj./sec)	Average num (projections)	Voxel size (μm)	Times (h)
PlasterE2/E5/E10/B2	67	120	2	8	8	3
PlasterF1/F3	67	120	3	12	8	3
ConcreteP2	79	130	3	12	10	3

Table 4.1: Summary of X-ray tomography settings

A summary for each in-situ test is given in Table 4.2 together with details about the specimens (number of inserted EPS beads, dimensions). For specimens PlasterE10, PlasterE2 and PlasterB2, the PMMA tabs were not polished. So cracks initiated from the bearing surfaces. For specimens PlasterE5, PlasterF1 and PlasterF3, polished PMMA or aluminum plates were used, solving the boundary condition issues presented above. However, in the sample PlasterE5, the EPS beads were distributed along the whole sample. This specimen is slided out of scan region during the loading so that obtained images were of poor quality. In short, two tests on plaster specimen will be used for the comparison to numerical results and will be fully studied in Chapter 8. Both specimens PlasterF1 and PlasterF3 contain two EPS beads. Cracking has respectively been observed for the last 13 and 4 steps before failure and it initiated near EPS beads. No side effects have been observed. An example of CT image showing cracking in

Name	Beads number	Loading steps	Cracked steps	F_{max} (kN)	Tabs	Valid results
PlasterE10	3	4	2	2.65	PMMA	No
PlasterE2	3	10	6	2.7	PMMA	No
PlasterB2	Multi	6	4	2.4	PMMA	No
PlasterE5	5	4	3	2.9	polished PMMA	No
PlasterF1	2	15	13	2.71	polished aluminum	Yes
PlasterF3	2	20	4	2.65	polished PMMA	Yes
ConcreteP2	Multi	12	6	1.939	polished aluminum	Yes

Table 4.2: Summary of performed in-situ compression tests . "Load number" is the number of loading steps, while "cracked steps" stands for the number of steps where cracks have been observed.

PlasterF3 is presented in Fig. 4.13. The load-deformation curve is also presented in Fig. 4.14, where the global axial strain is computed by DVC. Each color corresponds to a "loading phase" (between two loading phases, the sample is unloaded). A non-linearity in the form of a reduction of the slope of the force-strain curve within a loading phase, is observed at the end of the test, which confirms the quasi-brittle nature of this sample. Note that the sample has been taken out of the of in-situ machine at step 14 (because in-situ machine breaks down). A new reference image at almost zero load has been recorded after repositionning and served as reference for fifth and sixth loading phases. This may explain the big gap between fourth and fifth loading phases in the overall load-deformation curve.

This preparation protocol (cutting and polishing) has been also applied to another EPS concrete sample (ConcreteP2). It is made of the same typical EPS concrete material as the sample of the preliminary test. CT settings of the helical scan for one loading step are reported in Table 4.1. 12 loading steps have been applied on this specimen, including 6 steps showing cracks propagation (Table 4.2). Unlike the preliminary test, cracks did not initiate near boundaries but in the most porous area. This test will be fully analyzed in Chapter 8.

4.5 Elastic properties measurement by DIC

The comparison with predictive numerical simulations (detail in Chapter 8) requires elastic properties of plaster matrix. They are determined from homogeneous plaster specimens under uniaxial compressive load. The specimens are similar to those used for in-situ testing except that no EPS beads are included. The specimen deformation is measured using Digital Image Correlation (DIC) and strain gauges. We present here the experimental procedure and obtained results.

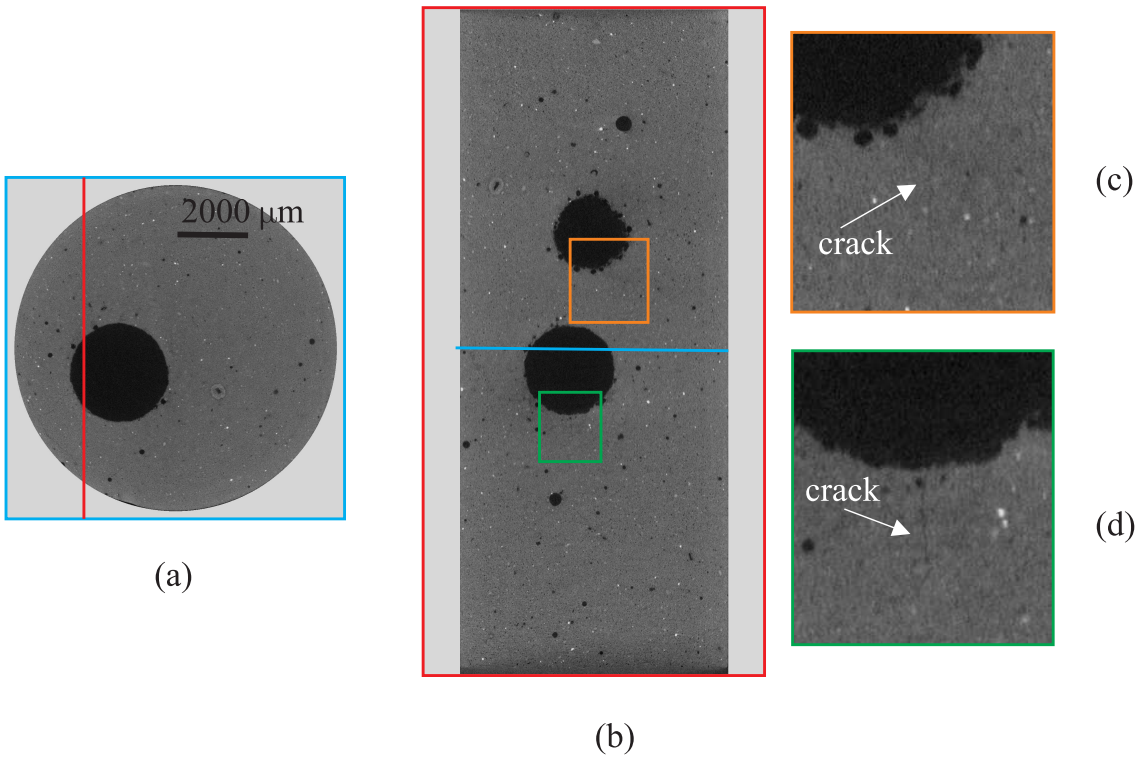

Figure 4.13: CT-image of PlasterF3 at 2.885 kN showing cracks: (a) cross section, (b) longitudinal section, (c) zoom on bead 1 and (d) zoom on bead 2.

4.5.1 Principle of DIC

DIC is a full-field measurement technique, based on the comparison of images acquired at different stages of a mechanical test and gives access to evaluation of the displacement field at the surface of the sample. The DIC principles have been introduced in experimental solid mechanics more than 20 years ago [207] and this techniques in currently used for many application. We refer to references [206] [4] for a detailed description of this technique. The specific 2D-DIC procedure used in this work is similar to the one used in reference [35]. The DIC analysis is performed using the in-house software “CMV". The procedure is based on four main steps.

Firstly, a regular grid of points, so-called “correlation points", is generated. Each point is associated with a correlation windows D centered on it. In this work, D is square with a uniform size for all points (20 pixels). Some points located in regions with bad image contrast are picked out. They will not be used in the procedure.

Secondly, the correlation procedure is performed. It consists in finding the most similar domain in the deformed image for each correlation window of the reference image. To do so, the correlation coefficient C measures the similarity of grey levels between correlation windows in the reference image and in the deformed image. This coefficient is optimized to find the best position for correlation points in the deformed image. The transformation is supposed to the simplest (order 0, i.e. pure translation) and a nearest neighbor interpolation of grey levels is

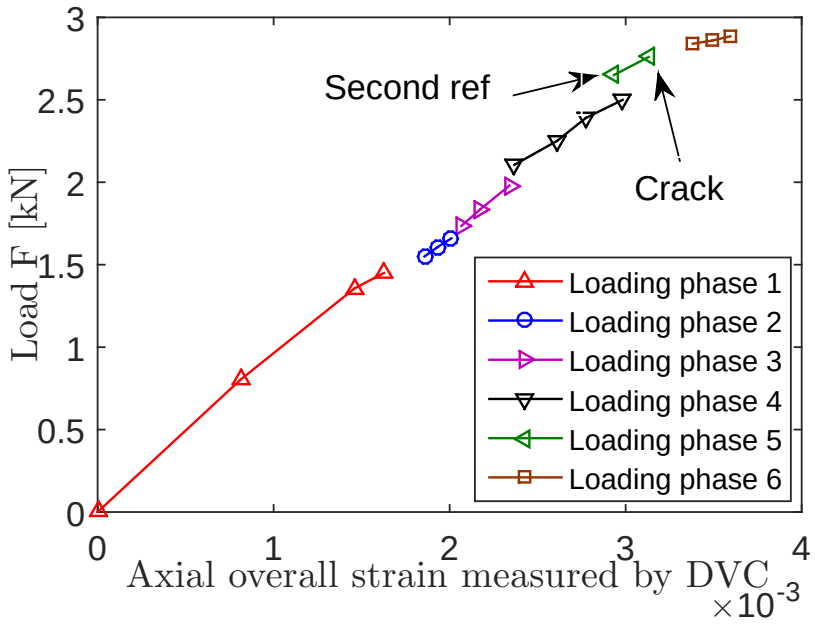

Figure 4.14: Macroscopic load-deformation response of PlasterF3 under compressive loading: the test was divided into six loading phases between which the specimen was unloaded for the night.

used.

After this first evaluation for all correlation points, a sub-pixel optimization is run. The correlation coefficient is optimized one more time considering a transformation with a higher order (affine transformation) and a more precise interpolation of grey levels (bi-linear or bi-cubic)

Finally, positions of correlation points are used to compute the local strain, which is defined as the average of the transformation gradient on a domain (neighboring measurement points) surrounding the considered point delimited by a set of neighbouring measurement points. This domain can be chosen as the whole region of interest to computer the overall strain. The detail of this method is described in [11]. This procedure is run for each image acquired during the compression test.

4.5.2 Set-up of the macroscopic compression test with camera and strain gauges

Homogeneous plaster specimens have been prepared following exactly the same procedure than in-situ samples. The specimen diameter is still 9 mm, with a height between 18.5 and 19.5 mm. The parallelism error is very small (20-30 μm), and bearing surfaces are very smooth. The average density of the six produced samples is estimated to 1675 kg/m^3 with a standard deviation of 8.8 kg/mm^3. This very low variability confirms the similarity of the specimens. Because there is no natural contrast at the surface of almost uniformly white plaster specimens, a random

speckle pattern is added with black painting. The typical size of the obtained speckle is about 0.1 mm but there are also some dots.

Two strain gauges were glued on two opposite faces to complement and validate the DIC measurement (see Fig.4.15(a)) [1]. The compression test were performed of a INSTRON machine with a 10 kN loading capacity. The set-up of the sample on the machine plates is similar to the one described in section 4.3.2 for in-situ tests, using polished PMMA tabs. The contact between the plates and the specimen is reached with a displacement rate of 0.005 mm/s. The latter is then decreased to 0.001 mm/s during the loading.

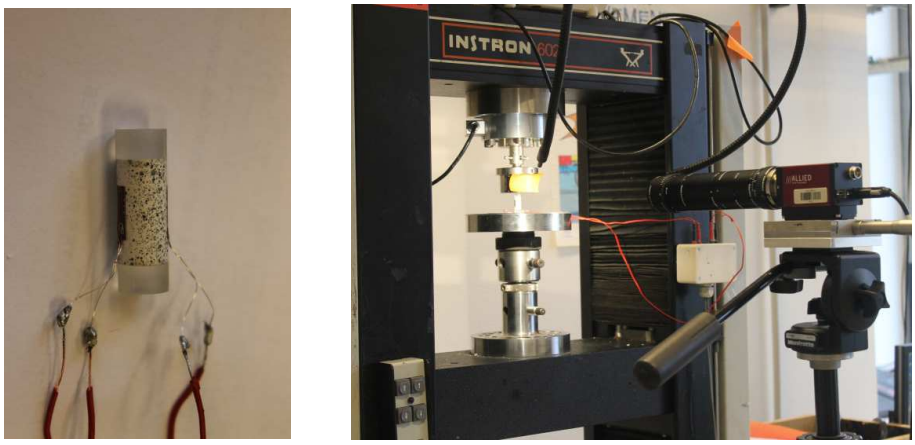

(a) (b)

Figure 4.15: Experimental setup for measurement of Young's modulus: (a) sample with gauge; (b) optical setup

The optical setup is based on a AVT camera Pike F−421B/C, with resolution 2048×2048 pixels, 15.2 mm sensor size, real pixels size of 7.4 μm. A macro lens (from Schneider Kreuznach) with focal length 120 mm is used. An optical magnification of 0.6 is obtained with appropriate extension tubes and the distance between camera and specimen is about 32 cm (see Fig. 4.15(b)). This configuration allows to capture the whole specimen and the PMMA plates. A long focal length has been selected to reduce the impact of magnification variations due to the motion along the optical axis of the specimen during the loading. Images are recorded in 8-bits mode.

After the capture of the reference image at the initial unloaded state, a "zoom image" is acquired by moving the camera 1 mm away from the sample, ie in the direction orthogonal to the observation plane. Similarly to in-situ tests, this image will be used to evaluate the correlation DIC errors. Besides, it will be used to correct magnification variations. A series of image of the sample during deformation are then captured during loading, with a frame rate of 4 images/s.

[1] Gauges (KFG-5-120-C1-11) are 5 mm long with a gauge factor of 2.09 ± 1.0%

4.5.3 Main assumptions of elastic parameters determination

Our specimen has a cylindrical form. On its coordinate, the strain contains three components: $[\varepsilon_{rr}, \varepsilon_{\theta\theta}, \varepsilon_{zz}]^{\mathrm{T}}$ as depicted in Fig. 4.16(a). But the homogeneous plaster specimen can be considered as an isotropic homogeneous material. Moreover, in the case of perfect uniaxial compression, components outside the diagonal of strain tensor are negligible, so we assume that: $\varepsilon_{rr} = \varepsilon_{\theta\theta}$, and we can use the surface cinematic measurement methods to determine its elastic parameters, as provided by 2D-DIC. The deformation in the surface contains only two components: $\varepsilon_{11} = \varepsilon_{\theta\theta}$; $\varepsilon_{22} = \varepsilon_{zz}$, see Fig. 4.16(c)

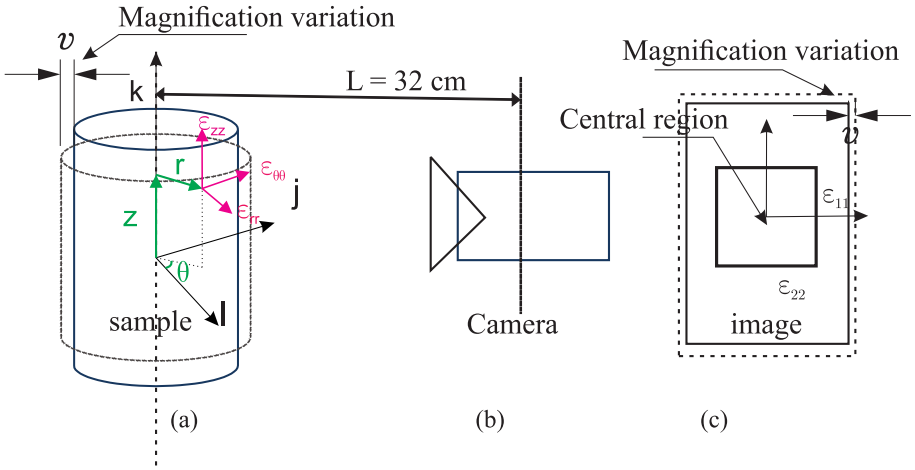

Figure 4.16: Assumption of surface observation for cylindrical plaster sample and Poisson effect

Because the sample is cylindrical, the camera cannot be focused on the entire observed surface. Here we focused on the central part of the surface, so DIC errors will be more pronounced on the peripheral part. Moreover, additional errors may appear due to rotation, motion and cracking during loading, especially at the edges of the sample. In order to minimize the effect of these phenomena, global strain will be computed on the central part of the specimen only (see Fig. 4.16 (c)).

4.5.4 Error assessment and correction of magnification variation

4.5.4.1 Sources of error

DIC measurements always include errors related to both imperfections of image acquisition and DIC processing. We can summarize the typical error sources by the following (see [69, 33, 62, 4]):

(SE1) Image noise

(SE2) Geometric errors due to optical distorsions.

(SE3) DIC algorithm: (a) shape function mismatch errors and (b) systematic error

(SE4) Non-controlled out of plane rigid body motion

First, errors due to the image noise (SE1) depend strongly on the characteristics of the sensor of the camera. In the work [183], this error has also to be associated with the actual contrast in the correlation domains. The study shows that DIC random error is more or less proportional to the ratio between noise and available local contrast. In this work, an enhancement of the local contrast by applying fine speckle painting will allow to reduce this error to a low level which will be quantified by the analysis of the zoomed image. The increase of correlation window size would decrease the random error at the price of a possible increase of shape function error (SE3a).

Second, the source of error (SE2) in 2D-DIC investigations is related to geometric errors in the reference or deformed images. The source this error might come from issues with instabilities or distortions the imaging system. Nevertheless, in our case: (a) CCD sensors have a fixed and well defined geometry; (b) the displacements are small, the optical distortions are similar in the reference and deformed images and may cancel out in the strain computation. Thus error (SE2) will be considered as negligible.

Third, deformation of plaster material is less than 0.4% (and about of [0.1-0.2%] to compute elastic parameter). Because of this very low strain, errors due to the shape function mismatch (SE3a) are very low too [33]. On the contrary, the systematic errors (SE3b) may remain important even at low strain. In fact, these errors are related to the available contrast, image quality, noise, chosen image correlation algorithm and interpolation of gray levels in the correlation domain, which is performed in order to get the displacement with sub-pixel accuracy. As introduced in the work of Dautriat et al [62, 230], systematic errors can be evaluated by performing the DIC analysis on the reference image and the zoomed image. They are determined as the difference between the evaluated and theoretical displacements, associated with the global camera motion. This procedure is used also to evaluate random errors due to image noise (SE1).

Finally, the source of error (SE4) can be the most important in this work. Because of non perfect boundary conditions and of the overall compliance of the testing machine, the sample might undergo some small overall rigid body motions (rotations and translations), in addition to the deformation dues to the compression. The out-of-plane parts of these motions cannot be precisely evaluated by a purely 2D-DIC method. Stereo-correlation techniques could have been used but would be much more cumbersome to apply and might induce other difficulties (e.g. calibration). The Poisson effect is also responsible for a slight out of plane motion of the observed surface.

In summary, sources of error related to geometric distorsion (SE2) and shape function mismatch (SE3a) are neglected. Image noise (SE1), systematic errors (SE3b) and errors related to out of plane motion (SE4) will be analyzed in the following.

4.5.4.2 Assessment of errors due to out of plane motion

In fact, the Poisson effect and any global motion along optical axis are responsible for an out of plane motion of the observed surface which induces a bias in the evaluation of the displacement

field because the optical lens performs a central projection and not a parallel one. The resulting error in the strain evaluation may be corrected using a simple approximation. Let $\boldsymbol{\varepsilon}^a = [\varepsilon^a_{11}, \varepsilon^a_{22}]^{\mathrm{T}}$ denote the apparent macroscopic deformation measured by DIC, while $\boldsymbol{\varepsilon}^v = [\varepsilon^v_{11}, \varepsilon^v_{22}]^{\mathrm{T}}$ is the macroscopic due to the magnification variation v (out of plane motion). The corrected deformation $\boldsymbol{\varepsilon}$ is defined from apparent deformation $\boldsymbol{\varepsilon}^a$ and magnification variation deformation $\boldsymbol{\varepsilon}^v$ as:

$$\begin{cases} \varepsilon^a_{11} = \varepsilon_{11} + \varepsilon^v_{11} \\ \varepsilon^a_{22} = \varepsilon_{22} + \varepsilon^v_{22} \end{cases} \tag{4.2}$$

Assuming the magnification variation is only due to Poisson effect, $\boldsymbol{\varepsilon}^v$ can be expressed:

$$\varepsilon^v_{11} = \alpha.v \tag{4.3}$$

where α is a variation coefficient corresponding to the Poisson effect. With D standing for the sample diameter, the displacement v is here determined by:

$$v = \varepsilon_{11}.D \tag{4.4}$$

Following Dautriat et al [62], the apparent strain induced by the out-of-plane motion can be quantified with the zoomed image obtained by moving the camera 1 mm away from the sample, ie $v = v_0 = 1$ mm. From (4.3) and the measured deformation $\varepsilon^{v=1\mathrm{mm}}_{11}$, α can be identified with:

$$\alpha = \frac{\boldsymbol{\varepsilon}^v_{11}}{v} = \frac{\boldsymbol{\varepsilon}^{v=1\mathrm{mm}}_{11}}{v_0} \tag{4.5}$$

So the horizontal deformation is determined by the following:

$$\varepsilon_{11} = \frac{\boldsymbol{\varepsilon}^a_{11}}{1 + D \times \dfrac{\boldsymbol{\varepsilon}^{v=1\mathrm{mm}}_{11}}{v_0}} \tag{4.6}$$

The correction for vertical deformation can be expressed from equations (4.2), (4.3) and (4.6):

$$\varepsilon_{22} = \varepsilon^a_{22} - \frac{D \times \dfrac{\boldsymbol{\varepsilon}^{v=1\mathrm{mm}}_{11}}{v_0}}{1 + D \times \dfrac{\boldsymbol{\varepsilon}^{v=1\mathrm{mm}}_{11}}{v_0}} \times \varepsilon^a_{11} \tag{4.7}$$

The strains defined in (4.6) and (4.7) will be used to determine E, ν. More precisely, above expressions will be applied to in-plane principal strains ε_{11} and ε_{22} to define E and ν. However, in the specific case of our experiments, the camera was well aligned with the sample and the testing machine, so that out-of-diagonal terms of the 2D strain tensor were negligible.

An alternative way to get rid of magnification variations due to out-of plane translation is to focus on purely deviatoric strains. In the case of isotropic material, devitoric stress and strain are linked by the shear modulus:

$$\sigma^{eq} = 3\mu\epsilon^{eq} \tag{4.8}$$

where the equivalent stress σ^{eq} and the equivalent strain ε^{eq} are defined for the case of uni axial compression:

$$\begin{cases} \sigma^{eq} = \sigma_{22} \\ \varepsilon^{eq} = \dfrac{2}{3}\sqrt{(\varepsilon_{11} - \varepsilon_{22})^2} \end{cases} \tag{4.9}$$

On other hand, from E.q. (4.6) and (4.7), equivalent strain can be also defined for apparent strain:

$$\varepsilon^{eq} = \frac{2}{3}\sqrt{(\varepsilon^a_{11} - \varepsilon^a_{22})^2} \tag{4.10}$$

We note that μ does not depend on the change of magnification due to Poisson effect, It will be computed from experimental data and compared to the evaluated Young's modulus and Poisson Ratio.

Finally, as commented above, in the case of uni axial compression (with perfect conditions), the strain component ε_{12} should be zero. However, the complex motions induced in the sample by damage may induce a the non null value of this component. Therefore, we can use it as a signal for the appearance of damage. Similarly, 2D-DIC gives acces to the in-plane rotation of the sample. Its value might be an indicator of the intensity of the overall rigid body rotations, including out of plane ones (which remain unknown).

4.5.5 Analysis of the results

In this subsection, we first present procedures to analyze the results of the specimen N° PlasH03. Then they will be applied for all tested samples.

4.5.5.1 DIC Errors analysis

Firstly, we perform the DIC on the reference image and the zoom image. The central region is chosen for result analysis. A view of the whole correlation mesh and its central region are depicted in Fig. 4.17.

The influence of the correlation window size on the accuracy of DIC can be determined by using the following analysis: we evaluate the standard deviation of the difference between the calculated displacement and the displacement corresponding to the homogeneous transformation equal to the mean global deformation gradient evaluated from a contour integration on the whole area of interest. We note σ_1, σ_2 obtained standard deviations for the horizontal and vertical components of the displacement. We plot these values as a function of the correlation window size in Fig. 4.18. Correlation windows with 30 pixels on a side are chosen and lead to an accuracy of displacement better than 0.04 pixels.

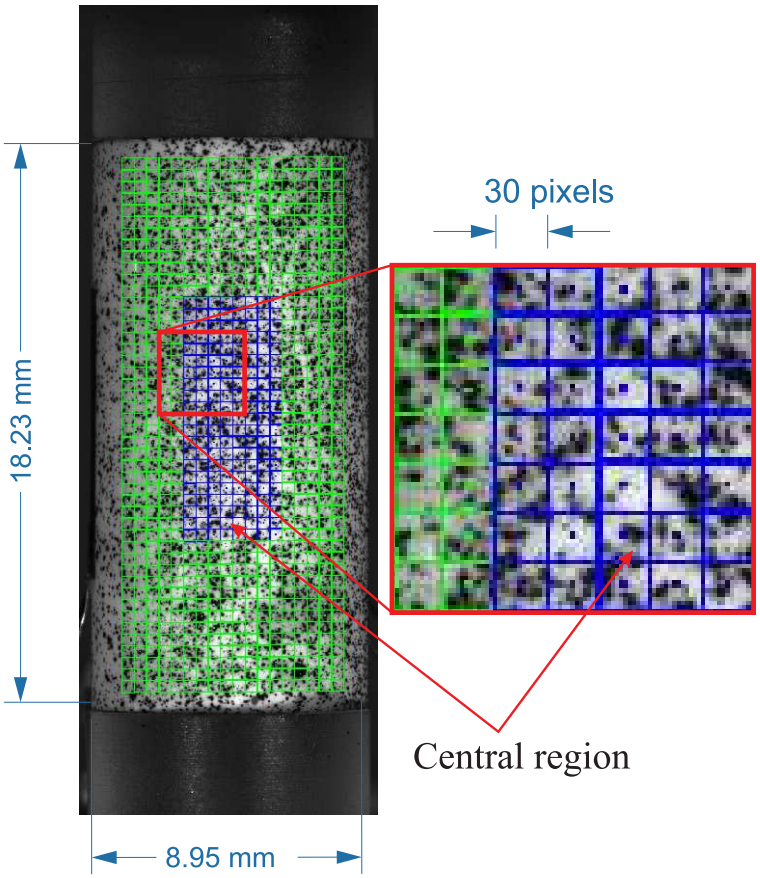

Figure 4.17: Reference image of sample N° PlasH03: Correlation mesh and description of central region

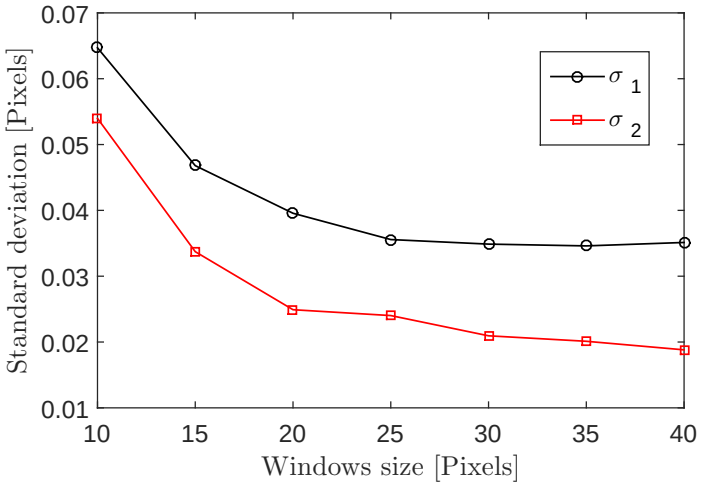

Figure 4.18: Influence of correlation windows size on DIC results

The following average apparent strain has been measured in the central region between the reference and the zoomed image (camera displacement $v = 1mm$):

$$\boldsymbol{\varepsilon}^{v=1mm} = \begin{bmatrix} 0.001524 & 0.000031 \\ 0.000031 & 0.001464 \end{bmatrix}$$

The theoretical strain obtained from this observation must be given $\varepsilon_{11} = \varepsilon_{22}$ and $\varepsilon_{12} = 0$, so that the above result shows an error of the order of 6×10^{-5} in the measurement of average apparent strain.

Systematic error (SE3b) and random errors (SE1), as introduced in section 4.5.4.1, are also computed. The systematic error is expressed as the average of the difference between the evaluated and theoretical displacements, associated with the global camera motion, as detailed in [195, 230, 62]. On average over all measurements, this systematic error is zero. It is however correlated with the fractional part of the displacement expressed in pixels. This error may induced spurious deformation bands in the strain maps. The results are depicted in Fig. 4.19. Random errors turn out to be somewhat larger than systematic errors, especially along the horizontal direction. Nevertheless, these errors are always reasonably small, with about 0.03 pixels for random errors and 0.02 pixels for systematic errors.

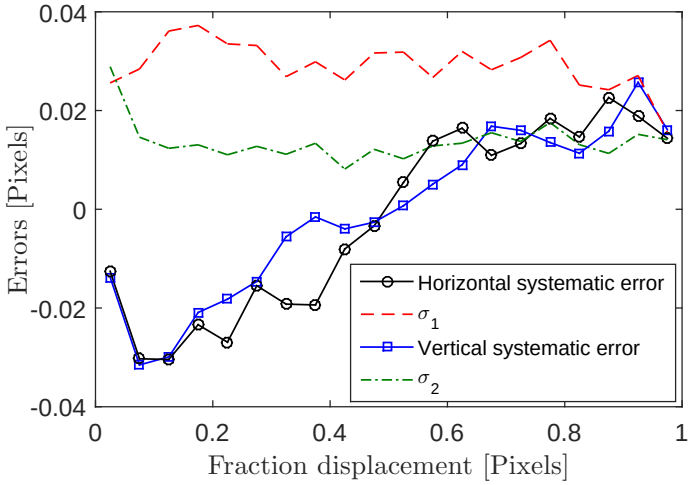

Figure 4.19: Systematic-error curves inferred from a magnification variation

The error of global strain measurement $\sigma(\varepsilon_{ij})$ can be here estimated by the analysis of error propagation see Allais et al [11]

$$\sigma(\varepsilon_{ij}) = \sqrt{\frac{2}{N_p}} \frac{\sigma_i}{L_j} \tag{4.11}$$

where N_p is the number of pairs of independent displacement measurements used for strain measurement, and L_j is an equivalent gauge length along direction j. In this case, we have $\sigma_1 = 0.03$ pixels, $\sigma_2 = 0.015$, $L_1 = 210$ pixels ($N_p = 21$), $L_2 = 630$ pixels ($N_p = 7$). we obtain:

$$\sigma(\varepsilon_1) = \sqrt{\frac{2}{21}} \times \frac{0.03}{210} = 4.4 \times 10^{-5} \tag{4.12}$$

and

$$\sigma(\varepsilon_2) = \sqrt{\frac{2}{7}} \times \frac{0.015}{630} = 1.27 \times 10^{-5} \tag{4.13}$$

These values are good agreement with the errors analysis of average apparent strain. In both cases, they are very small with respect to the expected elastic strain about $3 - 4 \times 10^{-3}$.

We now consider the non−controlled errors due to out of plane rigid body motion (SE4). Firstly, we plot the evolution of the equivalent stress according to equivalent strain in Fig. 4.20. The shear modulus is thus estimated to $\mu = 5.66$ GPa in the linear part of the curve. The first non linear domain might be to out of plane rotation of sample at beginning of loading which are non longer evolving once the sample is sufficiently loaded. The second may be due to another rotation at the end of the loading due to damage of the specimen.

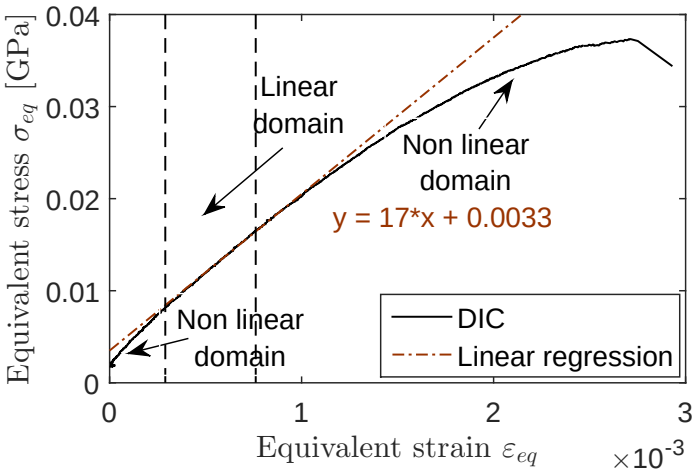

Figure 4.20: Relation between equivalent strain - equivalent stress of DIC result

The three components of the measured apparent strain are plotted in Fig. 4.21 with respect to the prescribed loading. At the moment when strain component ε_{12} deviates from zero, we note also perturbations of the components ε_{11} and ε_{22}. This perturbed domain is similar with the last nonlinear domain in Fig. 4.20. As discussed in subsection 4.5.4.2, we note that the non null ε_{12} component and nonlinear of shear modulus can be here due to the damage of the specimen. So, in the next, to reduce this error, the material parameters will be determined from data out of this domain.

The expressions defined in Eqs. (4.6) and (4.7) (section 4.5.4.2) are used to correct the Poisson effect. The errors due to Poisson effect along both vertical and horizontal directions are estimated through :

$$\text{Cor}\varepsilon_{11} = \frac{|\,(\varepsilon_{11} - \varepsilon^a_{11})\,|}{|\,\varepsilon^a_{11}\,|} \quad \text{and} \quad \text{Cor}\varepsilon_{22} = \frac{|\,(\varepsilon_{22} - \varepsilon^a_{22})\,|}{|\,\varepsilon^a_{22}\,|} \tag{4.14}$$

$\text{Cor}\varepsilon_{11}$ and $\text{Cor}\varepsilon_{22}$ are plotted in Fig. 4.22, showing a constant correction for ε_{11} (1.353%) consistently with its definition. A important fall in ε_{22} is observed at the beginning of the test.

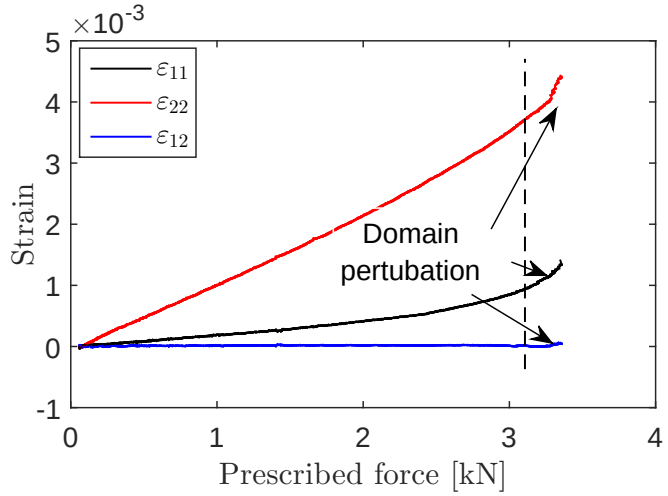

Figure 4.21: Deformation of sample with respect to the loading

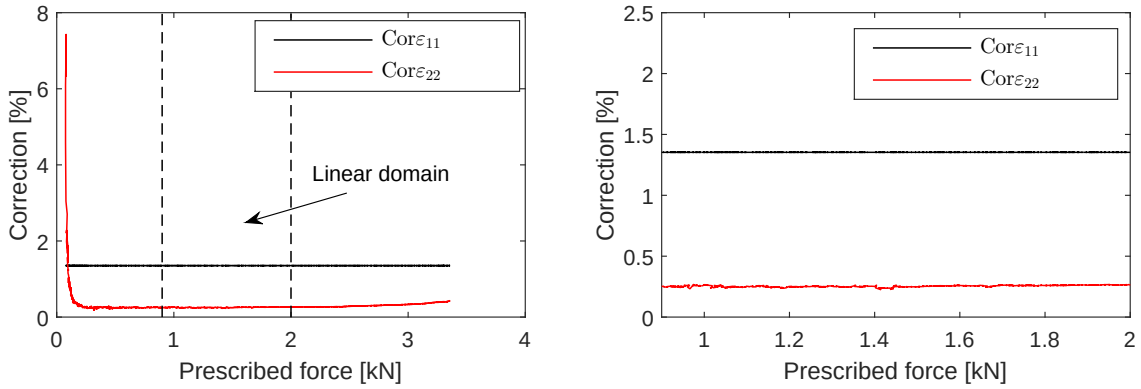

Figure 4.22: Corrected quantity for: (a) all loading; (b) linear domain to compute elastic parameters

This error stabilizes around 0.24%. It slightly increases just before rupture. Thus, the error due to Poisson effect are low in the part of the curved used to estimated the elastic parameters. This is mainly due to the distance between the camera and the sample ($L = 32$ cm, see Fig. 4.15) which is sufficient to reduce this error (because the out of plane motion of the sample due to Poisson effect is small with respect to this distance). To confirm this result, we compare the obtained strain before and after correction in Fig. 4.23.

Overall motions due to the machine compliance can however not be corrected this way. The measurements of E and ν are sensitive to out of plane translations, while that of μ are not, because μ is insensitive to magnification variations. μ might however be sensitive to out of plane rotations.

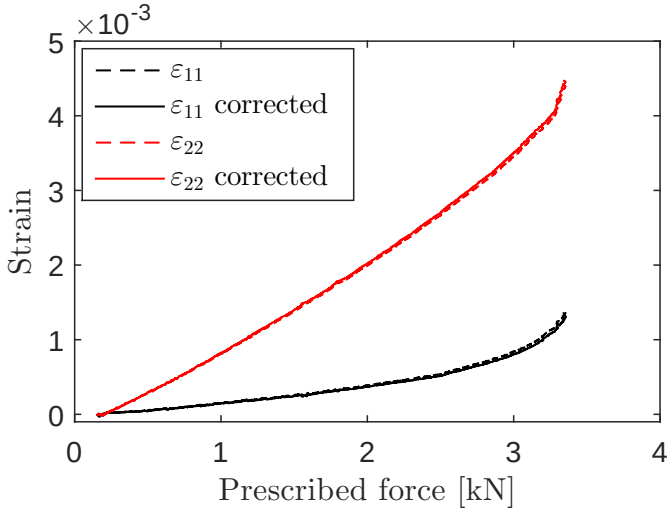

Figure 4.23: Comparison of strain before and after correction, with respect the loading

4.5.5.2 Results

The load-deformation curve for left gauge, right gauge and DIC after Poisson's effect correction in central region are plotted in Fig. 4.24 for the specimen N° PlasH03. We note a small difference between the three curves, showing that the DIC measurement is at least as reliable as the measurements by strain gauges which exhibit also some discrepancies. The Young's modulus is determined from the linear regression between the stress and ε_{22} (DIC) in the linear region depicted in Fig. 4.24. We obtain $E = 13.50$ GPa compared with $E^a = 13.51$ GPa before correction.

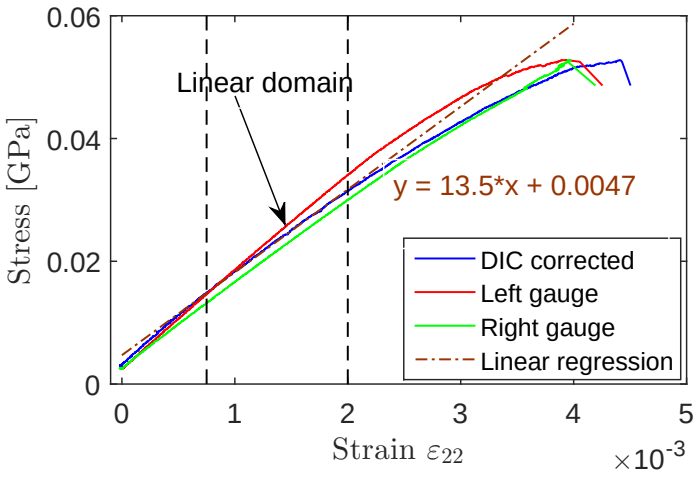

Figure 4.24: The load - deformation curve obtained by DIC after correction

The Poisson's ratio is determined by linearizing the evolution of the corrected vertical and horizontal deformations depicted in Fig. 4.25, leading to $\nu = 0.2$. Note that this value is only slightly influenced by the Poisson effect correction ($\nu_a = 0.21$ before correction). We have also

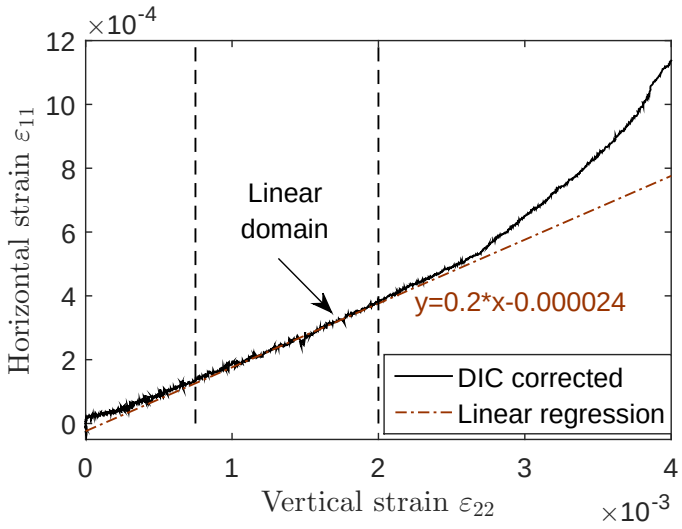

Figure 4.25: Relation between vertical and horizontal deformation after correction

the link between elastic moduli of isotropic material.

$$\mu = \frac{E}{2(1+\nu)} \tag{4.15}$$

Relation in Eq. (4.15) can be used to compute shear modulus associated with the measured E and ν, leading to $\mu_a = 5.57$ GPa before correction and $\mu_c = 5.625$ GPa after correction. We compare these values with the one obtained from the linear regression between equivalent strain and equivalent stress $\mu = 5.66$ GPa. The value after correction is better, suggesting that the magnification variation correction associated with the Poisson effect allows to correct some of the out of plane motion.

Finally, the DIC measurement has been performed for all of six samples. The obtained elastic parameters are listed in table 4.3, where E_{DIC} is the Young's modulus computed from DIC, E_{J1},E_{J2} are values obtained from right and left gauges, respectively. The behavior of plaster is reproducible since variations of both Young's modulus and Poisson ratio are relatively low (less than 10 %). The average values $E = 13.6$ GPa, $\nu = 0.2$ are similar to those obtained by Romani et al [180].

4.6 Conclusion

The two chosen materials for this study have been presented in this chapter: EPS concrete and EPS plaster. A protocol to perform in-situ compression tests combined with XR-CT is proposed to develop a stable crack network in the samples (at micro scale, and in 3D). In particular, this involves specific precautions to avoid detrimental boundary effects highlighted with a preliminary test on EPS concrete.

In order to validate the numerical model and develop the in-situ test procedure, specific

Name	E_{DIC}(Gpa)	E_{J1} (Gpa)	E_{J2} (Gpa)	ν
PlasH01	13.4	-	-	0.19
PlasH02	14.9	-	-	0.23
PlasH03	13.5	13.4	14.12	0.20
PlasH04	12.2	-	-	0.19
PlasH05	12.5	13.1	12.8	0.19
PlasH06	14.8	14.2	13.5	0.22
Average	13.6			0.20
STD	1.125			0.018

Table 4.3: Sample and E,ν.

samples of EPS plaster have been manufactured. Various issues had to be addressed to obtain usefull data for an efficient comparison with numerical simulations, relative to: (1) manufacturing of the EPS plaster material; (2) analysis and correction of the imperfections of the in situ uniaxial compression test. Two final samples satisfy the requirements for controlled porosity, simple geometry and parallelism or friction on bearing surfaces. Elastic properties of the plaster matrix have been estimated by DIC, whose errors ave been evaluated and corrected if possible. So the EPS plaster samples and tests may be considered as benchmarks for comparisons with numerical results. An additional test has also been performed on a more complex EPS concrete sample.

XR-CT images acquired during in-situ tests results will be analyzed as presented in Chapter 5. The 3D characterization of cracks networks will be compared with prediction of numerical simulation in Chapter 8.

Chapter 5

3D detection of damage evolution in porous brittle cement based materials

Contents

5.1 Introduction

The experimental validation of the numerical modeling requires a efficient method to detect and observe the cracks evolution at micro scale in a real sample. The images recorded during in-situ compression tests described in Chapter 4 show cracks that progressively develop in both types of samples (EPS plaster and EPS concrete). However a qualitative observation is not enough to quantify their precise location and propagation. Because their gray level is very similar to that of the porosity and because of the heterogeneity of the microstructure made of several components with different grey level s, and with fluctuating grey levels inside some component, the extraction of cracks from CT images with simple thresholding routines is not straightforward. Moreover, they may be hard to detect in their early stage of development, because of the low grey level

evolution. Therefore, we present a method in this chapter to detect and extract cracks more accurately. It is based on DVC techniques and image subtraction.

Based on the same principle as Digital Image Correlation techniques (DIC) presented in Chapter 4, the Digital Volume Correlation (DVC) technique is the main tool to perform full-field kinematic measurements in 3D from CT images and to observe small evolutions of microstructures. Many studies in the literature such as [21], [196], [34], [219], [184] have demonstrated the performance of this technique for the study of the mechanical behavior of materials. The application in the context of damage and fracture mechanics is introduced in the works [185], [90]. Another technique based on enriched local kinematics to describe displacement discontinuities is proposed in [177], [91] to evaluate the propagation of a macroscopic crack. However, the study of micro cracks location and propagation at microstructural scale in heterogeneous materials is still an open issue and methods to do so are still in their early stage of development.

Methods based on the computation of so-called corelations residuals, as reveiwed by Bornert et al [4], might be used to detect cracks, as they highlight evolutions of microstructures which induce evolutions of grey levels which are not directly induced by their advection by a mechanical transformations, as assumed by DVC algorithms. In our case, the local contrast is however insufficient to perform a DVC analysis uniformly over the whole sample, because gray levels in EPS beads and sand grains are rather uniform. Local DVC routines can be run only over positions in cement matrix, and near interfaces. In addition, a non perfect gray level convection may occur between reference and deformed images. Because of these reasons, the direct application of the “correlation residuals" method is inapplicable.

In this work, we introduce a method called “DVC-assisted image subtraction" to detect the cracks in the current situation of non uniformly distributed contrast and non perfect gray level convection. The main idea of this method is based on the same principle as exposed in [4]. The “image subtraction" method makes use of a local transformation which continuously extends the discrete DVC evalutations of the displacement field. It is based on a first order fit of the displacement field from at least 4 non-coplanar near neighbour positions successfully investigated by DVC. The gray level is obtained by either trilinear or tricubic interpolation. An adapted mesh with a selection of correlation points is also selected to use only the most reliable information of DVC result.

The overview of this chapter is as follows: in section 5.2 background of DVC and the correlation point selection is introduced. The principle of the image subtraction is proposed in section 5.3. Finally, the discussion on the choice of parameters and several results will be presented in section 5.4.

5.2 Digital Volume Correlation

5.2.1 Background

In the present work, the local approach to DVC presented in the work [34, 120] is used. Its principle is the same as the DIC method presenting in Chapter 4. The method is based on finding the homologous positions of a set of material points (called correlation point) in two or more images. To do so, we optimize a correlation coefficient, that measures the similarity of the gray level distribution in a small domain around the correlation points (called correlation window) in a reference and a deformed configuration. This distribution from the deformed configuration is converted to the reference by the material transformation according on the principle grey level conservation [148]: the texture of the medium is assumed to be passively adverted by the displacement field.

Let us consider a pair of three-dimensional gray-scale digital images, say f and g, concerning the reference and deformed states of a loaded sample, respectively. These images have been reconstructed by XR-CT. The estimation of the bulk displacements on the basis of the above image pair represents a severely ill-posed inverse problem. By definition $\mathbf{X}$ is a position in reference image, which is related with the respective position in the deformed image denoted $\mathbf{x}$ by the mechanical transformation $\mathbf{\Phi}(\mathbf{X})$:

$$\mathbf{x} = \mathbf{\Phi}(\mathbf{X}) = \mathbf{X} + \mathbf{u}(\mathbf{X}) \tag{5.1}$$

Unknown three-dimensional displacement field $\mathbf{u}(\mathbf{X})$ can be obtained as the optimal solution of a variational problem. Relation between f and g is given by the formulation of the grey level conservation principle.

$$g(\mathbf{\Phi}(\mathbf{X})) = f(\mathbf{x}) \quad \text{in case of strict gray level conservation} \tag{5.2}$$

Or in the case of a relaxed conservation with possible brightness and contrast evolution:

$$g(\mathbf{\Phi}(\mathbf{X})) = a \cdot f(\mathbf{x}) + b + g' \tag{5.3}$$

where: a, b are the coefficients of overall contrast and brightness evolution, g' is the noise, present in both reference and deformed image.

The minimizing of $C(\mathbf{\Phi}(\mathbf{X}))$ to determine $\mathbf{\Phi}(\mathbf{X})$ for each position $\mathbf{X}$ is an ill-posed problem. In fact, at each position, (or each voxel), we have only information related to grey level f and g. They are scalar values, hence determination of transformation $\mathbf{\Phi}$ (a vector) is impossible. To address it, we use the approximation $\mathbf{\Phi}_0$ of $\mathbf{\Phi}$ on the region D (“correlation window") of a point $\mathbf{X}_0$ (“correlation point"). The expression of approximated transformation can be described by using the neighboring development of correlation point $\mathbf{X}_0$ and local variation of displacement field $\mathbf{u}$:

$$\mathbf{\Phi}_0(\mathbf{X}) = \mathbf{X} + \mathbf{u}(\mathbf{X}_0) + \frac{\partial \mathbf{u}}{\partial \mathbf{X}}(\mathbf{X}_0)(\mathbf{X} - \mathbf{X}_0) + ... \tag{5.4}$$

The approximate transformation Φ_0 is then defined by a limited set of scalars, the number of which depends on the order of the approximation. The simplest one, used in the following, is a pure translation characterized by only three components:

$$\mathbf{\Phi}_0(\mathbf{X}) = \mathbf{X} + \mathbf{u}(\mathbf{X}_0) \tag{5.5}$$

Unknown mechanical transformation is here identified by optimizing (minimizing) three components (u, v, w) for each correlation window. This selection of local transformation is satisfactory, when the transformation gradient is small and one uses small correlation windows. The associated shape function mismatch errors might then be of the order of a few hundreds of a voxel, and noticeably, lower than errors due to image noise.

The similarity in terms of grey level distribution on the window D and its transformed $\mathbf{\Phi}(D)$ can be measured by computing the correlation coefficient $C(\mathbf{\Phi}_0)$. Various choices for $C(\mathbf{\Phi}_0)$ are possible. In our case, we chosen the "zero centred normalised cross-correlation coefficient" formulation is chosen:

$$C(\mathbf{\Phi}_0) = 1 - \frac{\int_D \left[f(\mathbf{u}) - \overline{f}\right] \cdot \left[g(\mathbf{\Phi}_0(\mathbf{u})) - \overline{g}\right] du}{\sqrt{\int_D \left[f(\mathbf{u}) - \overline{f}\right]^2 du} \sqrt{\cdot \int_D \left[g(\mathbf{\Phi}_0(\mathbf{u})) - \overline{g}\right]^2 du}} \tag{5.6}$$

where:

$$\overline{f} = \frac{1}{|D|} \int_D f(\mathbf{u}) du \qquad \overline{g} = \frac{1}{|D|} \int_D g(\mathbf{\Phi}_0(\mathbf{u})) du \tag{5.7}$$

It varies from 0 (perfect match) to a maximum of 2 (when fluctuations of f and g are opposite), the value 1 corresponding to no match at all. This measure of similarity is insensitive to a global contrast or brightness variation on the windows between both configurations (i.e a and b can be arbitrary in equation (5.3)). Even if in principle XR-CT images are 3D representations of local linear attenuation coefficients, which can be defined on an absolute scale, such fluctuations can in practice be observed because of instrument imperfections or various image manipulations.

Remark

This has little consequences in terms of accuracy, as noise levels in laboratory CT images are significantly larger than the dynamic range of 8 bits images. In order to increase the computational efficiency of the DVC routines, the optimization of the local translation components is split into two steps. In the first one, sets of discrete translations (i.e. with components equal to integer numbers of voxels) are systematically explored for the best correlation coefficient. This exploration can easily been parallelized on a multi-core computer. This is performed for all positions of the DVC mesh. In a second step, subvoxel accuracy is search for, by making use of a tri-linear grey level interpolation of grey levels to compute $g(\mathbf{P}hi(\mathbf{u}))$ and its gradients,

and an appropriate iterative optimization algorithm. While this optimization is hard to parallelize efficiently, it is easy to distribute the independent optimization tasks for each correlation point over several CPU-cores. In the general algorithm of the used CMV-3D software, the latter optimization is however only performed for points at which the correlation coefficient obtained after the first step is below a user-selected threshold. In our particular situation, this selection of reliable correlation points was somewhat more sophisticated as described in next section.

5.2.2 Correlation point selection

The local observation by using DVC requires a thin mesh of correlation point, and an appropriate local contrast is also required to ensure the DVC routines can run. The tomography images of EPS concrete contains three phases: cement paste (matrix), quartz sand, porosity (EPS-air). Among them, the quartz sand and porosity exhibit less contrast (i.e low local fluctuations of grey levels). DVC routines run only efficiently within the cement paste and near the interface between cement paste/quartz sand.

In this section we introduce a procedure to select the best correlation information, which includes two processing: (1) construction of an adapted mesh; (2) definition of an optimized correlation threshold. Now we present the details for each processing.

Firstly, we construct the adapted mesh, which can automatically detect the points in the well contrasted region. The principle is based on 4 steps:

- Step 1: A fine regular mesh is constructed over the whole sample with the standard tool of the DVC code
- Step 2: Exclusion of points in pores
- Step 3: Inclusion of points in sand and at the interface cement paste/quartz sand
- Step 4: Intersection of the result of step 2 and step 3.

The exclusion/inclusion of correlation points is based on the separation of these points into various phases. To do so, we compute the average grey level in a small surrounding window and then use appropriate threshold to separate correlation points into two different phases. This procedure is applied to analyze the same mesh (constructed in step 1) on both segmented images of pores (step 2) or sand grains (step 3). In order to exclude points on pores interfaces, an erosion was applied to the binary image. Conversely, in order to keep the interface of sand grains, we use the dilatation operator. The size of the balls associated with these operators is here taken equal to the mesh size. In both cases, the points which the average grey level in the surrounding window is above 0 are kept. An example of final mesh is depicted in Fig. 5.1 (c). Only the correlation points in the region with good local contrast are selected to perform DVC.

Second process is based on the sorting of correlated points. It is applied after the subvoxel optimization has been performed on all correlation points of the adapted mesh. A statistical

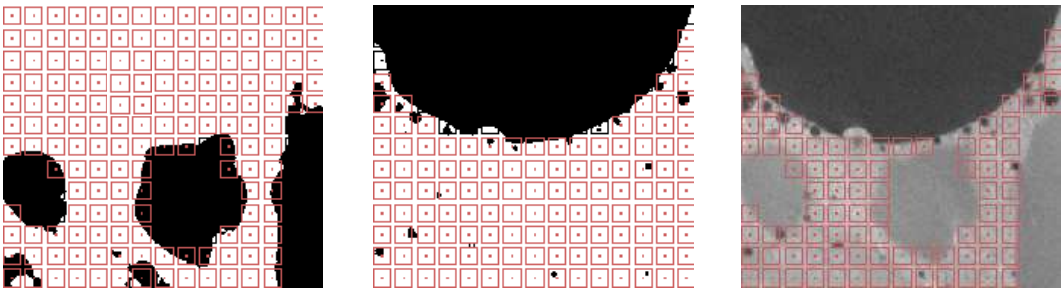

(a) (b) (c)

Figure 5.1: Correlation point selection with inter-points distance 15 voxels : (a) mesh of quartz sand segmentation; (b) mesh of porous segmentation; (c)final mesh

distribution of correlation coefficient is constructed to select only the points showing the best correlation. A typical result of DVC applied to EPS concrete material is depicted in Fig. 5.2

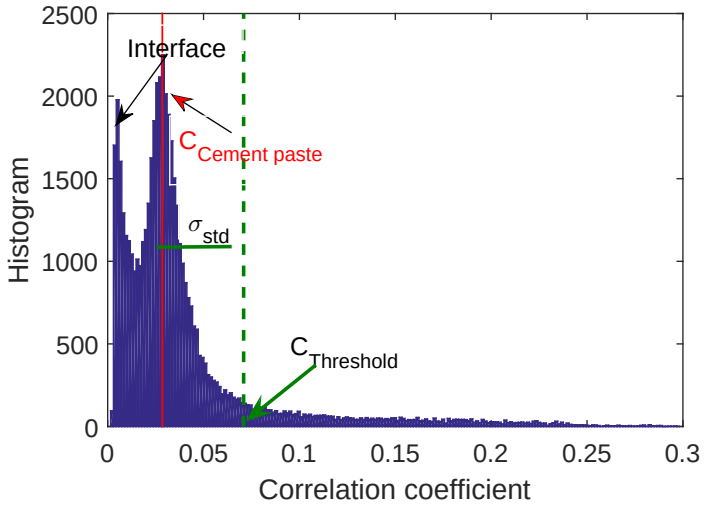

Figure 5.2: DVC result for EPS concrete: distribution of correlation coefficients

Fist peak of this histogram corresponds to correlation points near the interface between cement matrix/quartz sand region; second peak corresponds to points in the cement matrix. By computing the standard deviation σ_{std} of the correlation coefficients distribution, we propose here a threshold to select well correlated points, i.e. those for which the calculated coefficient below than $\text{C}_{\text{threshold}}$, with:

$$\text{C}_{\text{threshold}} = \text{C}_{\text{Cement paste}} + \sigma_{\text{std}} \tag{5.8}$$

where $\text{C}_{\text{Cement paste}}$ is the value of the correlation coefficient associated with the peak of cement paste. The result is depicted in Fig. 5.2. This criterion allows us to discard a second time suspicious correlation points, for a strict selection of reliable DVC information.

5.3 Image subtraction

5.3.1 General principle

On the context of cracks detection in the heterogeneous material at micro scale, a local observation is clearly required. Based on similar ideas as those reviewed by Bornert et al [4], the image subtraction (denoted $r(\mathbf{X})$) is here introduced to detect the cracks evolution for brittle heterogeneous material. Given the continuous transformation map $\mathbf{\Phi}$ extended throughout the whole sample, the gray level $g(\mathbf{\Phi}(\mathbf{X}))$ in the deformed image, at the final position $\mathbf{\Phi}(\mathbf{X})$ of any voxel $\mathbf{X}$ with gray level $f(\mathbf{X})$ in the reference image, is obtained by a tricubic (or trilinear) interpolation of the deformed image. Thus, the deformed image is back convected in the same frame as the reference image according to the estimated transformation. Finally, the difference between reference and deformed images defines the “subtracted image"

$$r(\mathbf{X}) = f(\mathbf{X}) - \left[a.g\left(\mathbf{\Phi}(\mathbf{X})\right) + b\right] \tag{5.9}$$

Note that this definition of the image subtraction allows for a possible variation in brightness and contrast, by the recourse to a coefficient of overall contrast a, and the coefficient of brightness evolution b, which are computed by the formulas:

$$a = \frac{\displaystyle\int_R \left(f(\mathbf{X}) - \overline{f}\right) \cdot \left(g\left(\mathbf{\Phi}(\mathbf{X})\right) - \overline{g}\right)}{\displaystyle\int_R \left(g\left(\mathbf{\Phi}(\mathbf{X})\right) - \overline{g}\right)^2} \tag{5.10}$$

and

$$b = \overline{f} - a\overline{g}, \tag{5.11}$$

where $\overline{f}$ and $\overline{g}$ are the average of gray level $f(\mathbf{X})$, $g\left(\mathbf{\Phi}(\mathbf{X})\right)$ on some domain R, which will be defined in the next section.

The image subtraction reflects the local evolution of the material, not described by the fit of the coarse evaluation of the transformation $\mathbf{\Phi}$. For a brittle material, it essentially gives access to the cracks. Note that on areas with sufficient local contrast, where DVC routines are run successfully, the subtracted image would coincide with standard so-called “correlation residuals" [4] (assuming a ZNCC correlation coefficient).

The subtracted image defined in (5.9) have gray levels about 0, some being positive / other negative. For the sake of an easy vision, and avoid the problem of visualizing images with negative grey levels, we add an offset gray level to the subtracted image. The final value for the case of unsigned 8 bit images is computed as:

$$r(\mathbf{X}) = \frac{1}{2}\left\{f(\mathbf{X}) - \left[a.g\left(\mathbf{\Phi}(\mathbf{X})\right) + b\right] + 255\right\} \tag{5.12}$$

5.3.2 Correction of gray level variation

The coefficients a and b related to gray level variation defined in (5.10), (5.11) could be easily computed for each considered point (or voxel) by the following: at a considered point, we could compute a, b on a domain R equal to the correlation window or the size of the neighbouring used to define the interpolated local transformation (presentation later). However this procedure is computationally too intensive. Hence we suppose that a and b are constant, and these values are computed by taking the average of some regions.

$$a = \frac{1}{n}\sum_i \left(a_i = \frac{\int_{R_i} (f - \overline{f}) \cdot (g - \overline{g}) dx}{(g - \overline{g})^2 dx} \right) \tag{5.13}$$

$$b = \frac{1}{n}\sum_i \left(\overline{f}_i - a_i \overline{g}_i \right) \tag{5.14}$$

where $i = 1..n$ refers to the setof n taken zones..

An example of EPS concrete image is shown in Fig. 5.3(a) together with its gray level histogram Fig. 5.3(b). We can see clearly the variation of gray level between reference image and deformed image. Consider first the use of a single pair a, b for all phases and whole sample to construct subtracted image in undamaged region. A typical result is depicted in Fig. 5.4(b), the obtained image is not uniform, with grey levels in the porosity clearly different from the rest. This may be due to a somewhat nonlinear evolution of the brightness and the contrast over the whole range of grey levels. To circumvent this problem, we define two coefficient pairs: a^s, b^s for both phases quartz sand and cement paste (called solid phase), a^p, b^p for porosity phase. They will be determined by using E.q. (5.13), (5.14), with R chosen correspondingly with phase of investigation (R^s and R^p). The size of interest region R depends only the size of constituent phases. We make here an analysis of this influence on the computation of a^s, a^p only(assuming that, if a^s, a^p are convergent, b^s and b^p will be convergent as well). Note that this analysis is performed in only one typical domain R.

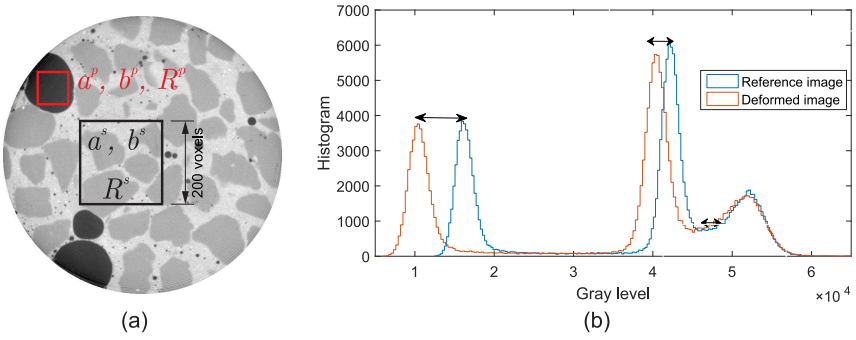

Figure 5.3: Variation principle of gray level of EPS concrete: (a) Zone definition for computation a and b; (b) gray level histogram

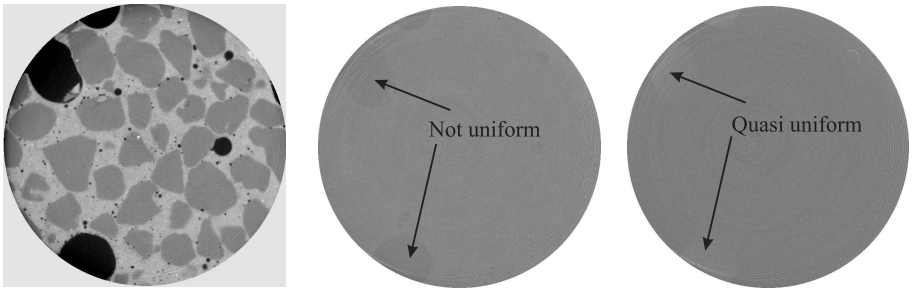

Figure 5.4: Subtracted image using correction of grey level variation: (a) reference image; (b) a, b homogeneous; (c) a, b heterogeneous

The result is depicted in Fig. 5.5. In the case of solid phase, the result of $R^s < 200$ and $R^s > 400$ voxels is not converging. The reason is due to the non representativity of the window R when R^s is very small. The fluctuations of a for large windows might be due to the fact that such windows might encounter some pores or even the boundary of the sample (recall that sample diameter is 800 voxels). The overall contrast coefficient is stable when R^s is between: $200 - 400$ voxels, which corresponds to a region of interest R containing about 3 to 4 quartz inclusions in the cement paste matrix. The size of the EPS pores for this material is bellow 250 voxels. Thus, the size of R^p for a^p,b^p must be found within a range $0 - 250$ voxels. However when R^p is very small, we have the same non representativity problem as with the solid phase. The result in Fig. 5.5 illustrates that the reasonable size for the R domain in the pore phase is about $150 - 250$ voxels, close to size of the EPS beads (when $R^p > 250$, the region of investigation will exceed the size of the porosity, so that the result fluctuates). Note that, using two coefficient pairs for each phases may be provided discontinuities of grey levels at interface between porosity/solid in image subtraction. Nevertheless this discrepancy is very small, this phenomenon will be illustrated in example bellow.

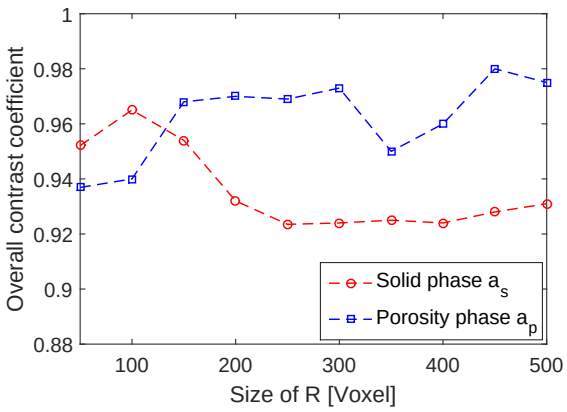

Figure 5.5: Influence of the size of domain R on the computation the contrast variation coefficients

The R^s, R^p chosen from the above analysis are applied to compute a^s, b^s and a^p, b^p in several regions spread over the whole sample. The obtained result is satisfactory as no discrepancy in grey levels between the pores and the solid phases can no longer be observed in the subtracted image of an undamaged zone, as shown in Fig. 5.4(c).

5.3.3 Local transformation approximation

As discussed in the previous section, the determination of the local transformation $\mathbf{\Phi}(\mathbf{X})$ at each voxel is an ill-posed problem. This work aims at constructing an approximation of the local transformation by using a continuous fit of the transformation of neighbor correlation points. After the correlation procedure, we know the position of well correlated correlation points in both reference image and deformed image. At each voxel, the local transformation is determined from the information of its neighboring correlation points.

Let $\mathbf{X}$ be the position of the voxel under consideration in the reference image (we consider $\mathbf{X}$ to be the center of the voxel), $\mathbf{X}_0$ the position of the its nearest neighbor correlation point with measured displacement $\mathbf{u}(\mathbf{X}_0)$. Using the development at order 1 of the displacement field near point $\mathbf{X}_0$, from E.q (5.4) we get the following expression of the approximation of the transformation $\mathbf{\Phi}_0$:

$$\mathbf{\Phi}_0(\mathbf{X}) = \mathbf{X} + \mathbf{u}(\mathbf{X}_0) + \frac{\partial \mathbf{u}}{\partial \mathbf{X}}(\mathbf{X}_0)(\mathbf{X} - \mathbf{X}_0) \tag{5.15}$$

In three dimensions, this transformation is defined by 12 parameters, including 3 components (u, v, w) and 9 components $(\frac{\partial u}{\partial x}, \frac{\partial u}{\partial y}, \frac{\partial u}{\partial z}; \frac{\partial v}{\partial x}, \frac{\partial v}{\partial y}, \frac{\partial v}{\partial z}; \frac{\partial w}{\partial x}, \frac{\partial w}{\partial y}, \frac{\partial w}{\partial z})$ of the displacement gradient. We have also:

$$\frac{\partial \mathbf{u}}{\partial \mathbf{X}}(\mathbf{X}_0) = \mathbf{F}(\mathbf{X}_0) - \mathbf{I} \tag{5.16}$$

where $\mathbf{I}$ is identity tensor, and $\mathbf{F}$ is the deformation gradient. We need to provide an estimate for the latter.

Assuming that we have determined by DVC the displacement of N neighbor correlation points of considered point $\mathbf{X}$, the approximate transformation $\mathbf{\Phi}_N$ used to determine its final position $\mathbf{x}$ in the deformed image, is here defined by the formulation:

$$\mathbf{x} = \mathbf{\Phi}_N(\mathbf{X}) = \mathbf{T}_N(\mathbf{X}) + \mathbf{F}_N(\mathbf{X}) \cdot \mathbf{X} \tag{5.17}$$

where $\mathbf{F}_N$ is the best fitting uniform transformation gradient for the N neighbor correlation points, and $\mathbf{T}_N(\mathbf{X}) = [u_N \ v_N \ w_N]^{\mathrm{T}}$ is the associated best fitting translation.

The vector $\mathbf{T}_N$ and the gradient $\mathbf{F}_N$ are determined by a classical least square fitting procedure, defined by :

$$\mathbf{F}_N = \mathrm{Argmin} \sum_{i=1}^{N} \| \mathbf{x}_i - (\mathbf{F}_N \mathbf{X}_i + \mathbf{T}_N) \|^2 \tag{5.18}$$

The optimal choice of $\mathbf{T}_N$ clearly is defined by the following:

$$\mathbf{T}_N(\mathbf{X}) = \langle \mathbf{\Phi}\left(\mathbf{X}_i\right)\rangle_N - \langle \mathbf{F}_N \cdot \mathbf{X}_i\rangle_N \tag{5.19}$$

where $i = 1 : N$, the operator $< . >_N$ is the average of N values, $\mathbf{X}_i$ is neighboring correlation points of $\mathbf{X}$ in reference configuration.

The second order tensor is then determined from the minimization of:

$$\mathbf{F}_N = \text{Argmin} \sum_{i=1}^{N} \parallel \left(\mathbf{x}_i - \langle \mathbf{x}_i\rangle_N\right) - \mathbf{F}_N\left(\mathbf{X}_i - \langle \mathbf{X}_i\rangle_N\right) \parallel^2 \tag{5.20}$$

where $\mathbf{x}_i$ is the DVC-estimated position of $\mathbf{X}_i$ in deformed configuration. The best fitting gradient transformation $\mathbf{F}_N$ is thus given by:

$$\mathbf{F}_N = \left[\sum_{i=1}^{N} \left\{\left(\mathbf{x}_i - \langle \mathbf{x}_i\rangle_N\right) \otimes \left(\mathbf{X}_i - \langle \mathbf{X}_i\rangle_N\right)\right\}\right]\left[\sum_{i=1}^{N} \left\{\left(\mathbf{X}_i - \langle \mathbf{X}_i\rangle_N\right) \otimes \left(\mathbf{X}_i - \langle \mathbf{X}_i\rangle_N\right)\right\}\right]^{-1} \tag{5.21}$$

Expression (5.17) can be rewritten as:

$$\mathbf{x} = \mathbf{X} + \left(\langle \mathbf{x}_i\rangle_N - \langle \mathbf{X}_i\rangle_N\right) + \left(\mathbf{F}_N - \mathbf{I}\right)\left(\mathbf{X} - \langle \mathbf{X}_i\rangle_N\right) \tag{5.22}$$

Second term of E.q. (5.22) is the average displacement of the N correlated points.

$$\mathbf{u}_N = \langle \mathbf{x}_i\rangle_N - \langle \mathbf{X}_i\rangle_N \tag{5.23}$$

Note that the position $\mathbf{x}$ in deformed configuration of point $\mathbf{X}$ in reference configuration can be given by E.q. (5.22), which defines the best overall fit of the transformation of the N neighbor points. It can also be given by equation (5.15) in which $\frac{\partial \mathbf{u}}{\partial \mathbf{X}}(\mathbf{X}_0)$ would be replaced by $\mathbf{F}_N - \mathbf{I}$. The second option provides a more local estimation of the displacement field but is much more sensitive to the DVC errors on the displacement of the sole nearest neighbor correlation point. The first option is less sensitive to correlation errors, which is averaged over N positions but leads to a smoother fitted displacement field. The following results have been obtained with expression (5.22).

The neighbor correlation points are selected according to a criterion of maximum distance d_{Tmax}, i.e we select the correlation points, whose distance with the consideration point $\mathbf{X}$ is less than d_{Tmax}. The neighbor transformation strongly depends on the maximum distance criterion. This influence will be analyzed in section 5.4.2. Note that the construction of the set of N neighbour points for each position $\mathbf{X}$ in the reference image is a computationally very expensive task, if a basic algorithm which would test all correlation points in the DVC mesh is used. To avoid this problem a somewhat more sophisticated procedure has been implemented, which takes advantage of the regular shape of the DVC mesh and the regular numbering of the correlation points within this mesh. It permits to restrict the distance test to points which are known to be close to voxel $\mathbf{X}$, so that reasonably short computational times are obtained.

The computation of $\mathbf{F}_N$ requires the inversion of the matrix $\mathbf{M}$ defined by:

$$\mathbf{M} = \sum_{i=1}^{N} \left\{ \left(\mathbf{X}_i - \langle \mathbf{X}_i \rangle_N \right) \otimes \left(\mathbf{X}_i - \langle \mathbf{X}_i \rangle_N \right) \right\} \tag{5.24}$$

This matrix is is symmetric and positive because it is the sum of rank-one tensors of the form $\mathbf{A}_i \otimes \mathbf{A}_i$. However, it might not be positive if the vectors $\mathbf{A}_i$ do not generate the whole 3D space. This is in particular the case when all neighbor correlation points are distributed in a same plane. The out-of-plane components of the transformation gradients can then not be defined. More generally, when points are close to be co-planar, these out of plane components will not be accurately determined. To treat this problem, we use a criterion to check the singularity of this matrix based on the analysis of its eigenvalues. We require that the ratio of the smallest to the largest eigenvalue is not too small. And then a solution proposed when it is too small: we increase the maximal distance d_{Tmax} to select more correlation points, then check again the singularity criterion. If the problem is still not solved, we make use of the global transformation for this position. The average displacement $\mathbf{u}_N$ is however not sensitive to this singularity. Therefore we can keep the first maximal distance to compute it. In such a situation, the number of neighbor correlation points for the computation of $\mathbf{u}_N$ and $\mathbf{F}_N$ are different. This procedure is in particular used for the badly contrasted regions (e.g EPS beads, big sand grain,...) where the neighbor point are far away from the considered voxel.

5.3.4 Gray level interpolation

The position $\mathbf{x} = \mathbf{\Phi}_N(\mathbf{X})$ is not always an integer (see Fig. 5.6), thus an interpolation is necessary to compute the gray level $g(\mathbf{\Phi}_N(\mathbf{X}))$ in the deformed image. Three interpolation procedures have been considered:

- Nearest neighbor interpolation
- Trilinear interpolation
- Tricubic interpolation

The nearest neighbor interpolation is not efficient, because this interpolation is very sensitive to small error of the local transformation (of about a voxel). In a region with large variations of contrast, e.g near the interface of porosity, this interpolation might generate an unacceptable gray level too close to either the grey level of the pore or of the matrix, event if the error in the displacement is small. An example is depicted in Fig. 5.6, where the gray level in the deformed image is searched for at non integer position (x, y, z). Assuming or simplicity that $z = k$, its gray level possibly takes value of voxel $(1, 7, 8, 9)$ depending on the distance to these voxels. We clearly see that the gray level of voxels $(1, 7)$ are really different. The obtained result would unacceptably be sensitive to a small error in the transformation.

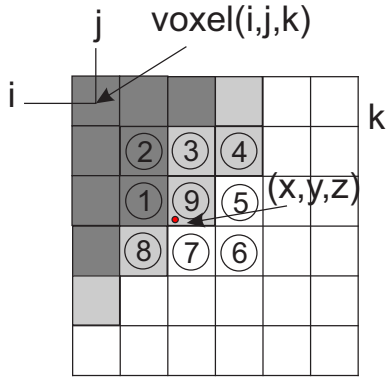

Figure 5.6: Real position of $\mathbf{\Phi}_N(\mathbf{X})$ and entire voxel in deformed image

The trilinear interpolation can reduce this error and provides good results in perfect conditions. However, the CT images of reference and deformed image are not exactly the same. This phenomenon is demonstrated by considering an interface in an undamaged zone defined in reference image as in Fig. 5.7 (a). It is observed that the blur in the interfacial region is more than one voxel and is not identical in reference and deformed image. We have observed that in such situation the trilinear interpolation is not enough. The subtracted image by using trilinear interpolation is depicted in 5.7(b); it clearly shows a visible interface. To avoid this problem, some filtering of the images is required. We have tested the tricubic interpolation; the subtracted image obtained with this interpolation is illustrated in 5.7(c), where no sign of interface is captured. This result suggests that the tricubic interpolation can reduce the interface phenomena, however it may be blurred the detected crack. Therefore, both interpolation modes have been used for this study.

(a) (b) (c)

Figure 5.7: Illustration of the effect of interpolation method in an undamaged region : (a) reference image; subtracted image obtained with (b) trilinear interpolation and (c) tricubic interpolation

5.4 Results and discussion

The method described above has been applied to the CT images acquired during the preliminary test described in Chapter 4. We use an inter-point distance of 10 voxels for the correlation mesh, and a correlation window of $20 \times 20 \times 20$ voxel^3. For the computation of the subtracted image, the initial distance criterion is $d = 50$ voxels.

5.4.1 DVC error assessment

For the assessment of the errors of the DVC method, we perform the DVC on the reference and zoomed images of EPS concrete sample used for the preliminary test described in Chapter 4 (tube voltage and current were respectively set to 120 kV and 125 μA; voxel size was 15 μm). The CT images of the whole specimen ($800 \times 800 \times 1200$voxel^3) was created from 1120 projections, resulting from a scan of about 80 minutes) The voxel size of the reference image was 14.9227μm and the voxel size of the zoomed image (which actually was a dezoomed image) was 14.993μm, that provides a theoretical negative magnification variation:

$$F_{xx} - 1 = F_{yy} - 1 = F_{zz} - 1 = -0.00471. \tag{5.25}$$

We will estimate here correlation errors associated with three polupations of DVC points: (CE1) observation of all well correlated points in the whole sample (selected with a correlation criterion threshold of 0.1); (CE2) observation of selected well correlated points according the the procedure described in section 5.2.2, making used of an adapted mesh and the optimized threshold of the correlation criterion; (CE3) consideration of points inside the quartz sand phase with low image contrast.

First, in the case of (CE1), the transformation computed from all correlated points for whole sample is:

$$\mathbf{F} - \mathbf{I} = \begin{bmatrix} -0.004188 & -0.000231 & -0.000114 \\ 0.000267 & -0.004321 & -0.000040 \\ 0.000113 & 0.000042 & -0.004562 \end{bmatrix} \tag{5.26}$$

The maximal error on the components of the overall transformation is about 0.000522. The local error in local displacement is statistically analyzed as a function of the fractional part of theoretical displacement. The systematic (i.e. average of errors) and random (i.e. standard deviation) errors are plotted as a function of the latter, as in [62]. The obtained result is described in Fig. 5.8, with the maximal systematic error about 0.1 voxels and maximal random error 0.38 voxels. The rather large random errors are induced by the presence of many point with a poor local contrast.

Second, in the case of (CE2), the transformation is computed (by the best fit procedure described earlier) from the selected well correlated point over whole sample is:

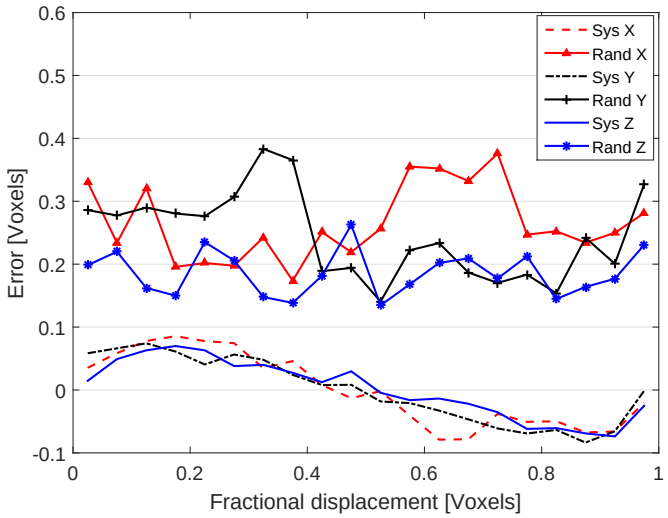

Figure 5.8: The systematic and random errors for all correlated points of whole sample

$$\mathbf{F}-\mathbf{I}=\begin{bmatrix} -0.004580 & -0.000226 & -0.000114 \\ 0.000276 & -0.004582 & -0.000036 \\ 0.000104 & 0.000039 & -0.004671 \end{bmatrix} \tag{5.27}$$

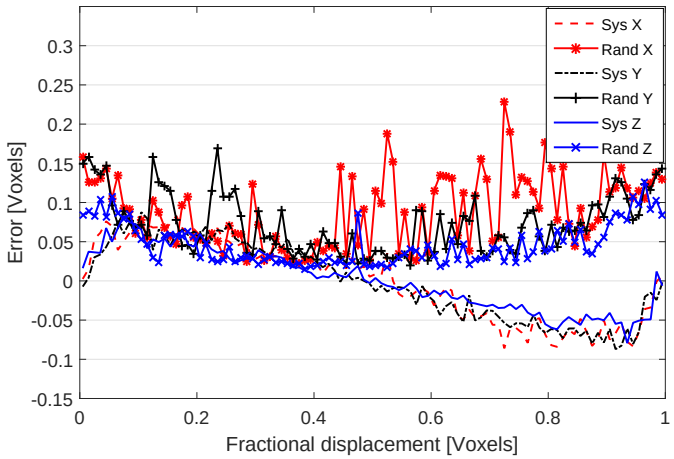

Figure 5.9: The systematic and random errors of selected well correlation points

The overall transformation estimated by DVC is now very closer to the prescribed magnification variation with an absolute accuracy better than 0.0002. We compute also the systematic and random errors, the result is depicted in Fig. 5.9 now a much smaller random, and a somewhat reduced systematic error (maximal in systematic errors of about 0.07 voxels). We clearly observe that the error associated with the selected correlation points (CE2) is noticeably lower than the one obtained with all points (CE1). This phenomena may be due to the badly correlated points in the quartz sand phase. To confirm this conclusion, we compute the best fitting

gradient of transformation for this phase in the central region of sample (CE3); the obtained value is:

$$\mathbf{F}-\mathbf{I}=\begin{bmatrix} -0.003971 & -0.000190 & -0.000249 \\ 0.000175 & -0.004156 & -0.000103 \\ 0.000093 & 0.000107 & -0.004577 \end{bmatrix} \tag{5.28}$$

The maximal error of $\mathbf{F}-\mathbf{I}$ in this case is about 0.00074, the biggest of all three case. The systematic and random errors are also computed and depicted in Fig. 5.10. This result shows also larger error (maximum of about 0.4 voxels for random errors and 0.1 voxels for maximal systematic errors) than with the selected correlation points (CE2).

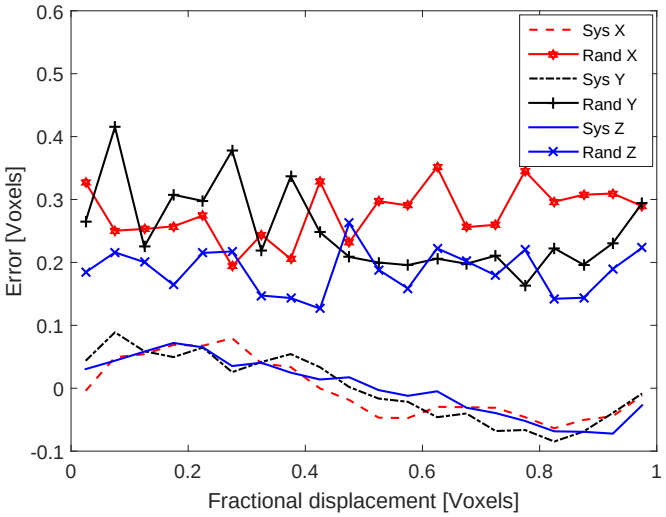

Figure 5.10: The systematic and random errors of quartz sand phase of EPS concrete

The summary of maximal errors for the overall transformation gradient $\text{Error}_{\max}(\mathbf{F}-\mathbf{I})$, the systematic error $\text{Error}_{\max}(\text{Sys})$, and the random error $\text{Error}_{\max}(\text{Rand})$ estimated from three above cases is given in table 5.1. It confirms the efficiency of the proposed procedure to select appropriated correlations points, which will be used for all subsequently presented results.

Name	$\text{Error}_{\max}(\mathbf{F}-\mathbf{I})$	$\text{Error}_{\max}(\text{Sys})$ [voxels]	$\text{Error}_{\max}(\text{Rand})$ [voxels]
Sand grain	0.00074	0.1	0.4
All Corel points	0.00052	0.1	0.38
Selected Corel points	0.0002	0.07	0.2

Table 5.1: Summary of error estimation for EPS concrete material

We now quantify the impact of the DVC error on displacement to the error on the components of the local transformation gradient $\mathbf{F}_N$, by means of error propagation considerations [120]. As

a first approximation, this error is

$$\sigma(F_{ij}) = \frac{2}{\sqrt{N_j}} \frac{\sigma(u_i)}{L_j} \tag{5.29}$$

where N_j is the number of independent displacement measurements used for strain measurement, L_j is an equivalent gauge length along direction j, and $\sigma(u_i)$ is the standard deviation of displacement along direction i. In our case, the local transformation is computed from neighboring correlation points. We mostly make use of a maximal distance equal to four or five times the inter-point distance of correlation mesh, hence we have about 216 correlated points (see section 5.4.2). Thus we have here $N_j = 216$, $L_j \approx 50$ voxels, from Fig. 5.9, $\sigma(u_x) = 0.15$ voxels, $\sigma(u_y) = 0.125$ voxels, $\sigma(u_z) = 0.08$ voxels, we obtain:

$$\sigma(F_{xx}) = 4 \times 10^{-4}; \quad \sigma(F_{yy}) = 2.2 \times 10^{-4}; \quad \sigma(F_{zz}) = 2.2 \times 10^{-4}$$

These estimates of errors reasonably well reproduce the observed fluctuations for the overall gradient, which validates the proposed analyses.

5.4.2 Effect of neighbor distance for local transformation

The local transformation $\mathbf{\Phi}_N(\mathbf{X})$ used to subtract the images strongly depends on the maximal distance defined in section 5.3.3. Small distance gives a more "local" transformation which may reflect more accurately local strain heterogeneities of discontinuities in the material, but the obtained result is more sensitive to DIC errors. This errors will be decreased when we use a larger distance, which however provides the less local observation, and requires more computation time. Objective of this section is to look for an optimized distance, which is here considered in different regions: (1) the unbroken region in the solid phase (quartz sand and cement matrix), called ($ED01$); (2) the interface EPS/solid phase, called ($ED02$); (3) the damaged region called ($ED03$).

We consider a representative sub-volume for all three above cases, with size ($450 \times 450 \times 450$ voxel^3) containing one EPS bead and microcrack networks. A regular mesh is used, with a correlation point spacing of $10 \times 10 \times 10$ voxel^3, and correlation windows of $20 \times 20 \times 20$ voxel^3. The final correlation threshold is taken as $C \leq 0.07$. The distance to have at least 4 neighboring correlation points is respected (in the case of regular mesh) if

$$\frac{\sqrt{3}}{2} h_e \leq d_{\mathrm{Tmax}} \tag{5.30}$$

where h_e is distance between correlation point (here 10 voxels).

We computed the subtracted image for the distances $d = 20, 30, 50,$ and 80 voxels.

Firstly, the subtracted image for the problem ($ED01$) is analyzed. We consider a region with no damage and no EPS bead (zone of low gray level variation), see Fig. 5.11. The standard deviation of gray level, with respect to the maximal distance is plotted in Fig. 5.12. We see that the standard deviation decreases when we increase the distance. This phenomenon is due

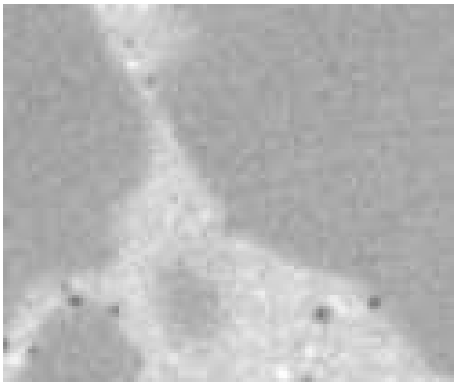

Figure 5.11: Solid region to consider influence of maximal distance criterion

to two reasons: (1) the local transformation is less heterogeneous in the undamaged region, (2) the correlation errors is reduced when we use a big distance. Hence, in this typical region the subtracted image is better with the big distance.

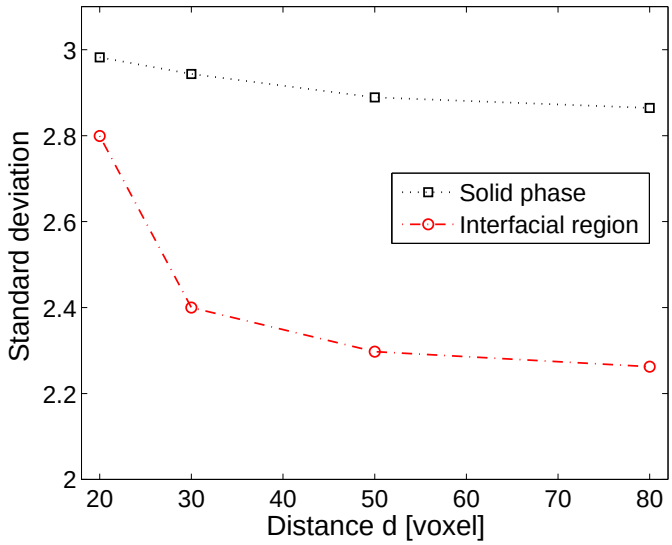

Figure 5.12: The standard deviation of gray level in the subtracted image in the solid phase and near an EPS bead

Secondly, the problem ($ED02$) is analyzed. We consider the interfacial region of a large EPS bead (diameter $\simeq$ 200 voxels). This zone is still undamaged material, so the correct solution has to give a uniform image. The detailed view is depicted in Fig. 5.13. The gray level profile on a line crossing the interface (L=35 voxels, see Fig. 5.12 (a)) is depicted in Fig. 5.13. The overall standard deviation is also plotted in Fig. 5.12. The same phenomenon as in the case ($ED01$) is observed. The small distance generate a visible interface in the subtracted image. Beside the reasons of problem ($ED01$), we note another reason for problem ($ED02$): the EPS bead is a badly contrasted region, the number of well correlated windows is low. Hence, we have to use

the big distance to obtain more correlation points.

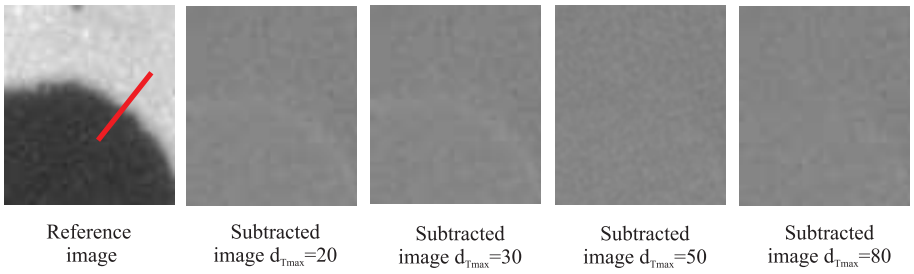

Figure 5.13: Comparison of subtracted image in the interfacial region of EPS bead, with respect to the distance

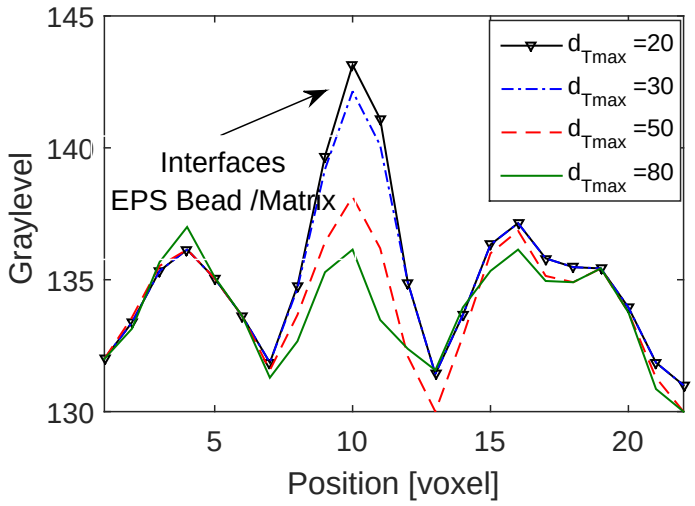

Figure 5.14: Effect of nearest neighbor distance on the subtracted image near an interface EPS bead/matrix: grey level profile along a line crossing the interface

On the contrary, in the damage region ($ED03$), we observe another phenomenon. A region containing a micro crack is considered (see Fig. 5.15 (a)). The gray level profile along a line crossing the crack is plotted in Fig. 5.15 (b). We can see that the small distance provides a sharper crack, with better defined contour. This is probably the effect of the more heterogeneous response in this zone, i.e the transformation is here very heterogeneous. We conclude that a small distance might be better in the damaged region.

The analyzed results of this section have demonstrated that: (1) the big distance is well adapted in undamaged and badly contrasted (big EPS bead, big grain) regions. (2) the small distance is better in a cracked zone. However, due to the difficulty to distinguish these cases in the real application, we take a constant distance criterion: $d = 50$. This value gives a subtracted image, which is less perturbed in the undamaged region and still sharp enough to extract the crack contour. The distance increasing process is used in the badly contrasted zone (see section 5.3.3).

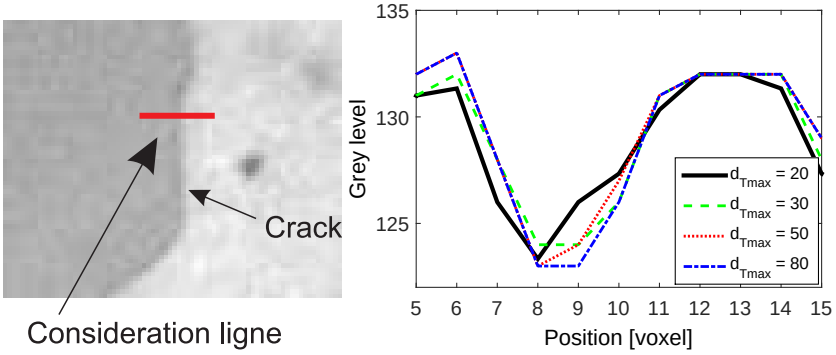

(a) (b)

Figure 5.15: (a) CT image of a region containing a micro crack; (b) gray level profiles of its subtracted image for various nearest neighbor distances

5.4.3 Benefits of the procedure

The first advantage of the presented image subtraction method is the application for situations, where DVC routines are not run successfully on large regions. In practice , in our case, the CT images of EPS concrete material contains several badly contrast zones: big porosities (EPS bead, big air), big sand grain. An example is depicted in Fig. 5.16. The cracks are well detected in the bad local contrast situation.

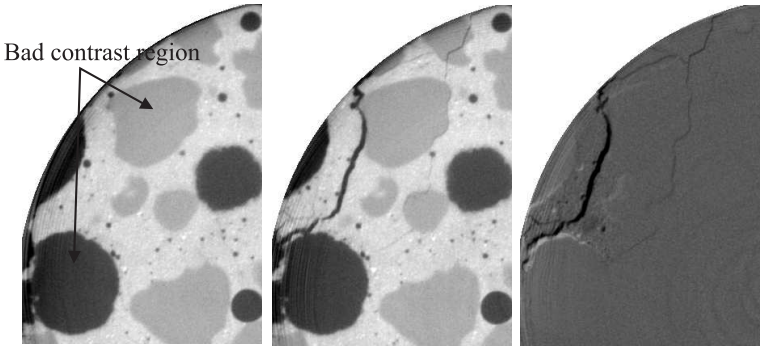

(a) (b) (c)

Figure 5.16: Crack detection in the situation of bad local contrast

The second advantage of this method is the detection of very tiny cracks. Fig. 5.17 shows an example, where the crack is almost not visible in the CT images Fig. 5.17(a), but in the subtracted image Fig. 5.17(b), we can see clearly the micro cracks. Moreover it would have been very hard to separate cracks from EPS beads in the deformed CT images. But with subtracted image the propagation of the crack along the EPS bead/cement matrix interface is clearly visible.

The CT deformed images in Fig. 5.17 (a) shows strong ring artefacts, which is a unfavorable situation to detect the cracks (because the DVC runs less efficiently). Nevertheless, image

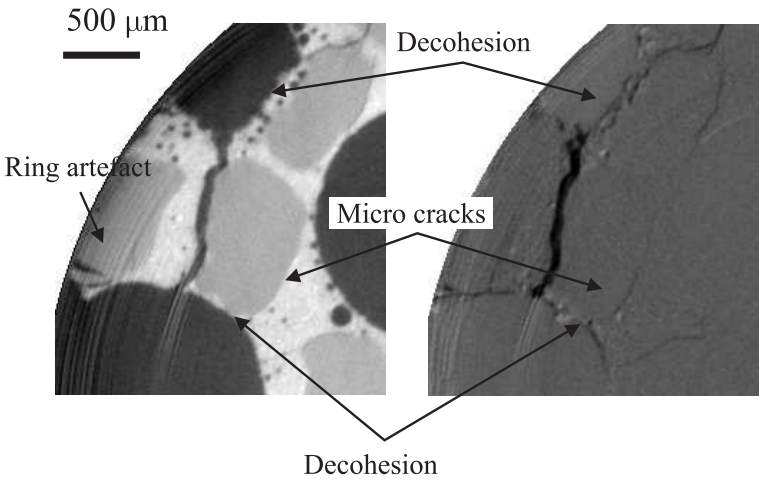

Figure 5.17: Detection of tiny micro crack and interfacial cracks around EPS beads, not visible in gray level CT images: (a) CT deformed image; (b) subtracted image

subtraction method leads to an acceptable result in terms of crack detection. Of course the artifact are still visible in the subtracted image, but they do not perturbate strongly the geometry of the cracks. This is a third benefit of this method, which still works on CT images with artefacts.

The most important advantage is that we can perform a segmentation of the cracked areas in the subtracted image. In this example, we perform a extraction cracks from the heterogeneous structure by using the classical threshold criterion and the opening operator in the FiJi image processing software [1]. The obtained 3D cracks network is depicted in Fig. 5.18 (b).

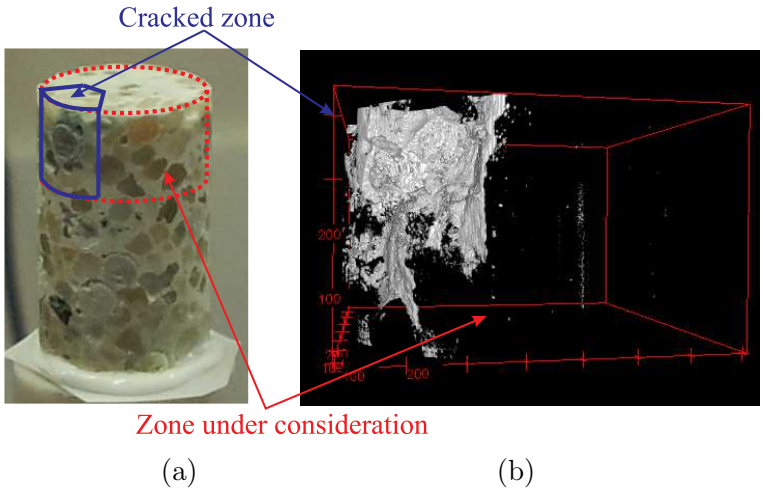

Figure 5.18: The segmentation of cracked areas in the subtracted image: 3D view of the damaged region

Because of the out-of-plane motion under loading, it is very hard to compare the same region of reference and deformed image within 2D cross section of a CT volume. Hence we can not

exactly visualize the cracks evolution within the CT images. As the subtracted image is constructed in the same frame as the reference image, we can easily observe the cracks propagation for different loading steps by comparing a chosen reference plan in subtracted image. This is another favorable point of this method.

5.4.4 Crack detection, extraction and propagation

In this section, we present the results of the crack propagation analysis of the preliminary test introduced in Chapter 4. During steps (1-7), the material is still undamaged. The cracks have appeared from step 8. Thus, we use step 7 as the reference image to compute the image subtractions.

Firstly, we compare the crack evolution at a chosen plane. The subtracted image is computed and segmented, then the detected crack network is added to the segmented microstructure of the reference image (step 7). Note that, in this example we use only the classical threshold method and the “opening" filter after segmentation within the Fiji software. The detail of the crack propagation during the four loading steps is depicted in Fig. 5.19.

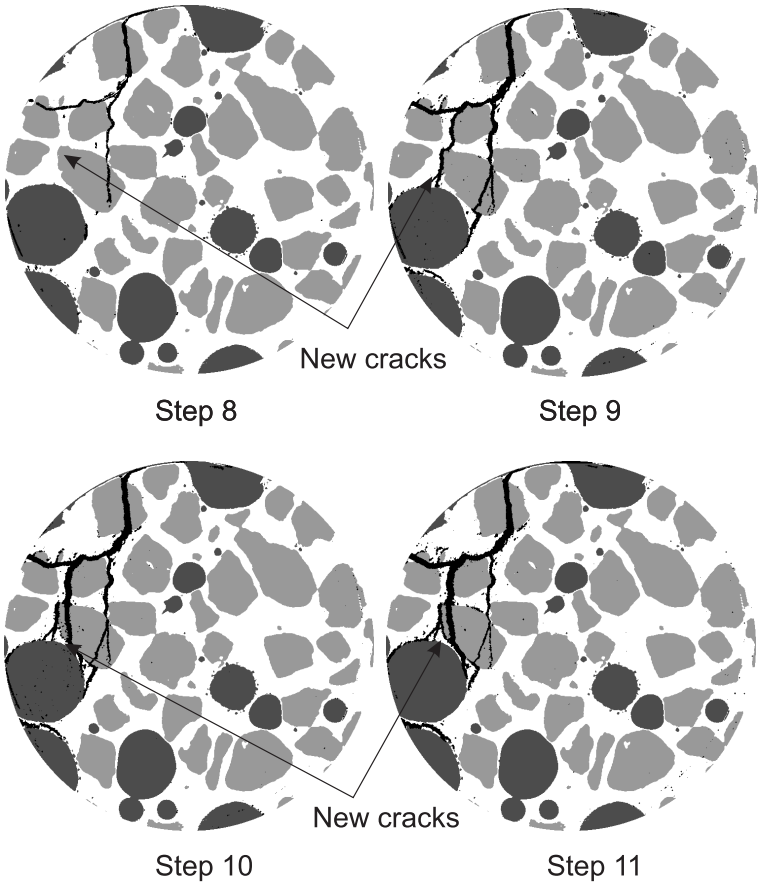

Figure 5.19: Segmentation of subtracted images of the EPS concrete specimen under 1.2 kN (Step 8), 1.26 kN (Step 9), 1.28 kN (Step 10) and 1.36 kN (Step 11). The detected crack network is superimposed on the segmented microstructure of the reference image (Step 7).

Between step 8 and step 9 we have detected new cracks, as well as the propagation of old cracks. The same phenomena are observed between step 9 and step 10. There is small evolution between step 10 and step 11: the old cracks have slightly opened, and a few new cracks have been created.

We consider also the evolution of cracks by using the 3D segmented image subtraction. A sub-volume in the damage region is analyzed. Fig. 5.20 provides a 3D view of the detected cracks in the four last deformation steps.

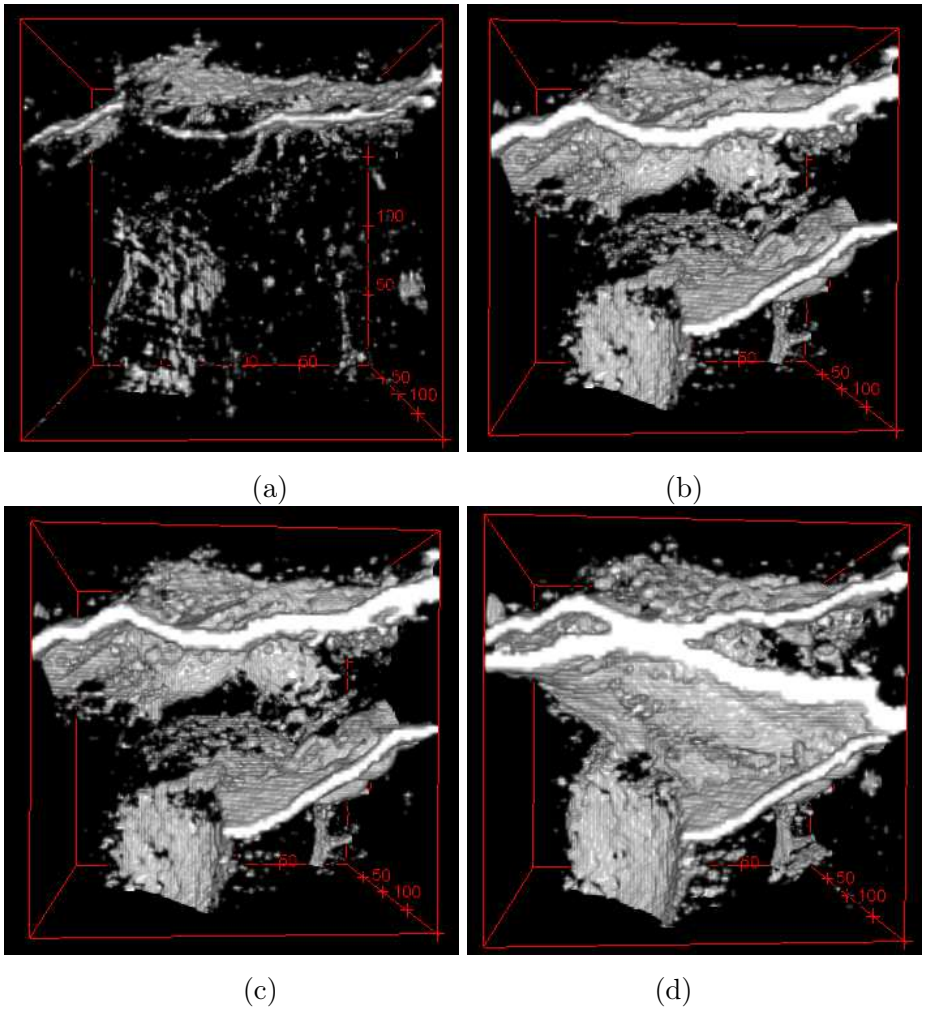

Figure 5.20: The 3D crack propagation in the upper part of the sample

5.5 Conclusion

The direct observation of damage in CT images is not straightforward, because very tiny cracks are hardly visible, and even larger cracks may have similar grey levels as the surrounding materials. This is especially the case in multiphase materials and porous ones in particular. In addition, it is hard to observe crack evolutions by a comparison between images taken in differ-

ent mechanical configurations, because one cannot distinguish within a 2D view an actual crack growth from the apparent crack motion due to the rotation of the sample with respect to the observation plane.

In this chapter, we have developed an image subtraction method. The main idea follows the reviewed by Bornert et al [4]. Using Digital Volume Correlation and associated image subtraction, the crack network and its evolution through the heterogeneous microstructure could be characterized in a lightweight EPS-beads concrete.

When compared to previous methods, our procedure can be used on CT images with local contrast not well adapted to DVC routines, e.g non uniformly distributed contrast and no perfect gray level convection. The application of the method to images containing several artefacts has always given satisfactory results.

Using the adapted mesh and the approximation of the local transformation, the proposed method is well adapted for brittle heterogeneous material. The application to study the damage phenomena in EPS concrete material has demonstrated its performance. We can detect the very tiny cracks no directly visible in CT images. Thanks to the construction of the crack network on the same frame as the reference image, we can easy compare the crack evolution at different loading states. The crack networks can also be extracted by segmentation of the subtracted image; this benefit has been illustrated on several typical examples in 2D and 3D. The proposed method is a promising tool to detect the crack initiation and propagation in other brittle heterogeneous material.

Further developments of this technique will aim at improving the description of the local transformation, especially in highly cracked areas, for a better separation of cracks from other features in the subtracted images. A quantification of the damage will also be attempted in terms for instance of surface of the cracks or opening, in view of comparisons with numerical simulations.

Part III

Confronting: Comparison between model and experiments

Chapter 6

Modeling in-situ compression of concrete or plaster samples in a microtomograph

Contents

6.1 Introduction

The objective of this chapter is to model the experimental tests conducted during this thesis, i.e. the in-situ compression of cylindrical samples made of EPS plaster or EPS lightweight concrete, in order to perform numerical simulations using the tools developed in the previous chapters and to compare the simulations results with the experimental ones. The setup has been described in Chapter 4. A novelty of the present work is that we aim at comparing the experimentally observed microcrack network generated at microscale during the in-situ compression test, to

the corresponding network predicted by the numerical simulation based on the actual complex microstructure of the sample obtained by microCT imaging. Unlike earlier studies, this comparison is not just performed in terms of global and statistical quantities, but also in terms of local geometry and chronology of the evolution of the crack network.

This chapter is divided into three parts, related to the following questions: (i) how to model the microstructural geometry from microtomography images and how to construct the Finite Element mesh for the numerical simulation; (ii) how to model the effects of the imperfections of the real experimental conditions in the simulations, and how to use these simulations to correct these issues in the experiments; (iii) how to save computational time by performing numerical simulations on sub-volumes extracted from the full microtomography image, and how to use the Digital Volume Correlation (DVC) measurements to prescribe appropriate boundary conditions on these sub-volumes.

6.2 Modeling the microstructural geometry from microtomography images

In the present work, two materials, lightweight plaster and lightweight concrete, are investigated. By “lightweight", we mean that the material contains very light inclusions or pores, here EPS beads. The introduction of these beads into a homogeneous plaster specimen induces first stress concentration when the sample is loaded and then cracks initiation. These two materials have different microstructures (see Fig. 6.1): the lightweight plaster is essentially made of two phases: the plaster and the large EPS beads (pores). The pores are almost spherical, which will render the modelling of the microstructure easier. On the other hand, the lightweight concrete has 3 phases: the less-regularly shaped pores (EPS beads), the matrix (cement paste) and the inclusions (sand grains with somewhat angular shapes), leading to a much more complex geometry. Note that both samples exhibit also some small-scale heterogeneities within the matrix, in the form of micropores or small more dense areas (which appear in white in Fig. 6.1). These details are usefull for DVC but will not be taken into account in the numerical simulations.

In this section, we provide methodologies to convert the segmented images of the microstructures to geometrical models and finite elements meshes for the simulation purposes.

6.2.1 Microstructures with spherical pores: lightweight plaster

In the case of lightweight plaster (see Fig. 6.1), the geometry of the microstructure is quite simple, roughly constituted by a cylindrical domain containing spherical pores. Then, it is not necessary to convert each voxel into a single element, which would lead to prohibitive computational costs. Instead, we use the microtomography image to determine the positions of the centers of the EPS beads (which are considered as pores) and their radii, and construct an idealized geometry involving the cylinder and spheres, which is meshed with tetrahedra. This simplification allows performing simulations with much less elements than direct conversion of voxels to regular

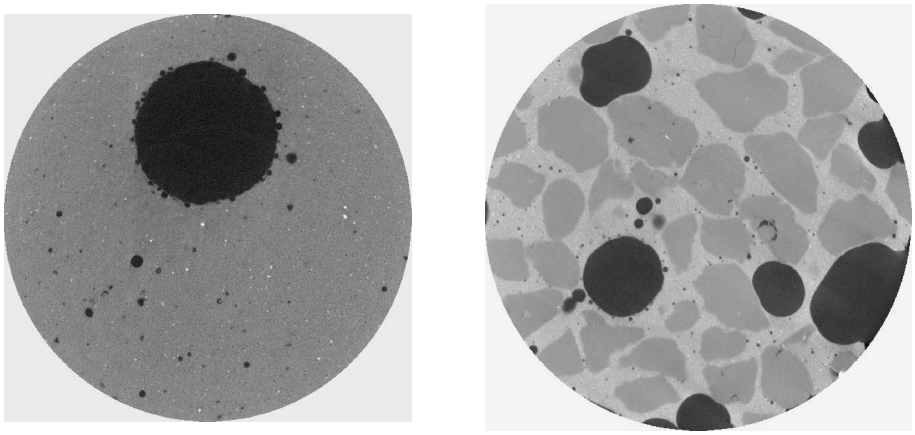

(a) (b)

Figure 6.1: Microtomography images of: (a) lightweight plaster; (b) lightweight concrete.

elements. Here, we neglect the smallest pores in the model (with diameters lower than 40 voxels). The positions and diameters of the pores are determined by using the plugin *3D Objects Counter* of the FiJi image processing software. It is applied on the binary image resulting from a basic thresholding of the full CT volumes. Because of the clearly different grey levels of both phases and of the sharp interfaces, the choice of the critical grey level used to separate phases is not critical. An example of reconstructed idealized geometry for one sample is provided in Fig. 6.1(b). In Fig. 6.3, two meshes using regular elements and conforming elements from idealized geometry are compared. Using the conforming elements saves up to 6 times the number of elements in the mesh.

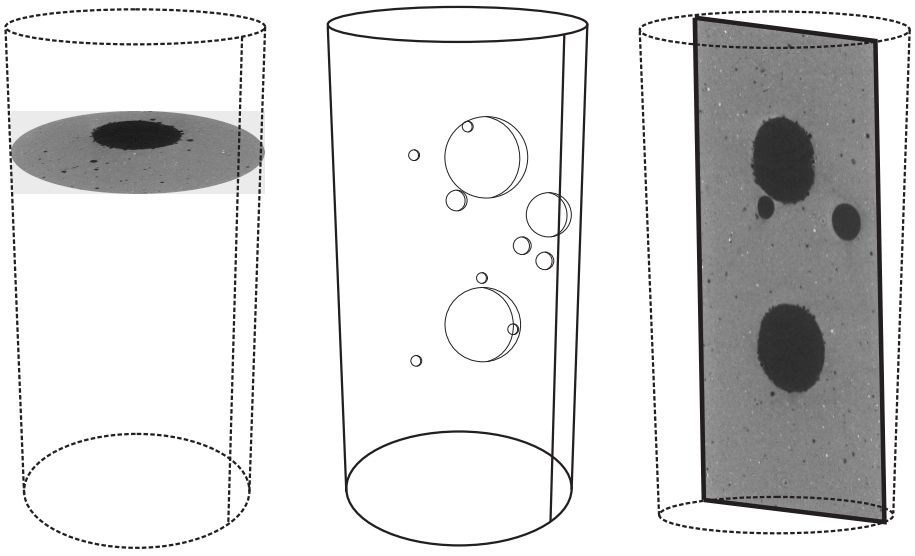

(a) (b) (c)

Figure 6.2: Geometry of the EPS plaster material: (a) horizontal plane of CT images; (b) idealized geometry; (c) vertical plane of CT images.

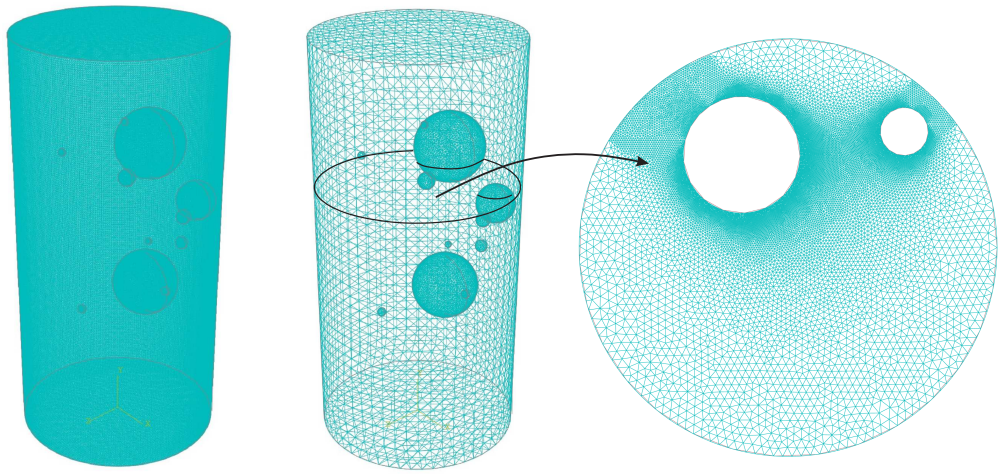

(a) (b) (c)

Figure 6.3: (a) regular mesh with of about 24 millions elements constructed from the voxel based model; (b) conforming mesh constructed from an idealized geometry of the sample (only of about 4 millions elements); (c) view of a section crossing porosities

6.2.2 Complex microstructures: lightweight concrete

In the case of lightweight concrete (see Fig. 6.1(b)), it is not possible to model the geometry with a collection of simple geometrical volumes (spheres, poyhedra...). In the present work, we have used two procedures: (a) each voxel is converted to a cubic element and the properties of each phase are mapped from voxels to the corresponding elements in a regular mesh; (b) a specialized software is employed to construct a mesh with meshed interfaces from the segmented voxel-based model.

6.2.2.1 Direct conversion of voxels to regular elements

The simplest solution to construct a mesh from an XR-CT image is to directly map each voxel and its material properties to a regular mesh of finite elements. The procedure consists in two steps: (1) the CT image is segmented into labeled image,in which grey levels of pixels refer to the phase to which they belong . For this purpose, several filters and morphological operators can be used (*open, close, median, anisotropic diffusion,...*, details can be found in [7]), we present here a proposed procedure to segment the quartz sand phase in Fig. 6.4 with the illustration of a typical section. The obtained result for a sub-volume is depicted in Fig. 6.5; (2) each voxel data (or pixel in 2D) is transferred to a regular grid associated with a regular mesh, i.e. cubic geometrical domains. Then, each domain can be associated to one or several cubic element, or decomposed into tetrahedral elements (see the 2D schematic illustration in Fig 6.6).

The advantages of this strategy are: (a) its simplicity; (b) the possibility to use parallel solving procedures related to regular meshes in the numerical simulations. Its drawbacks are:

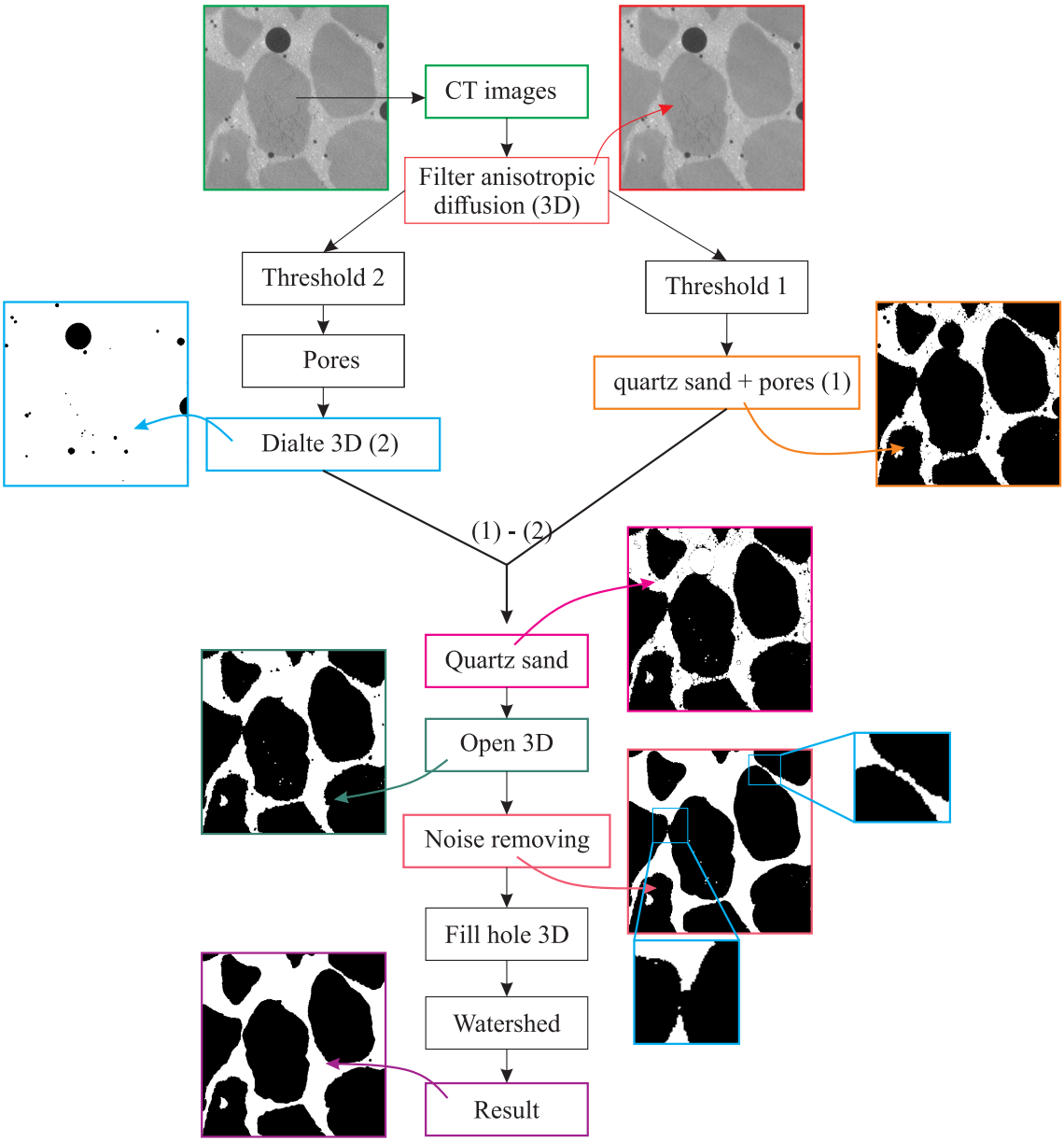

Figure 6.4: Procedures to segment quartz sand from CT images

(a) the size of the obtained meshes can be prohibitive when the number of voxels is too large; (b) the discretization error is directly related to the image resolution. For example, is is not possible to refine the mesh in some parts of the domain.

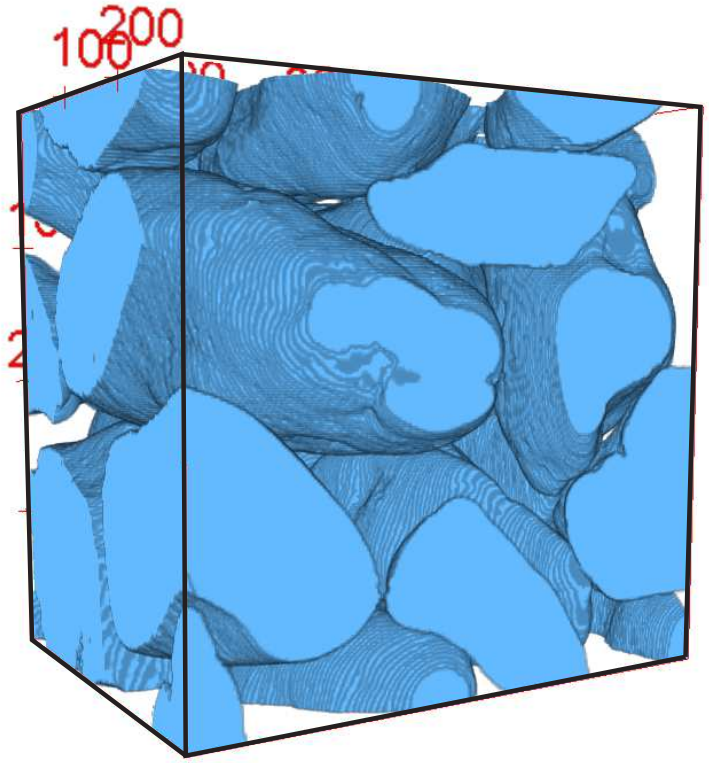

Figure 6.5: Binary image of quartz sand segmented from CT images

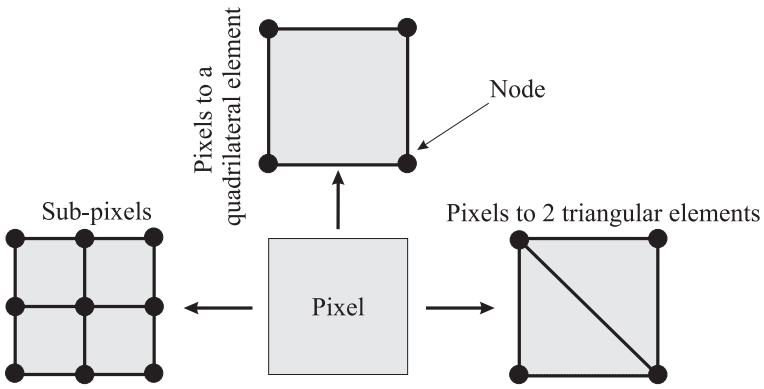

Figure 6.6: Construction of regular mesh from segmented image

6.2.2.2 Meshing softwares

Another possibility is to use a software to construct unstructured meshes where the interfaces are explicitely meshed, from the voxel-based images. Today several softwares are capable to perform this task (e.g. Cgal, Tetgen, Iso2mesh, AVIZO,...). In the present work, in the context of a collaboration with LEMTA Lab. (F. Bilteryst, E. Steib), the Avizo ® software has been used to construct a mesh from our CT images (see Fig. 6.7). The software is able to construct meshes from very complex geometries, but seems to lack of robustness for a too large number of voxels. However, the advantage is that a lower number of element can be obtained as the mesh is not regular, allowing the study of larger domains for the simulations. Examples of simulations using such an unstructured mesh are presented in Chapter 2.

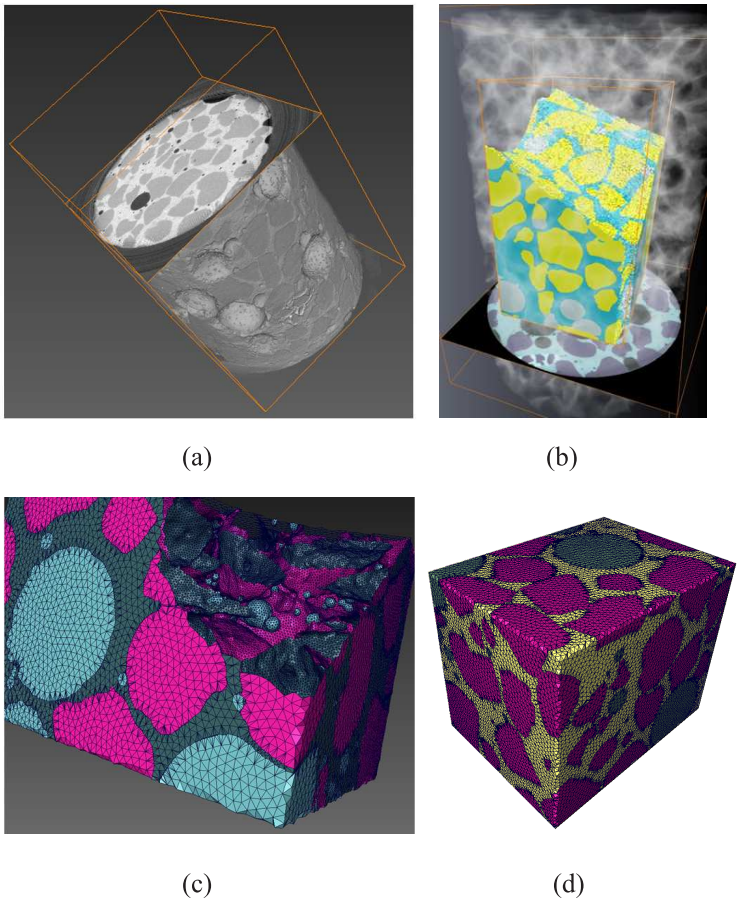

Figure 6.7: (a) Full CT image of a lighweight concrete; (b)-(c)-(d) views of the unstructured mesh constructed from the CT image (AVIZO software, in coll. with LEMTA).

6.3 Modeling spurious boundary cracking in experiments by the numerical simulations

6.3.1 Problem of cracks initiation at bearing surfaces

At the beginning of our experimental investigations, many tests turned out to be useless and had to be rejected because cracks initiate on the top and lower surfaces at an early stage to the compression test, which lead to a premature and abrupt failure of the sample (see Fig. 6.8). In these conditions, it was not possible to observe by microtomography the cracks nor their evolution within the sample during the loading. To understand this phenomena and fix it, we have used the numerical simulation, in which we have modified the boundary conditions to observe their impact on the crack initiation. Three types of defects have been investigated:

- The friction of PMMA tabs on the lower and upper faces of the sample.
- The lack of parallelism, roughness and flatness of the upper and lower faces.
- The influence of the transverse deformations prescribed by the Poisson effect of the PMMA (or Aluminum) tabs (see Fig. 6.9).

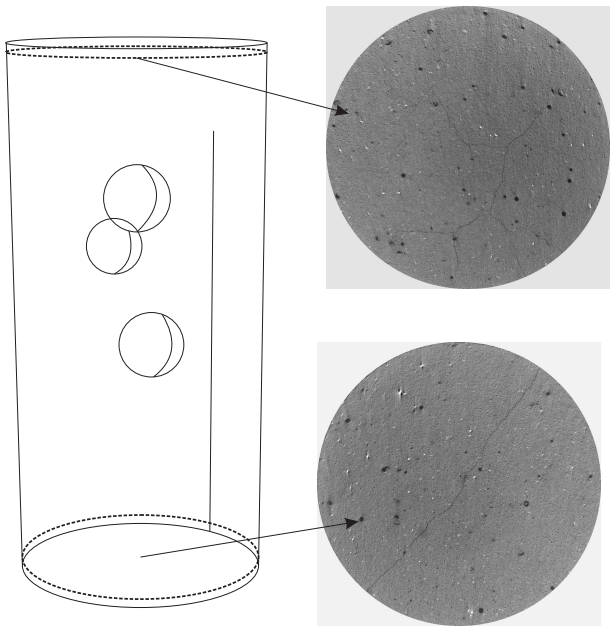

Figure 6.8: Cracks initiating on the top and bottom faces of the specimen, leading to spurious fracture modes.

6.3.2 Numerical model

The numerical model of the plaster structure is presented in the following. A 2D domain containing several pores is considered, as depicted in Fig. 6.10. Note that, to enhance the sensitivity

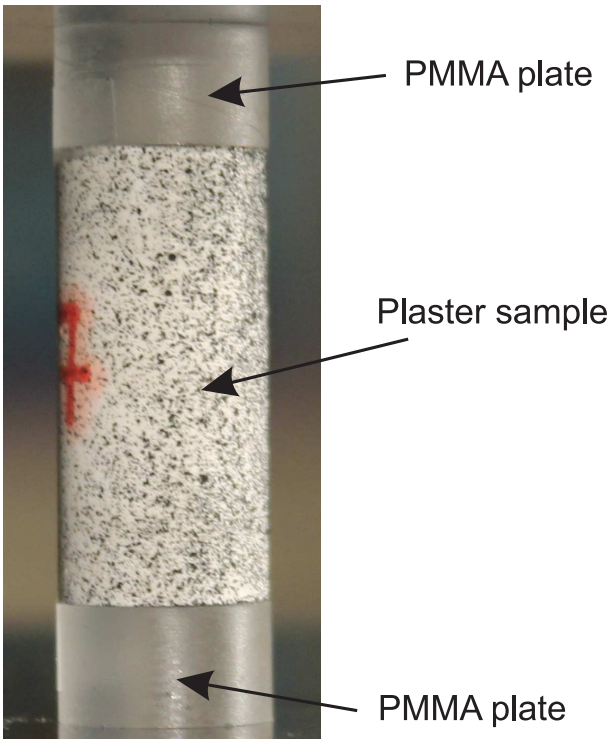

Figure 6.9: Setup of the compression in-situ test with PMMA plates

to boundary conditions, several small pores are distributed in the matrix phase, at least near the ends of the sample. The dimensions are chosen as $H = 20$ mm, $L = 10$ mm. Loading in compression in considered to model the experiment, even though we will provide more details on these conditions in the following.

The material parameters are taken as $E = 13.6$ GPa, $\nu = 0.2$ and $g_c = 1.5$ N/m. The regularization parameter is chosen as $l = 0.1$ mm. A regular mesh is considered with $h_e = 0.03$ mm such that the crack thickness is always covered by several elements in all the studied cases. Monotonic compressive axial displacement increment of $\overline{U} = -5\times10^{-3}$ mm are prescribed for 250 time steps.

6.3.3 Influence of friction

The PMMA is used to reduce the defects of roughness, parallelism and flatness of the upper and lower faces, as the PMMA is much more compliant than the plaster. In this section, we study the effects of the friction between PMMA and the plaster. First, we consider zero friction, which is modeled by prescribing only the $y-$displacements on the upper and lower faces of the specimen. The morphologies of cracks are depicted in figure 6.11. We observe that in this ideal reference case the cracks initiate from the pores in the center of the specimen, as expected.

Then, we model conditions of perfect sticking on the top and bottom faces and rigid tabs. For this purpose, we block the $x-$ displacements on the top and bottom faces, while the $y-$ displacements are set to zero on the bottom faces and prescribed on the upper faces.

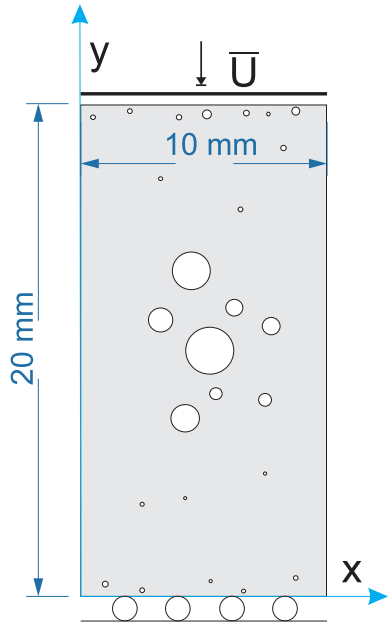

Figure 6.10: Numerical model used to study the influence of the boundary conditions on the location of the first crack initiation: geometry and boundary conditions.

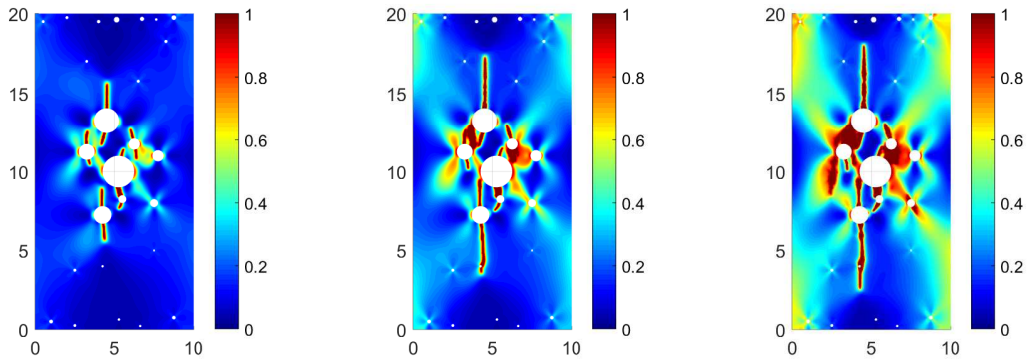

(a) (b) (c)

Figure 6.11: Crack propagation of the sample for perfect sliding conditions on the top and bottom faces: $\overline{U}_a = 0.02$mm, $\overline{U}_b = 0.025$mm, $\overline{U}_c = 0.0295$mm.

Note that in this test, we do not take into account the deformations induced by the presence of the PMMA (it will be considered in the next section). The results of the simulation are depicted in Fig 6.12 (b) and compared for the same load with perfect sliding conditions (Fig. 6.12 (a)). Results show that the presence or absence of friction on the top and bottom faces does not significantly modify the crack paths. In Fig. 6.13, we plot the stress - displacement curve for both cases:the difference is small. We conclude that the initiation of damage near the ends of the samples cannot be explained by frictions effects, at least under the assumption of a rigid behavior of the tabs.

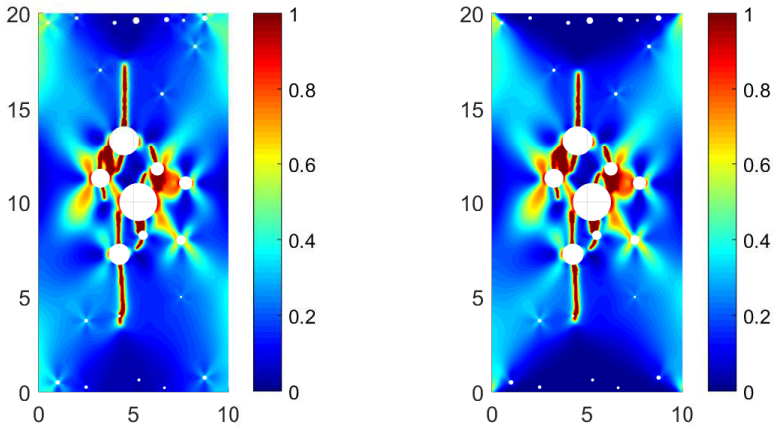

Figure 6.12: Comparison of cracks for (a) perfect sliding conditions between PMMA plates and plaster (b) perfect sticking conditions with rigid end tabs.

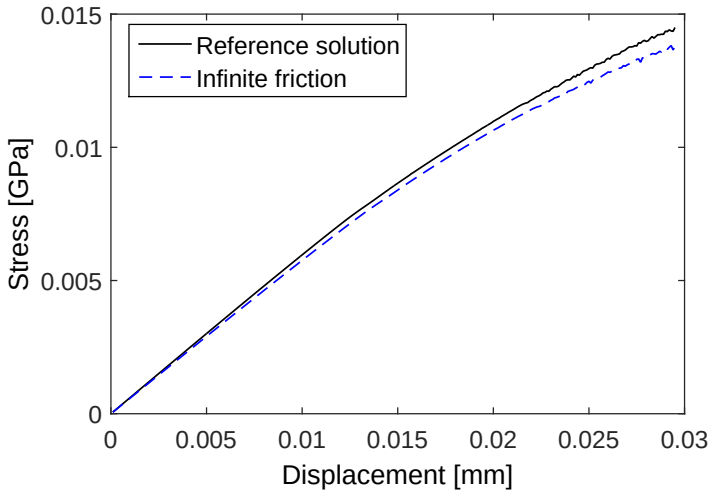

Figure 6.13: Comparison of mechanical response in the cases of perfect sliding conditions between PMMA and plaster and perfect sticking conditions with rigid tabs.

6.3.4 Influence of non parallelism and roughness of the bearing surfaces

The defects of parallelism and roughness of the top and bottom surfaces (where the loading is prescribed) is studied in the following for evaluating its influence on the formation of cracks starting from these surfaces. For this purpose, the problem described in subsection 6.3.2 is considered with perturbed boundary conditions to mimic experimental imperfections.

First, the different loading cases depicted in Fig. 6.14 (a), (b), (c) are considered, where non uniform displacement fields are applied to mimic imperfect contact conditions, and called "LackPb01", "LackPb02", "LackPb03", respectively. To avoid spurious singularities, an elastic layer is added on top of the surface, so as the top surface is subjected to smoother force distri-

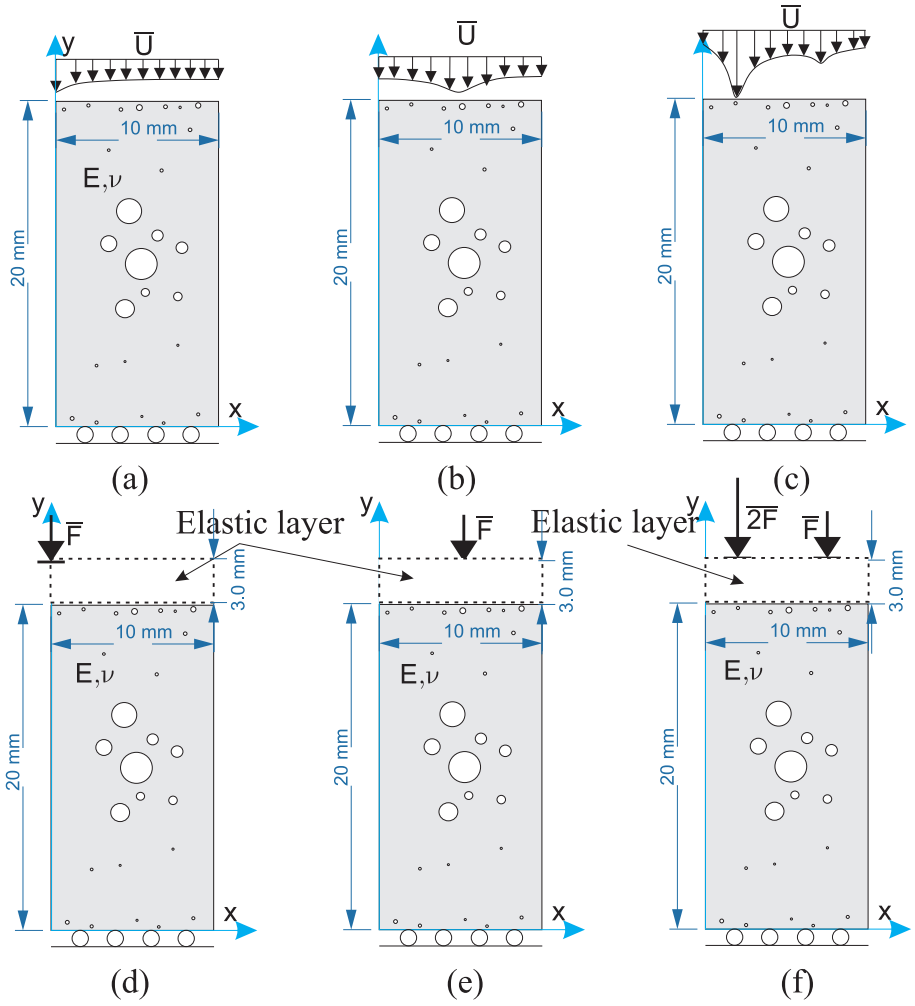

Figure 6.14: Several cases studied for evaluating the influence of surface roughness on crack propagation in the sample: cases (a), (b) and (c), called LackPb01, LackPb02, LackPb03, respectively, are approached by the numerical loading conditions (d), (e), (f), where one or several punctual forces are applied in a symmetric or non-symmetric way to the top of the sample, through a complaint elastic layer intended to smooth out singularities.

butions. Properties of elastic layer are chosen to be much more compliant than sample material; we take here $E_{\text{elastic layer}} = 2$ GPa (we recall that for the plaster matrix $E = 13,6$ GPa). The thickness of this layer is 3.0 mm. To avoid a Poisson effect which would prescribe spurious transverse strains (see later), we choose its Poisson's ratio, such that the traversal deformation of the heterogeneous sample and the elastic layer are identical, i.e. it is taken by:

$$\nu_{\text{elastic layer}} = \frac{E_{\text{elastic layer}}}{E} \times \nu, \tag{6.1}$$

where E, ν are the elastic properties of the matrix of the porous sample.

Results are presented in Figs. 6.15, 6.16 and 6.17, showing systematically the initiation of cracks from the top and bottom surfaces, and indicating a strong influence of the imperfections

of the geometry of the extreme surfaces of the sample on the location of crack initiation.

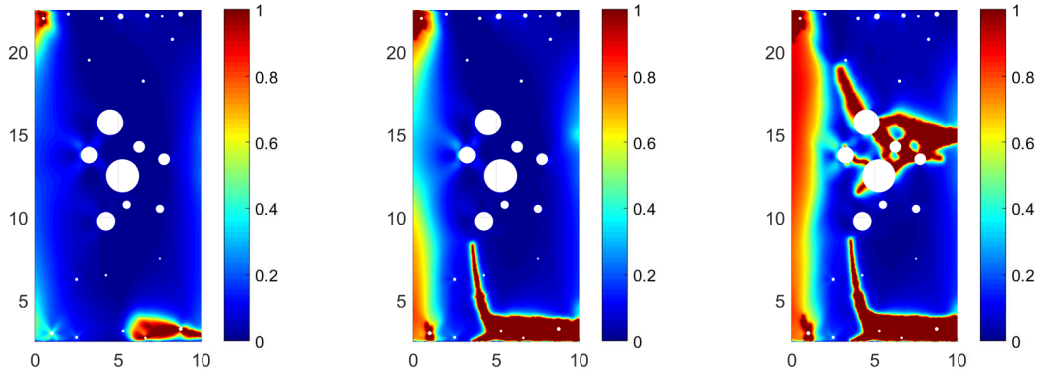

(a) (b) (c)

Figure 6.15: Damage maps in case LackPb01 for the prescribed loading levels: (a) $\overline{F}_a = 0.042$ kN; (b) $\overline{F}_b = 0.052$ kN; (c) $\overline{F}_c = 0.055$ kN

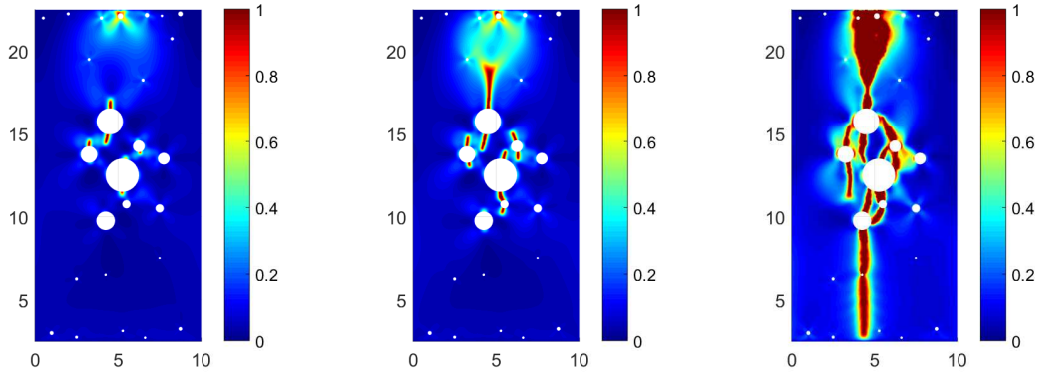

(a) (b) (c)

Figure 6.16: Damage maps in case LackPb02 for the prescribed loading levels: (a) $\overline{F}_a = 0.0765$ kN; (b) $\overline{F}_b = 0.078$ kN; (c) $\overline{F}_c = 0.081$ kN

Clearly, the above three loading cases show that imperfect boundary conditions might strongly perturb the crack network with respect to an ideal situation. This illustrates the fact that damage in brittle materials is a somewhat random process, because it is linked to small experimental imperfections which are hard to control and to reproduce exactly in a numerical simulation. In particular, there is no obvious way to quantitatively link the above three theoretical imperfect loading cases to the actual situation, because the tiny details of the real geometry of the sample and the testing machine are almost impossible to quantify in detail. This might suggest, on the one hand, that a direct comparison between experimental observation and numerical simulation of a crack network in such a material would be an unrealistic task.

One the other hand, this also highlights that such a comparison can only be possible if exper-

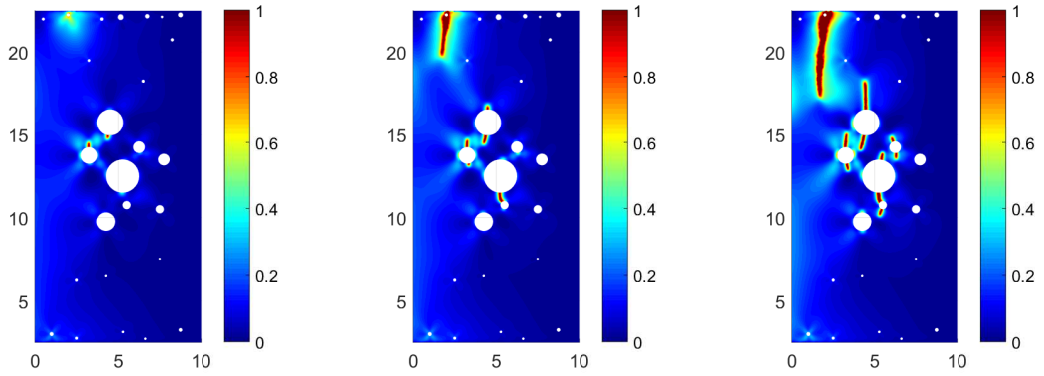

(a) (b) (c)

Figure 6.17: Case LackPb03 problem for the prescribed loading: (a) $\overline{F}_a = 0.064$ kN; (b) $\overline{F}_b = 0.068$ kN; (c) $\overline{F}_c = 0.07$ kN

iments are run in such a way that the random non controlled features of the loading conditions are set to a sufficiently small level. To do so, various improvement of the sample preparation process and of the in-situ loading conditions have been proposed and tested. Essentially three direction have been followed: improvement of the parallelism of the external faces of the sample, polishing of the latter to reduce their roughness, and interposition of compliant PMMA tabs between the sample and the machine to smooth out mechanical singularities. Practical details of these procedures are given in Chapter 4 and Appendix A.4

6.3.5 Influence of the Poisson ratio of the end plates

In this section, we explicitly model the real PMMA plates (see Fig. 6.9) in the numerical simulation to investigate the their effect on the deformation of the sample deformation during the compression. The PMMA is a polymer, which is more compliant than the plaster ($E_{\text{PMMA}} = 2$ GPa $< E_{\text{plaster}} = 13.6$ GPa). We consider the worst situation of prefect sticking conditions (perfect interface) between PMMA and plaster. Compression boundary conditions are applied on top and bottom of the PMMA plates.

The properties of PMMA are taken as $E_{\text{PMMA}} = 2$ GPa, $\nu_{\text{PMMA}} = 0.4$. The parameters of plaster are taken the same as in the previous example. The prescribed incremental displacement are $\overline{U} = -2 \times 10^{-4}$ mm until $d_{\max} > 0.8$, and then taken as $\overline{U} = -2 \times 10^{-5}$ mm. The simulation of crack propagation is depicted in Fig. 6.19. We clearly observe that the cracks initiate in that case from the top and bottom surfaces.

We observe in the simulations that even with the presence of the PMMA tabs, cracks still initiate from top and bottom. This can be explained by the fact that the transverse deformation of PMMA is significantly larger than that of plaster. For a same uniaxial load, this transverse deformation is proportional to ν/E, which is much larger for PMMA that for plaster ($\nu_{\text{plaster}}/E_{\text{plaster}} = 0.2/13,6 < \nu_{\text{PMMA}}/E_{\text{PMMA}} = 0,4/2$) GPa. This incompatibility of trans-

verse deformation, if it cannot be accommodated by interfacial sliding, induces a strong local shear at the interface, which is balanced by a tensile transverse stress in the plaster sample. This stress explains the premature initiation of cracks around micropores near the sample ends, as observed in the simulations. Then, it seems that the Poisson effect, in tandem with a strong friction is indeed a important reason that may explain the spurious cracking from the top of the sample.

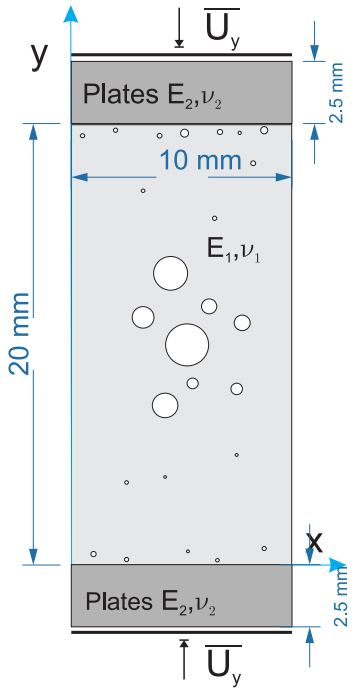

Figure 6.18: Model including the presence of deformable PMMA plates on top and bottom of the specimen.

To verify this point, we change the elastic properties of the plate in the numerical simulation to $\nu = 0.35$ and $E = 60$ GPa (close to properties of aluminium), while keeping the perfect interface conditions between the plate and the plaster. In that case, the Poisson effect difference more limited, and more importantly, its effect in reversed: transverse deformation of the tabs is lower that that of the plaster sample ($0.35/60 < 0.2/13,6$), so that the strain incompatibilities at the interface now generate compressive stresses in the sample, with moderate intensity, much less prone to initiate damage. Results are presented in Fig. 6.20. Indeed, as expected, the cracks do not initiate from the interface.

These last simulations allow us to conclude that the main physical effects responsible of crack initiation from the faces of the sample, are the Poisson effect combined with roughness. During compression, the roughness of the plaster does not allow sliding between PMMA and plaster, and the difference of ν/E ratios induces a strong local shear, which yields to cracking in this region when transverse strain is larger in the tabs than in plaster. This has guided us for modifying the sample preparation to avoid this issue in the experiment: we have carefully

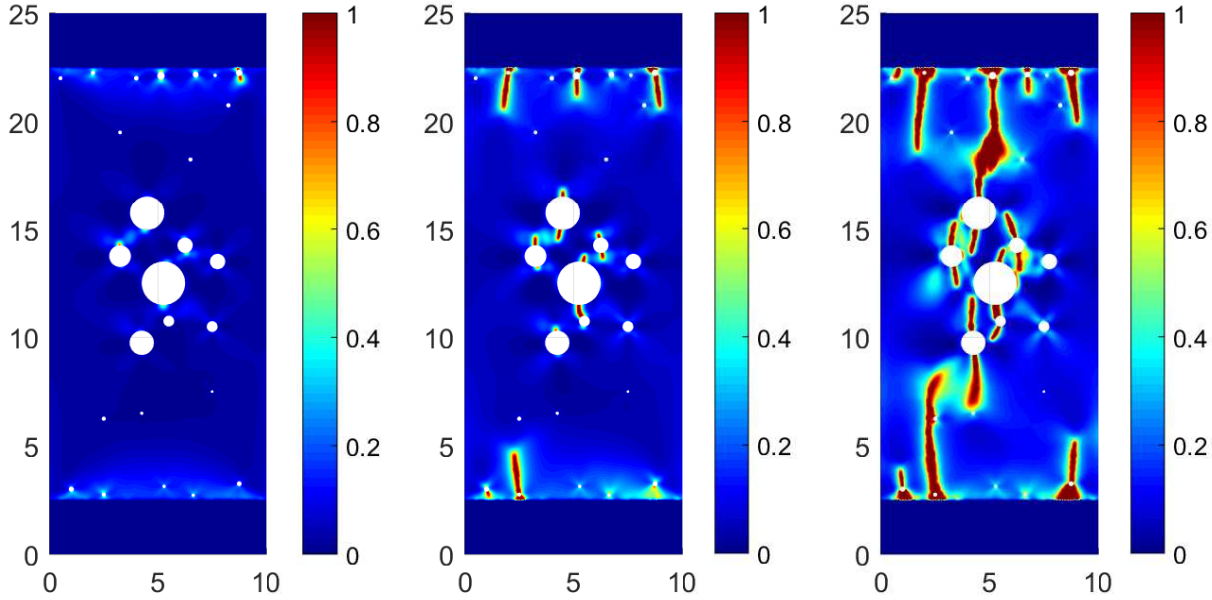

(a) (b) (c)

Figure 6.19: Damage maps for compresion test with PMMA tabs for prescribed displacement: (a) $\overline{U}_a = 0.03$ mm; (b) $\overline{U}_b = 0.04$ mm; (c) $\overline{U}_c = 0.05$ mm

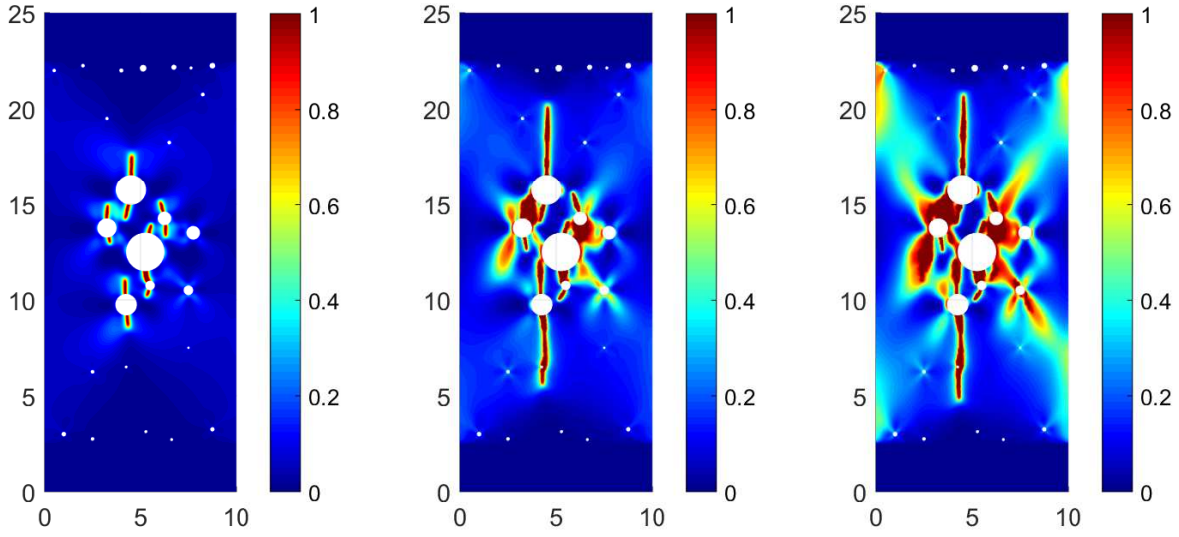

(a) (b) (c)

Figure 6.20: Damage maps of compression test with aluminum tabs: (a) $\overline{U}_a = 0.02$ mm; (b) $\overline{U}_b = 0.03$ mm; (c) $\overline{U}_c = 0.036$ mm

polished the contact surfaces of both the PMMA tabs and the plaster sample to reduce the friction due to the roughness . A SiC grinding paper up to grade 4000 has been used. As

a result, the Poisson effect has drastically decreased and we have been able to obtain crack propagation initiating from the pores within the samples in the experiments. As another route to reduce this effect, aluminum plates, which naturally have a lower Poisson effect difference with the plaster, have also been tested. They have also be polished to reduce friction effects. It should however be noted that aluminum is stiffer than plaster so that the "singularity smoothing effect" of these tabs, as discussed in section 6.3.4, is almost inexistent. Some experiments with aluminum tabs were however successful (see Chapter 4), which indicated that the improvement sample preparation routines were sufficient to correct to geometric imperfections of the sample.

Note finally that an ideal interface material should be at the same time compliant and with limited transverse deformation under uniaxial load: a material with a low elastic modulus (of the order of 1 GPa) and a Poisson ratio very close to zero would be required. We do not know of such a material. Fortunately, successful experiments could be run without it.

6.4 Simulation on sub-volumes of the XR-CT image

In the present work, one of our main objectives is to directly compare the crack paths obtained from the in-situ experimental testing at the microstructural level and the associated simulations. One obstacle is the size of the 3D finite element model (number of elements) when considering the whole sample with all microstructural details. Using a regular mesh corresponding to voxels (see section 6.2.2.1) induces a number of elements whose related finite element system cannot be solved by most of nowadays computers. For example, the XR-CT images obtained in this thesis are typically of size $1125 \times 1125 \times 2500$ voxel^3, yielding $\simeq 2.6 \times 10^{10}$ cubic elements in 3D. Even with a software allowing the construction of non-regular meshes from the XR-CT segmented image (see section 6.2.2.2), the number of elements would remain prohibitive. In this section, we define a methodology to study sub-volumes of interest within the global XR-CT image. The main idea is to extract a sub-volume in the image, e.g. in a region where the cracks are expected to pass, and to prescribe Dirichlet boundary conditions on the boundary of the associated domain corresponding to the experimental displacements. These displacements can be obtained thanks to the in-situ testing and DVC. The simulation is performed on the sub-domain with the corresponding experimental displacement conditions on the boundary of the mesh. First, we evaluate the accuracy of such a procedure on a benchmark, then we define the procedure to prescribe at the boundary of the mesh of the sub-volume, the experimental displacements obtained by DVC.

6.4.1 Evaluation of the procedure on a benchmark

To evaluate the accuracy of the procedure, we use a benchmark where we first simulate numerically the response of the structure with loading prescribed on its boundary to obtain the whole displacement field at each loading step. The obtained displacement field is used as a surrogate model for the experimental DVC measurements of the displacements. Then, a sub-volume is

defined around a pore, where cracks are expected to initiate. The geometry of the studied structure and the sub-volume are depicted in Fig. 6.21. The sample is made of plaster, the material parameters being the same as in section 6.3. The sample is subjected to compression. Computations are performed with monotonic displacement increments of $U = 5 \times 10^{-4}$ cm during 130 load increments. A regular mesh of 100×250 elements is used. The obtained crack path is depicted in Fig. 6.22(a). Then, we prescribe the displacement field obtained by the simulation on the boundary of the sub-volume. Dirichlet boundary conditions are prescribed because DVC provides displacements only during the experiment.

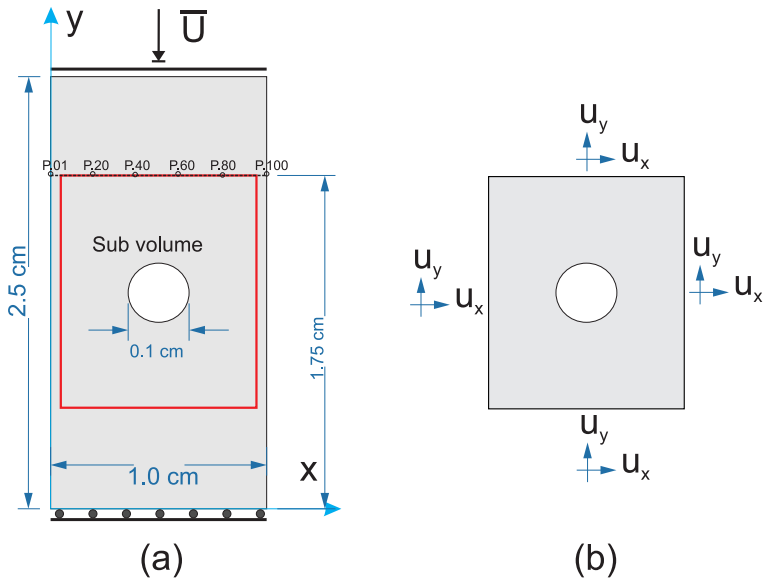

Figure 6.21: Benchmark for the sub-volume procedure; (a) whole structure (25000 elements); (b) sub-volume (9000 elements).

We now consider in Fig. 6.23, the $x-$displacement evolution of several points on the boundary of the sub-volume. The location of these points are plotted in Fig. 6.21, denoted by points $P60, P80, P100$ corresponding with nodes of mesh. We can note that strong nonlinearities occur for large prescribed displacements see Fig. 6.23. They are due to the nonlinear development of damage. This displacement field is applied at the boundary of the sub-volume simulation. The crack path obtained is illustrated in Fig. 6.22(b). The crack paths are compared at the same loading step $\overline{U} = 0.065$ mm. We can note a very good agreement of the solution inside the sub-volume and in the whole structure. In Fig. 6.24 the evolution of the norm of the damage field is compared for both simulations, where the result of the whole structure is computed from the same region as the sub-volume. Both curves show a good agreement.

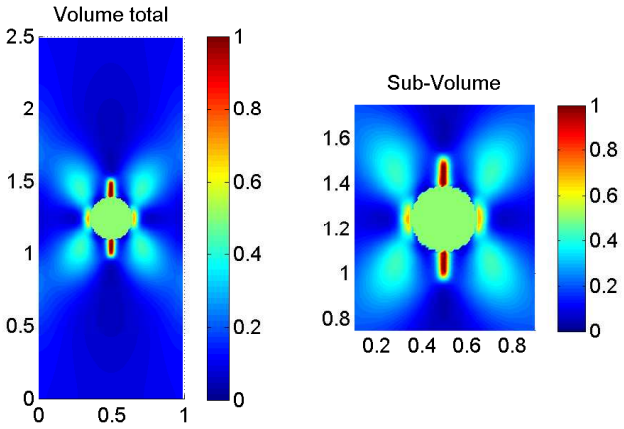

(a) (b)

Figure 6.22: Comparison of crack trajectory for $\overline{u} = 0.065$ mm: (a) global problem; (b) sub-volume problem

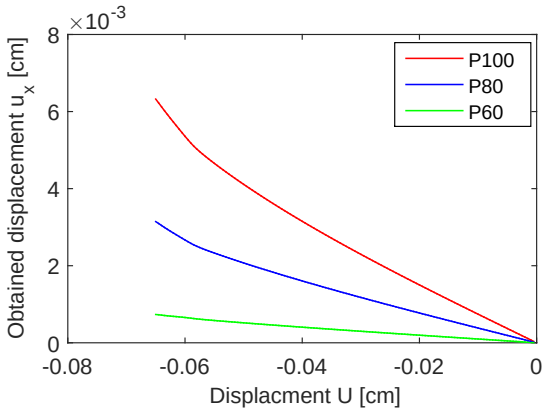

Figure 6.23: x-displacement response of several points of investigation on sub-volume boundary

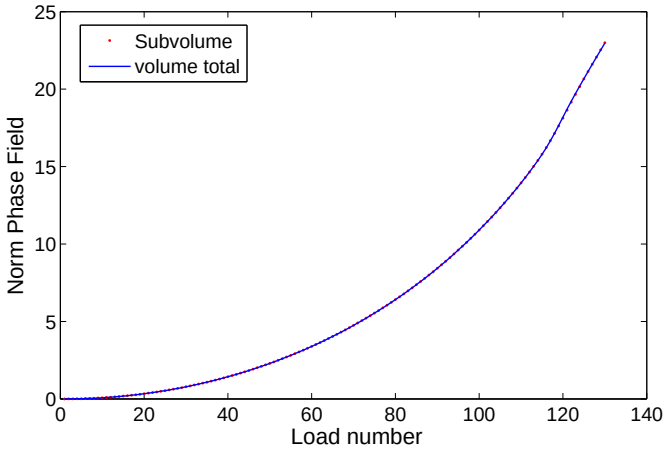

Figure 6.24: Comparison of crack amount in sub-volume problem

6.4.2 Using the experimental DVC measurements to prescribe the boundary conditions on the sub-volume

In this section, we develop a methodology to extract the experimental displacements to be prescribed on the sub-volume, these displacements being obtained by DVC of the different XR-CT images recorded during the in-situ test.

6.4.2.1 Systematic error correction

The first difficulty is the noise and errors inherent to the experimental data obtained by DVC, which have to be filtered or corrected before these data can be used as Dirichlet boundary conditions in the finite element simulation. Indeed, the obtained displacements include always systematic errors (see Chapter 4, Chapter 5). This error may induce non physical gradients on the displacement field, which may generate false local stress concentrations near the boundaries of the sub-volume. DVC errors are known to contain a systematic part, correlated with the fractional part of the real displacement field components, expressed in voxels in the reference image axes. Fortunately, the procedure proposed in [62], extended to 3D images as explained in Chapter 5, provides the systematic error curves along the three directions, associated with the actual experimental conditions (i.e. available contrast, in sample, used imaging conditions, and specific DVC parameters). This error is assumed to be the same for the preliminary test (zoomed image) and for the in-situ test. An example of such systematic errors for specimen PlasterF3 is depicted in Fig. 6.25, with a typical amplitude of the order of 0.1 voxels for our experimental conditions.

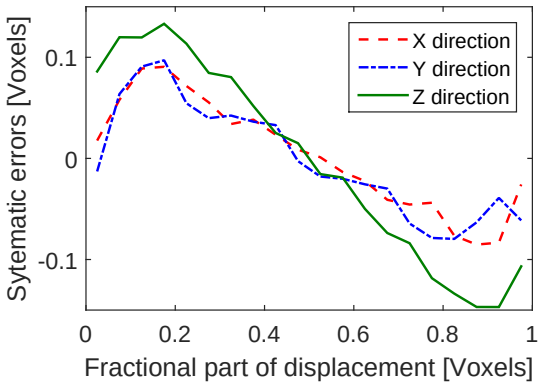

Figure 6.25: Systematic errors analysis for specimen PlasterF3

Using the systematic errors curve, we can construct the relation between measured and real displacements (see Fig. 6.26). This relation is periodic along the 3 directions when considered as a function of the real displacement components, with a period of 1 voxel. Within a period, it can be approximated by a polynomial function. We present in Fig. 6.26 polynomial approximations (order 5) for the three displacement components, which will be used to correct DVC results. Data correspond again to sample PlasterF3.

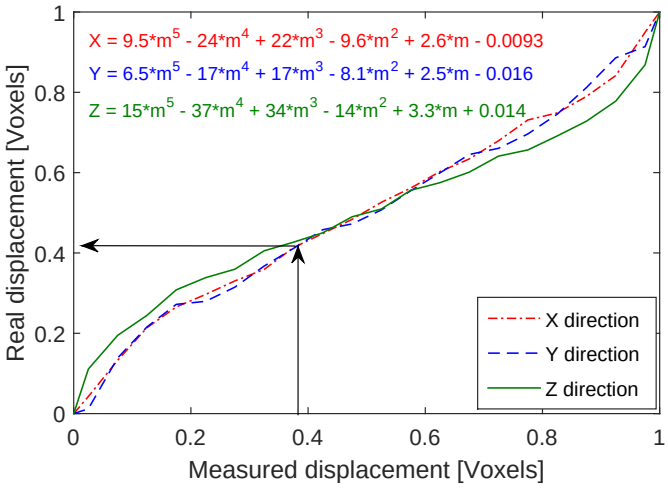

Figure 6.26: Relation between real and measured displacements

To illustrate the benefit of this procedure, we consider a sub-volume, where the displacements of a plane of investigation are corrected by using the above polynomial approximations. The z−displacements before and after correction are depicted in Fig. 6.27. We note that the systematic sub-voxels correction reduces the fluctuations of the displacement field. However the obtained value still exhibit some local spurious singularities, that may induce erroneous of damage phenomena. The detailed analysis of these problems will be considered in Chapter 9.

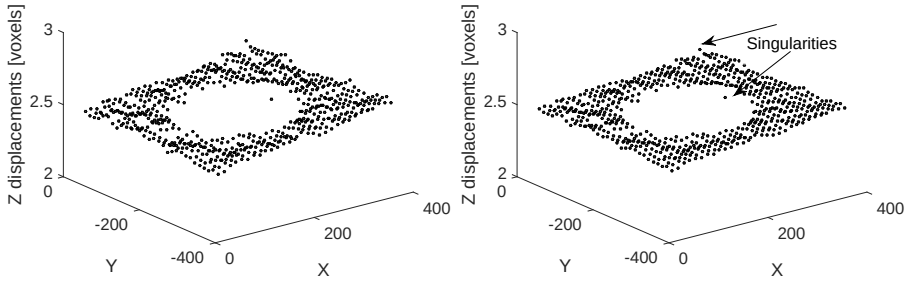

Figure 6.27: Z displacement of a plane of investigation: (a) before correction; (b) after correction

6.4.2.2 Definition of loading data

After apply the above correction procedure for each loading step, the obtained displacement fields are used to construct the full incremental displacement history to be prescribed at the boundary of the sub-volume. To do so, we have to face another problem if we consider an isolated point at the boundary, the displacement evolution is not smooth. To illustrate this phenomenon, we plot the load - displacement curve of one correlation point during the test in Fig. 6.28(a). This curve clearly shows a non smooth evolution of the displacement. These

apparent fluctuations may have various sources. First remember that the sample has undergone several loading-unloading stages, because the test lasted several days and the sample has been partially unloaded during nights. These loading cycles may induce overall rigid body motions of the sample. More generally, the overall behavior of the compression device might also induce such motions at sample scale, because it is not perfectly rigid.

These rigid body motions would not induce any spurious stresses if the computation would be performed in a finite strain framework. However, they have an effect in the used small strain framework. A procedure will in the future be developed to subtract these rigid body motions, to be consistent with a small strain framework, but has not yet been developed. Another source of possible fluctuations are DVC random errors which have been shown to be of the order of 0.1 voxel, which is close to the order of magnitude of some of the observed fluctuations in Fig. 6.28(a). Some smoothing would be required to filter these DVC errors.

For the sake of simplicity and as a first route to address these issues, and in order to remove all possible sources of spurious local displacement fluctuations which could induce non physical damage, we propose to filter the DVC measurements at each point of the boundary of the subvolume, by a quadratic fit, as illustrated in Fig. 6.28(b). This quadratic fit will also serve as a temporal interpolation to define displacements at numerical loading increments which do not coincide with experimental load steps.

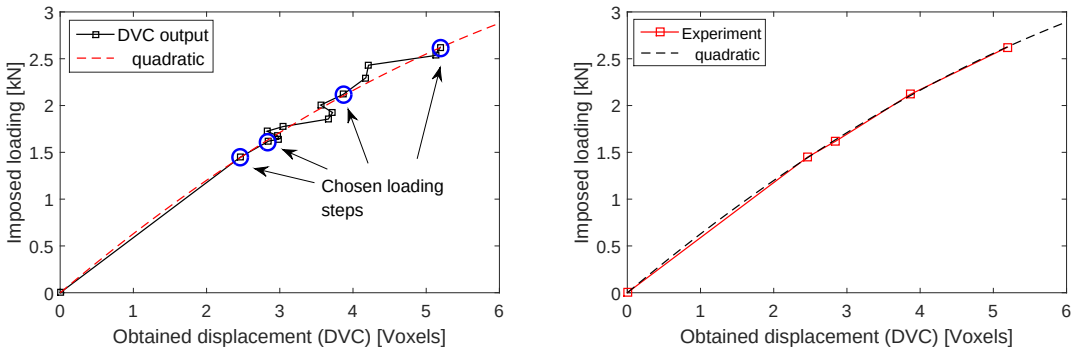

Figure 6.28: (a) Displacement of one voxel with time obtained by DVC during the in situ test; (b) quadratic polynomial fit.

Finally, the correlation points are usually not the same as the nodes used for boundary conditions. Therefore, an interpolation is needed to compute displacements for each node at the boundaries of the sub-volume. We use here the same principle as the construction of subtracted image in Chapter 5. The local transformation $\mathbf{\Phi}_N$ computed from neighbor correlated points is applied, i.e for each node at the boundaries we select the neighbor correlated points to compute $\mathbf{\Phi}_N$, which is used to determine its positions in deformed configuration and then give the displacement. Details of this procedure are illustrated in Fig. 6.29

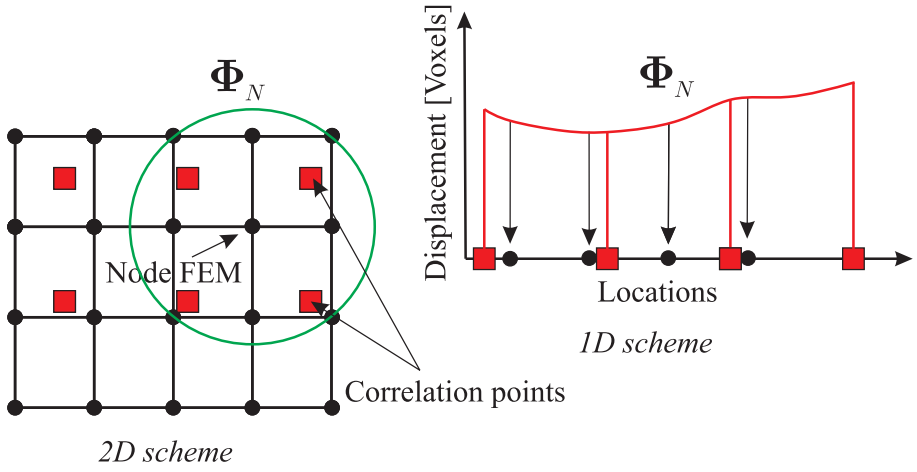

Figure 6.29: Extraction of FE boundary conditions from DVC data: interpolation procedure

6.4.2.3 Summary : overall data flow for sub-volume simulations

The general work-flow is summarized Fig. 6.30. After performing the mechanical test, the reference image is segmented to define the input geometry of the sub-volume on which we intend to perform the numerical simulation. This geometry is meshed with an appropriate software, with an appropriate mesh size. In parallel, DVC routines are applied to quantify displacement field for all loading stages. We perform the correction and filtering procedures on the obtained results for all node of the DVC mesh which are close to the boundary of the sub-volume. Finally, the displacements at the external nodes of the FE mesh are obtained, far all loading steps in the numerical simulation, by interpolation of the filtered DVC data.

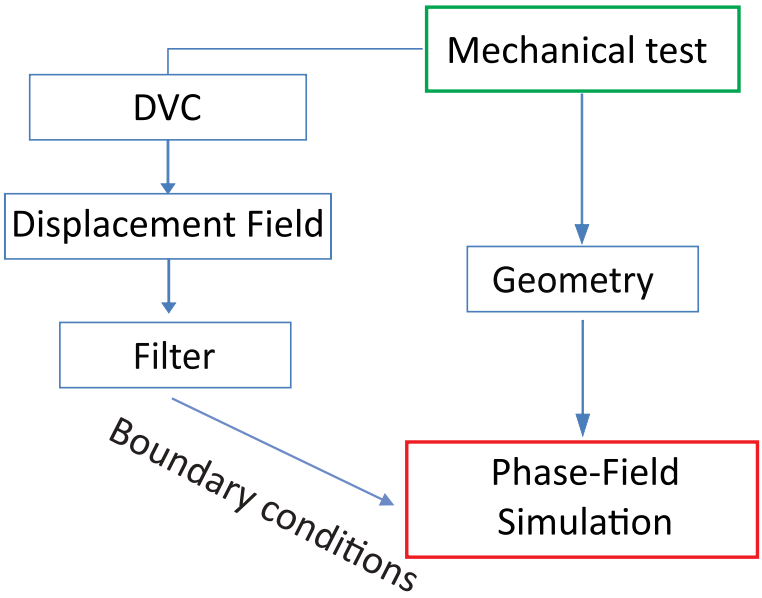

Figure 6.30: General data flow to perform sub-volume simulations based on actual geometry of the microstructure and the filtered local displacements measured by DVC.

6.5 Conclusion

In this chapter, we have discussed how to model the experimental in-situ test in order to simulate it numerically and to compare in detail the predictions of the numerical model with the experimental observations of damage.

First, we have described some techniques to construct the mesh of the initial microstructural geometry from a XR-CT image. When the lightweight plaster material is considered, then the heterogeneities mainly consist into spherical pores which can easily be modeled and meshed. The position of their centers and their radii can directly be identified on the XR-CT image. When more complex geometries of microstructures are involved, like in lightweight concrete, the geometry cannot be idealized. Then, the segmented voxel data must be directly used to construct a mesh of elements. We have constructed both regular meshes and unstructured meshes using available softwares from our experimental images.

Secondly, we have simulated the crack propagation in lightweight plaster samples and have modeled the effects of imperfect loading conditions, like defects of parallelism or roughness at the upper and lower faces of the sample, when loaded in the test machine. We have evidenced the same phenomena in these case, i.e. that the crack initiate from the upper and lower surfaces when these imperfections exist, in tandem with the friction. We have proposed to use polished PMMA (or aluminum) plates on the upper and lower surface to remove these spurious effects. The simulations and the experiments both agree in that case, and the cracks initiate from the large pores rather that from the external surfaces. Indeed, when appropriate care is taken to perform the experiments, damage initiation and evolution is controlled by the complex heterogeneous strain and stress field generated by the central pores, whose geometry can be controlled and quantified, and no longer by non-controlled and barely-measurable boundary condition details. As a consequence, we can reasonably expect to reproduce the damage history by the numerical simulation, since the latter account for the actual sources of damage.

Finally, we have proposed a sub-domain technique to simulate the crack propagation during the testing in sub-volumes to save computational times. In this methodology, the experimental displacement of the boundaries of the sub-domain is extracted from the XR-CT using DVC. We will use these techniques to directly compare the local crack paths within the microstructure during the in-situ tests with numerical simulations in Chapters 8.

Chapter 7

Validation of crack propagation in 2D plaster specimen

Contents

The main content of this chapter has been adapted from our submitted paper [156].

7.1 Introduction

The phase field method presented in Chapter 2 is able to simulate brittle crack initiation and propagation with low dependence to the mesh in a classical FEM framework. It allows handling very complex, multiple crack fronts and branching in both 2D and 3D without ad hoc numerical treatment. In Chapter 2, we have demonstrated the capability of the method to simulate crack onset and propagation in complex image-based models, as such obtained by segmenting 3D X-Ray computed tomography images of real materials like concrete.

However, the method requires choosing a regularization parameter related to the smeared approximation of discontinuities. This parameter induces a characteristic length l in the model which must be chosen by the user. In [17], Amor et al. have shown that a relationship can be established between l and at least two other material parameters. This seems consistent with a recent crack initiation criterion of Leguillon et al. [119] where two material parameters need to be identified for predicting crack onset. In Chapter 1, we have followed this line and have shown that l may be interpreted as a material parameter and should be deduced from experimental material parameters identification when available. In this Chapter, we validate

this by comparing simulations of crack initiation with experiments on drilled plaster samples, where the material parameters, including l, have been identified in other simple experimental tests [180]. Experimental data provided in [180] have been used to provide reference solutions associated with onset of cracks in plaster structures containing drilled holes in compression or in three-point bending of a beam.

7.2 Experimental validation: three-point bending test

7.2.1 Pre-notched beam

In this test, we validate the phase field solution on an experimental 3-point bending test of a beam containing an initial crack of length 15 mm. The geometry, dimensions, and boundary conditions of the structure are depicted in Fig. 7.1. The material is dry plaster, composed of plaster powder of the Siniat Company named Prestia Profilia 35®. The plaster sample preparation are details in a previous work [180]. In the mentioned study, the materials parameters have been identified experimentally and are the same as in the previous example: $E = 12$ GPa, $\nu = 0.3$, $g_c = 1.4$ N/m and $\sigma_c = 3.9$ MPa, which gives the value of $l = 0.1$ mm from Chapter 1. Note that here the Poission ration is non zero and the problem is not one-dimensional, thus this expression only provides an estimation for l. The $z-$component of displacements $\overline{U}$ is prescribed along a line in the middle of the upper face, while the all components of displacements are blocked along two lines on the lower face (see Fig. 7.1).

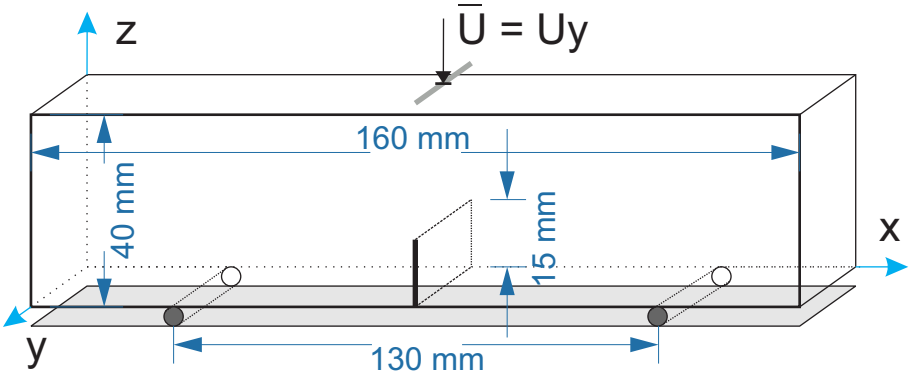

Figure 7.1: 3D 3-point bending test: Geometry and boundary conditions.

Three-dimensional simulations have been conducted. A refined mesh was constructed using tetrahedral elements, with $h_{\max} = 3$ mm and $h_{\min} = 0.05$ mm in the region of expected crack path, to satisfy the condition $h_{\min} \leq l/2$. Monotonic compressive displacement increments of $\Delta\overline{U} = -5 \times 10^{-4}$ mm have been prescribed as long as $d < 0.9$ in all elements and $\Delta\overline{U} = -5 \times 10^{-5}$ mm as soon as $d > 0.9$ in one element. The crack propagation evolution is depicted in Fig. 7.2 for two loading steps.

Fig. 7.3 provides the load-displacement curve obtained with the simulation. The critical load F_r is defined as the maximum resultant load before softening due to crack propagation. We

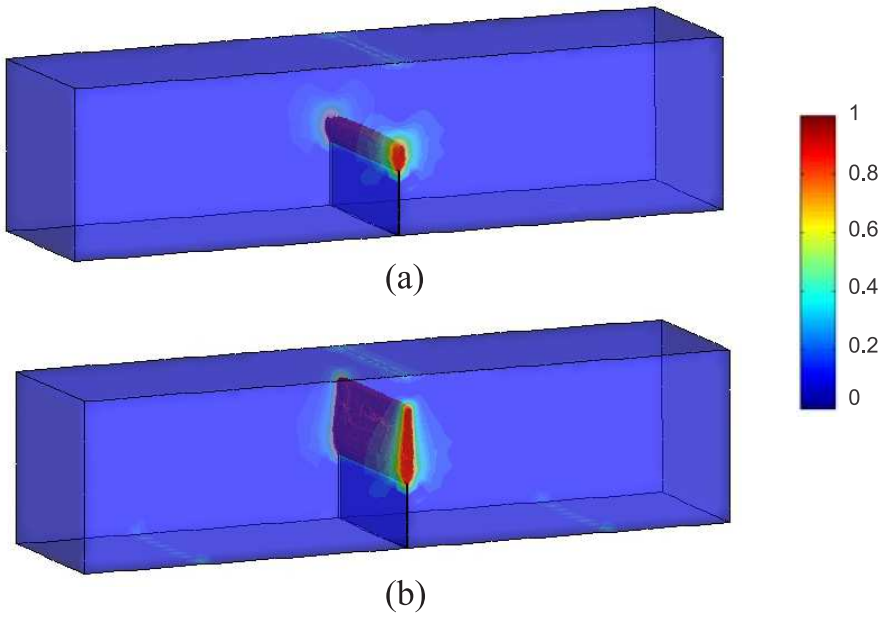

Figure 7.2: 3-point bending test, crack evolution (damage variable $d(\mathbf{x})$) for two prescribed displacements: (a) $\overline{U} = 0.15$ mm and (b) $\overline{U} = 0.18$ mm.

compare this critical load with the experimental values provided in [180] for several samples in Fig. 7.4 and can note that we obtain a good agreement for the values of F_r with respect to experiments.

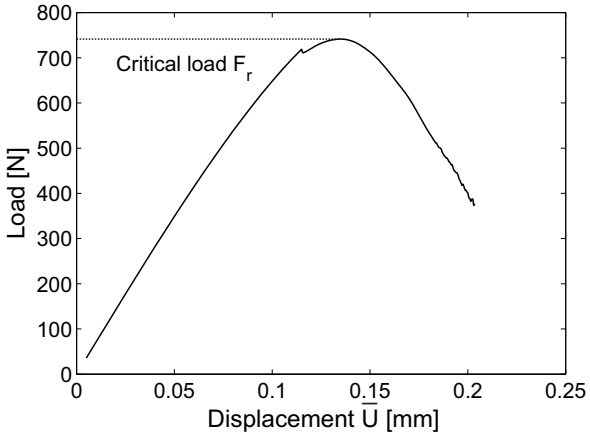

Figure 7.3: Load - displacement curve for the 3-point bending test: numerical model.

7.2.2 Un-notched beam

We investigate now the capability of the phase field method to provide a correct value of σ_c for crack initiation in a structure different from the one with which the critical stress σ_c was identified. For this purpose, we consider an uncracked beam under three-point bending, as

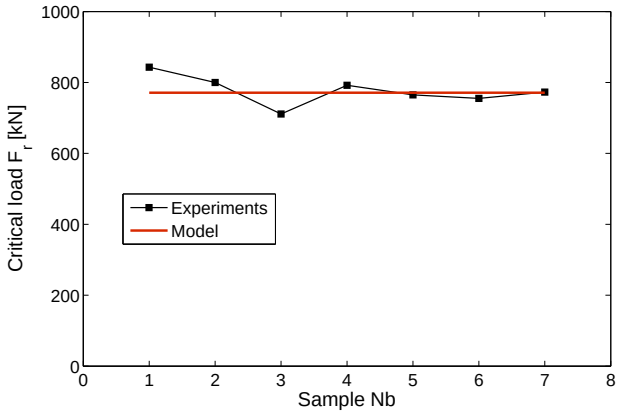

Figure 7.4: Critical load for the 3-point bending problem: comparison between experiments and numerical predictions.

depicted in Fig. 7.5.

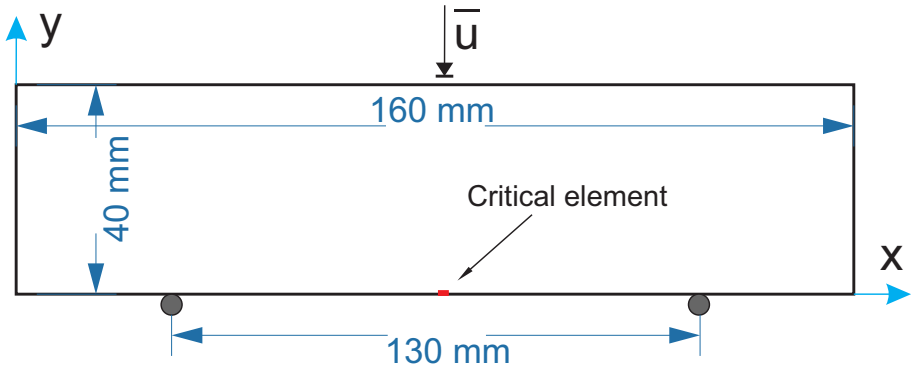

Figure 7.5: 2D 3-point bending test of non cracked beam: Geometry and boundary conditions.

The stress is evaluated during the simulation in an element located on the known path of the crack. The tensile strength σ_c is then evaluated numerically as depicted in Fig. 7.6. All material parameters are the same as in the previous example and is l again set to 0.1 mm. Monotonic compressive displacement increments of $\Delta\overline{U} = -2\times10^{-3}$ mm have been used for 180 increments. We obtain a good agreement between the value predicted numerically ($\sigma_c = 4.01$ MPa) and the experimental value identified from another experiment in [180] ($\sigma_c = 3.9$ MPa).

7.3 Experimental validation: compression of a drilled plaster specimen containing a single cylindrical hole

In the following, we investigate crack initiation and propagation in a more involved test, and compare the numerical prediction with experimental results provided in [180]. All material parameters are the same as in the previous example, as well as the value of l. The objective is

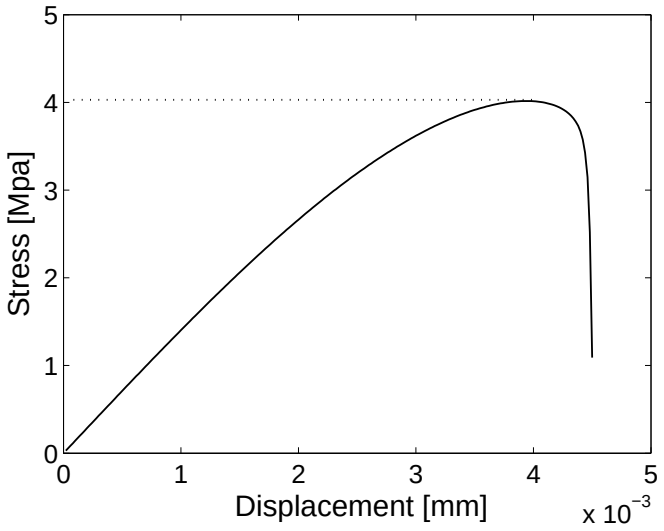

Figure 7.6: Tensile strength for the 3-point bending problem: stress - displacement curve of the critical element

to evaluate if the numerical model is able to predict accurately the response of cracked structure in other configurations that the ones used to identify the material parameters.

A drilled sample is considered, as depicted in Fig. 7.7. A thick plate contains one single cylindrical hole with diameter D. Several sample with various hole diameters, ranging from $D = 3$ to $D = 6$ mm, have been tested. The dimensions of the plate are 100 mm $\times$ 65 mm $\times$ 40 mm. The material (plaster) is the same as in the previous example. The sample is loaded in compression. In the experimental tests, the load is applied continuously at a speed of 0.2 mm/min. Consistently, the numerical calculations are run in the quasi static regime, as for previous cases. PMMA plates were used on top and bottom face to reduce the lack of planarity, parallelism and friction conditions [179] to avoid stress concentration.

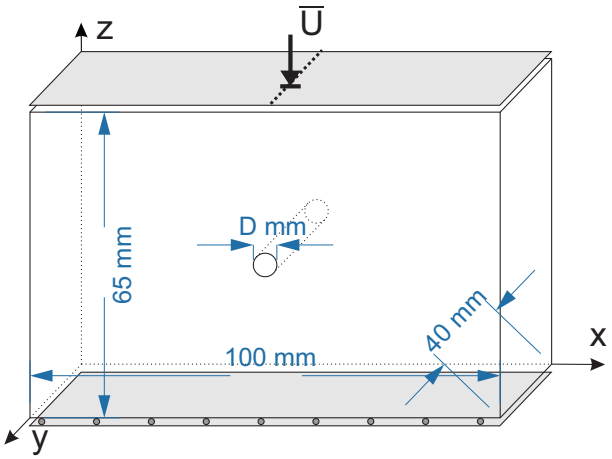

Figure 7.7: Plaster sample containing one cylindrical drilled hole: geometry and boundary conditions for both experimental setup and simulation.

Experimental image correlation data were provided in [180], together with force measurement to detect the crack experimentally. A high-resolution camera (Baumer HXC20, progressive scan sensor with 2048×1088 pixels), with a pixel size of 5.5×5.5 μm^2, and equipped with a ZEISS Makro-Planar 100 mm macro lens was used to continuously acquire images of the specimen during loading at a frame rate of 20 Hz. As the detection of the crack onset is not possible with naked eye, the recorded images were processes by 2D digital image correlation (DIC) techniques. Cracks are detected by high levels of local 11−strain components, measured for a gage length defined by the mesh of correlation points (20 pixels spacing), which are the signature of the presence of displacement discontinuities between to points of the mesh.

2D technique of digital image correlation 2D-DIC was used. When the sample is subjected to a compressive load, two opposite cracks initiate on top and bottom of the hole and grow from the cavity, in a direction parallel to the load. In [180], the experimental results have been compared to the semi-analytical model of Leguillon [119], which requires numerical FEM computations to evaluate the stress intensity factors. In the mentioned work, 2D FE simulations with plane strain assumptions were used. In view of the dimensions of the sample and owing to the fact the measurements are performed at the surface of the sample, the plane strain assumption might be discussed. For this purpose, we have performed 2D simulations with both plane strain and plane stress assumption, as well as full 3D simulations. The boundary conditions model the experimental ones on the sample, and are described in Fig. 7.7: on the lower surface ($y = 0$), the $y-$ displacements are fixed, the $x-$ displacements are free. On the upper end, the $y-$ displacements are fixed, while the $x-$ displacements are prescribed, with an increasing value $\overline{U}$ during the simulation. Monotonic compressive displacement increments of $\overline{U} = -10^{-3}$ mm are prescribed for first load increments and as soon as $d_{\max} > 0.9$ at some integration in the domain, we use $\overline{U} = -10^{-4}$. A finite element mesh with varying element size ($h_{\min} = 0.05$ mm around the hole and $h_{\max} = 0.25$ mm in the rest of domain) is used.

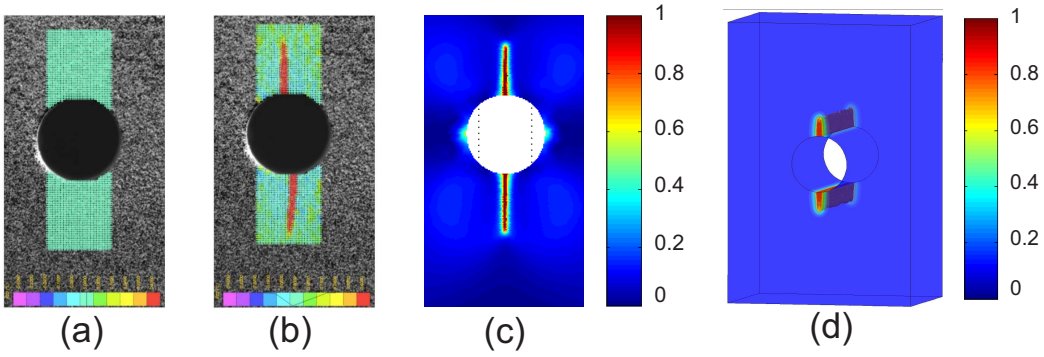

Figure 7.8: Crack path evolution near the cylindrical hole ($D = 5$ mm); (a) and (b): Strain maps obtained with digital image correlation for initial and loaded state [180], for 15.2 MPa and 14.1 MPa, respectively; (c) 2D simulation (plane strain); (d) 3D simulation (damage variable $d(\mathbf{x})$).

In Fig. 7.8, we show a comparison of the experimental digital image correlation technique used to detect the crack evolution and the simulation, were the damage field, associated with the crack, is depicted. This case corresponds to a diameter $D = 5$ mm. We can note that the numerical solution based on the phase field method can capture the crack initiation on top and bottom of the hole and the vertical path of the two cracks. In addition, the length of the crack for the given load is accurately predicted (Figs. 7.8 (b) and (c)).

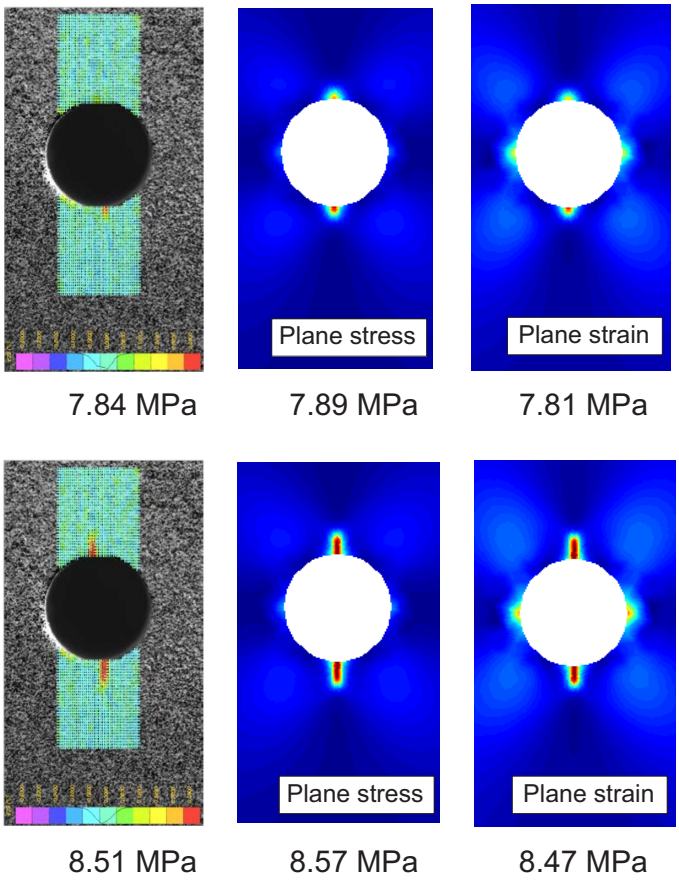

Figure 7.9: Crack propagation at different values of the applied stress around the cylindrical hole: comparison between experiments (digital image correlation) and simulations (damage variable $d(\mathbf{x})$).

In the simulations, the crack length is computed as the distance between the last point for which $d = 1$ and the hole boundary, assuming a straight crack. The same procedure is employed in 3D. In Figs. 7.9-7.10 we quantitatively compare the crack length evolution with respect to the applied load computed at the point where the displacement is prescribed. Results for 2D plane strain and plane stress, 3D simulations and experimental DIC results are compared in Fig. 7.9. Fig. 7.10 shows that all three models provide a satisfying prediction for the critical load corresponding to the onset of the crack. However, we can note that during propagation, the experimental evolution deviates from 2D predictions. The 3D simulation is in that case in better agreement with the experimental response for both top and bottom cracks.

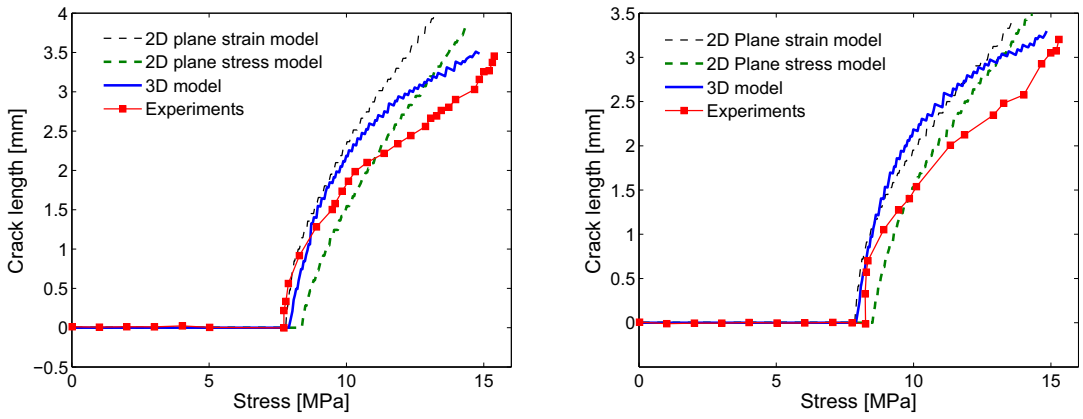

(a) (b)

Figure 7.10: Evolution of the crack length with respect to the resultant stress on the upper boundary, comparison between models and experimental data: (a) top crack; (b) bottom crack.

To analyze the influence of the diameter of the hole on the stress at the time cracks onset, several samples with diameters varying between 3 and 6 mm have been prepared and tested. Simulations have been performed here also in 2D and 3D. Results are provided in Fig. 7.11. They show the good ability of the simulation model to accurately predict the evolution of critical load σ^* (onset of the crack) with hole diameters and related size effects.

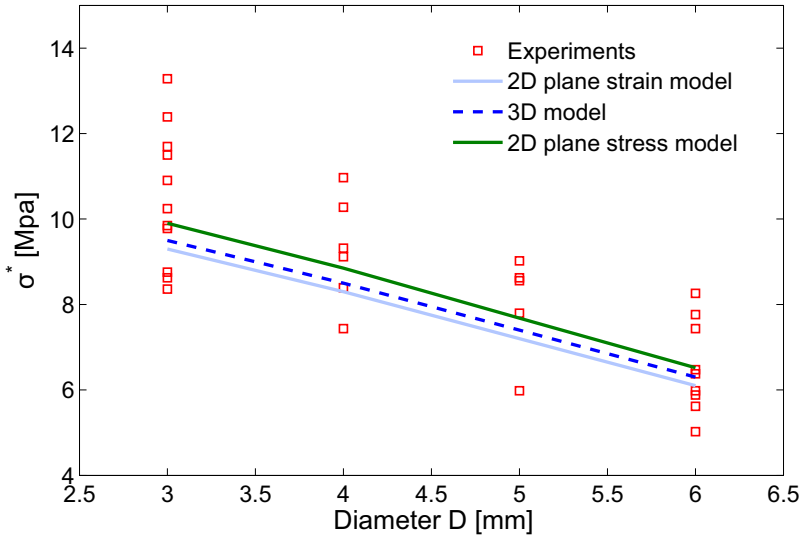

Figure 7.11: Stress associated with the cracks onset with respect to the cylindrical hole diameter: comparison between experiments and numerical simulation.

7.4 Microcracking in a plaster specimen containing a periodic distribution of cylindrical holes

In this last example, we investigate the microcracking of two plaster specimens containing many holes, whose configurations are depicted in Fig. 7.12. In both cases, the diameter of the holes is $D = 4$ mm. Configuration of Fig. 7.12(a) corresponds to a volume fraction of 12.2%, and in Fig. 7.12 (b) to 13.5%. A FE adaptive mesh with characteristic size $h_{min} = 0.05$ mm has been used around the holes, and larger elements whose size are $h_{max} = 0.5$ mm have been employed away from holes. The whole mesh contains 905437 elements. All material parameters are the same as previously, including the value of l.

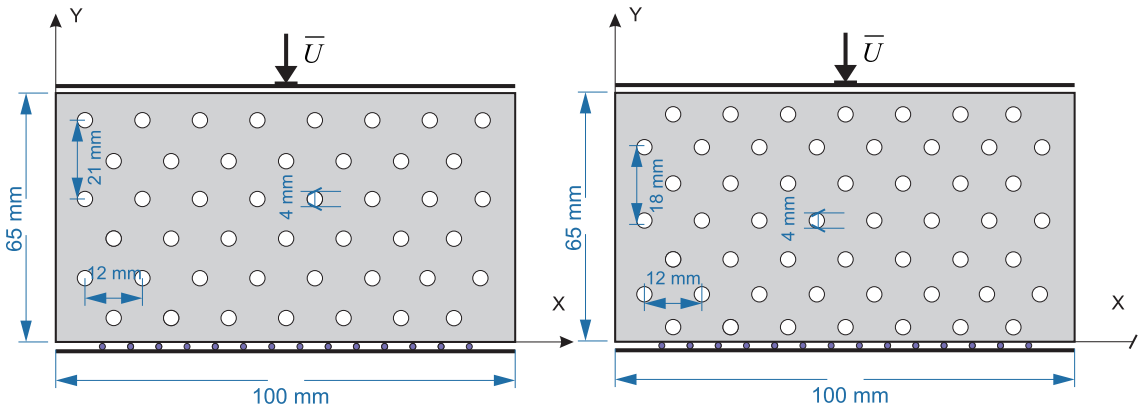

Figure 7.12: Plaster specimen containing a regular distribution of cylindrical holes: (a) surface fraction 12.2 % and (b) surface fraction 13.5 % [179].

2D plane strain simulation was conducted. Monotonic compressive displacements increments are prescribed on the top edge of the specimen, with $\Delta\overline{U} = -10^{-3}$ mm in the first 1000 increments and $\Delta\overline{U} = -5 \times 10^{-5}$ mm in the last 1500 increments. The evolution of microcracking within the specimen is depicted in Fig. 7.13. The simulation model captures well the vertical propagation of the different microcracks. The microcracks propagate faster near the left and right boundaries than in the central region, probably because of the influence of the free boundary conditions on the lateral surfaces. In addition, there is also a slight dissymmetry between upper and lower parts of the sample (a), whose successive damage map are reproduced in figure 18. This is linked to the absence of horizontal symmetry for this sample. For sample (b), the hole distribution is symmetric between upper and lower parts, and the resulting simulated damage map is also symmetric.

The microcracking pattern obtained from numerical simulation are qualitatively compared with DIC in 7.14 for the 13.5% sample. In Fig. 7.14 the microcracking pattern for the case of porous fraction 13.5% depicted and numerical simulations and digital correlation image obtained in [179] are qualitatively compared. Globally speaking, the heterogeneity of the damage map between central a lateral parts of the sample is nicely captured by the computation. In Fig. 7.15,

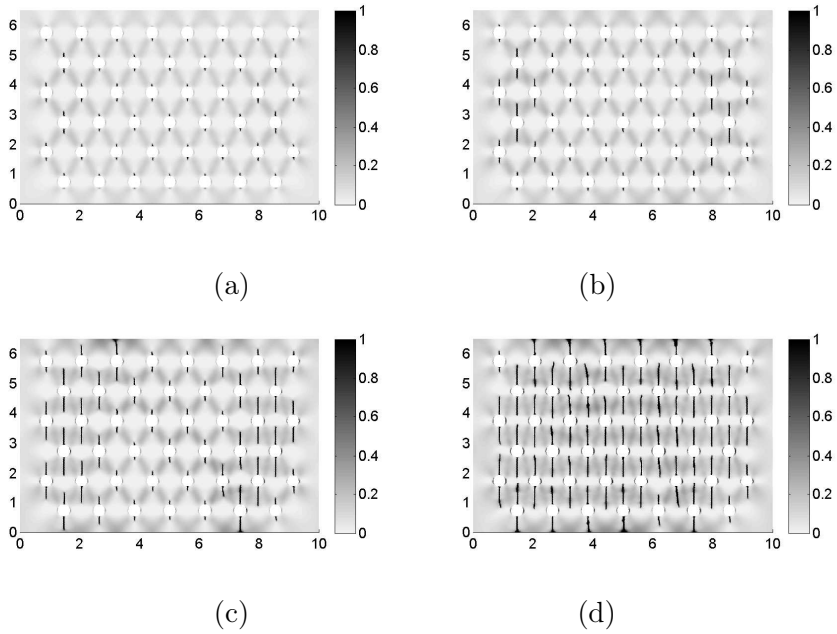

(a) (b)

(c) (d)

Figure 7.13: Plaster specimen containing regular distribution of cylindrical holes: evolution of the microcracking for different compressive loads (damage variable $d(\mathbf{x})$): (a) $\overline{U} = 0.544$ mm; (b) $\overline{U} = 0.594$ mm; (c) $\overline{U} = 0.64$ mm; (d) $\overline{U} = 0.67$ mm;

we compare with more details the microcracking morphology between the simulation and the experiment provided in [179], [180], and note that it is qualitatively captured, both regarding the vertical propagation of the different cracks, and regarding the non uniform propagation of the microcracks within the sample.

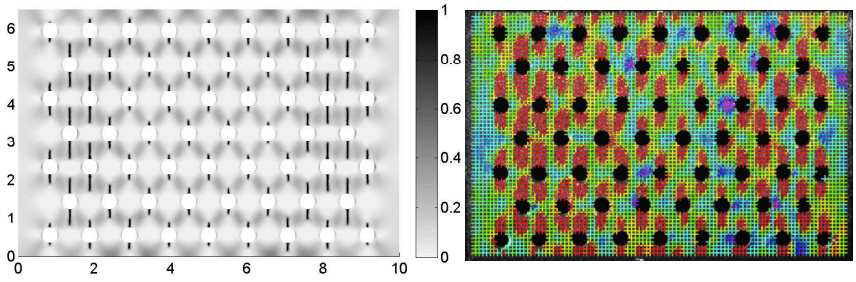

(a) (b)

Figure 7.14: Crack trajectory comparison between the present simulation (a) and the experiment (b) provided in [179] (damage variable $d(\mathbf{x})$) for $\overline{U} = 0.614$ mm.

To compare more quantitatively the predictions provided by the numerical simulation, we analyze the effects of changing the configuration (volume fraction and distribution) with respect to the stress required to initiate the first cracks in the sample and to generate cracks around all holes. Again, the corresponding experimental values have been provided in [179]. Comparisons

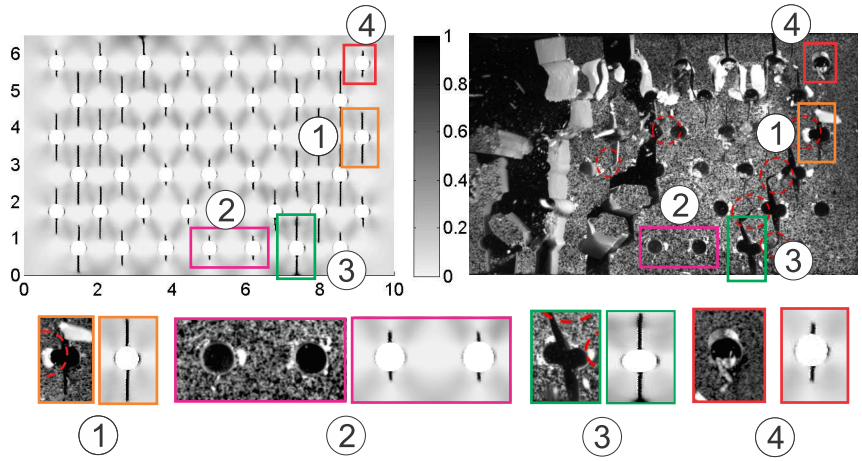

Figure 7.15: Qualitative comparison of the microcracking propagation between the present simulation and the experiment provided in [179] (damage variable $d(\mathbf{x})$) for $\overline{U} = 0.64$ mm.

are provided in Fig. 7.16. The numerical simulation method is here again in good agreement with the experimental values.

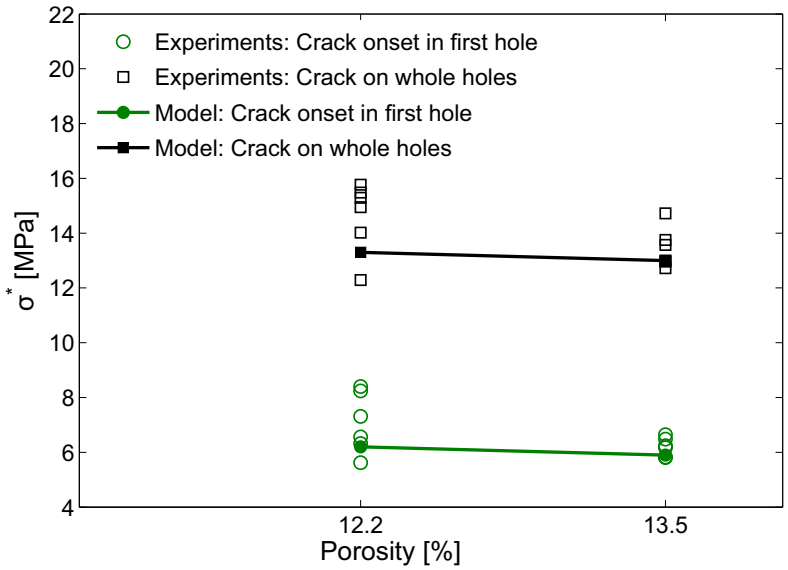

Figure 7.16: Stress corresponding to crack onset within the specimen: comparison between experimental results and the numerical model for two porosities.

7.5 Conclusion

In this chapter, we have shown that the regularization parameter describing the width of the smeared crack approximation is linked to material parameters, and thus requires experimental measures to be identified, and characterizes an internal length for the damage model. Then, from

the knowledge of the elastic parameters, of the toughness and of the regularization parameter of the phase field method, essentially identified from experimental measurements of critical stress in uniformly stressed samples, we have conducted several simulations, including crack initiation and propagation in three-point bending beam and in drilled samples of plaster in compression. Remarkably, the phase field model is able to predict quantitatively crack paths, crack propagation morphologies, and mechanical response in good agreement with experimental results for other geometrical configurations than the ones used to identify the material parameters. Thus, this model provides a promising tool for prediction of strength in brittle heterogeneous or lightweight materials for civil engineering.

Chapter 8

Experiment - Model comparison of crack propagation in 3D specimens

Contents

8.1 Introduction

The objective of this chapter is the 3D observation of cracking in EPS plaster and EPS concrete. After the preparation of samples, we have performed in-situ compression tests combined with

tomography on obtained specimens (see Chapter 4). The obtained images will be used to (1) detect microcrack and (2) to generate input data for the numerical simulations.

Firstly, the image subtraction proposed in Chapter 5 will be used to detect crack evolution. Noise sources of this method will be estimated, and then its accuracy to detect cracks will be analyzed. Secondly, the compression tests are simulated using the phase field method introduced in Chapter 2. The fracture parameters are here estimated by inverse analysis. The results will be compared with those obtained from image processing.

Two typical comparisons will be considered: *global observation* and *local observation*. *Global observation* is performed on simplified geometries, while *local observation* is performed on the real geometry of the structure. We will also present the application of the sub-volume method (see Chapter 6) to simulate several regions of interest within EPS plater and EPS concrete samples.

Both qualitative and quantitative comparisons will be performed. The results of this chapter will confirm: (1) the performance of the proposed image processing and experimental method to provide reference data to be compared to numerical simulations; (2) the accuracy of the model assumptions used to reproduce the phenomena captured in experiments; (3) the predictive capability of the numerical model.

8.2 Experimental data

8.2.1 Specimens

In this chapter, we consider 3 specimens: one EPS concrete sample (ConcreteP2) and two EPS plaster specimens (PlasterF1, PlasterF3). Detailed information about each sample is provided in Table 8.1.

Specimen	Height (mm)	Diameter (mm)	Mass (g)	Beads nb	Porosity (%)	Parallelism error (μm)
PlasterF1	18.20	9.0	2.5	2	5.3	20
PlasterF3	18.21	9.0	2.6	2	4.3	10
ConcreteP2	19.86	11.68	2.3	Multi	21.5	30

Table 8.1: Information about observed specimens

Identical DVC parameters have been used for both EPS plaster material samples. Thanks to a better local contrast, a finer mesh can be used for correlation points together with a lower correlation threshold C for the concrete sample. Details on the chosen correlation parameters are given in Table 8.2.

A parametric study following Chapter 5 has been conducted to define the optimal value of the neighbor distance d_{Tmax}; obtained result also reported in Table 8.2. In badly correlated regions, this distance has been increased to $2d_{\mathrm{Tmax}}$.

Specimen	Inter-point [Voxels]	D [Voxels]	C	d_{Tmax} [Voxels]	Voxel size [μm]
PlasterF1/F3	15	40	0.352	50	8.0
ConcreteP2	10	40	0.073	40	10.0

Table 8.2: DVC and subtracted image parameters: "Inter-point" is the step between points in the regular correlation mesh, D is the size of the correlation window and d_{Tmax} is the distance criterion to select neighbor correlated points

8.2.2 Error estimation of DVC

The principle presented in Chapter 4 and Chapter 5 is used to estimate the accuracy of DVC. For each test, a zoom image has been acquired. DVC between reference and zoom images is performed to analyze the errors of DVC routines. In this section, we will consider only the errors of two specimens: Plaster F3 and ConcreteP2. Indeed, imaging and correlation conditions for PlasterF1 are similar to PlasterF3, leading to similar errors.

The imposed magnification variation in the case of ConcreteP2 sample leads to a theoretical transformation gradient: $F_{\mathrm{xx}}-1 = F_{\mathrm{yy}}-1 = F_{\mathrm{zz}}-1 = -0.00484$. The best-fitting transformation gradient obtained by DVC on the whole sample is:

$$\mathbf{F}-\mathbf{1} = \begin{bmatrix} -0.004995 & 0.000145 & 0.000017 \\ -0.000144 & -0.005004 & 0.000031 \\ -0.000065 & 0.000054 & -0.004838 \end{bmatrix}$$

This demonstrates the good agreement with theoretical solution with a small error of maximum 1.64×10^{-4}. In the case of PlasterF3 specimen, the theoretical transformation gradient $F_{\mathrm{xx}} - 1 = F_{\mathrm{yy}} - 1 = F_{\mathrm{zz}} - 1 = -0.00454$. The best-fitting transformation gradient obtained by DVC on the whole sample is:

$$\mathbf{F}-\mathbf{1} = \begin{bmatrix} -0.004364 & 0.000104 & -0.000004 \\ -0.000108 & -0.004364 & -0.000138 \\ -0.000033 & 0.000023 & -0.004551 \end{bmatrix}$$

The maximal gradient transformation error of EPS plaster sample is about 1.76×10^{-4}. This value is similar to the error observed on the concrete sample. We compare also the systematic errors for both materials. The results are depicted in Fig. 8.1. The systematic error of EPS plaster is always bigger than EPS concrete (especially along Z−direction). Larger errors for plaster may be explained by its badder local contrast less suited to DVC interpolation routines.

The random errors are similarly evaluated for both samples; the obtained result are depicted in Fig. 8.2. Errors are similar for both samples along all three directions, with a standard deviation of about 0.05 voxel in most cases. This error increases to about 0.1 voxel for displacements with integer values. This feature is know for DVC procedures (see e.g. Amiot et al [15]). An

exception to this observation is the random error in plaster samples along the z direction, which seems to be somewhat smaller, for a reason that is not clear at this stage.

However, one can retain that the errors (random and systematic) on local displacement evaluated by DVC in our experimental conditions are of the order of 0.1 voxel or better. Error propagation relations (see Chapter 5) show that these local errors are consistent with the errors observed above for the overall transformation gradients.

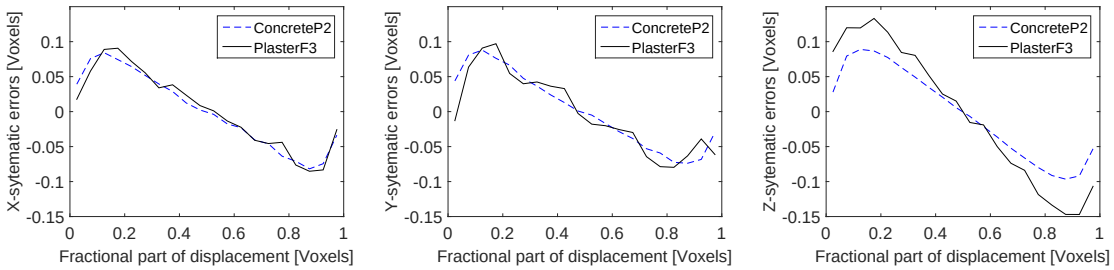

Figure 8.1: Comparison of DVC systematic errors for EPS concrete and EPS plaster specimen

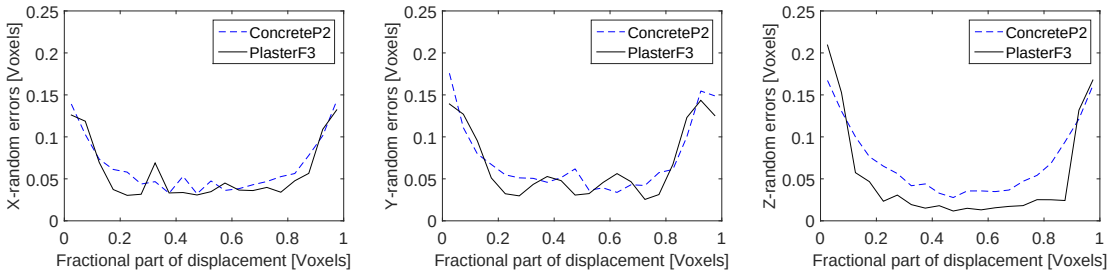

Figure 8.2: Comparison of DVC random errors for EPS concrete and EPS plaster specimen

8.3 Estimation of crack detection accuracy by using subtracted image

8.3.1 Main principle

In this work, the detection of tiny cracks is very important to observe the phenomenon of crack initiation. The objective of this section is to estimate the crack detection capability, i.e. the smallest crack opening that can be detected by our method.

The size of the crack directly influences its grey level in CT images. In the case of a large enough crack opening (greater than 1 voxel), the lowest grey level along a profile crossing the crack should be identical to the grey level of porosity. On the contrary, when crack size is null, its grey level will be identical to that of the solid phase (plaster matrix in case of EPS plaster, or cement paste/quartz sand in EPS concrete). Let D_g be the difference between the grey level of a crack and that of the solid phase, D_g^{max} be the difference between the grey level of the crack

and that of the porous phase, and e be the crack width. Assuming that the evolution of grey level is linear according to crack width (crack opening), we have the relation:

$$\begin{cases} \mathrm{D_g} = \mathrm{D_g^{max}} & \text{if e} \geq 1 \\ \mathrm{D_g} = e\mathrm{D_g^{max}} & \text{if e} < 1 \end{cases} \tag{8.1}$$

This phenomenon is illustrated in Fig. 8.3. This idea is based on the physical process at the origin of the grey level in X-Ray absorption CT images, which reflects the average attenuation coefficient of the matter present in the volume corresponding to a voxel.

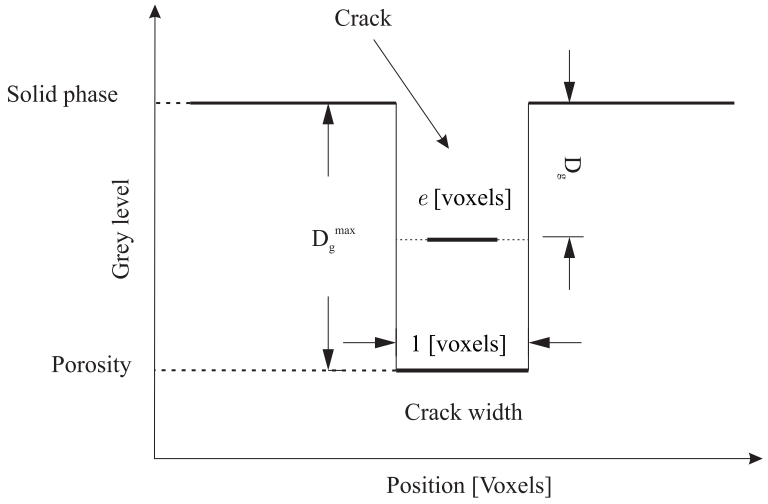

Figure 8.3: Influence of crack size on grey level

The variation of grey level $\mathrm{D_g}$ in CT images leads also to a similar variation of the grey level in the reference image. This evolution is obtained from the difference between the interpolated grey level of the deformed image and that of the solid phase in subtracted image, Because the grey level in an interpolated image is always less contrasted than that of a initial image, the profile across a crack in the subtracted image will be less sharp: The $\mathrm{J_g}$ be the maximal grey level drop in the subtracted image. We present an example for both definitions ($\mathrm{D_g}$ and $\mathrm{J_g}$) in the case of an EPS plaster sample. We consider the profile of grey levels on a line crossing a crack in the CT image (Fig. 8.4(a)) and in the corresponding subtracted image (Fig. 8.4(b)). The obtained results for $\mathrm{J_g}$ and $\mathrm{D_g}$ are depicted in Fig. 8.4(c).

Note that in perfect conditions with a large enough crack width (greater than 1 voxel), $\mathrm{J_g}$ is equal to $\mathrm{D_g}$. However, due to the interpolation processing during image subtraction, the obtained $\mathrm{J_g}$ can be found within the range:

$$\frac{\mathrm{D_g}}{2} \leq \mathrm{J_g} \leq \mathrm{D_g} \tag{8.2}$$

This phenomenon is clearly illustrated in the above example. From Fig. 8.4(c), with $\mathrm{D_g}$ being about 65, we obtain the singularity $\mathrm{J_g}$ of about 39 in the subtracted image. More generally, E.q. (8.2) results from an analysis if the image interpolation procedure. If the voxel close to the

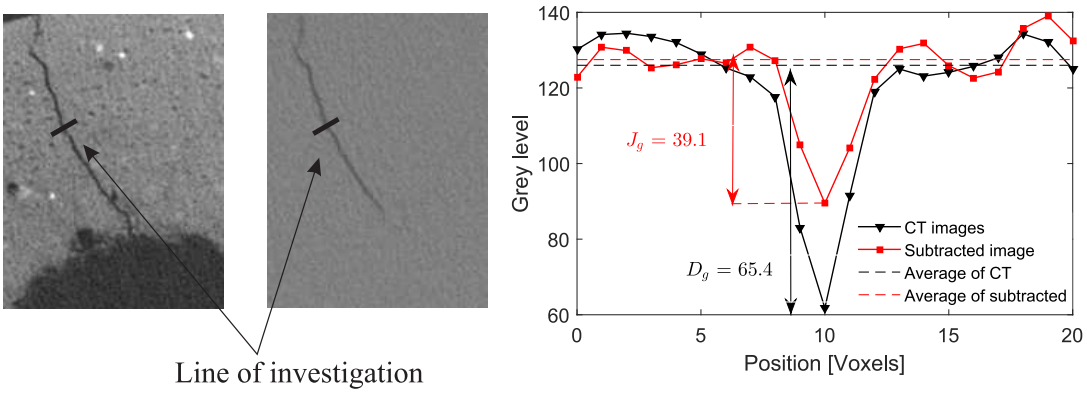

(a) (b) (c)

Figure 8.4: Definition of D_g and J_g : (a) CT image; (b) subtracted image; (c) grey level profile along a line crossing the crack

crack in the reference configuration is associated with an integer position in the deformed image, then no interpolation is required, and we have $J_g = D_g$. If it is associated with a half integer position, than its grey level will be the average between the crack grey level and the surrounding grey level.

Thus, the crack detection accuracy is linked to the ability to detect such a grey level drop J_g in the subtracted image. To easily detect a crack, J_g must be distinct from the noise of the subtracted image. In other words, the grey level drop corresponding to the crack must be greater than the standard deviation of the grey level of undamaged phase in the subtracted image (called STD):

$$J_g > \text{STD} \tag{8.3}$$

Note that, this noise STD here includes all sources of errors (DVC, CT images,...). From the expressions (8.1), (8.2), (8.3) we can define a detection range of minimal crack opening detection $e_{\min}$ by the following:

$$\frac{\text{STD}}{D_g^{\max}} \leq e_{\min} \leq \frac{2\text{STD}}{D_g^{\max}} \tag{8.4}$$

8.3.2 Application to EPS plaster

We firstly estimate noise in the subtracted image of EPS plaster (specimen PlasterF3). To do so, we consider the subtracted image in an undamaged region. A plane of deformed image and corresponding subtracted image are depicted in Fig. 8.5(a)(b). We plot in Fig. 8.5(c) the grey level profile of the subtracted image along a line of investigation. We recognize a periodic variation with period of about 2-3 voxels, that may be due to inconsistency between reference and deformed images (scanning, reconstruction effects and natural image noise)

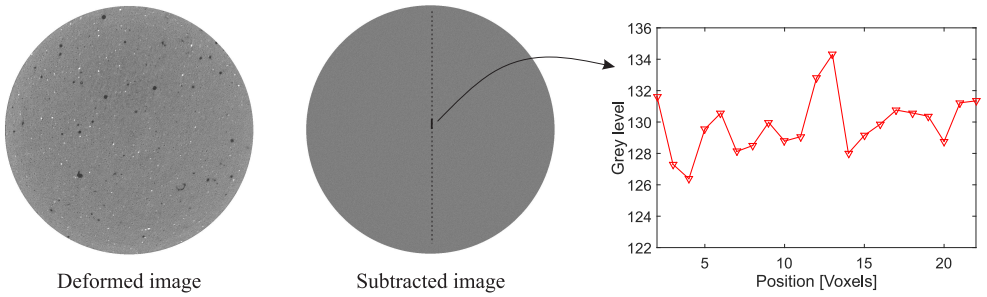

(a) (b) (c)

Figure 8.5: Non damaged region of EPS plaster: (a) CT images of deformed image; (b) corresponding subtracted image; (c) grey level profile along a line of investigation

Noise of the subtracted image is evaluated by computing the standard deviation on a subvolume. The average grey level of the plaster phase in the subtracted is measured to be 127.25 and STD is 3.821. Moreover, in this case, the difference between grey level of porosity and that of plaster matrix D_g^{max} is evaluated to 70. Using the expression (8.4), the minimal crack opening $e_{min}^{Plaster}$ that can be detected is in the range:

$$\frac{1}{20} \leq e_{min}^{Plaster} \leq \frac{1}{10} \tag{8.5}$$

To confirm our estimation, we consider a damaged region in an EPS plaster sample. Fig. 8.6 depicts a slice of subtracted and deformed images, which contain here a crack.

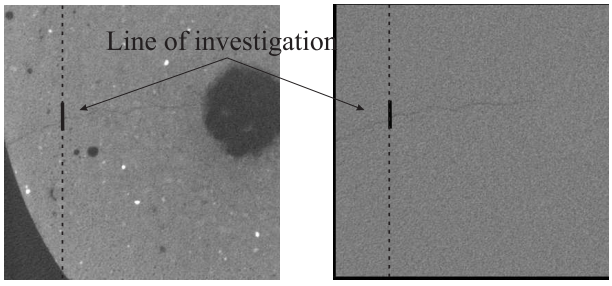

(a) (b)

Figure 8.6: Chosen plane of EPS plaster sample containing a crack : (a) deformed image; (b) subtracted image

The systematic error correction procedures (see Chapter 6) is applied to DVC displacements around the crack. We plot the positions of correlation points in the plane of observation in Fig. 8.7. Singular displacements are clearly measured in the damaged region. To locate the crack, we plot the displacements along a line of investigation in Fig. 8.8(a). We capture Y− and Z− displacement jumps around location 165 voxels. This result is in good agreement with the location of the observed grey level drop in the subtracted image Fig. 8.8(b).

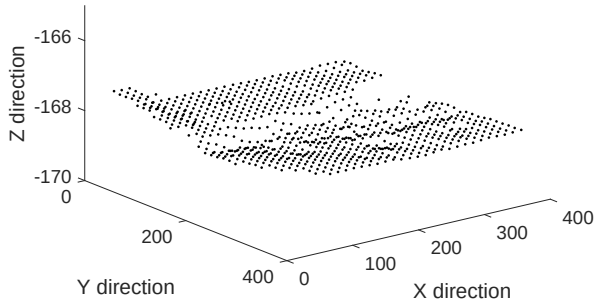

Figure 8.7: 3D view of correlation points on the plane of observation at deformed state

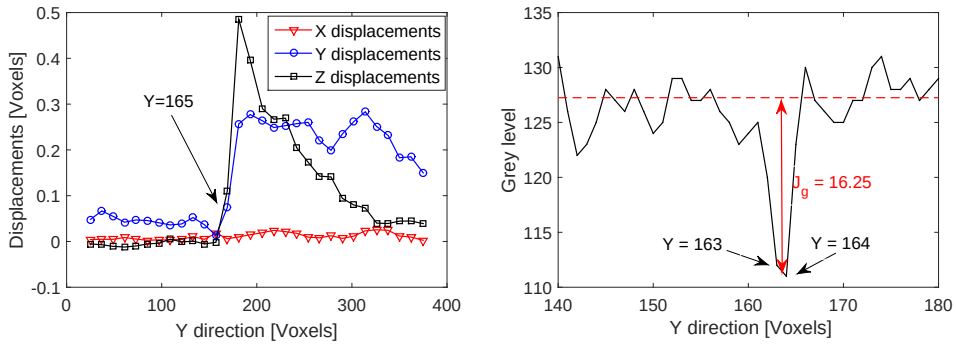

(a) (b)

Figure 8.8: Observation along a line of investigation crossing a crack: (a) displacements; (b) grey levels profile

We measured here a grey level drop J_g of about 16.25 in the subtracted image, so that the crack opening can be estimated to be in the range:

$$0.232[\text{voxels}] = \frac{J_g}{D_g^{\max}} \leq e \leq \frac{2J_g}{D_g^{\max}} = 0.464[\text{voxels}] \tag{8.6}$$

This is in good agreement with the displacement jump (crack opening) measured in Fig. 8.8(a), where $[\![u_y]\!] = 0.28$ voxels and $[\![u_z]\!] = 0.49$ voxels. Note that the displacement jump can have a normal and an in-plane component, but crack opening reflects only normal component, which is here close to $[\![u_y]\!]$ (the crack is almost normal to the Y− direction of the image).

8.3.3 Application to EPS concrete

The noise of the subtracted image of EPS concrete is estimated using the sample principle than for EPS plaster in subsection 8.3.2. We consider an undamaged region depicted in Fig. 8.9. We also observe a periodic variation with a period of about 2-3 voxels in Fig. 8.9(c) (because of the inconsistency of local fluctuations induced by image reconstruction between reference and deformed images and of natural image noise).

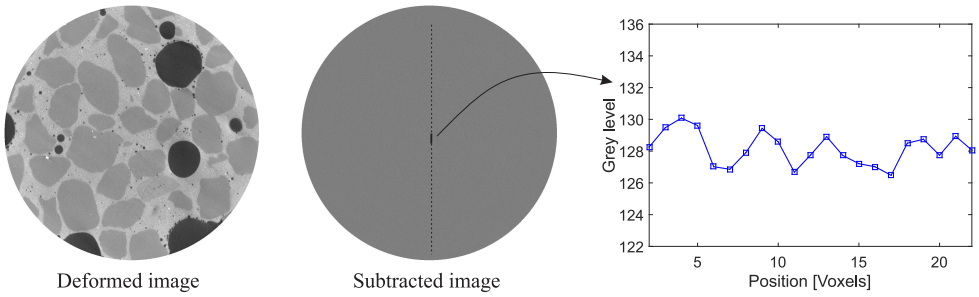

(a) (b) (c)

Figure 8.9: Non damaged region of EPS concrete: (a) CT images of deformed image; (b) corresponded image subtraction; (c) grey levels profile along a line of investigation

We obtain in this case an average grey level for the solid phase of 126.8, with STD estimated to 2.532. This value is lower than that of EPS plaster, which confirms again the better local contrast for EPS concrete. D_g^{max} is evaluated to 102 between quartz sand and porosity, and to 130 between cement paste and porosity. Thus, the minimal crack opening that can be detected is then estimated to be in the range:

$$\frac{1}{40} \leq e_{\text{min}}^{\text{quartz sand}} \leq \frac{1}{20}$$

and

$$\frac{1}{50} \leq e_{\text{min}}^{\text{cement paste}} \leq \frac{1}{25}$$

We present a crack detected using subtracted image in Fig. 8.10(a). The grey level profile along a line crossing the crack is plotted in Fig. 8.10(b). We observe that: (1) the grey level drop for the crack in concrete is greater than that for the crack in EPS plaster; (2) the fluctuations of grey levels around the crack are smaller. Hence, we conclude that the crack of EPS concrete is better defined than that of EPS plaster for similar opening. Results for both samples are compared in Table 8.3. It is noted that the smallest crack opening that can be detected is comparable to the accuracy of the DVC measurements. An alternative method to detect cracks could have been based on a detailed analysis of the discontinuities of the displacement field. measured by DVC. It would however have been much more complex to implement, and will be left for further investigations.

Material	STD	e_{limit} [Voxels]
EPS plaster	3.821	1/10
EPS concrete	2.532	1/20

Table 8.3: Noise estimation of subtracted image, and smallest crack size e_{limit} that can be detected in the worst situation

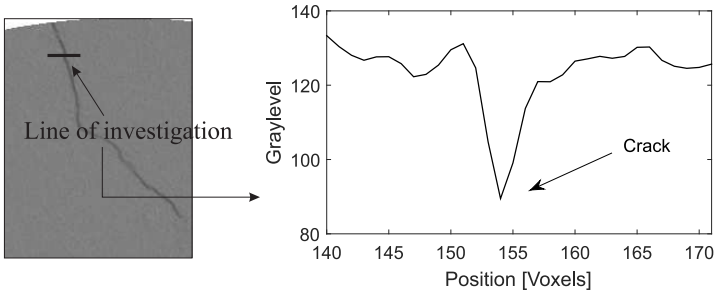

(a) (b)

Figure 8.10: Grey level profile along a line crossing a crack: (a) definition of line of investigation; (b) grey level profile

8.4 Determination of fracture parameters by inverse analysis

8.4.1 Overview

In this section we present the basic principles of the inverse identification procedure used to determine the numerical values of some parameters of the constitutive relation of a material, namely in our case the fracture toughness and the regularization parameter. The values obtained in chapter 7 are relative the a similar plaster, prepared from the same powder but with a different elaboration protocol, so that fracture parameters in our samples might be different from those measured by Romani et al [180]. If these parameters are unknown, the idea is to run several numerical simulations and to modify these parameters at each iteration until an objective function, e.g. a distance measured between a given experimental response and the numerical simulation, reaches an acceptable tolerance. This problem can be highly nonlinear and involve non unique solutions. For this purpose, several minimization algorithms available in the literature may be used, see e.g. [2] and [3]. The main issue in the present work is that the numerical simulations run at each iteration involve very large models with several millions of elements. To limit the number of FE problems to be solved with the phase field method, we have chosen the Newton-Raphson method for solving the nonlinear problem associated with the cost function minimization when identifying the parameters, due to its efficiency. The drawback is that a good initial estimation must be made for the parameters to be identified, e.g. by using values of similar parameters found in the literature or of preliminary studies, e.g. the 2D analysis performed on a similar material in chapter 7.

Let $(x_1, x_2, ..., x_N)$ be the input parameters and $f(x_1, x_2, ..., x_N)$ a given cost function, to be minimized with respect to these parameters (see Fig. 8.11). In the following, we present the algorithm for solving such a problem, when the output function $f(x_0, x_1, ..., x_N)$ is derived from the numerical result of a FEM solver.

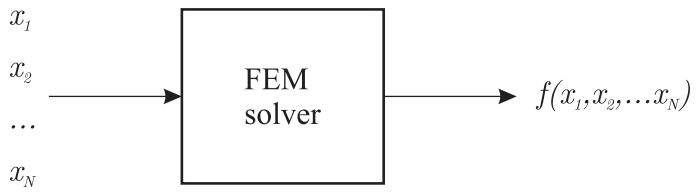

Figure 8.11: Description of inverse problem to identify material parameters

8.4.2 Identification of fracture parameters g_c and l from in-situ compression test

We recall that the elastic parameters of the matrix phase (plaster) have been measured experimentally with compression tests (see section 4.5). To perform the numerical simulation of the lightweight plaster compression, the material parameters g_c (toughness) and l (regularization length) need to be specified. In this section, we use an inverse approach based on a Newton-Raphson algorithm (see Appendix A.5) to identify these two material parameters from the experimental data of specimen PlasterF3. For the sake of simplicity, the identification is restricted to a comparison between experimental and simulated global stress-strain curve. More elaborated procedures taking also into account local measurements available from the experiments, in the line of e.g. Heripre et al [88], are left for further investigations. We can note from Fig. 8.12 that the experimental curve is discontinuous, because of the experimental conditions described in Chapter 4. To obtain a continuous curve and construct an error function, the experimental curve is replaced by a cubic polynomial fit.

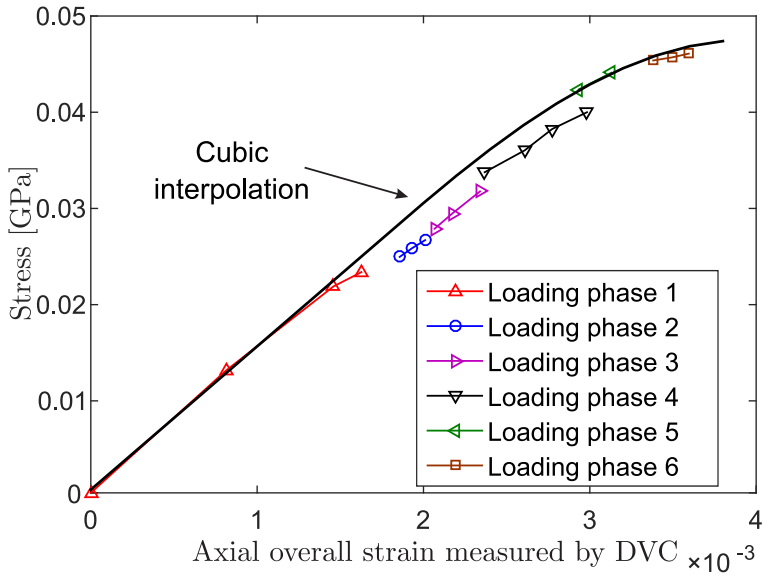

Figure 8.12: Experimental load - strain curve for the compression of the lightweight plaster sample PlasterF3 and cubic polynomial fit.

The details of the numerical model used for the simulation are described in Chapter 6 and

section 8.6. The numerical finite element model used during each iteration of the inverse procedure involves 4 million elements. The elastic material parameters are taken from Chapter 4: $E = 13.6$ GPa, $\nu = 0.2$. Monotonic compressive displacement increments of $\mathrm{U} = -3 \times 10^{-4}$ mm are prescribed for 240 increments. We initialize the values of g_c and l from the experimental values identified in [179]: $g_c^0 = 1.4$ N/m and $l^0 = 0.1$ mm.

The cost function is here defined as:

$$f(g_c^k, l^k) = \sum_i^N \mid \sigma_{\varepsilon_i}^{\exp} - \sigma_{\varepsilon_i}^{\mathrm{num}}(g_c^k, l^k) \mid, \tag{8.7}$$

where N is the number of loading increments ($N = 240$), $\sigma_{\varepsilon_i}^{\exp}$ is the the cubic fit of the experimental stress, $\sigma_{\varepsilon_i}^{\mathrm{num}}$ is the numerical stress obtained for given fracture toughness g_c^k and length scan l^k at iterations k. Both stresses are taken at the same strain value ε_i, which is here defined as the overall strain at the i^{th} increment of the numerical simulation. This definition can be illustrated in Fig. 8.13

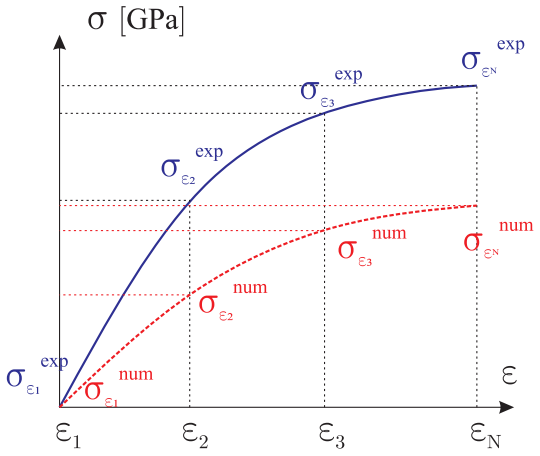

Figure 8.13: Definition of $\sigma_{\varepsilon_i}^{\exp}$ and $\sigma_{\varepsilon_i}^{\mathrm{num}}$ to compute cost function

Note that at each iteration of the procedure, the whole loading of the sample is simulated to obtain the whole curve. Each iteration takes about 52 h on a 40 processors workstation running at 2.7 - 3.2 GHz on our Matlab code.

The evolution of the residual is depicted in Fig. 8.14, where the convergence can be observed. The procedure stops after 8 iterations, for a tolerance $f(g_c^k, l^k) = 0.05$ GPa (or 50 MPa), which corresponds to a distance of about $50/240 \approx 0.2$ MPa for each incremental step in the stress-strain curve. Recall that as the numerical derivatives and second-order derivatives of the residual are obtained by perturbation (see Appendix A.5), each iteration involves in total five 3D phase field computations (but independent) for the whole loading. The total procedure took 416 h to be achieved. For this error criterion, we obtained the values $g_c \approx 1.80$ N/m and $l \approx 0.0250$ mm. The evolution of the parameters with the iterations of the inverse analysis is depicted in Fig. 8.15. We note that our material compared with one in the work of Romani [179] is dryer (drying time

is much longer), which indues that its strength is larger. This explains that the obtained g_c (1.8 N/m) is larger than the one measured in the previous study of Romani et al [180] of about (1.4 N/m). The increased strength may also induce a larger critical stress σ_c, which is associated with a smaller internal length l, according to the analysis presented in Chapter 2. Indeed l was found to be 0.1 in [179] and is now identified to be four times smaller.

The same inverse procedure has been applied to sample PlasterF1, for which we obtain $g_c = 1.76$ N/m and $l = 0.0254$ mm. These value are very close to those obtained with sample PlasterF3, which provides some credit to our identification methodology. We have used $l = 0.025$ mm and $g_c = 1.8$ N/m to perform the simulations.

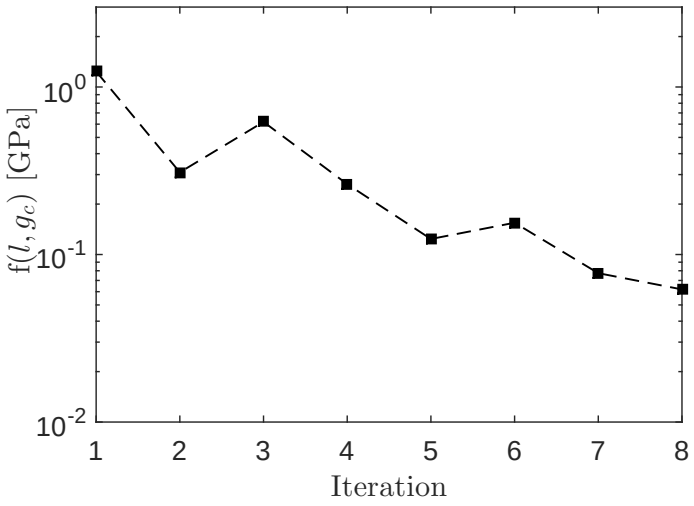

Figure 8.14: Residual error $f(l, g_c)$ for the inverse problem validation test, with respect to the iteration number

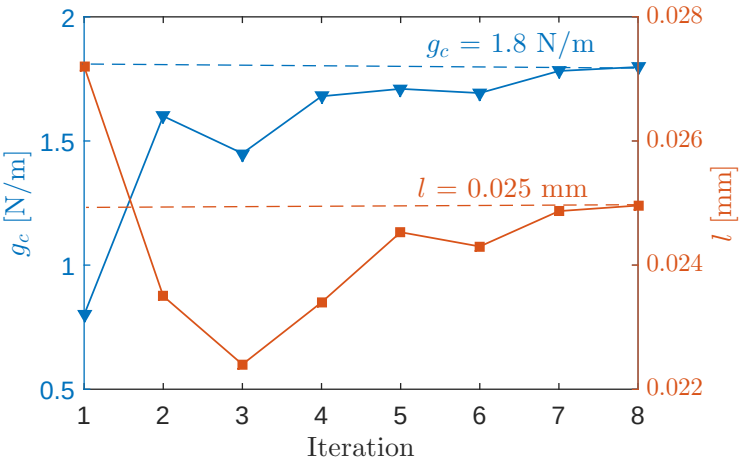

Figure 8.15: Evolution of the parameters l and g_c during the inverse identification

8.5 Microcracking in lightweight plaster sample containing two EPS beads

In this section, we directly compare the cracks network produced in a lightweight plaster sample in compression and detected in microtomography images during an in-situ test with a direct numerical simulation using the phase field method. Two types of comparisons will be investigated. In the first one, the whole sample is considered, where only beads are considered as heterogeneities, the small pores being ignored. In the second one, a sub-volume will be used in the sample to consider a higher level of detail in the microstructure, including micro-pores.

8.5.1 Comparison at the level of the sample

8.5.1.1 Experimental results and construction of the initial numerical model

Details about the specimen plasterF3 and its preparation have been presented in Chapter 4 and section 8.2.1. During the experimental in-situ test, we have prescribed and processed 19 successive compression loading steps. In Fig. 8.16, the experimental force/strain curve is depicted, where 6 loading phases can be distinguished.

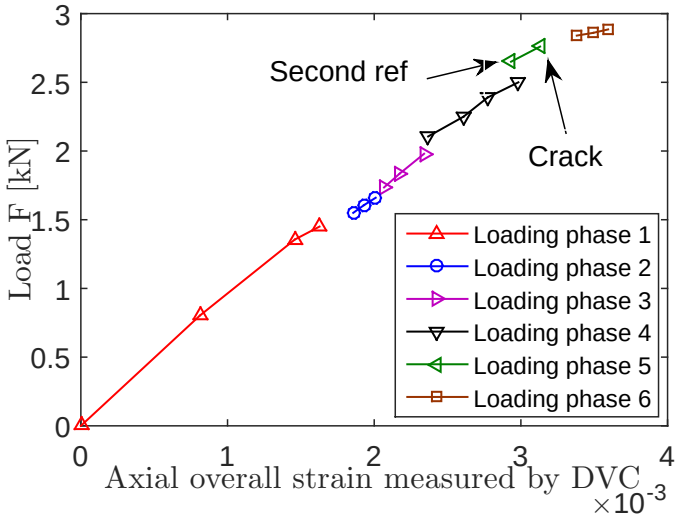

Figure 8.16: Experimental load-strain response curve for the lightweight plaster sample PlasterF3, divided in 6 loading phases.

We recall that, at step 14, the sample has been taken out of in-situ machine, and has been installed again. Another reference image at zero force has been acquired before loading steps 15-19. The first visible cracks appear at step 16 for a force $F = 2.76$ kN (see Chapter 4).

Details about the construction of the initial geometrical model have been provided in Chapter 6. In this test, we only take into account the beads, not the micro porosity and small pores. The obtained geometry for the considered test is depicted in Fig. 8.17. The mesh is com-

posed of unstructured tetrahedral elements, with minimal and maximal sizes $h_{min} = 0.0125$ mm, $h_{max} = 0.35$ mm and contains about 12 millions elements.

Following the experimental procedure described in Chapter 4, two polished PMMA plates were used to remove spurious crack initiation from the top and bottom faces of the sample. In the simulation, uni-axial compression is prescribed (see Fig. 8.17): on the lower surface, the z-displacements are blocked, while on the upper surface, the z-displacements are prescribed. The x and y-displacements are free on these two surfaces.

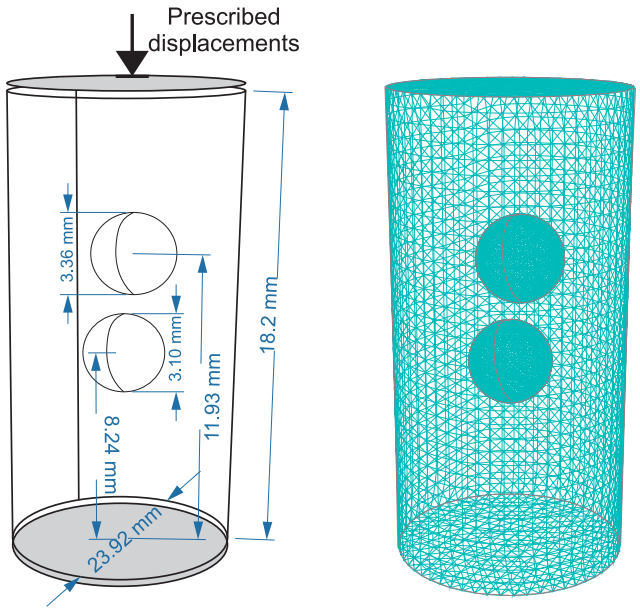

(a) (b)

Figure 8.17: Ideal model used as input of numerical simulation of PlasterF3 sample: (a) geometry and boundary conditions; (b) detailed view of the mesh.

The material parameters, the toughness g_c and regularization parameter l have been determined by the inverse identification procedure described in section 8.4 leading to: $g_c = 1.8$ N/m, and $l = 0.025$ mm. The elastic parameters have been given in Chapter 4 for the plaster material: $E = 13.6$ GPa, $\nu = 0.2$. In the simulation, monotonic compressive displacement increments $\overline{U} = -5 \times 10^{-4}$ mm have been prescribed as long as $d_{max} < 0.9$, then decreased to $\overline{U} = -5 \times 10^{-5}$ mm.

8.5.1.2 Results and discussion

The extraction of very tiny crack is not straightforward, especially in the early stage of crack initiation. Moreover, the subtracted images do not include the microstructure of sample. So, if we cannot extract the cracks, we will not see the influence of microtructure on crack trajectory. To avoid this problem, we propose to consider the “transformed image", obtained by back-convecting the deformed image in the same frame as the reference image according to the

estimated local transformation. The construction of this transformed image is exactly the same as for the subtracted image, but without the subtraction step.This transformed image can be used almost as the subtracted image for the crack detection and the analysis of their evolution, by a comparison of the transformed images at various loading stages. Since the grey level is almost uniform in the plaster matrix, subtraction is less usefull than for concrete. In addition, porosities (including EPS beads and micropores) are visible, so that crack propagation can be related to microstructure. Such an analysis of the crack network evolution would be much more difficult in the deformed (not backconvected) images, because of the change of point of view.

The transformed image was used here for comparison with numerical simulation. The three-dimensional crack paths is observed in the experiment and predicted by the computation are compared at the last step of the loading (F=2.885 kN), and observed in two regions near the two EPS beads, called "Bead 1" and "Bead 2" (see Fig. 8.18(a)).

First, we compare the trace of the 3D crack network in a plane located at the height $H = 7.28$ mm from the bottom of the specimen, and cutting Bead 1. We observe in the experiment, a crack initiating from the bead and propagating towards the external boundary, as shown in Fig. 8.18(b). The same crack morphology is clearly observed in the numerical simulation, as shown in Fig. 8.18(c). We remind here that in the numerical simulation, we start from an unnotched specimen and did not make any assumption on where the cracks initiate and propagate. To make a quantitative comparison, we have compared the angle between the crack and the X axis of the image in the plane of observation defined in Fig. 8.18(b) and (c) for both the experiment and the numerical simulation. The obtained values are 26.11° for the experiment, and 23.41° for the numerical simulation, showing a very good agreement between the experiment and the simulation. However, the location of crack initiation for both observation is slightly different: in the numerical simulation the crack follows the closest path from bead to boundary of the sample. In the experiment, it is slightly shifted. The reason for that is probably that the real patched was deviated by the presence of some micropores, which can be seen in Fig. 8.18(b), which are not reproduced in the simplified ideal geometry of the numerical model.

Secondly, we compare the trace of the 3D crack network in a plane located at the height $H = 9.73$ mm from the bottom of the specimen, and located between the two beads (see Fig. 8.19(a)). The experimental crack path is compared to the simulated one Figs. 8.19(b) and 8.19(c), showing that the numerical simulation is able to capture the morphology of the crack in a satisfactory way in this complex configuration, even though some differences are noticed. Note that in this case, we did not take into account the small pores in the numerical simulation.

A similar comparison has been performed in a plane located at a height $H = 10.53$ mm (see Fig. 8.20(a)), which crosses the second bead. Here again, the morphology of the crack network is correctly captured. Several geometrical features are quantitatively compared in Figs. 8.20(b) and 8.20(c) and a rather good similarity is observed, in terms of both length and orientation of the cracks.

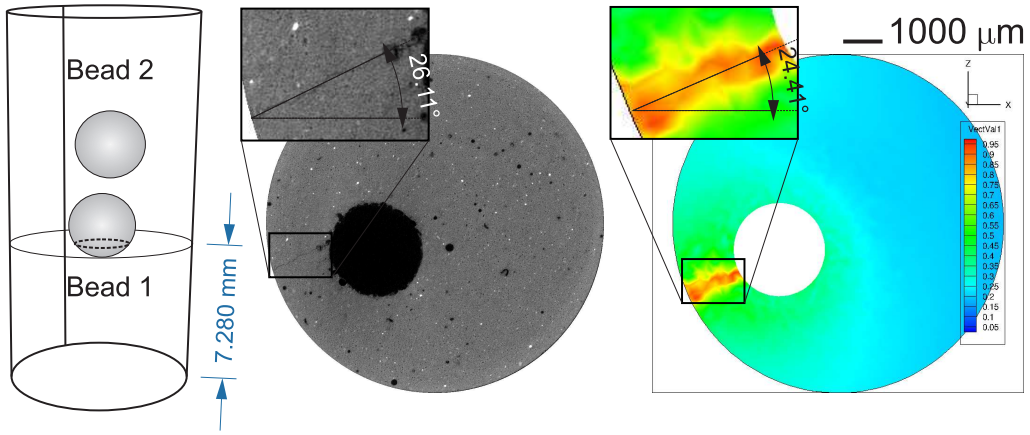

(a) (b) (c)

Figure 8.18: Crack path comparison in a region bellow Bead 1: (a) position; (b) experimental result; (c) simulation result.

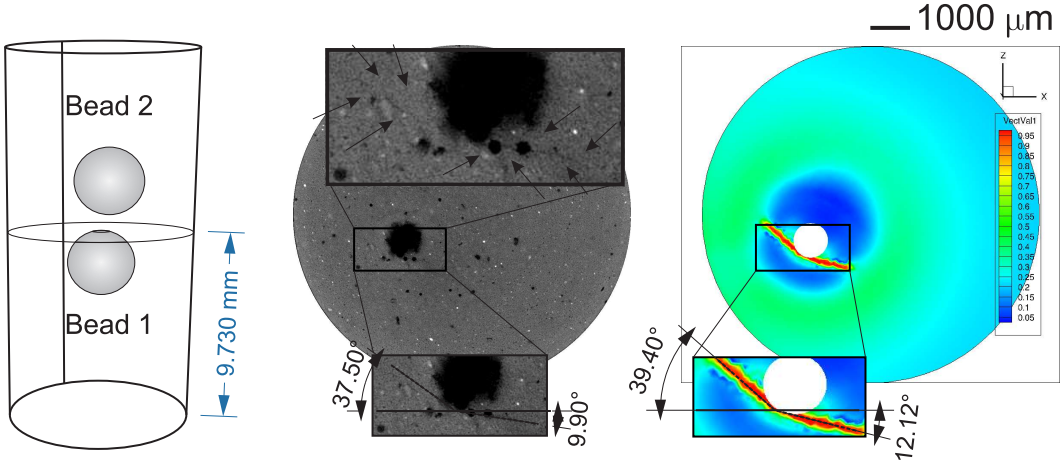

(a) (b) (c)

Figure 8.19: Crack path comparison in a region above Bead 1: (a) position; (b) experimental result; (c) simulation result.

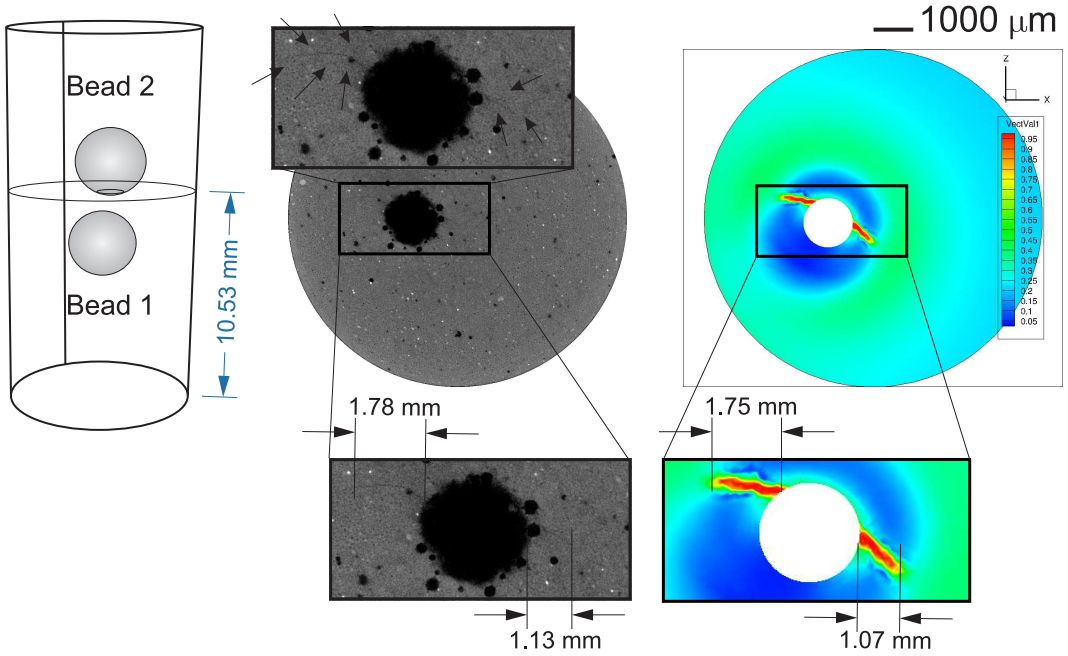

Figure 8.20: Crack path comparison in a bellow region of Bead 2: (a) position; (b) experimental result; (c) simulation result.

The last plane of investigation is located at the height $H = 13.70$ mm (see Fig. 8.21(a)), on a plane cutting the top of Bead 2. This zone is interesting because in compression, we can observe three crack surfaces roughly developing with an angle of 120° from a point located on the top of the spherical void (bead), as shown in Fig. 8.21(b). Remarkably, the simulation captures the same morphology of the crack network, see Fig. 8.21(c), without any assumption on the location of the initiation of the cracks neither on their orientation.

These results, showing a direct comparison between the formation of a 3D complex crack network in an experiment and in a numerical simulation, are to our knowledge the first of their kind and prove the high level of predictability of the phase field method to simulate complex crack propagation in complex heterogeneous materials. We emphasize also on the fact that these computations rely on simple isotropic elastic and fracture models, depending on a very limited number of parameters (4), which can easily be identified on standard tests (even though, in the present case, the fracture parameters were adjusted to fit the overall response of the sample).

In addition, these results show also that crack propagation, even in brittle materials for which often some unpredictable randomness is assumed, is essentially deterministic and can be assessed as soon as the main sources of the cracking phenomenon is taken into account in the numerical model. In the present case, the main source seems to be the heterogeneity of the elastic stress and strain field induced by the particular geometry of the large beads within the sample. The additional randomness induced by smaller pores seems to have only a second order influence. This will be confirmed in next section.

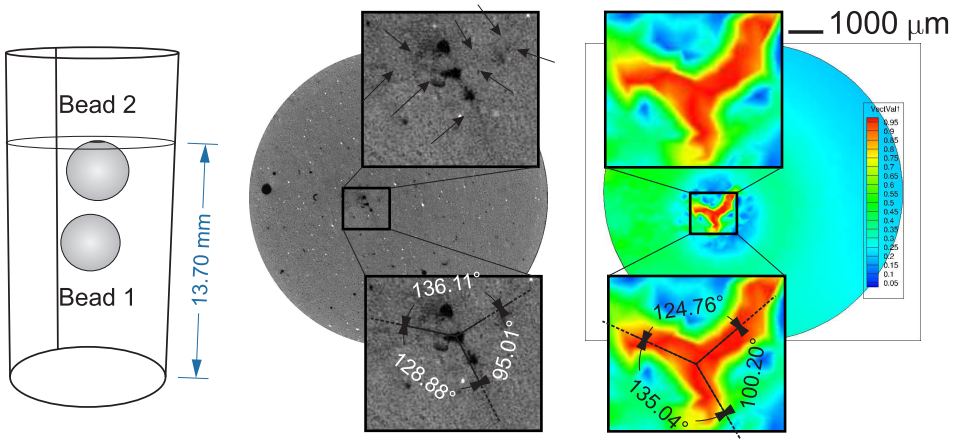

(a) (b) (c)

Figure 8.21: Crack path comparison in a plane just above Bead 2: (a) position; (b) experimental result; (c) simulation result.

8.5.2 Local comparisons of microcracking in the plaster specimen

In this section, we compare the microcracking propagation in the sample at a smaller scale, taking into account much finer details in the microstructure like pores which have a diameter much smaller than the EPS beads. As mentioned previously, meshing the whole sample from the microtomography image with small-scale microstructural details is not tractable for nowadays simulation capabilities. Therefore, we use the technique of sub-volume simulation described in Chapter 6: we model only a sub-volume encompassing some detail of interest in the sample, and prescribe experimental kinematic boundary conditions at the border of this sub-volume.

8.5.2.1 Definition of the numerical model

A sub-volume of dimensions $350 \times 350 \times 30$ voxel^3 (or $2.8 \times 2.8 \times 0.24$ mm^3) is taken below the Bead 2 (see Fig. 8.22). To ensure the detection of very tiny crack, we keep the resolution of the initial image for the input geometry for the simulation (i.e. a voxel is transferred into an 8-node elements). All elements in pores are removed in order to reduce the computational costs.

Boundary conditions obtained from DVC data are prescribed all around the boundary of the sub-volume for the simulation, as described in Chapter 6. However, we noted that some local spurious singularities can be generated over the boundary due to some noise in the DVC data, leading to unphysical damage located near the boundary (see an illustration in Fig. 8.23). A first attempt to correct this issue was to run a median filter over the data obtained from DVC. However, as shown in Fig. 8.24, the obtained results were not satisfactory, showing completely different crack paths between simulation and experiment. This issue might come from the filtering process, which excessively smooths out the displacement discontinuities on the boundary of the sub-volume, which do actually exist when the crack crosses the boundary of the sample in the experiment.

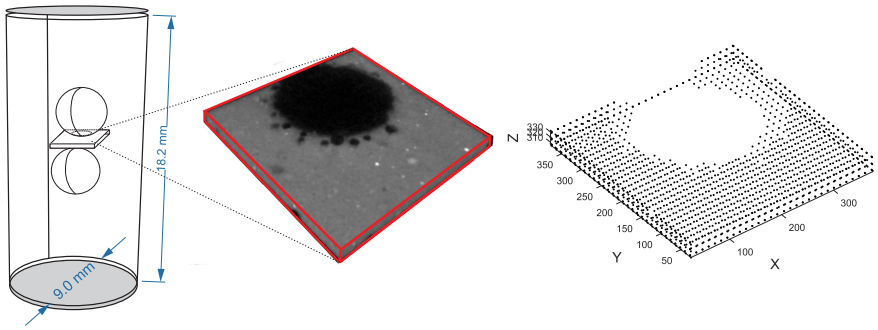

(a) (b) (c)

Figure 8.22: Sub-volume considered for comparisons of microcracking propagation in the lightweight plaster sample: (a) location in the sample; (b) associated CT image; (c) 3D correlation points on the surface used to define the boundary conditions.

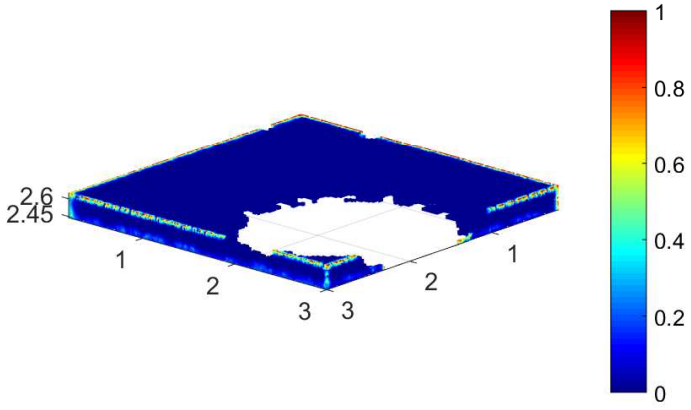

Figure 8.23: Spurious damage on the boundary of the domain used for the simulation due to noise in the DVC data obtained from the experiments.

To face this issue, we have tested another solution which consisted in removing the bad correlation points by using the same procedure as described in Chapter 4. After this treatment, some singularities still remain, but in limited number and have been removed manually. We show the location of the 3D correlation points on the surface of the sub-volume used to define the boundary conditions in Fig. 8.22(c). Then, by using the interpolation procedures (from local transformation $\mathbf{\Phi}_N$) introduced in Chapter 6, we compute the prescribed displacements for each node of the mesh belonging to the boundary of the sub-volume.

8.5.2.2 Comparisons of crack growth within the sub-volume in the lightweight plaster specimen

We compare the evolution of microcracks in the sub-volume for the three loading steps 15, 17 and 19. Results for step 15 (load $F = 2.65$ kN) are depicted in Fig. 8.25. The black and red

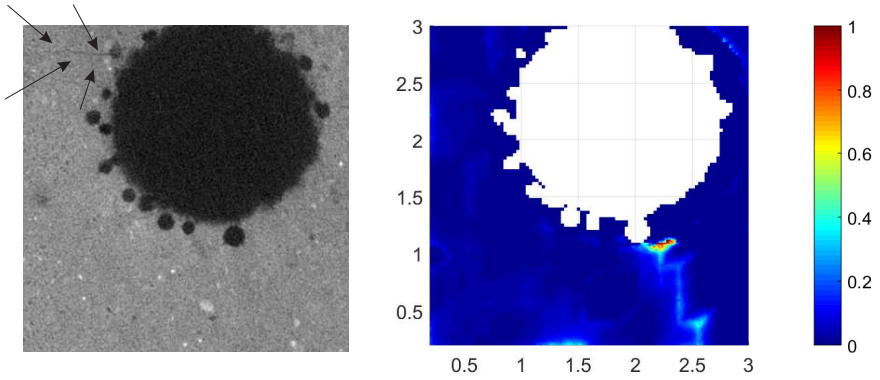

(a) (b)

Figure 8.24: Differences in crack morphology observed when smooth filtered DVC data are prescribed to the boundary of the sub-volume: (a) cracks detected from experiment; (b) crack obtained by numerical simulation.

colors refer to existing pores and generated cracks, respectively. We note that the crack on the right side of the EPS bead is well captured for both experiment and simulation, but the crack on the left is not observed in the experiment. This might be due to the image treatment which does not allow detecting very short cracks in the early stage of initiation.

However, for steps 17 and 19, we can detect the left crack also in the experiment, confirming this assumption, as seen in Figs. 8.26 and 8.27. A good agreement is obtained between the experiment and simulation.

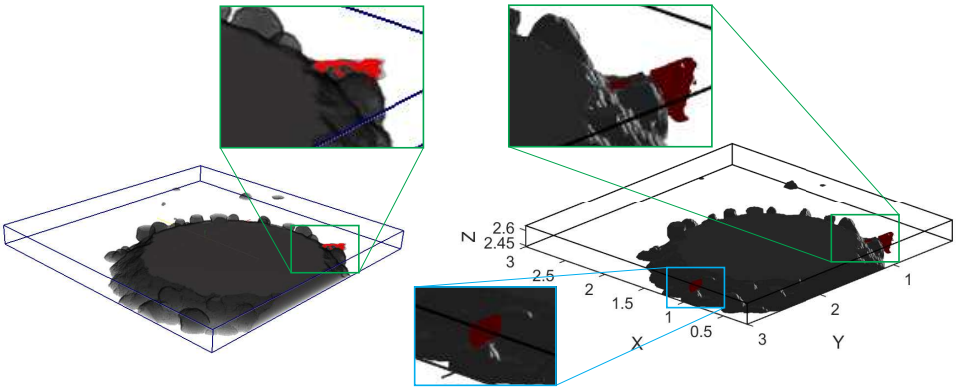

(a) (b)

Figure 8.25: 3D crack path in the sub-volume of lightweight plaster for loading step 15: (a) crack extracted from experiment; (b) numerical simulation.

In order to perform quantitative comparisons, we have chosen a plane (see Fig. 8.28) passing through the sub-volume and have compared the length of one crack for several loadings. Results are compared in Fig. 8.29. We observe remarkably similar crack lengths for all three loading steps. One should again keep in mind that in the simulation there is no a priori assumption

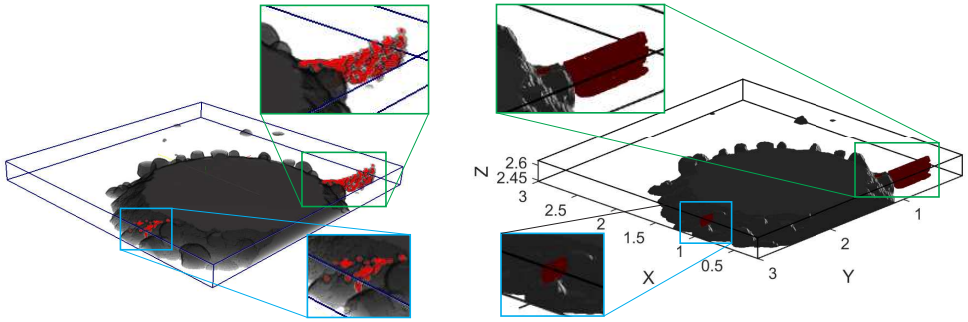

(a) (b)

Figure 8.26: 3D crack path in the sub-volume of lightweight plaster for loading step 17: (a) crack extracted from experiment; (b) numerical simulation.

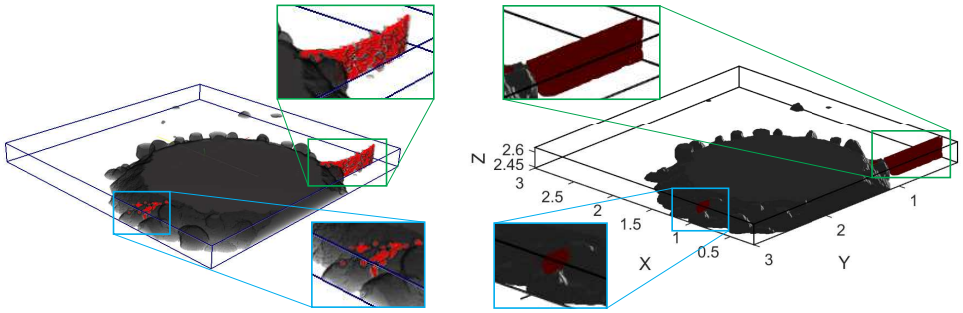

(a) (b)

Figure 8.27: 3D crack path in the sub-volume of lightweight plaster for loading step 19: (a) crack extracted from experiment; (b) numerical simulation.

about the initiation location and path of the crack and that all material parameters have been identified by an inverse approach.

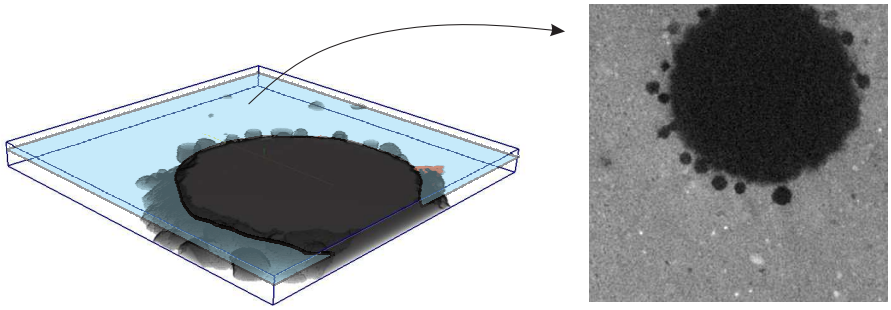

(a) (b)

Figure 8.28: Definition of plane of investigation: (a) location in sub-volume; (b) CT images of loading step 17

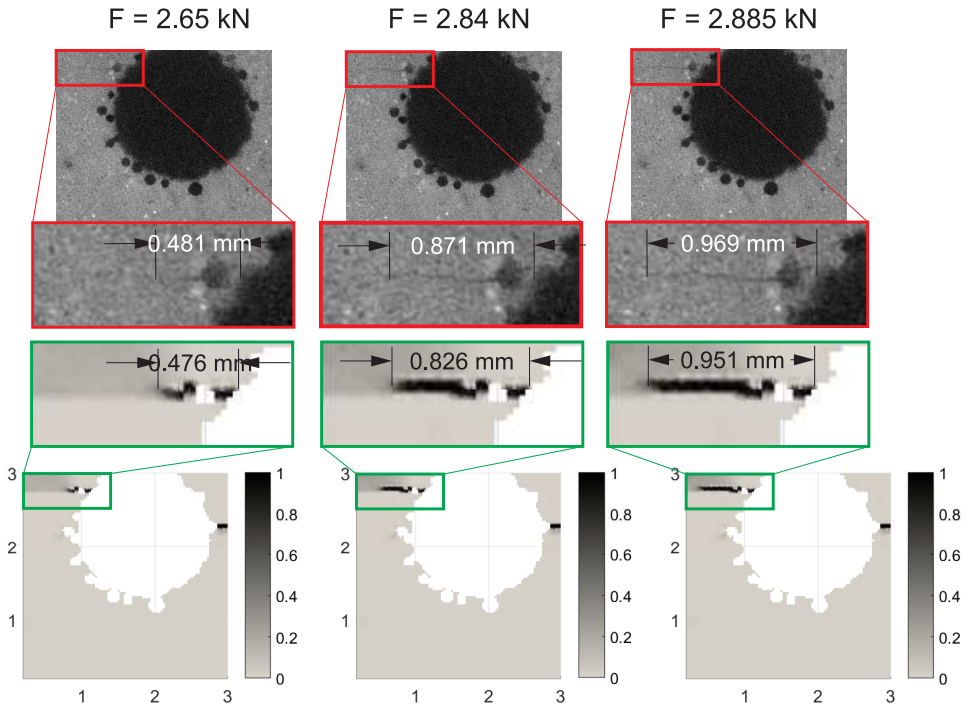

Figure 8.29: Comparison between experiment and simulation in terms of crack length for several loading steps, for a particular crack inside the sub-volume of the lightweight plaster sample.

8.6 Microcracking in lightweight plaster sample containing multiple pores

In this section, we present comparisons of 3D crack propagation between experiments and simulations for a sample containing multiple pores. These pores consists in 2 EPS beads, a large bubble of air, and several smaller bubbles of air, as depicted in Fig. 8.31.

8.6.1 Experimental results and construction of the initial numerical model

In this case, we have prescribed 14 loading steps, where 12 steps are associated with crack propagation. The experimental load-deformation curve is plotted in Fig. 8.30. Each color corresponds to a loading phases. Note that in this test 3 loading phases have been prescribed.

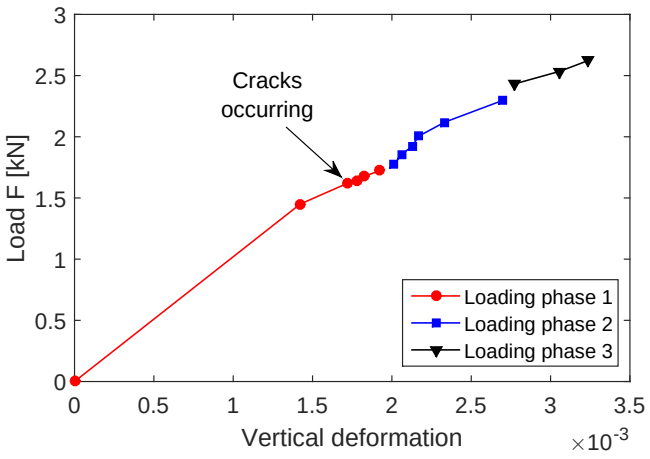

Figure 8.30: Experimental compression response of the lighweight plaster specimen containing several pores (specimen PlasterF1).

The first crack has been detected at $F = 1.62$ kN, while for the previous sample (PlasterF3), the first cracks initiated at $F = 2.76$ kN. This can be easily understood from the larger porosity of the second specimen. Furthermore, the large pores and beads are located near the boundary, inducing weaker zones. Here, small pores with diameters larger than 40 voxels are kept in the numerical model of the whole sample. An unstructured and adaptive mesh of 11 million tetrahedra has been constructed, with minimum and maximum element sizes $\mathrm{h_{min}} = 0.0125$ mm and $\mathrm{h_{max}} = 0.35$ mm. The detailed geometry, mesh and boundary conditions are depicted in Fig. 8.31. The material parameters are the same as in the previous example. Monotonic compressive loading steps $\overline{U} = -3 \times 10^{-4}$ mm are prescribed as long as $d_{\max} < 0.9$ and then set to $\overline{U} = -3 \times 10^{-5}$ mm.

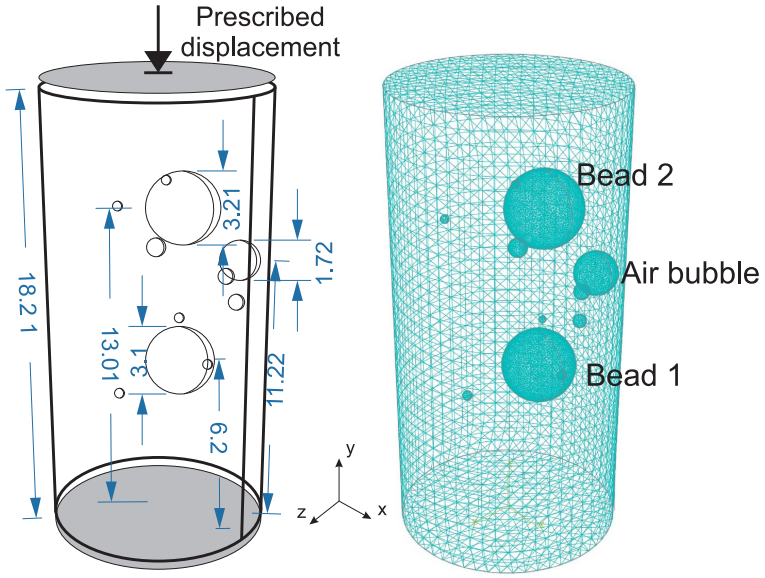

(a) (b)

Figure 8.31: (a) Geometry of the numerical model used for the simulation for the sample PlasterF1 containing several pores (units are in mm); (b) corresponding mesh.

8.6.2 Results and discussion

The subtracted and transformed experimental images have been used for comparisons with the predictions of the simulations performed with the phase field method on the initial model described above. Details of the procedure to construct the model from images have been provided in section 8.2.1.

First, a plane parallel to the section of the sample located above Bead 2 has been chosen, as depicted in Fig. 8.32(a). The plane cuts the EPS bead together with two small pores. The evolution of the 3D crack network is compared between experiment and simulation for steps 3, 6 and 10 in Fig. 8.32(b),(c)and (d).

Experiment and simulation results agree qualitatively well, as confirmed by the zoom image provided in Fig. 8.33. Nevertheless, we observe here a difference in the crack length, that will be explained below by considering the longitudinal plane.

Next, the crack network is studied in a vertical plane for loading steps 3, 6 and 10. Results of the simulation are provided in Fig. 8.34(a), (b), (c). We can observe mainly two vertical cracks initiating from Bead 2. Experimental results are provided in Figs. 8.34 (d), (e), (f), showing that we observe a similar cracking pattern in this more complex example. However, the crack length is here not validated: : its propagation is much shorter in the simulation than in reality. A possible explanation might be linked to the ideal Dirichlet boundary conditions which might not reflect the actual ones in the experiment. Indeed, vertical displacements are prescribed uniformly on the upper an lower ends of the sample. A crack propagating towards these ends will thus not be allowed to develop a displacement discontinuity with a vertical component when

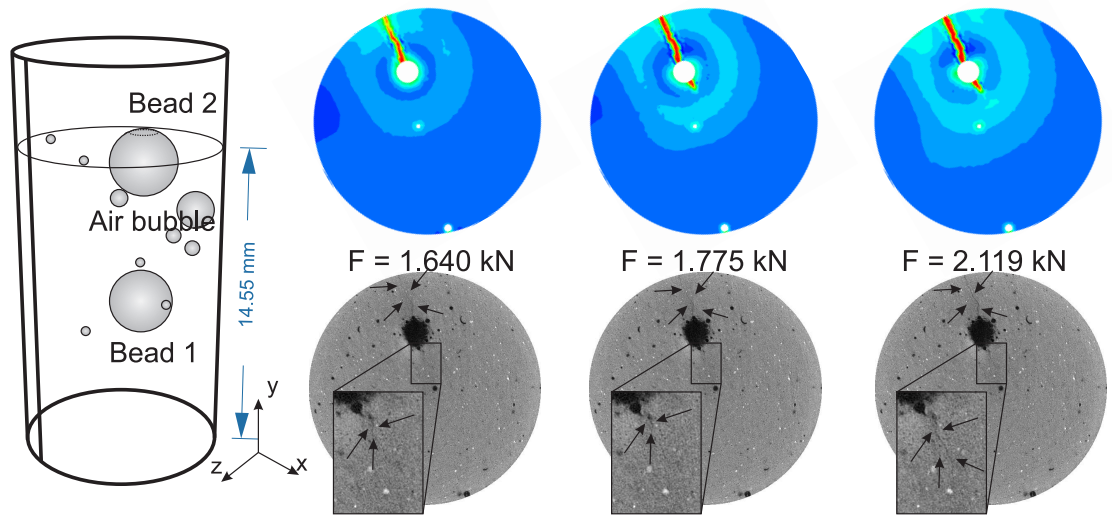

Figure 8.32: Crack path evolution in a region above Bead 2: (a) Position of the plane chosen for the comparisons; upper images (in color): numerical simulations; lower images: experiments; (b) loading step 3; (c) loading step 6; (d) loading step 10.

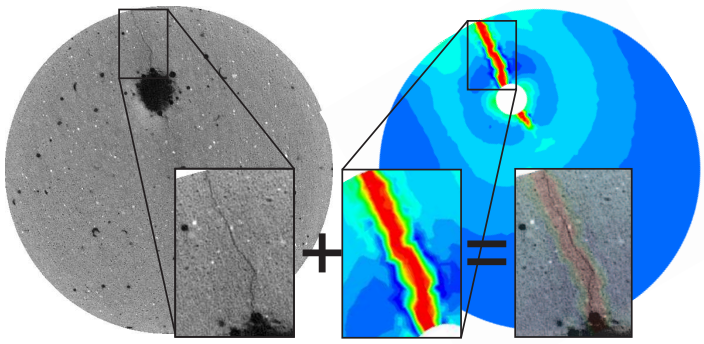

Figure 8.33: Detailed comparison between experimental crack path (a) and simulation (b) for step 10.

it gets close to the ends. Conversely, the propagation towards the ends of a crack presenting such a discontinuity will be difficult. To face such a limitation of the numerical simulation, one should use less strict displacement boundary conditions; a solution might be to include in the model the softer PMMA tabs, together with unilateral jump conditions at the tabs/sample interface. Such more complex computations are left for further investigations.

The rupture of the sample occurs on the top half part. The cracks nucleate and propagate

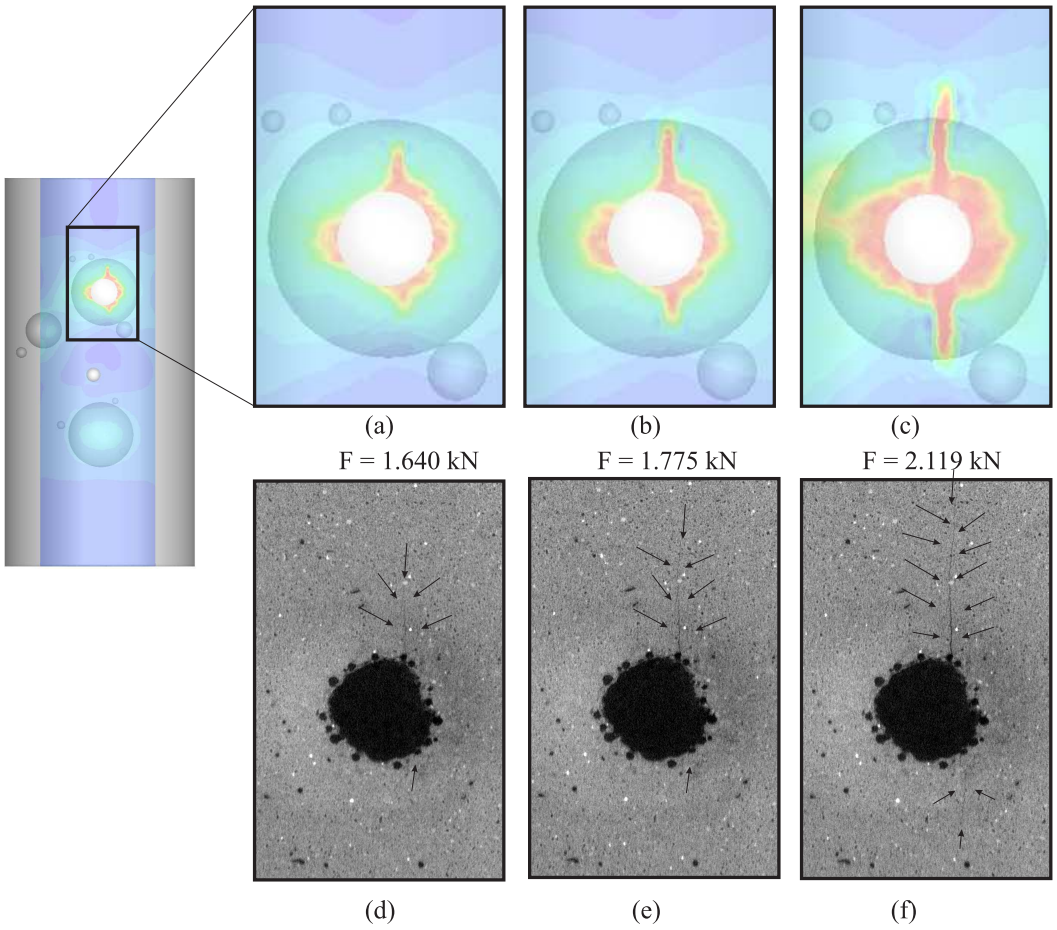

Figure 8.34: Comparisons in a vertical plane. upper images (in color): numerical simulation; lower images (grey levels): experiments. (a), (d); loading step 3; (b), (e): loading step 6; (c), (f): loading step 10.

mainly in a region near Bead 2 and the biggest bubble of air. Views of the simulated and of the experimental crack are provided in Fig. 8.35. Again a very nice consistency between model and experiment is observed. Not only, the model is able to predict apparitions and propagation of cracks; it is also able to predict which areas will not be damaged.

For the last two comparisons, we chose first a horizontal plane passing below Bead 2 and above an air bubble, at height $H = 11.9$ mm (see Fig. 8.36(a)), and secondly a plane passing through Bead 2, at height $H = 14.15$ mm (see Fig. 8.37(a)). Comparisons between experimental and numerical results are depicted in Fig. 8.36(b)-(c) and Fig. 8.37(b)-(c) for both respective cases.

In the second case, we have compared quantitatively the angle of the crack. We have found a value of 112.71° for the experiments, and 114.21° for the simulation. The accurate superposition of computed damage maps on transformed experimental CT images highlights the similarity of the crack path.

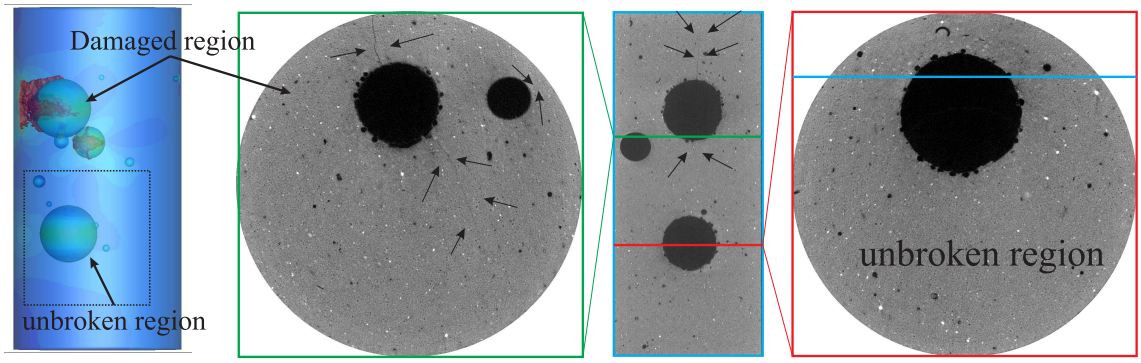

Figure 8.35: View of the damage zone in the lightweight plaster sample PlasterF1

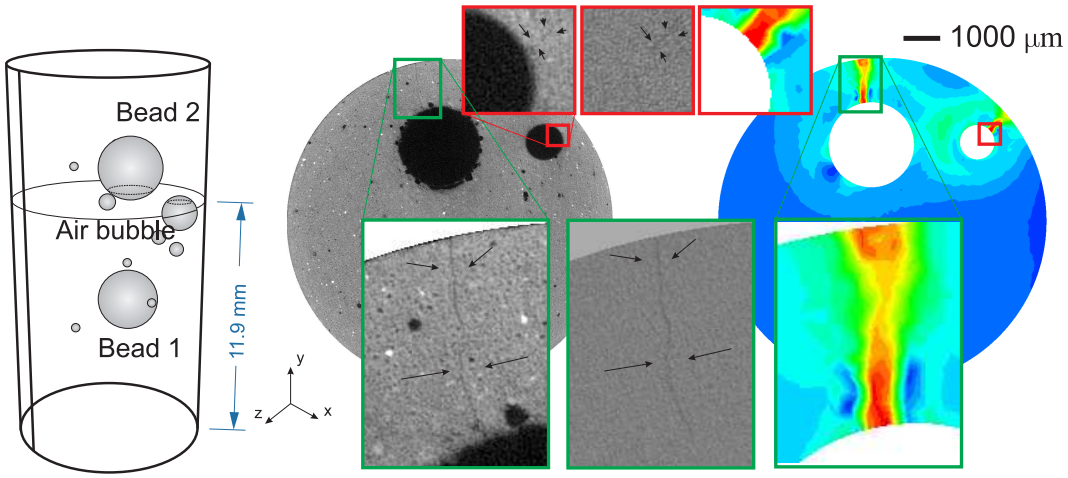

(a) (b) (c)

Figure 8.36: Crack path in a region below Bead 2: (a) position of the observation plane; (b) Experimental cracks; (c) Simulated cracks.

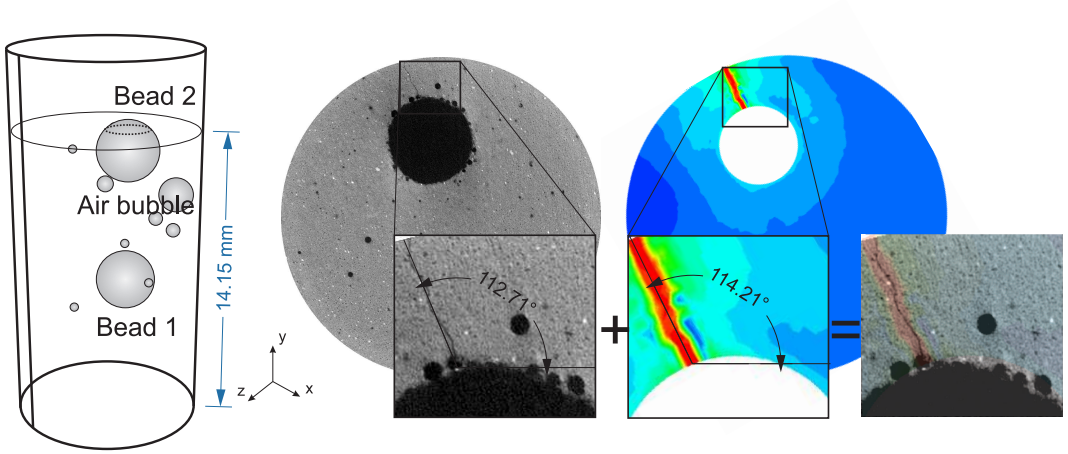

(a) (b) (c)

Figure 8.37: Crack path in a region above Bead 2: (a) position of the observation plane; (b) Experimental cracks; (c) Simulated cracks.

8.7 Microcracking in lightweight concrete sample

In this section, we will compare the microcracking network propagation obtained from the experiments and the numerical simulations in the case of a lightweight concrete sample. This case is much more complex that for lightweight plaster, because the microstructural details are much more complex forbid to mesh the whole microtomography image of the sample. In addition, the material is composed of 3 phases with complex shapes.

8.7.1 Experiments

8.7.1.1 Experimental in-situ test on the lightweight concrete sample

In this test, we have used polished aluminum plates instead of PMMA plates, because of the lower Poisson's effect of aluminum. In addition, since $\nu_{\text{aluminum}}/E_{\text{aluminum}} < \nu_{\text{concrete}}/E_{\text{concrete}}$, we hope to minimize the spurious effects discussed in Chapter 6.

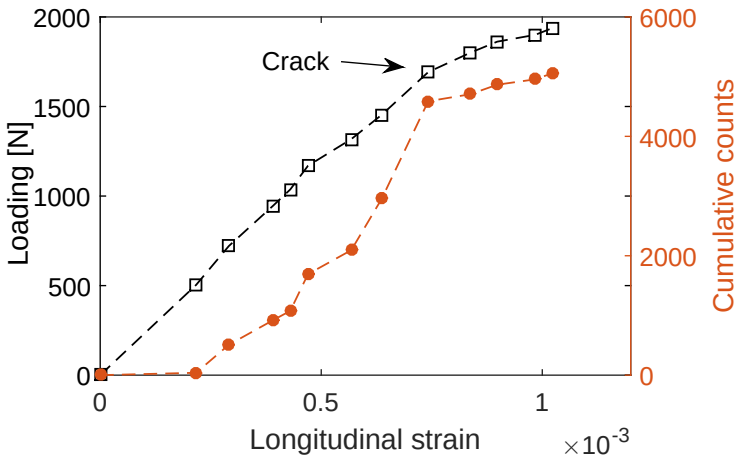

Figure 8.38: Load-strain curve obtained from in-situ compression test of specimen ConcreteP2

The details of the experimental in-situ loading procedure have been provided in Chapter 4 and section 8.2.1. The initial sample presents a few micro cracks caused by the drilling and the cutting processes. The whole test has been preformed in only one loading phase (without intermediate unloading). The load−strain curve is plotted in Fig. 8.38, where the longitudinal strain is computed from DVC of CT images. In EPS plaster samples for which no AE (acoustic emission) signals could be recorded, we have continuously recorded acoustic activity in the concrete sample. In the second EPS concrete sample, we observe always a clear rise in AE counts at the initiation of cracking as presented in Fig. 8.38, that confirms the ability of acoustic emission recording to detect crack initiation in concrete. We compare in Fig. 8.39 the macroscopic mechanical response of the sample with optimized boundary conditions (polished surface and inserted Aluminum plate) to the response of concrete sample of the preliminary test described in chapter 4. When optimized conditions are used, the strength is higher as expected.

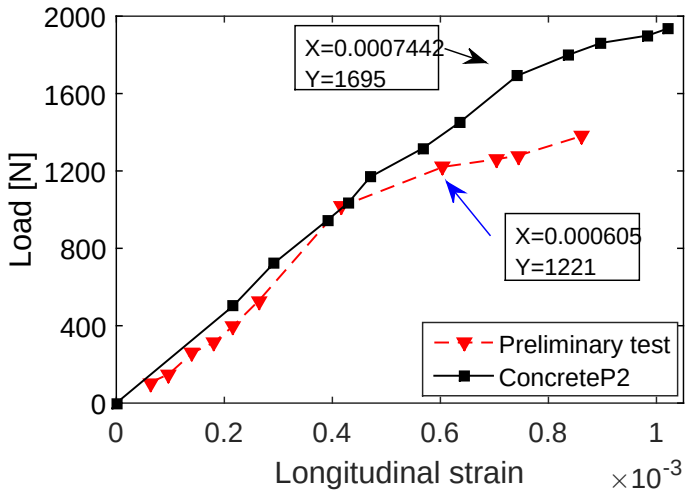

Figure 8.39: Comparison of load deformation curve for both EPS concrete samples: before optimization (preliminary test) and after optimization (ConcreteP2) of experimental loading conditions and sample preparation procedures

8.7.1.2 Experimental observation of the micro cracks in the lightweight concrete sample

The pore volume fraction can be estimated from thresholding CT images. In Fig. 8.40, we have plotted this porosity in the sample as a function of the z-coordinate (height), the origin being the bottom face. We have observed that most of cracks initiate from the regions where the porosity is maximum (indicated by arrows in Fig. 8.40). No cracks where found on the top and bottom faces. Fig. 8.41(a) shows a CT image vertical cut of the sample. In Figs. 8.41(b) and (c), the cut corresponding to planes indicated in red and green in Fig. 8.41(a) are presented. Some microcracks are indicated.

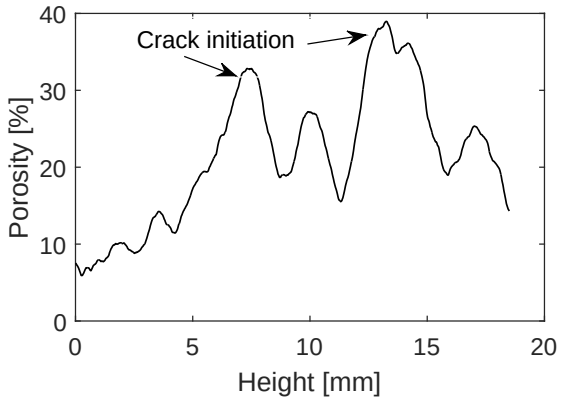

Figure 8.40: Evolution of pore volume fraction in the lightweight concrete sample (ConcreteP2) along the vertical direction of the sample.

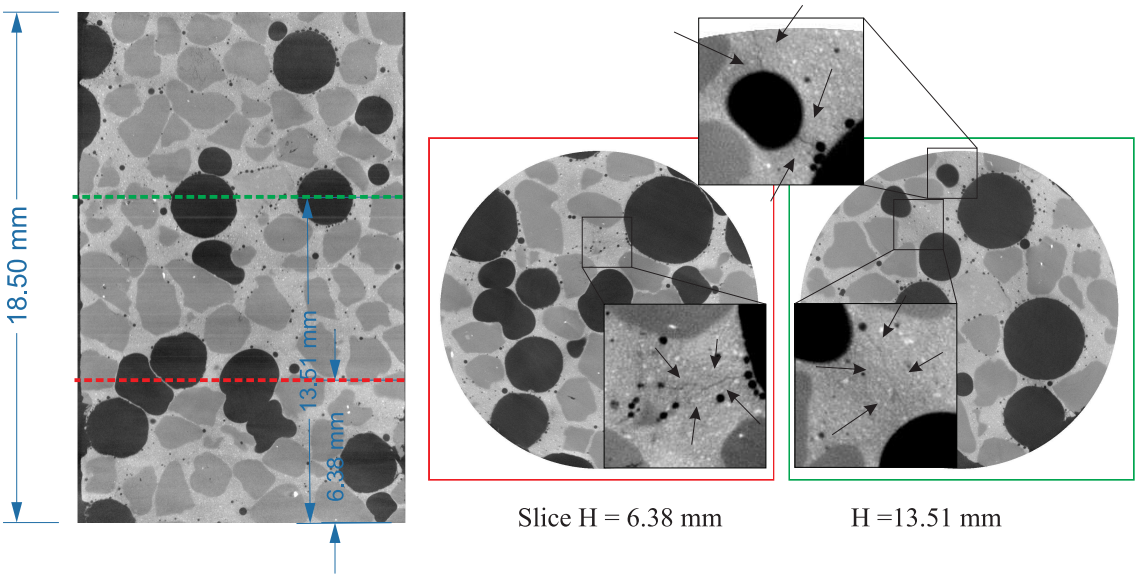

Figure 8.41: CT image of the sample under loading: (a) longitudinal view; (b) and (c): traversal views

We used CT, transformed and subtracted images to detect cracks under loading. The details of these procedures have been described in Chapter 4 and section 8.2.1. An example of crack detection by using the subtracted image technique is depicted in Fig. 8.42, showing that an additional treatment is really required to capture cracks in some cases where they are not visible in initial CT images.

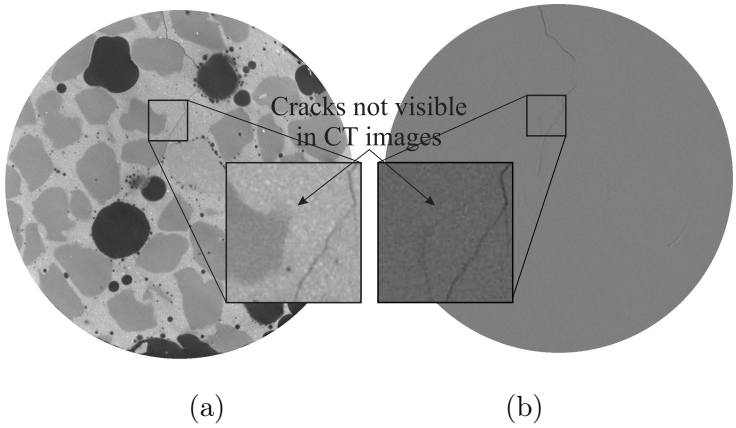

Figure 8.42: Detection of non visible cracks by using subtracted image for loading step 12: (a) CT images; (b) corresponding subtracted image.

The crack propagation in this material is different from that in the lightweight plaster. Here, cracks initiate from the pores but also from the interfaces. The interfaces also constitute weak zones where the cracks propagate. An example is illustrated in Fig. 8.43, and it is in qualitative

agreement with numerical simulations performed using the method described in Chapter 3 on 2D microstructures. However, because of a lack of time, the interfacial phase field method described in Chapter 3 has not yet been implemented in 3D. Thus, in the next series of comparisons, the numerical simulation results have been obtained using the standard phase field method described in Chapter 2.

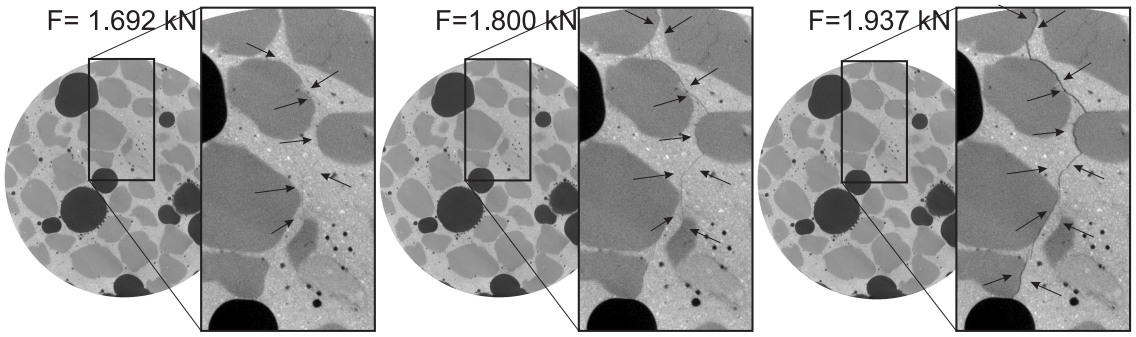

(a) (b) (c)

Figure 8.43: Cracks propagation in the lightweight concrete sample for different loads: (a) loading step 8; (b) loading step 9; (c) loading step 12

An example of cracks initiating from the pores is presented in Fig. 8.44.

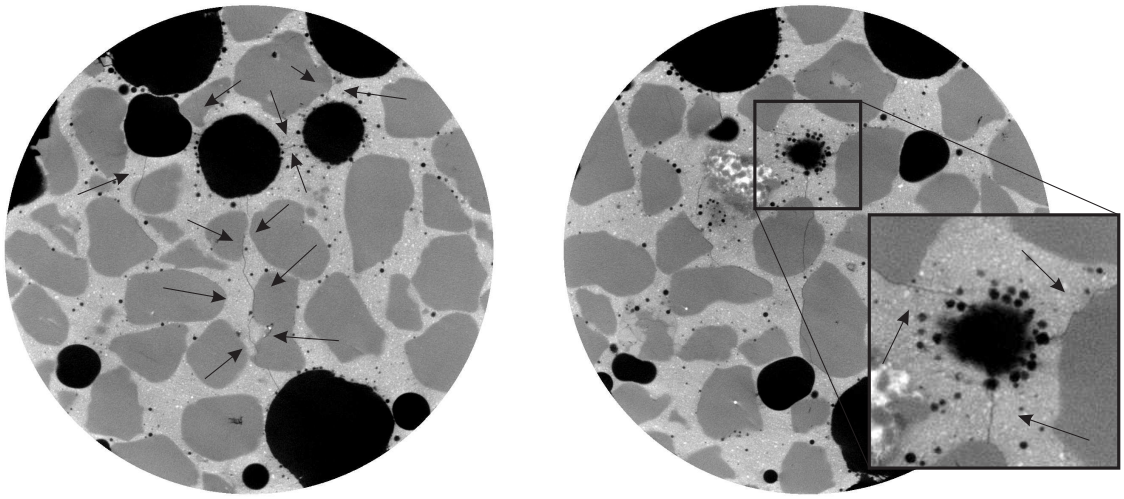

(a) (b)

Figure 8.44: Cracks initiating from pores in the lightweight concrete sample in two different traversal planes.

8.7.2 Comparisons between numerical simulations and experimental results

8.7.2.1 Initial numerical model

As mentioned previously, meshing the whole 3D segmented CT-image for the simulation would lead to hundreds of millions to billions of elements which is not tractable. Then, we adopt here once more the sub-volume technique described in section 8.5.2.

Compared to the lightweight plaster, the lightweight concrete sample presents additional difficulties: (a) it contains 3 phases, the pores, the quartz sand and the cement matrix; (b) it shows more badly correlated regions than EPS plaster, as in quartz sand or porosity. DVC has only been performed in cement paste and near interfaces. Considering that, three groups, corresponding to quartz sand, cement matrix and porosity, have been distinguished among correlation points to define boundary conditions for the sub-volume method. We present an example in Fig. 8.45, where red color and green color are correlation points of quartz sand and cement matrix respectively. Then, for the construction of the boundary condition at FEM nodes in-between DVC points, the neighbor correlation points used for the interpolation are required to belong to the same phase: prescribed displacements at FE nodes in cement result from DVC points in cement only (green in Fig. 8.45) and those in sand grains depend on red interfacial DVC points only. Nodes in pores are removed from the mesh.

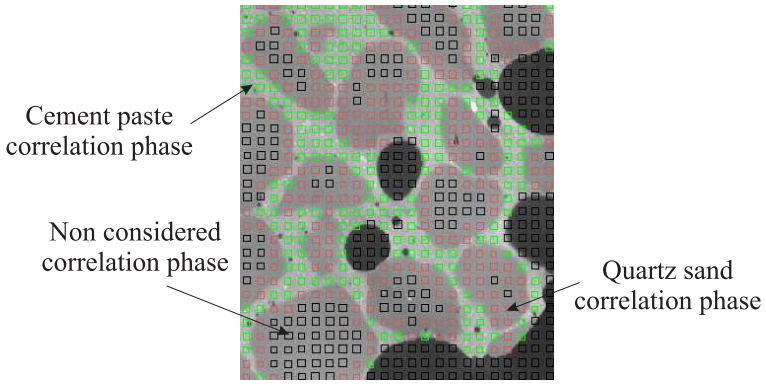

Figure 8.45: Correlation phase separation in EPS concrete material

In the following, two sub-volumes are considered for a detailed comparison between the experimentally observed crack propagation and its numerical prediction by the phase-field method.

8.7.2.2 Comparison of crack propagation between experiments and numerical simulation in lightweight concrete: sub-volume 1.

We first consider a sub-volume of size $480 \times 480 \times 72$ voxel^3 (or $4.8 \times 4.8 \times 0.72$ mm^3), where cracks have been observed in the experiments. A regular mesh is used, where each 8-node corresponds to a voxel in the segemented image, its material properties being projected on the mesh. Note that a *median filter* and then a *watershed operator* were used to extract the sand phase (inclusions). The resolution was reduced to $300 \times 300 \times 45$ to limit the computational costs. In addition, we removed all elements within the pores. The resulting mesh contains 3.6 million elements.

The material parameters of inclusions and matrix have been extracted from literature and are respectively set to: $E_i = 60$ GPa, $\nu_i = 0.3$, $E_m = 18$ GPa, $\nu_m = 0.2$. The toughness $g_c = 59.3$ N/m is assumed to be identical for the different phases (following the work of [182]). The characteristic length is chosen as $l = 30\mu$m. The evolving boundary conditions obtained from DVC are applied on the boundary of the sub-volume during 300 steps. The crack propagation will be compared for several loading steps. For the sake of clarity, we do not show the matrix phase (cement paste).

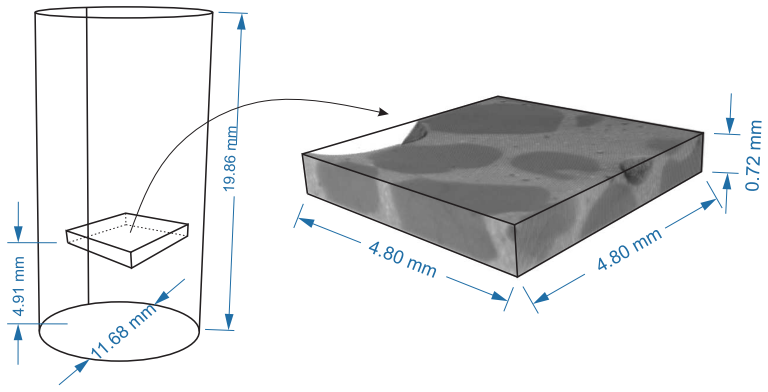

(a) (b)

Figure 8.46: Geometry of the sub-volume 1: (a) location in sample; (b) CT images of the sub-volume

The results are presented in Fig. 8.47 and Fig. 8.48 for three loading step 9, step 10 and step 11. At loading step 9, we observe that the numerical crack (on the right) has a similar path than the experimental one (on the left), but seems to propagate slower. This might be due to the choice of material parameters, which have been set with a less sophisticated methodology than for plaster samples. For the loading step 10 and step 11, the numerical and experimental crack morphologies are remarkably similar: even the crack length are comparable. The main discrepancies concern the crack path near the interface. This can be explained by the fact that in the experiment, we can clearly observe that interfacial damage occurs, which is not taken into account in the simulation.

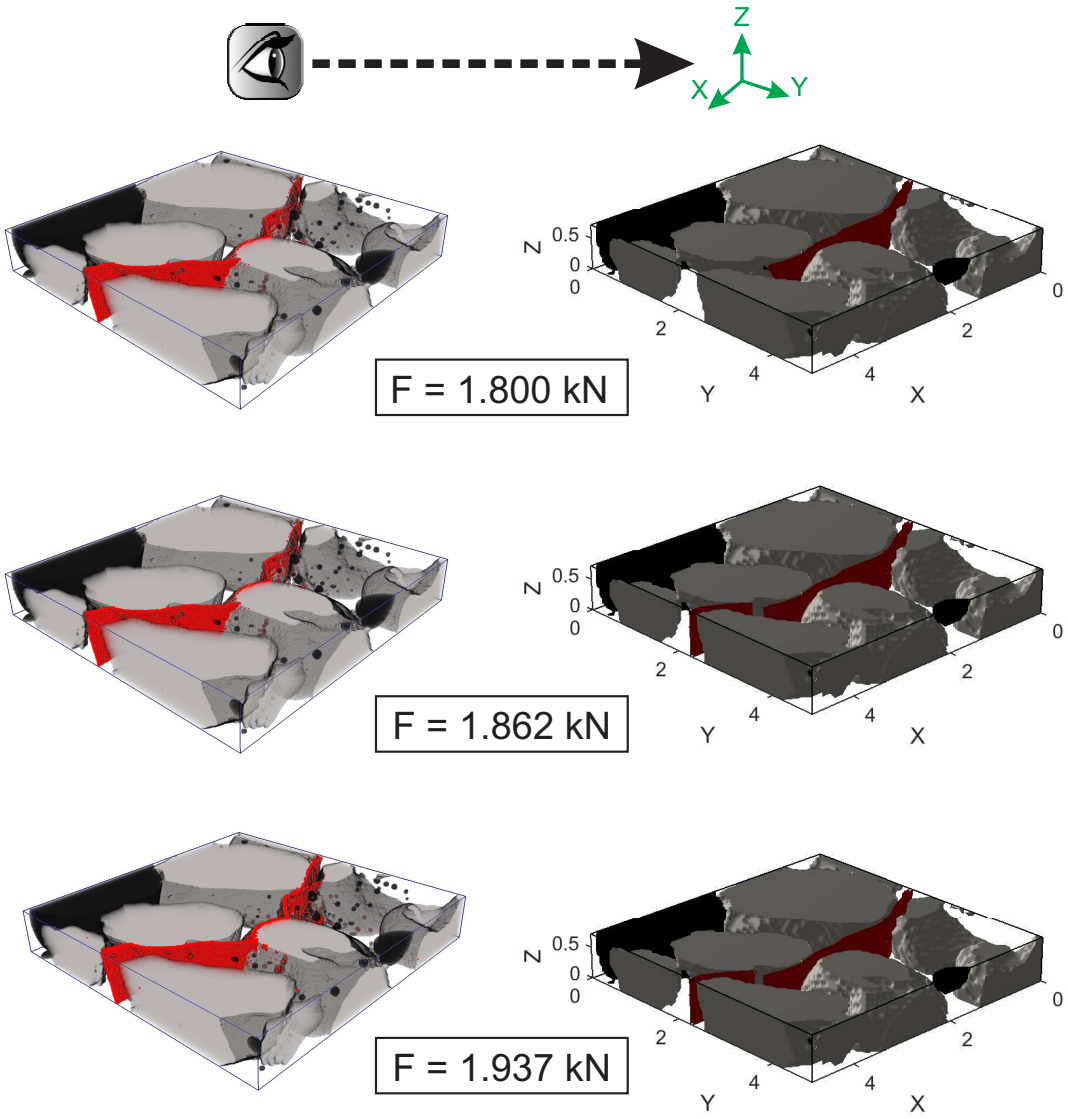

Figure 8.47: Comparison between experimental crack obtained from microtomography and from phase field method of the lightweight concrete sample in sub-volume 1 for several loads, view 1 (Left: experiment; right: numerical simulation.)

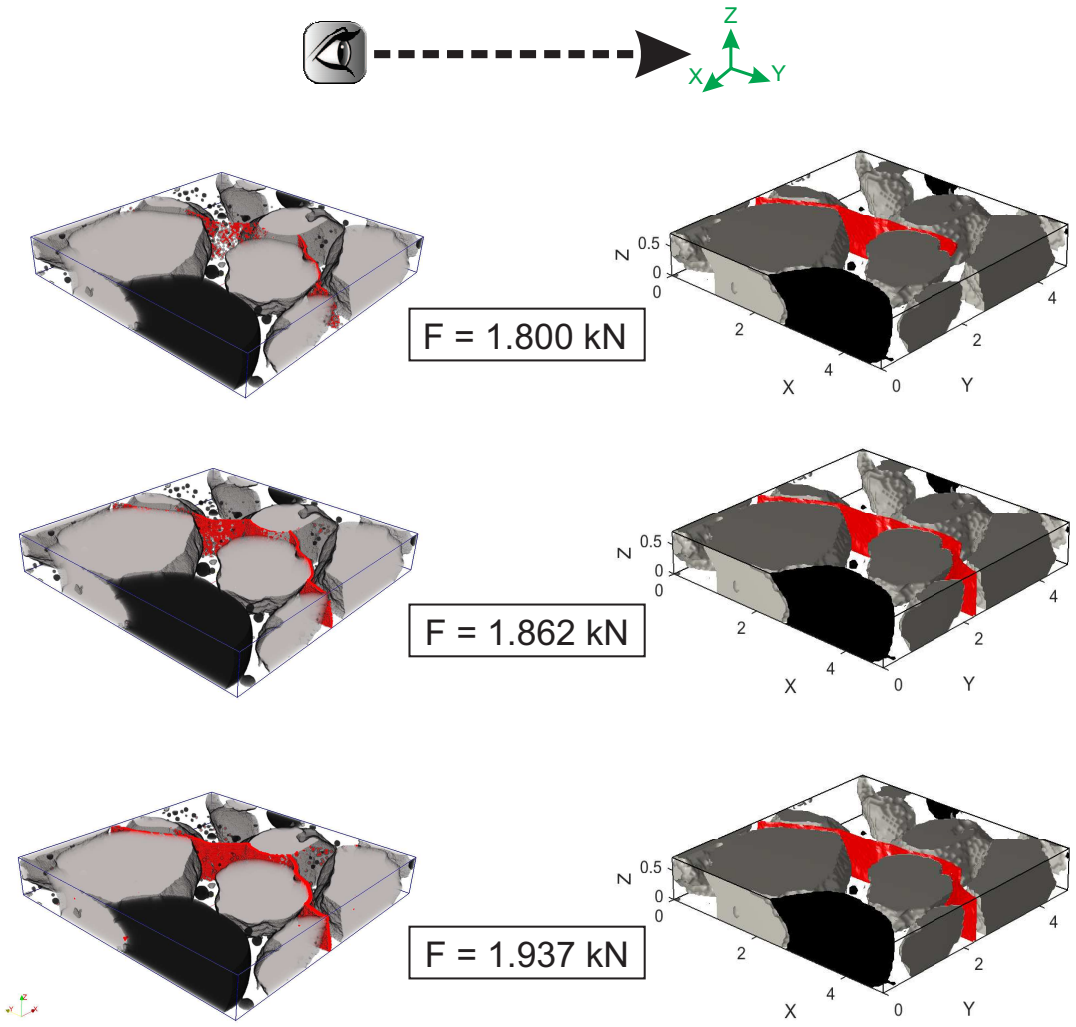

Figure 8.48: Comparison between experimental crack obtained from microtomography and from phase field method of the lightweight concrete sample in sub-volume 1 for several loads, view 2 (Left: experiment; right: numerical simulation.)

8.7.2.3 Comparison of crack propagation between experiments and numerical simulation in lightweight concrete: sub-volume 2

A second sub-volume is studied, of size $360 \times 360 \times 96$ voxel^3 (or $3.6 \times 3.6 \times 0.96$ mm^3). Its resolution is reduced to $240 \times 240 \times 64$ voxel^3. The obtained mesh is composed of 3.7 million of regular 8-node elements. We compare the crack propagation for experiment and numerical simulation for the loading steps 9, 10 and 12.

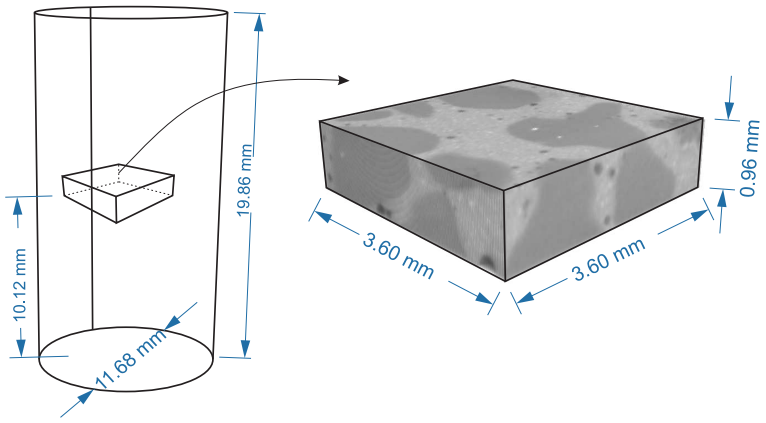

(a) (b)

Figure 8.49: Geometry of the sub-volume 2: (a) location in the sample; (b) CT images of the sub-volume

The crack path for both simulation and experiment are compared for three loads in Fig. 8.50 and Fig. 8.51. At loading step 9 (F = 1.8 kN) we obtain here a very good agreement regarding crack morphology and crack length. In this case, we believe that the agreement is better than in the first sub-volume because there is less interfacial cracking in the experiment. To confirm the good accuracy of the numerical model, we also compare the 3D crack morphology for steps 10 ($F = 1.862$ kN) and 12 ($F = 1.937$ kN). Here again, the accuracy of the numerical model is demonstrated. The crack length of both results are also in good agreement.

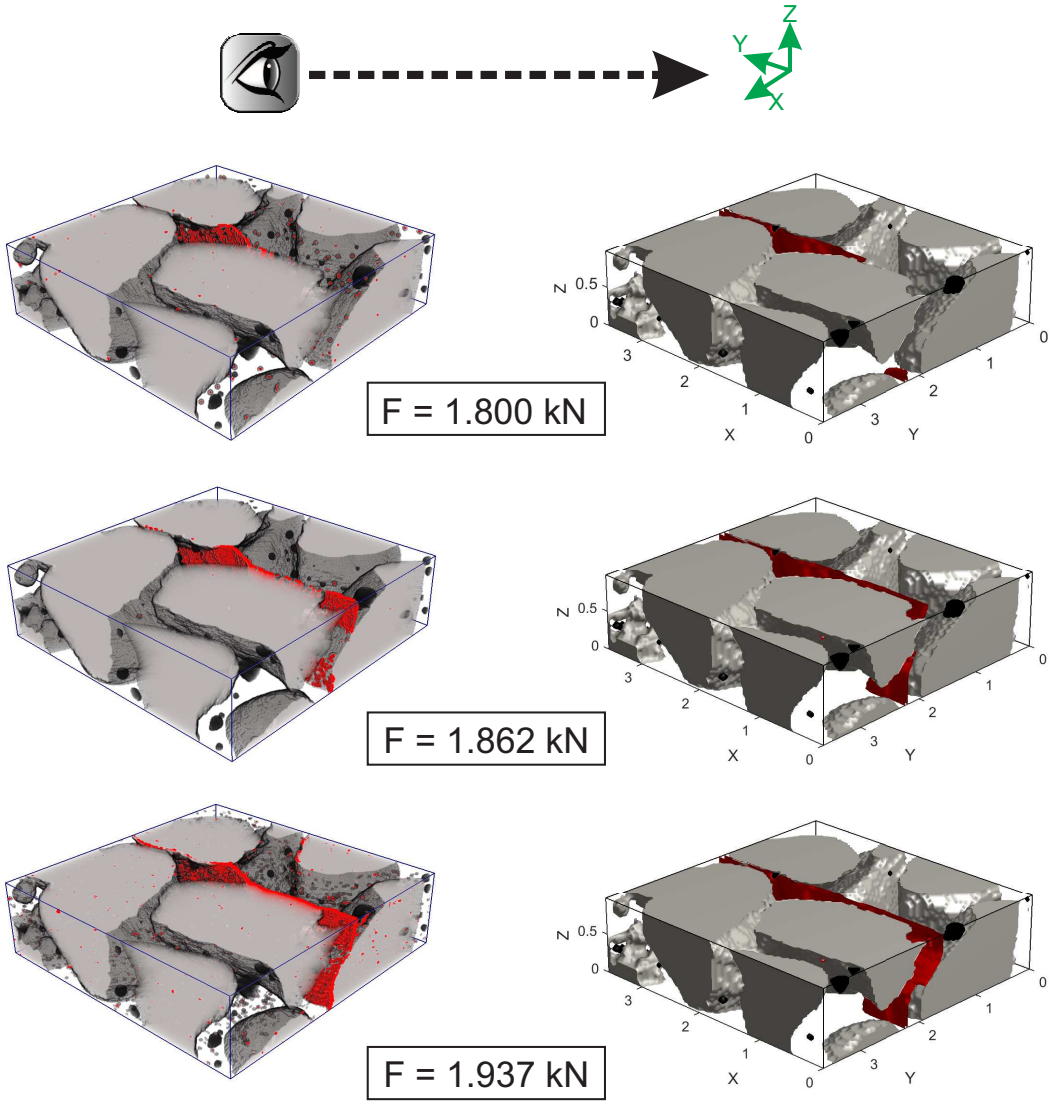

Figure 8.50: Comparison between experimental crack obtained from microtomography and from phase field method of the lightweight concrete sample in sub-volume 2 for several loads, view 1. (Left: experiment; right: numerical simulation.)

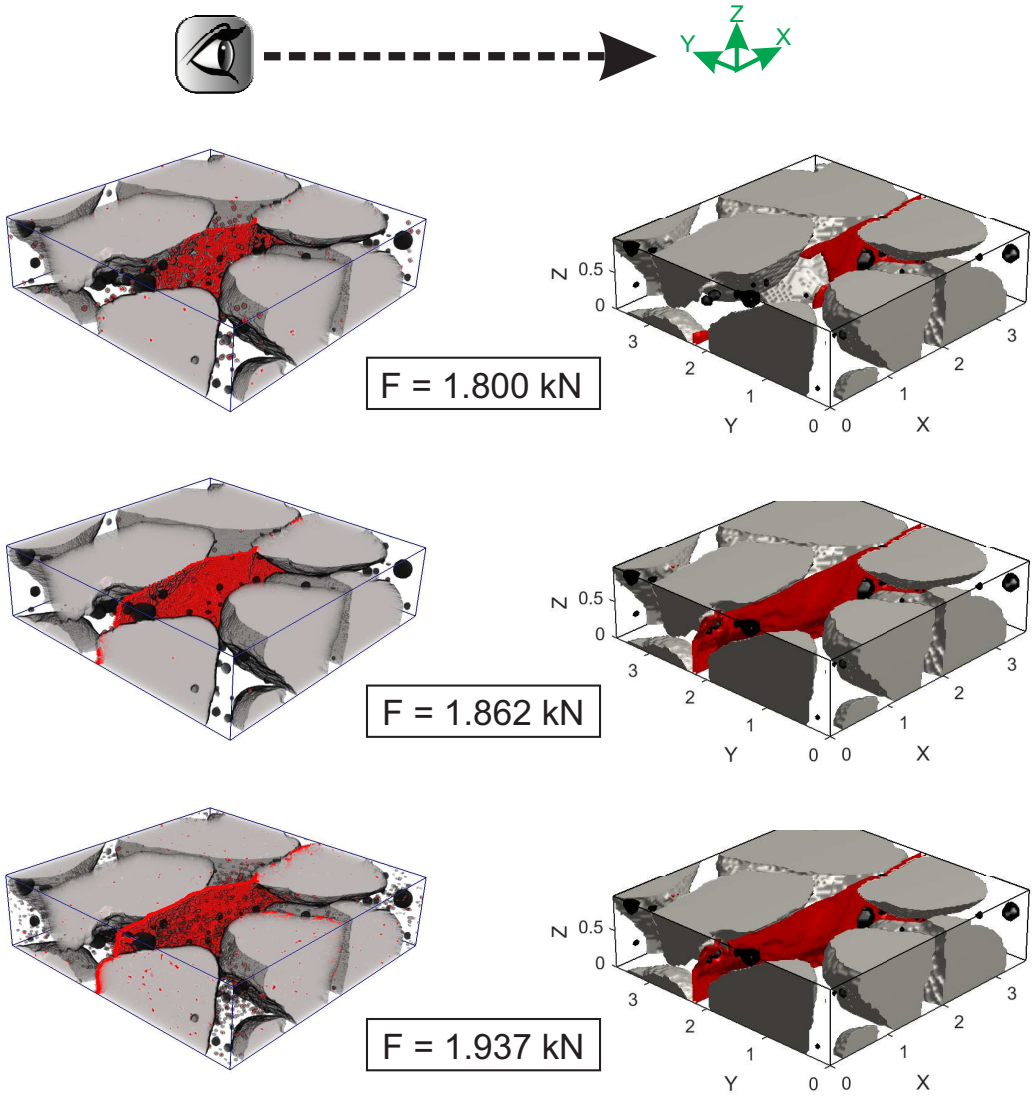

Figure 8.51: Comparison between experimental crack obtained from microtomography and from phase field method of the lightweight concrete sample in sub-volume 2 for several loads, view 2. (Left: experiment; right: numerical simulation.)

8.8 Conclusion

In this chapter, we have performed direct comparisons of 3D crack propagation within highly heterogeneous plaster and concrete samples between experiments and numerical simulations, at both sample and microstructure scales, for the first time, to our knowledge. The crack evolution has been followed by means of an in-situ testing machine inside a CT-scan and appropriate image processing. The numerical simulations have been performed on models reproducing in a very realistic way the microstructure of the material, by using the segmented CT-images of the initial samples. First, we have performed comparisons over complete samples including a few heterogeneities (pores). Then, to include fine microstructural details, we have performed comparisons in sub-volumes within the samples. The numerical simulations have been performed with the phase field method. No assumption has been made on the location of crack initiation and paths. The initial geometries have been obtained by the CT-scans of the undamaged samples. The main conclusions of this chapter are summarized as follows.

- The image processing techniques described in Chapter 5 have been successfully applied to provide the reference solution for the numerical simulations. Complex microcracking networks have been detected in complex microstructures such that in porous plaster or concrete embedding EPS beads.

- The accuracy analysis of DVC-assisted image subtraction has demonstrated the capability to detect very tiny cracks, of about 1/10 voxels for EPS plaster and 1/20 for EPS concrete.

- Comparisons of 3D cracks propagations have shown a very good agreement regarding the obtained 3D crack morphologies and lengths of propagated microcracks. This has been confirmed by many tests and quantitative measures of crack features (orientation, length) in the different materials and different samples.

- To obtain the numerical crack paths in the numerical material models, very large phase field simulations involving millions of elements have been performed for highly heterogeneous microstructures. The largest simulation model involved 12 millions elements.

- The sub-volume procedure technique developed in this work, i.e. using the displacement field obtained from the experimental 3D DVC has been successfully applied to realistic models of materials, allowing to simulate crack propagation in complex materials and to directly compare the obtained results with the simulation. Such simulations could not be possible by considering the whole sample and are the first of their kind to our knowledge.

Chapter 9

Conclusions and perspectives

9.1 General conclusions

In the present thesis work, we have provided contributions to the modeling of microcracking in cementitious materials, and have proposed both numerical tools for simulation and experimental procedures to study 3D crack propagation in highly heterogeneous materials like lightweight concrete or lightweight plaster samples. In addition, we have combined both approaches to identify the microstructural damage parameters and provide the first validations to our knowledge of 3D crack propagation fronts in highly heterogeneous materials, by directly comparing in-situ CT-scans of compressed samples and full simulations using phase field method based on the real imaging of the samples used in the experiment. The contributions developed in this thesis are summarized as follows.

First, an original application of the phase field method to highly heterogeneous materials whose geometry is provided by XR-CT scans has been proposed. Extensive 2D and 3D simulations have been performed, involving up to 18 million of elements in a specific code developed during this PhD at MSME Lab. To improve the efficiency of the phase field method for such problem, a shifted algorithm has been introduced to transfer the nonlinear problem induced by the positive-negative split of the strain tensor to previous iterations in a staggered scheme.

A second contribution to the developed numerical tools is an extension of the phase field method to interfacial cracking to model decohesion between inclusions and matrix in concrete. The proposed formulation differs from the one proposed by Verhoosel and de Borst [218], as no internal variable is required to model the displacement jump, and as the phase field variable can be used directly as a history parameter to model the irreversible damage of interfaces. In addition, an original framework has been proposed so as the method can be applied to voxel-based models of microstructure, by the use of level-set functions.

Experimental procedures to perform in-situ compression tests of lightweight concrete and plaster samples have been described and carried out at Navier Lab. More specifically, we have developed a protocol to obtain stable crack networks during the in-situ test, by appropriate preparation of the ends of samples and enhancement of the compression setup and protocol. Samples with controlled porosity using EPS beads have been manufactured and tested. The elastic properties of the plaster matrix have been estimated by Digital Image Correlation (DIC), whose errors have been evaluated and corrected whenever possible.

An image subtraction technique based on Digital Volume Correlation (DVC)or 3D DIC,

has been specifically developed to detect and to extract cracks from XR-CT images of such heterogeneous microstructures. Such process allows the detection of subvoxels microcracks, some of which are not visible on XR-CT images, for all loading steps of the in-situ steps. As a results, sets of data describing the evolution of a microcrack network in a lighweight concrete and two EPS plaster samples have been obtained and can be directly compared with numerical simulations.

Then, we have described procedures to model the experimental in-situ tests for simulation purposes. For lightweight plaster, the XR-CT can be used to define position and radii of spherical pores and to construct an idealized geometry with boolean operators, easily usable for constructing meshes. For more complex geometries like concrete, the voxel data can be used directly to construct a regular mesh of elements. Simulations of the experimental boundary conditions prescribed on the samples have helped determining the best support and conditions on the top and bottom faces of the sample to avoid spurious external cracks and inducing stable cracks of networks which can be imaged by the previously mentioned developed methodologies.

Finally, the experiments and simulations have been combined to validate the numerical predictions of 3D crack networks propagation in highly heterogeneous microstructures. First, we have validated the predictions of crack propagation in complex 2D configurations of drilled plaster samples in compression, where stable cracks can be obtained and measured experimentally. Second, we have directly compared the numerical simulations of phase field 3D crack propagation in complex 3D microstructures with the experimentally detected crack networks using the different techniques described in the previous chapter of this thesis. A sub-volume methodology has been developed to avoid analyzing the whole sample when the microstructure is complex, as in the case of concrete. For this purpose, DVC, has been used to provide the boundary conditions to be prescribed over a sub-volume of the sample in the numerical simulation. We have obtained very encouraging results regarding the accuracy of the predicted crack paths in 3D over a large set of tests involving several microstructures.

9.2 Perspectives

There are many potential research directions from the results and methodologies developed in this work, and some questions remain to be addressed.

First, regarding the developed models and numerical methodologies to simulate microcracking with the phase field method, several points, among many other, could be mentioned: the mechanical models describing the brittle damage under compression could be enhanced, by incorporating friction within the crack, or compression-based damage mechanisms when the crack closes, to be representative of some observed phenomena in brittle materials under compression and in geosciences. As outlined in May et al. [132], the presently developed staggered algorithms to solve the equations of the phase field method cannot take into account snap-back instabilities, and other efficient numerical solving schemes should be developed in that context for large

meshes. New numerical strategies have to be developed to reach the resolution of larger models, incorporating all voxels of XR-CT images without reducing the problem to sub-volumes.

The experimental works initiated in this thesis could also be pursued in future works by: performing similar in-situ tests to observe microcracking in plaster samples with rigid inclusions, or including both rigid beads and EPS beads to manufacture materials with controlled microstructural geometry; manufacturing smaller samples with controlled heterogeneous microstructures to reach a higher resolution of XR-CT images; improving the description of local transformations within image processing (DVC-assisted image subtraction), especially within the regions of highly cracked areas to better separate cracks from other artifacts of residual images. The systematic errors correction processing is also attempted to improve quality of subtracted image. Another point is the enhancement of segmentation procedure to detect smaller cracks. One could also mention possible enhancements of the DVC procedures, making use of the detected crack paths, for an accurate quantification of the displacement discontinuities across the cracks, over the whole network of cracks. This would provide an additional quantitative way to validation the numerical models.

Finally, when coupling experimental in-situ tests with simulations, one open question is the identification of microstructural and local damage parameters for multi phase materials, when the number of parameters drastically increases. Then, efficient numerical solving procedures, construction of surrogate models and optimization strategies should be developed. Certainly, the use of local quantities like the above mentioned crack discontinuities, in addition to the overall load-displacement curves already used in the present study, would enhance the accuracy of the identification.

Appendix A

Appendix

A.1 Appendix 1: Analytical solution for the discontinuous benchmark problem

In the following, we provide the exact solution of the discontinuous benchmark presented in example 3.7.1. The u_1 component of the displacement is linear in each domain, i.e.

$$\begin{aligned} u_1(x) &= A_1 x + B_1 \quad \forall \mathbf{x} \in \Omega_1, \\ u_1(x) &= A_2 x + B_2 \quad \forall \mathbf{x} \in \Omega_1. \end{aligned} \tag{A.1}$$

The constants are found by verifying the displacement boundary conditions and the continuity conditions at the interface $x = L/2$:

$$\begin{cases} u_1(x=0) = 0 \\ u_1(x=L) = \overline{U} \\ [\![\sigma_{11}(x=L/2)]\!] = 0 \\ \sigma_{11}(x=L/2) = t([\![u_1(x=L/2)]\!]) \end{cases} \tag{A.2}$$

which leads to the solution:

$$u_1(x) = \frac{E_2 \overline{U}}{\frac{L}{2}(E_1+E_2) + \frac{E_1 E_2 v_n^2}{g_c}} \; x \qquad \text{for} \;\; (\mathrm{x} > \frac{\mathrm{L}}{2}) \tag{A.3}$$

$$u_1(x) = \overline{U} - \frac{\overline{U}}{\frac{L}{2}(1+\frac{E_2}{E_1}) + \frac{E_2 v_n^2}{g_c}} \; (L-x) \;\; \text{for} \;\; (\mathrm{x} < \frac{\mathrm{L}}{2}). \tag{A.4}$$

A.2 Appendix 2: Expressions of tangent components of the cohesive law

The expressions of the terms in (3.47) are given by:

$$D_{nn} = \frac{g_c^I}{\delta^n}\left(1 - \frac{\mathrm{w^n}}{\delta^n}\right)\exp\left(-\frac{\mathrm{w^n}}{\delta^n}\right)\exp\left(-\frac{\left(\mathrm{w^t}\right)^2}{(\delta^t)^2}\right), \tag{A.5}$$

$$D_{nt} = -2g_c^I\left(\frac{\mathrm{w^n}}{\delta^n}\right)\left(\frac{\mathrm{w^t}}{(\delta^t)^2}\right)\exp\left(-\frac{\mathrm{w^n}}{\delta^n}\right)\exp\left(-\frac{\left(\mathrm{w^t}\right)^2}{(\delta^t)^2}\right), \tag{A.6}$$

$$D_{tt} = \frac{2g_c^I}{\delta^t}\left(1 - 2\frac{\left(w^t\right)^2}{(\delta^t)^2}\right)\left(1 + \frac{\mathrm{w^n}}{\delta^n}\right)\exp\left(-\frac{\mathrm{w^n}}{\delta^n}\right), \tag{A.7}$$

$$D_{tn} = -2g_c^I\left(\frac{\mathrm{w^t}}{\delta^t}\right)\frac{\mathrm{w^n}}{(\delta^n)^2}\exp\left(-\frac{\mathrm{w^n}}{\delta^n}\right)\exp\left(-\frac{\left(\mathrm{w^t}\right)^2}{(\delta^t)^2}\right). \tag{A.8}$$

A.3 Appendix 3: Plaster manufacturing in syringe

The tools and ingredients for plaster manufacturing in the syringe include:

. Syringe: we use a classical syringe (a production of TERUMO). Typically 2.5 ml, which gives a sample with a diameter of about 9 mm and maximal height 30 mm.

. EPS bead: the expanded polystyrene (EPS) beads in this study are made of Polystyrene, with a diameter of about 1.5 - 4 mm. The nominal density is less than 30 kg/m3. We can consider the EPS aggregates to have almost zero strength.

. Water: the waster used for the plaster paste manufacturing is at temperature about 20 °C .

. Balance: the balance for the measurement of aggregate have an accurate of about 0.01 g.

. Mixing machine

The overall for plaster specimens manufacturing in the syringe could be described on two main steps: the first step is the manufacturing of plaster material. In this study, we use the protocol proposed in the work of Romani et al [179]. The second step is the aspiration of plaster paste and EPS beads into the syringe. The detail of each step is described by the following:

- Preparation
  - Cutting the nozzle of the syringe. Because the original nozzle can aspirate at most beads of diameter 1 mm.
  - Taking the plaster and water. Using the balance, we take about 300 g plaster and 99 g water ($E/P = 0.33$) for the preparation of a dozen of samples
- Manufacturing of plaster material:
  - Pouring the water into the tank of the mixer
  - Gradually pouring the plaster (powder) into the water while mixing with the mixing rate lowest. This steps must be realized slowly and regularly to avoid the creation of air bubbles.
  - Manual homogenization, after all plaster powder has been poured, we stop the mixing and use the arm mixer to make the homogenization of plaster powder and water.

  - Main mixing: mixing by using the machine for 1 min.
  - Relax the plaster paste in the tank for 1 min.
  - Fill a cup with obtained paste

- Aspiring of plaster paste and EPS beads into the syringe

  - The aspiration of plaster paste into the syringe. This processing must be realized slowly and regularly to ensure the homogeneity of matrix plaster. The rate of aspiration has been performed constant to have the stable behaviour for divers specimen. Moreover, the syringe is immersed enough to avoid aspiration of air bubbles.
  - The aspiration of the EPS bead into the syringe. We place the EPS bead on the plaster paste. We put the syringe above the EPS bead, then we immerse both the syringe and EPS bead into the paste before aspiring the rest part of paste. To obtains the good position of EPS bead in the final specimen (in the central region), in this processing the syringe must be kept always vertical. We can use the same principle for the case of several beads. However, dues to the effect of Archimedes law, the EPS bead position will be changed during the hardening of plaster. This change should be mentioning during the aspiration. This method is worked well for at most 5 beads.
  - Preservation of the plaster in the syringe. After the end of aspiration, the syringe is closed by cork and paper. Then, they are placed in the support. To ensure that of the EPS beads remain in the central region, the syringe should be kept vertical during the hardening.

A.4 Appendix 4: Process for cutting and polishing of plaster sample

We use a Secotom-15 machine from struers to cut the samples. The operating principles of this machine is described by the following: The specimen is blocked in a sample holder. By the advance of a rotational disk (Cut-off wheels: $\oslash$ 125 mm, rotational speed: 3000 rpm), the specimen will be cut. Hence, to optimize the parallelism condition, the sample should be well blocked in the sample holder.

Moreover, the error parallelism depends strongly with the advanced rate of cutting disk. The small rate gives the better specimen with small error, but it requires more cutting time. We performed an analysis of its influence to the parallelism error. The result is depicted in Fig. A.3, where parallelism has been quantified by measurement introduced in section 4.3.3.4. We have selected the rate $V = 0.02$ mm/s.

- The specimen polishing

The parallelismOPT machine Tegramin-25-30 is used to polish the two bearing surfaces of samples. The operating principles of this machine is described by the following: The sample is

Figure A.1: Installation of sample in the cutting machine: (a) global view; (b) zoom view

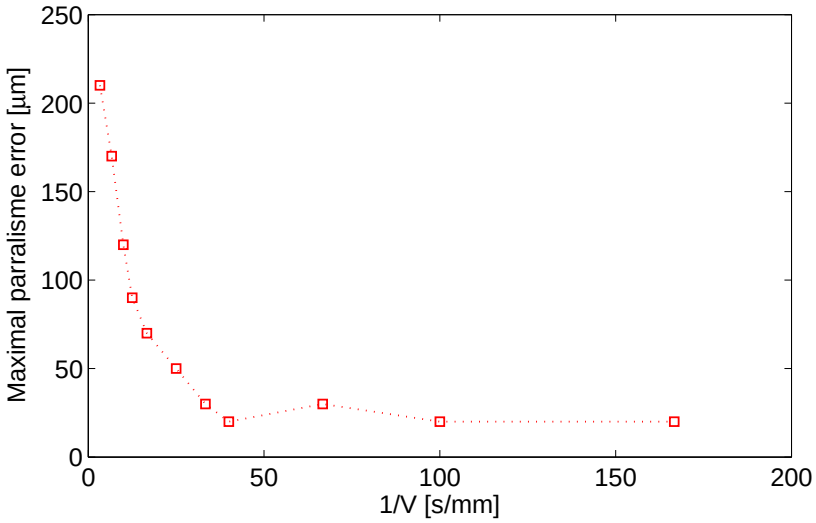

Figure A.2: Influence of cutting rate on the parallelism error

blocked in a sample holder, an then, they is placed contact with a paper (sticking on a rotational disk) by a force. Dues to the rotation of disk, the surface of specimen is polished. The details are described in Fig. **??** Similarly to the cutting process, to ensure a good parallelism, the sample must be well blocked in the sample holder. Polishing was performed with Sic papers, with grades 1200 and 2000.

A.5 Appendix 5: Identification procedure with Newton-Raphson solver for many parameters

Let us consider a pair of modeling result and experiment result, say $\mathrm{M}_{\mathrm{result}}(\boldsymbol{x})$ and $\mathrm{EXP}_{\mathrm{result}}(\boldsymbol{x})$, concerning the same typical behavior of material. Where $\boldsymbol{x} = [x_1, x_2, ...x_N]$ be N unknown material parameters to be identified. The cost function to be minimized can be described by

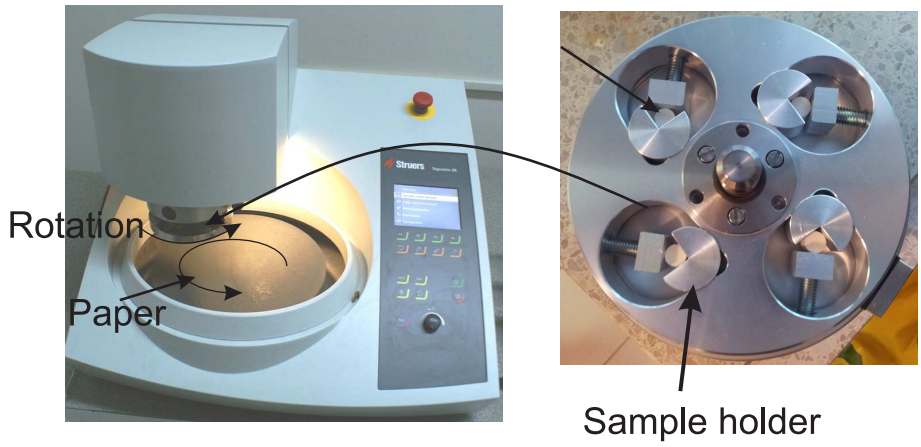

Figure A.3: Installation of sample in polishing machine

the following:

$$f(\boldsymbol{x}) = \sqrt{\left(\mathrm{M}_{\mathrm{result}}(\boldsymbol{x}) - \mathrm{EXP}_{\mathrm{result}}(\boldsymbol{x})\right)^2} \tag{A.9}$$

The inverse problem can be defined as:

$$\boldsymbol{x} = \underset{\boldsymbol{x}\in\mathbf{X}}{\mathrm{Argmin}}\left(f(\boldsymbol{x})\right) \tag{A.10}$$

The minimizing problem $f(\boldsymbol{x})$ with respect to the parameters leads to

$$\begin{cases} \dfrac{\partial f(\boldsymbol{x})}{\partial x_1} = F_1(\boldsymbol{x}) = 0 \\ \vdots \\ \dfrac{\partial f(\boldsymbol{x})}{\partial x_N} = F_N(\boldsymbol{x}) = 0 \end{cases} \tag{A.11}$$

Recall that this problem is nonlinear as $f(\mathbf{x})$ is given numerically as a result of a numerical simulation and its derivatives have to be evaluated numerically be perturbation (finite differences).

$$F(x) = \frac{\partial f(x^k)}{\partial x} = \frac{f(x + \epsilon - f(x))}{\epsilon} \tag{A.12}$$

Where ϵ is numerical parameter, $\epsilon \ll 1$. The resulting system of equations to be solved reads:

$$\mathbf{K}\Delta\boldsymbol{x} = \mathbf{F} \tag{A.13}$$

where the Hessian matrix $\mathbf{K}$ is determined by:

$$\mathbf{K} = \begin{bmatrix} \dfrac{\partial F_1(\boldsymbol{x})}{\partial x_1} & \dfrac{\partial F_1(\boldsymbol{x})}{\partial x_2} & \cdots & \dfrac{\partial F_1(\boldsymbol{x})}{\partial x_N} \\ \dfrac{\partial F_2(\boldsymbol{x})}{\partial x_1} & \dfrac{\partial F_2(\boldsymbol{x})}{\partial x_2} & \cdots & \dfrac{\partial F_2(\boldsymbol{x})}{\partial x_N} \\ \vdots & \vdots & \cdots & \vdots \\ \dfrac{\partial F_N(\boldsymbol{x})}{\partial x_1} & \dfrac{\partial F_N(\boldsymbol{x})}{\partial x_2} & \cdots & \dfrac{\partial F_N(\boldsymbol{x})}{\partial x_N} \end{bmatrix} \tag{A.14}$$

The derivatives are evaluated numerically as:

$$\frac{\partial F_i(\boldsymbol{x})}{\partial x_i} = \frac{f(x_1, x_i + 2\epsilon, ...x_N) - 2 \times f(x_1, x_i + \epsilon, ...x_N) + f(x_1, x_N)}{\epsilon^2} \tag{A.15}$$

and

$$\frac{\partial F_i(\boldsymbol{x})}{\partial x_j} = \frac{f(x_1, x_i + \epsilon, x_j + \epsilon, ...x_N) - f(x_1, x_i, x_j + \epsilon, ...x_N)}{\epsilon^2} - \frac{f(x_1, x_i + \epsilon, x_j, ...x_N) - f(x_1, x_N)}{\epsilon^2}. \tag{A.16}$$

The algorithm is presented as follows.

- **Initialization:**
  - Trial solution $\boldsymbol{x}_0$
  - Experimental data: EXP_{result}
- **WHILE** $\parallel f(x^k) \parallel > \delta, \delta << 1$
  (a) Initialize $\boldsymbol{x}^k = x^0$
  (b) Solve the FEM problem with $\mathbf{x}^k$
  (c) Compute $f_(\boldsymbol{x}^k)$
  (d) Compute the tangent matrix $\mathbf{K}$ from Eq. (A.14)
  (e) Compute $\Delta\boldsymbol{x}^{k+1}$ from Eq.(A.13)
  (f) Update $\boldsymbol{x}^{k+1} = \boldsymbol{x}^k + \Delta\boldsymbol{x}^{k+1}$
  (g) $(.)^k \leftarrow (.)^{k+1}$ and go to (a)

  END

The accurate of proposed algorithm is validated by using two virtual problem. The detail has been described in appendix A.6.

A.6 Appendix 6: Validation of the inverse approach procedure

In this section, we validate the inverse approach using Newton-Raphson algorithm by defining a reference solution substituting the experimental one by means of a preliminary numerical simulation where the material parameters to be identified are given.

A.6.1 Validation test 1: Identification of g_c from a three points test on a notched beam

In this first example, the simulation result of the three-point test on a pre-notched beam proposed in Chapter 7 is considered (with $g_c = 1.4$ N/m). The obtained load - deflection curve obtained numerically is the reference solution, reproducing the experiment data ($\text{EXP}_{\text{result}}$), called $\boldsymbol{\sigma}^{\text{ref}}$. The residual $f(g_c^k)$ is here computed as

$$f(g_c^k) = \sum_i^N \mid \sigma_{U_i}^{\text{ref}} - \sigma_{U_i}^{\text{num}}(l^k) \mid, \tag{A.17}$$

where, N is the incremental steps, $\sigma_{U_i}^{\text{ref}}$ is the stress of reference solution, $\sigma_{U_i}^{\text{num}}$ is numerical stress obtained for given fracture toughness g_c^k at iterations k. Both stress are taken at the same displacement value U_i, which is here defined as the displacement corresponding for each incremental step of numerical simulation.

The inverse procedure is stopped when the convergence criterion $f(g_c^k) < 10^{-3}$ is reached. The details of geometry and boundary conditions for the numerical model solved by phase field are depicted in Fig. A.4. The $y-$component of displacements $\overline{U}$ is prescribed on the middle of the upper edge. On the lower edge, the $y-$ components of displacements are blocked along two points, while its $x-$ components of displacements are free.

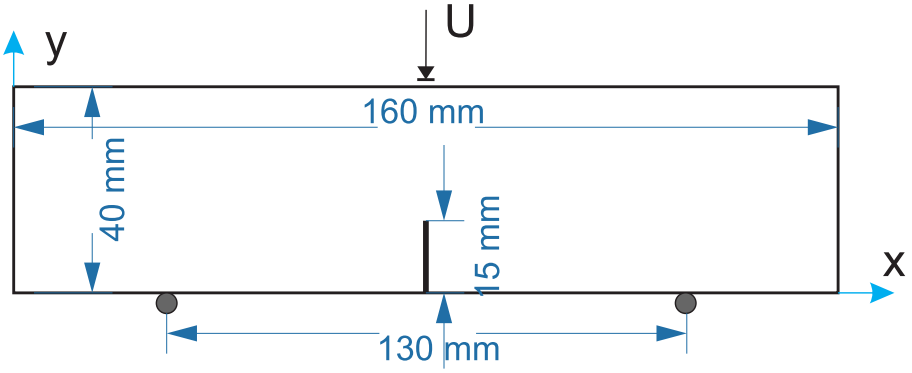

Figure A.4: Geometry and boundary condition of pre-notched beam for the inverse problem validation.

The elastic parameters have been identified experimentally and are the same as in the Chapter 7: $E = 12$ GPa, $\nu = 0.3$, and $\sigma_c = 3.9$ MPa, which gives the value of $l = 0.1$ mm. An adaptive mesh was constructed using triangular elements, with $h_{\max} = 2$ mm and $h_{\min} = 0.03$mm in the

region of the expected crack path, to satisfy the condition $h_{\min} \leq l/2$. Monotonic compressive displacement increments of $\Delta\overline{U} = -5 \times 10^{-4}$ mm have been prescribed until $d \leq 0.9$ in all elements and $\Delta\overline{U} = -5 \times 10^{-5}$ mm when $d > 0.9$ in one element; 2D plane strain assumption is adopted.

We initialize $g_c^0 = 0.1N/m$. The convergence of the Newton-Raphson algorithm is illustrated in Fig. A.5.

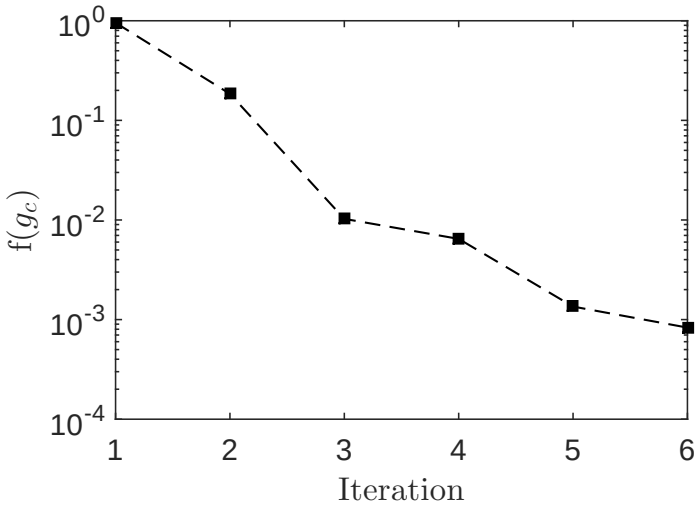

Figure A.5: Residual error for the inverse problem validation test, with respect to the iteration number.

From Fig. GcInverse, we can note that the value of g_c converges to reference solution.

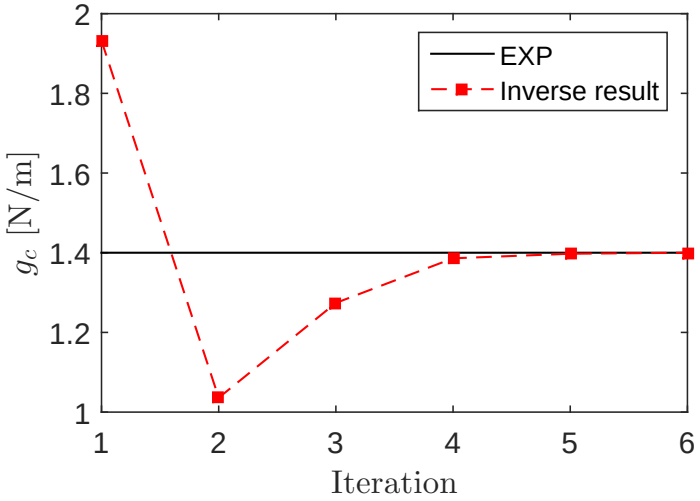

Figure A.6: Evolution of the parameter g_c during the inverse identification procedure (validation test).

A.6.2 Validation test 2: Identification of l from a three point test on unnotched beam

In the next test, we proceed as follows to validate the Newton-Raphson algorithm for the identification of the regularization length l, using a numerical solution with given l to mimic the experimental data. An uncracked beam is considered under three-point bending. We use the result of this test in Chapter 7 as the reference solution. Elastic parameters and g_c are given as $E = 12$ GPa, $\nu = 0.3$, and g_c is set to 1.4 N/m. The parameter l is assumed unknown and will be determined by the inverse procedure.

The geometry and boundary conditions for this example are the the same as in Chapter 7, and described in Fig. A.7.

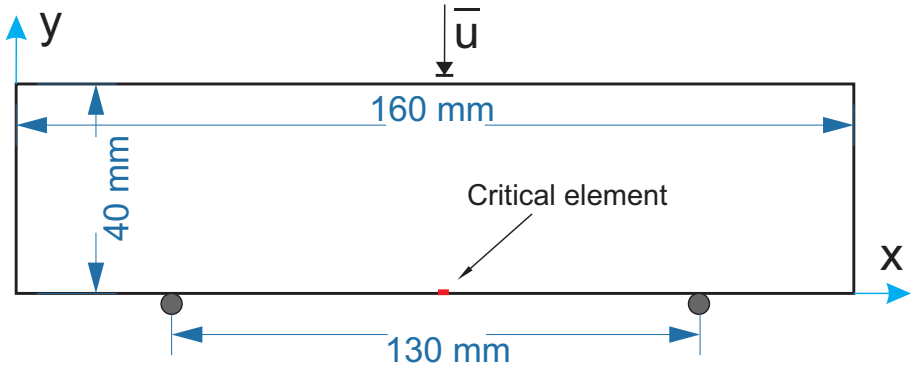

Figure A.7: 3-point bending test of non cracked beam used for validation of the inverse approach: geometry and boundary conditions.

The load-deflection curve is computed in an element located on the expected crack in the middle of the beam, as depicted in Fig. A.7 (see Chapter 7). The residual error is here defined as follows:

$$f(l^k) = \sum_{i}^{N} \mid \sigma_{U_i}^{\text{ref}} - \sigma_{U_i}^{\text{num}}(l^k) \mid, \tag{A.18}$$

where, N is the incremental steps, $\sigma_{U_i}^{\text{ref}}$ is the stress of reference solution, $\sigma_{U_i}^{\text{num}}$ is numerical stress obtained for given length scan l^k at iterations k. Both stress are taken at the same displacement value U_i, which is here defined as the displacement corresponding for each incremental step of numerical simulation.

Monotonic compressive displacement increments of $\Delta\overline{U} = -10^{-3}$ mm have been used for 400 increments for each simulation of phase field. We initialize $l^0 = 0.5$ mm. We plot the residual $f(l^k)$ with respect to the iteration number in Fig. A.8.

The convergence of the Newton-Raphson algorithm is illustrated in Fig. A.8. The evolution of the regularization with respect to the iteration number is depicted in Fig. A.9. The identified parameter converges in 4 iterations to the desired value with and error of roughly 10^{-3} in 4 iterations.

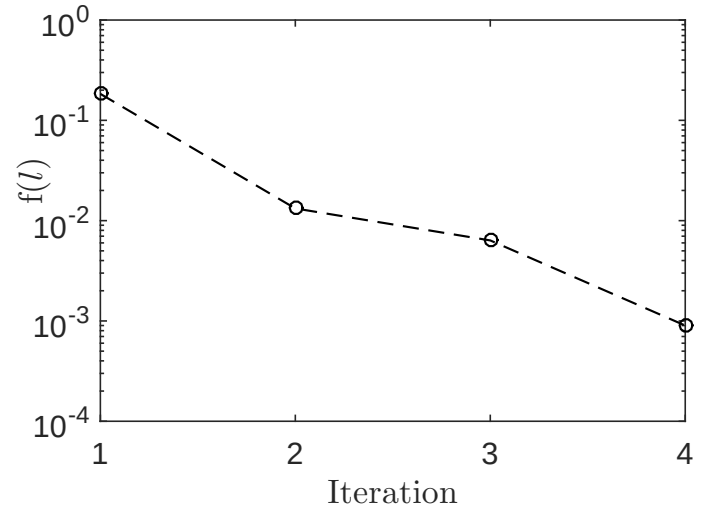

Figure A.8: Residual error $f(l)$ for the inverse problem validation test, with respect to the iteration number.

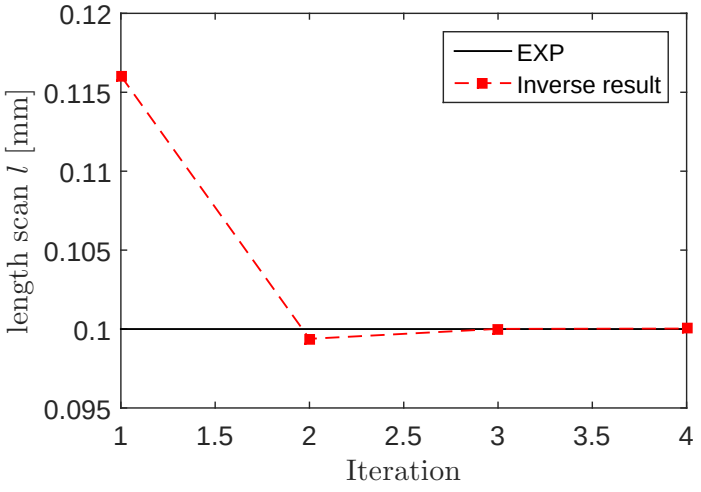

Figure A.9: Evolution of the parameter l during the inverse identification procedure (validation test).

Bibliography

[1] Fiji. *http://www.fiji.sc/Fiji*. (Cited on page 151.)

[2] Global optimization software. *http://www.mat.univie.ac.at/ neum/glopt/software_g.html*. (Cited on page 202.)

[3] Local optimization software. *http://www.mat.univie.ac.at/ neum/glopt/software_l.html*. (Cited on page 202.)

[4] *Full-field measurements and identification in solid mechanics*, chapter 6: digital image correlation. John Wiley & Sons, 2012. (Cited on pages 117, 120, 132, 137 and 154.)

[5] J. Abanto-Bueno and J. Lambros. Investigation of crack growth in functionally graded materials using digital image correlation. *Engineering Fracture Mechanics*, 69(14):1695–1711, 2002. (Cited on page 12.)

[6] A. Abdollahi and I. Arias. Phase-field modeling of crack propagation in piezoelectric and ferroelectric materials with different electromechanical crack conditions. *Journal of the Mechanics and Physics of Solids*, 60:2100–2126, 2012. (Cited on page 6.)

[7] M.D. Abràmoff, P.J. Magalhães, and S.J. Ram. Image processing with imagej. *Biophotonics international*, 11(7):36–42, 2004. (Cited on page 160.)

[8] R.D. Adams, D. Walton, J.E. Flitcroft, and D. Short. Vibration testing as a nondestructive test tool for composite materials. *Composite Reliability, ASTM STP*, 580(1975):159–175, 1975. (Cited on page 9.)

[9] D.G. Aggelis and T.P. Philippidis. Ultrasonic wave dispersion and attenuation in fresh mortar. *NDT & E International*, 37(8):617–631, 2004. (Cited on page 8.)

[10] K. Akutagwa, K. Yamaguchi, A. Yamamoto, H. Heguri, H. Jinnai, and Y. Shinbari. Mesoscopic mechanical analysis of filled elastomers. *Rubber Chemistry and Technology*, 81(2):182–189, 2008. (Cited on page 2.)

[11] L. Allais, M. Bornert, T. Bretheau, and D. Caldemaison. Experimental characterization of the local strain field in a heterogeneous elastoplastic material. *Acta Metallurgica et materialia*, 42(11):3865–3880, 1994. (Cited on pages 118 and 125.)

[12] L. Ambrosio and V.M. Tortorelli. Approximation of functional depending on jumps by elliptic functional via Γ-convergence. *Communications on Pure and Applied Mathematics*, 43(8):999–1036, 1990. (Cited on page 66.)

[13] L. Ambrosio and V.M. Tortorelli. Approximation of functionals depending on jumps by elliptic functionals via Γ-convergence. *Communications on Pure and Applied Mathematics*, 43:999–1036, 1990. (Cited on page 6.)

[14] L. Ambrosio and V.M. Tortorelli. On the approximation of free discontinuity problems. *Boll. U.M.I.*, 6-B:105–123, 1992. (Cited on page 6.)

[15] F. Amiot, M. Bornert, P. Doumalin, J.C. Dupré, M. Fazzini, J.J. Orteu, C. Poilâne, L. Robert, R. Rotinat, E. Toussaint, et al. Assessment of digital image correlation measurement accuracy in the ultimate error regime: main results of a collaborative benchmark. *Strain*, 49(6):483–496, 2013. (Cited on page 195.)

[16] H. Amor, J.J. Marigo, and C. Maurini. Regularized formulation of the variational brittle fracture with unilateral contact: Numerical experiments. *Journal of the Mechanics and Physics of Solids*, 57(8):1209–1229, 2009. (Cited on pages 6, 24, 35 and 57.)

[17] H. Amor, J.J. Marigo, and C. Maurini. Regularized formulation of the variational brittle fracture with unilateral contact: Numerical experiments. *Journal of the Mechanics and Physics of Solids*, 57(8):1209–1229, 2009. (Cited on pages 36 and 181.)

[18] L. Babout, E. Maire, and R. Fougeres. Damage initiation in model metallic materials: X-ray tomography and modelling. *Acta Materialia*, 52(8):2475–2487, 2004. (Cited on page 13.)

[19] D.S. Babu, K.G. Babu, and W. Tiong-Huan. Effect of polystyrene aggregate size on strength and moisture migration characteristics of lightweight concrete. *Cement and Concrete Composites*, 28(6):520–527, 2006. (Cited on page 103.)

[20] G.I. Barenblatt. The formation of equilibrium cracks during brittle fracture. general ideas and hypotheses. axially-symmetric cracks. *Journal of Applied Mathematics and Mechanics*, 23(3):622–636, 1959. (Cited on page 6.)

[21] B.K. Bay, T.S. Smith, D.P. Fyhrie, and M. Saad. Digital volume correlation: three-dimensional strain mapping using x-ray tomography. *Experimental mechanics*, 39(3):217–226, 1999. (Cited on page 132.)

[22] Z.P. Bazant and T.B. Belytschko. Wave propagation in a strain-softening bar: exact solution. *Journal of Engineering Mechanics*, 111(3):381–389, 1985. (Cited on page 3.)

[23] Z.P. Bazant and G. Pijaudier-Cabot. Nonlocal continuum damage, localization instability and convergence. *Journal of applied mechanics*, 55(2):287–293, 1988. (Cited on page 3.)

[24] S.R. Beissel, G.R. Johnson, and C.H. Popelar. An element-failure algorithm for dynamic crack propagation in general directions. *Engineering Fracture Mechanics*, 61(3):407–425, 1998. (Cited on page 4.)

[25] T. Belytschko, N. Moës, S. Usui, and C. Parimi. Arbitrary discontinuities in finite elements. *International Journal for Numerical Methods in Engineering*, 50(4):993–1013, 2001. (Cited on page 5.)

[26] A. Benallal and J.-J. Marigo. Bifurcation and stability issues in gradient theories with softening. *Modelling and Simulation in Materials Science and Engineering*, 15:S283–S295, 2007. (Cited on page 6.)

[27] P.E. Bernard, N. Moës, and N. Chevaugeon. Damage growth modeling using the thick level set (TLS) approach: Efficient discretization for quasi-static loadings. *Computer Methods in Applied Mechanics and Engineering*, 233:11–27, 2012. (Cited on pages 6 and 61.)

[28] J. Bisschop and J.G.M. Van Mier. How to study drying shrinkage microcracking in cement-based materials using optical and scanning electron microscopy? *Cement and Concrete Research*, 32(2):279–287, 2002. (Cited on page 10.)

[29] L. Bodelot, L. Sabatier, E. Charkaluk, and P. Dufrenoy. Experimental determination of fully-coupled kinematical and thermal fields at the scale of grains under cyclic loading. *Advanced Engineering Materials*, 11(9):723–726, 2009. (Cited on page 9.)

[30] M.J. Borden. Isogeometric analysis of phase-field models for dynamic brittle and ductile fracture. 2012. (Cited on page 26.)

[31] M.J. Borden, T.J.R Hughes, C.M. Landis, and C.V. Verhoosel. A higher-order phase-field model for brittle fracture: Formulation and analysis within the isogeometric analysis framework. *Computer Methods in Applied Mechanics and Engineering*, 273:100–118, 2014. (Cited on page 7.)

[32] M.J. Borden, C.V. Verhoosel, M.A. Scott, T.J.R Hughes, and C.M. Landis. A phase-field description of dynamic brittle fracture. *Computer Methods in Applied Mechanics and Engineering*, 217:77–95, 2012. (Cited on pages 7 and 29.)

[33] M. Bornert, F. Brémand, P. Doumalin, J.C. Dupré, M. Fazzini, M. Grédiac, F. Hild, S. Mistou, J. Molimard, J.J Orteu, et al. Assessment of digital image correlation measurement errors: methodology and results. *Experimental mechanics*, 49(3):353–370, 2009. (Cited on pages 120 and 121.)

[34] M. Bornert, J.M. Chaix, P. Doumalin, J.C. Dupré, T. Fournel, D. Jeulin, E. Maire, M. Moreaud, and H. Moulinec. Mesure tridimensionnelle de champs cinématiques par imagerie volumique pour l'analyse des matériaux et des structures. *Instrumentation, Mesure, Métrologie*, 4(3-4):43–88, 2004. (Cited on pages 132 and 133.)

[35] M. Bornert, F. Vales, H. Gharbi, and M.D. Nguyen. Multiscale full-field strain measurements for micromechanical investigations of the hydromechanical behaviour of clayey rocks. *Strain*, 46(1):33–46, 2010. (Cited on pages 11 and 117.)

[36] R. De Borst, L.J. Sluys, H.B. Muhlhaus, and J. Pamin. Fundamental issues in finite element analyses of localization of deformation. *Engineering computations*, 10(2):99–121, 1993. (Cited on page 3.)

[37] B. Bourdin. Numerical implementation of the variational formulation of quasi-static brittle fracture. *Interface Free Bound.*, 9:411–430, 2007. (Cited on page 6.)

[38] B. Bourdin, G.A. Francfort, and J.J. Marigo. Numerical experiments in revisited brittle fracture. *Journal of the Mechanics and Physics of Solids*, 48:797–826, 2000. (Cited on page 6.)

[39] B. Bourdin, G.A. Francfort, and J.J. Marigo. *The Variational Approach to Fracture*. Springer-Verlag, Berlin, 2008. (Cited on page 6.)

[40] B. Bourdin, C.J. Larsen, and C.L. Richardson. A time-discrete model for dynamic fracture based on crack regularization. *International journal of fracture*, 168(2):133–143, 2011. (Cited on pages 6 and 7.)

[41] D.P. Braides. *Approximation of Free Discontinuity Problems*. Springer Verlag: Berlin, 1998. (Cited on pages 6, 22 and 25.)

[42] D.P. Braides. Γ-*Convergence for Beginners*. Oxford University Press: New York, 2002. (Cited on page 6.)

[43] P.R.H.J Brekelmans and R. de Borst. Gradient enhanced damage for quasi-brittle materials. 1996. (Cited on page 4.)

[44] E. Budyn, G. Zi, N. Moës, and T. Belytschko. A method for multiple crack growth in brittle materials without remeshing. *International journal for numerical methods in engineering*, 61(10):1741–1770, 2004. (Cited on page 5.)

[45] J.Y. Buffiere, E. Ferrie, H. Proudhon, and W. Ludwig. Three-dimensional visualisation of fatigue cracks in metals using high resolution synchrotron x-ray micro-tomography. *Materials science and technology*, 22(9):1019–1024, 2006. (Cited on page 14.)

[46] J.Y. Buffiere, E. Maire, J. Adrien, J.P. Masse, and E. Boller. In situ experiments with x ray tomography: an attractive tool for experimental mechanics. *Experimental mechanics*, 50(3):289–305, 2010. (Cited on page 14.)

[47] J.Y. Buffiere, E. Maire, P. Cloetens, G. Lormand, and R. Fougeres. Characterization of internal damage in a mmc p using x-ray synchrotron phase contrast microtomography. *Acta materialia*, 47(5):1613–1625, 1999. (Cited on page 13.)

[48] M. Buliga. Energy minimizing brittle crack propagation. *Journal of Elasticity* ., 52:201–238, 1999. (Cited on page 6.)

[49] W. Fabian C. Miehe, H. Martina. A phasefield model for rate-independent crack propagation: Robust algorithmic implementation based on operator splits. *Computer Methods in Applied Mechanics and Engineering*, 199:2765–2778, 2010. (Cited on pages 66, 68 and 70.)

[50] G.T. Camacho and M. Ortiz. Computational modelling of impact damage in brittle materials. *International Journal of solids and structures*, 33(20):2899–2938, 1996. (Cited on page 6.)

[51] N. Carrère, E. Martin, and J. Lamon. The influence of the interphase and associated interfaces on the deflection of matrix cracks in ceramic matrix composites. *Composites Part A: Applied Science and Manufacturing*, 31(11):1179–1190, 2000. (Cited on page 60.)

[52] P. Cawley and R.D. Adams. The location of defects in structures from measurements of natural frequencies. *The Journal of Strain Analysis for Engineering Design*, 14(2):49–57, 1979. (Cited on page 9.)

[53] F. Cazes and N. Moës. Comparison of a phase-field model and of a thick level set model for brittle and quasi-brittle fracture. *International Journal for Numerical Methods in Engineering* ., In press, 2015. (Cited on pages 6 and 61.)

[54] N. Chandra, H. Li, C. Shet, and H. Ghonem. Some issues in the application of cohesive zone models for metal–ceramic interfaces. *International Journal of Solids and Structures*, 39(10):2827–2855, 2002. (Cited on page 6.)

[55] C. Chateau. *Analyse expérimentale et modélisation micromécaniques du comportement élastique et de l'endommagement de composites SiC/SiC unidirectionnels*. PhD thesis, Ecole Polytechnique X, 2011. (Cited on page 12.)

[56] Y. Chen, M. Pani, F. Taddei, and C. Mazzà. Large-scale finite element analysis of human cancellous bone tissue micro computer tomography data: a convergence study. *J Biomech. Eng.-T. ASME*, 136(10):101013, 2014. (Cited on page 2.)

[57] C. Comi. A non-local model with tension and compression damage mechanisms. *European Journal of Mechanics-A/Solids*, 20(1):1–22, 2001. (Cited on page 24.)

[58] L. Contrafatto and M. Cuomo. Comparison of two forms of strain decomposition in an elastic -plastic damaging model for concrete. *Modelling and Simulation in Materials Science and Engineering*, 15(4):S405, 2007. (Cited on page 25.)

[59] François Cuvelier, Caroline Japhet, and Gilles Scarella. An efficient way to perform the assembly of finite element matrices in matlab and octave. *INRIA Research Report*, 2013. (Cited on page 33.)

[60] D. Darwin, M.N. Abou-Zeid, and K.W. Ketcham. Automated crack identification for cement paste. *Cement and concrete research*, 25(3):605–616, 1995. (Cited on page 12.)

[61] S. Das, A. Kizilkanat, and N. Neithalath. Crack propagation and strain localization in metallic particulate-reinforced cementitious mortars. *Materials & Design*, 79:15–25, 2015. (Cited on page 12.)

[62] J. Dautriat, M. Bornert, N. Gland, A. Dimanov, and J. Raphanel. Localized deformation induced by heterogeneities in porous carbonate analysed by multi-scale digital image correlation. *Tectonophysics*, 503(1):100–116, 2011. (Cited on pages 11, 12, 120, 121, 122, 125, 144 and 176.)

[63] C. Daux, N. Moës, J. Dolbow, and T. Belytschko. Arbitrary branched and intersecting cracks with the extended finite element method. *International Journal for Numerical Methods in Engineering*, 48:1741–1760, 2000. (Cited on page 5.)

[64] R. de Borst, J.J.C. Remmers, and C.V. Verhoosel. Evolving discontinuities and cohesive fracture. *Procedia IUTAM*, 10:125–137, 2014. (Cited on page 83.)

[65] S.C. de Wolski, J.E. Bolander, and E.N. Landis. An in-situ x-ray microtomography study of split cylinder fracture in cement-based materials. *Experimental Mechanics*, 54(7):1227–1235, 2014. (Cited on page 102.)

[66] M.J. Van den Bosch, P.J.G Schreurs, and M.D.G. Geers. An improved description of the exponential xu and needleman cohesive zone law for mixed-mode decohesion. *Engineering Fracture Mechanics*, 73(9):1220–1234, 2006. (Cited on page 71.)

[67] F. Desplentere, S.V. Lomov, D.L. Woerdeman, I. Verpoest, M. Wevers, and A. Bogdanovich. Micro-ct characterization of variability in 3d textile architecture. *Composites Science and Technology*, 65(13):1920–1930, 2005. (Cited on page 14.)

[68] H.B. Dhia and G. Rateau. The arlequin method as a flexible engineering design tool. *International journal for numerical methods in engineering*, 62(11):1442–1462, 2005. (Cited on page 4.)

[69] P. Doumalin and M. Bornert. Micromechanical applications of digital image correlation techniques. In *Interferometry in Speckle Light*, pages 67–74. Springer, 2000. (Cited on page 120.)

[70] D.S. Dugdale. Yielding of steel sheets containing slits. *Journal of the Mechanics and Physics of Solids*, 8(2):100–104, 1960. (Cited on page 6.)

[71] R. Fan and J. Fish. The rs-method for material failure simulations. *International journal for numerical methods in engineering*, 73(11):1607, 2008. (Cited on page 4.)

[72] B.P. Flannery, H.W. Deckman, W.G. Roberge, and K.L. Damico. 3-dimensional X-ray microtomography. *Science*, 487:1439–1444, 1987. (Cited on pages 2 and 20.)

[73] J. Fortin, S. Stanchits, G. Dresen, and Y. Guéguen. Acoustic emission and velocities associated with the formation of compaction bands in sandstone. *Journal of Geophysical Research: Solid Earth (1978–2012)*, 111(B10), 2006. (Cited on page 8.)

[74] J. Fortin, S. Stanchits, G. Dresen, and Y. Gueguen. Acoustic emissions monitoring during inelastic deformation of porous sandstone: comparison of three modes of deformation. In *Rock Physics and Natural Hazards*, pages 823–841. Springer, 2009. (Cited on page 8.)

[75] G.A. Francfort and J.J. Marigo. Revisiting brittle fracture as an energy minimization problem. *Journal of the Mechanics and Physics of Solids*, 46(8):1319–1342, 1998. (Cited on pages 6 and 22.)

[76] M. Frémond and B. Nedjar. Damage, gradient of damage and principle of virtual power. *Int. J. Sol. Struct.*, 33:1083–1103, 1996. (Cited on page 6.)

[77] L.B. Freund. *Dynamic Fracture Mechanics*. Cambridge University Press, Cambridge, 1990. (Cited on page 3.)

[78] Y. Fujita, Y. Mitani, and Y. Hamamoto. A method for crack detection on a concrete structure. In *Pattern Recognition, 2006. ICPR 2006. 18th International Conference on*, volume 3, pages 901–904. IEEE, 2006. (Cited on page 12.)

[79] J.J. Marigo G.A. Francfort. Revisiting brittle fracture as an energy minimization problem. *Journal of the Mechanics and Physics of Solids*, 46:1319–1342, 1998. (Cited on page 68.)

[80] A. Godman and A. Bentur. Bond effects in high-strength silica fume concretes. *ACI Materials Journal*, 86(5), 1989. (Cited on page 60.)

[81] H.C. Gran. Fluorescent liquid replacement technique. a means of crack detection and water: binder ratio determination in high strength concretes. *Cement and concrete research*, 25(5):1063–1074, 1995. (Cited on page 10.)

[82] A. Gravouil, N. Moës, and T. Belytschko. Non-planar 3D crack growth by the extended finite element and level sets-partii: level set update. *International Journal for Numerical Methods in Engineering.*, 53(11):2569–86, 2002. (Cited on page 5.)

[83] A.A. Griffith. The phenomena of rupture and flow in solids. *Phil. Trans. Royal Soc. Lond. A*, 221:163–198, 1921. (Cited on page 3.)

[84] M.E. Gurtin. On the energy release rate in quasistatic elastic crack propagation. *J. Elasticity*, 9(2):187–195, 1979. (Cited on page 3.)

[85] M.E. Gurtin. Thermodynamics and the Griffith's criterion for brittle fracture. *International Journal of Solids and Structures.*, 15:553–560, 1979. (Cited on page 3.)

[86] D.E. Hardt and J.M. Katz. Ultrasonic measurement of weld penetration. *Welding Journal*, 63(9):273s–281s, 1984. (Cited on page 8.)

[87] T. Hatada and F. Saitoh. Crack detection method for drain by using directional smoothing. *IEEJ Transactions on Electronics, Information and Systems*, 127:241–246, 2007. (Cited on page 12.)

[88] E. Heripre, M. Dexet, J. Crepin, L. Gélebart, A. Roos, M. Bornert, and D. Caldemaison. Coupling between experimental measurements and polycrystal finite element calculations for micromechanical study of metallic materials. *International Journal of Plasticity*, 23(9):1512–1539, 2007. (Cited on page 203.)

[89] F. Hild, A. Fanget, J. Adrien, E. Maire, S. Roux, et al. Three-dimensional analysis of a tensile test on a propellant with digital volume correlation. *Archives of Mechanics*, 63(5-6):1–20, 2011. (Cited on page 14.)

[90] F. Hild and S. Roux. Evaluating damage with digital image correlation: A. introductory remarks and detection of physical damage. In *Handbook of Damage Mechanics*, pages 1255–1275. Springer, 2014. (Cited on page 132.)

[91] F. Hild, S. Roux, D. Bernard, G. Hauss, and M. Rebai. On the use of 3d images and 3d displacement measurements for the analysis of damage mechanisms in concrete-like materials. In *VIII International Conference on Fracture Mechanics of Concrete and Concrete Structures*, pages 1–12, 2013. (Cited on pages 14 and 132.)

[92] M. Hofacker and C. Miehe. A phase field model of dynamic fracture: Robust field updates for the analysis of complex crack patterns. *International Journal for Numerical Methods in Engineering.*, 93:276–301, 2013. (Cited on page 6.)

[93] M. Holl, T. Rogge, S. Loehnert, P. Wriggers, and R. Rolfes. 3D multiscale crack propagation using the XFEM applied to a gas turbine blade. *Computational Mechanics.*, 53:173–188, 2014. (Cited on page 5.)

[94] D.B.P. Huynh and T. Belytschko. The extended finite element method for fracture in composite materials. *International Journal for Numerical Methods in Engineering.*, 77:214–239, 2009. (Cited on page 5.)

[95] C. Ibarra-Castanedo, M. Genest, J.M Piau, S. Guibert, A. Bendada, and X.P.V Maldague. Active infrared thermography techniques for the nondestructive testing of materials. *Capter XIV of the book:ŞUltrasonic and Advanced Methods for Nondestructive Testing and Material CharacterizationŤ, ed. Chen CH*, pages 325–348, 2007. (Cited on page 9.)

[96] A. Ingraffea and V. Saouma. Numerical modelling of discrete crack propagation in reinforced and plain concrete. In *In: Sih, G., Di Tommaso, A. (Eds.), Fracture Mechanics of Concrete. Martinus Nijhoff Publishers*, pages 171–225, Dordrecht, 1984. (Cited on page 4.)

[97] C. Jaeger. *Rock mechanics and engineering*. Cambridge University Press, 1979. (Cited on pages 42, 86 and 89.)

[98] R.P. Janeiro and H.H. Einstein. Experimental study of the cracking behavior of specimens containing inclusions (under uniaxial compression). *International Journal of Fracture*, 164(1):83–102, 2010. (Cited on page 110.)

[99] M. Jirasek. Nonlocal models for damage and fracture: comparison of approaches. *International Journal of Solids and Structures.*, 35:4133–4145, 1998. (Cited on page 3.)

[100] M. Jirásek and Z.P. Bazant. *Inelastic analysis of structures*. John Wiley & Sons, 2002. (Cited on page 4.)

[101] G.R. Johnson and R.A. Stryk. Eroding interface and improved tetrahedral element algorithms for high-velocity impact computations in three dimensions. *International Journal of Impact Engineering*, 5(1):411–421, 1987. (Cited on page 4.)

[102] T. Kanit, S. Forest, I. Galliet, V. Mounoury, and D. Jeulin. Determination of the size of the representative volume element for random composites: statistical and numerical approach. *International Journal of Solids and Structures.*, 40(13-14):3647 – 3679, 2003. (Cited on page 93.)

[103] A. Karma, D. Kessler, and H. Levine. Phase-field model of mode iii dynamic fracture. *Physical Review Letters*, 87(4):45501, 2001. (Cited on page 26.)

[104] K. Kesner, M.J. Sansalone, and R.W. Poston. Detection and quantification of distributed damage in concrete using transient stress waves. *ACI Materials Journal*, 101(4), 2004. (Cited on page 8.)

[105] M. Kikuchi, Y. Wada, Y. Shintaku, K. Suga, and Y. Li. Fatigue crack growth simulation in heterogeneous material using s-version FEM. *Int. J. Fatigue*, 58, 2014. (Cited on page 4.)

[106] L.I. Knab, H.N. Walker, J.R. Clifton, and E.R. Fuller. Fluorescent thin sections to observe the fracture zone in mortar. *Cement and concrete research*, 14(3):339–344, 1984. (Cited on pages 10 and 11.)

[107] D.C. Ko, B.M Kim, and J.C. Choi. Finite-element simulation of the shear process using the element-kill method. *Journal of Materials Processing Technology*, 72(1):129–140, 1997. (Cited on page 4.)

[108] J. Krautkrâmer and H. Krautkrâmer. Ultrasonic testing of materials, 1990. (Cited on page 8.)

[109] C. Kuhn and R. Müller. A continuum phase field model for fracture. *Engineering Fracture Mechanics*, 77(18):3625–3634, 2010. (Cited on page 7.)

[110] G. Lancioni and G. Royer-Carfagni. The variational approach to fracture mechanics. a practical application to the French Panthéon in Paris. *Journal of elasticity*, 95(1-2):1–30, 2009. (Cited on page 7.)

[111] E.N. Landis and D.T. Keane. X-ray microtomography for fracture studies in cement-based materials. In *SPIE's International Symposium on Optical Science, Engineering, and Instrumentation*, pages 105–113. International Society for Optics and Photonics, 1999. (Cited on page 13.)

[112] E.N. Landis and E.N. Nagy. Three-dimensional work of fracture for mortar in compression. *Engineering Fracture Mechanics*, 65(2):223–234, 2000. (Cited on page 102.)

[113] E.N. Landis, E.N. Nagy, and D.T. Keane. Microstructure and fracture in three dimensions. *Engineering Fracture Mechanics*, 70(7):911–925, 2003. (Cited on pages 13 and 102.)

[114] E.N. Landis, T. Zhang, E.N. Nagy, G. Nagy, and W.R. Franklin. Cracking, damage and fracture in four dimensions. *Materials and Structures*, 40(4):357–364, 2007. (Cited on page 14.)

[115] C. Landron, O. Bouaziz, E. Maire, and J. Adrien. Characterization and modeling of void nucleation by interface decohesion in dual phase steels. *Scripta Materialia*, 63(10):973–976, 2010. (Cited on page 14.)

[116] C. Landron, E. Maire, O. Bouaziz, J. Adrien, L. Lecarme, and A. Bareggi. Validation of void growth models using x-ray microtomography characterization of damage in dual phase steels. *Acta Materialia*, 59(20):7564–7573, 2011. (Cited on page 14.)

[117] D. Lasry and T. Belytschko. Localization limiters in transient problems. *International Journal of Solids and Structures*, 24(6):581–597, 1988. (Cited on page 3.)

[118] K.M. Lee and O. Buyukozturk. Fracture mechanics parameters influencing the mechanical properties of high-performance concrete. *ACI Special Publication*, 149, 1994. (Cited on page 60.)

[119] D. Leguillon. Strength or toughness? a criterion for crack onset at a notch. *European Journal of Mechanics-A/Solids*, 21(1):61–72, 2002. (Cited on pages 181 and 186.)

[120] N. Lenoir, M. Bornert, J. Desrues, P. Bésuelle, and G. Viggiani. Volumetric digital image correlation applied to x-ray microtomography images from triaxial compression tests on argillaceous rock. *Strain*, 43(3):193–205, 2007. (Cited on pages 133 and 146.)

[121] T. Liebe, P. Steinmann, and A. Benallal. Theoretical and computational numerical aspects of a thermodynamically consistent framework for geometrically linear gradient damage. *Computer Methods in Applied Mechanics and Engineering*, 190:6555–6576, 2001. (Cited on page 6.)

[122] N. Limodin, J. Réthoré, J.Y. Buffière, A. Gravouil, F. Hild, and S. Roux. Crack closure and stress intensity factor measurements in nodular graphite cast iron using three-dimensional correlation of laboratory x-ray microtomography images. *Acta materialia*, 57(14):4090–4101, 2009. (Cited on page 14.)

[123] N. Limodin, J. Réthoré, J.Y. Buffiere, F. Hild, S. Roux, W. Ludwig, J. Rannou, and A. Gravouil. Influence of closure on the 3d propagation of fatigue cracks in a nodular cast iron investigated by x-ray tomography and 3d volume correlation. *Acta Materialia*, 58(8):2957–2967, 2010. (Cited on page 14.)

[124] N. Liu and B. Chen. Experimental study of the influence of eps particle size on the mechanical properties of eps lightweight concrete. *Construction and Building Materials*, 68:227–232, 2014. (Cited on page 103.)

[125] E. Lorentz and A. Benallal. Gradient constitutive relations: numerical aspects and applications to gradient damage. *Computer Methods in Applied Mechanics and Engineering*, 194:5191–5220, 2005. (Cited on pages 3 and 6.)

[126] S. Lu, E.N. Landis, and D.T. Keane. X-ray microtomographic studies of pore structure and permeability in portland cement concrete. *Materials and Structures*, 39(6):611–620, 2006. (Cited on pages 13 and 103.)

[127] Y. Mahadik, K.A.R. Brown, and S.R. Hallett. Characterisation of 3d woven composite internal architecture and effect of compaction. *Composites Part A: Applied Science and Manufacturing*, 41(7):872–880, 2010. (Cited on page 14.)

[128] X. Maldague, A. Ziadi, and M. Klein. Double pulse infrared thermography. *NDT & E International*, 37(7):559–564, 2004. (Cited on page 9.)

[129] G. Dal Maso. *An Introduction to* Γ*-Convergence*. Birkhäuser Verlag: Boston, 1993. (Cited on page 6.)

[130] F. Mathieu, P. Aimedieu, J.M. Guimard, and F. Hild. Identification of interlaminar fracture properties of a composite laminate using local full-field kinematic measurements and finite element simulations. *Composites Part A: Applied Science and Manufacturing*, 49:203–213, 2013. (Cited on page 14.)

[131] F. Mathieu, F. Hild, and volume=36 number=1 pages=146–154 year=2012 publisher=Elsevier S. Roux, journal=International Journal of Fatigue. Identification of a crack propagation law by digital image correlation. (Cited on page 12.)

[132] S. May, Julien J. Vignollet, and Rene De Borst. A numerical assessment of phase-field models for brittle and cohesive fracture: γ-convergence and stress oscillations. *European Journal of Mechanics-A/Solids*, 52:72–84, 2015. (Cited on pages 33 and 234.)

[133] S.R. McNeill, W.H. Peters, and M.A. Sutton. Estimation of stress intensity factor by digital image correlation. *Engineering fracture mechanics*, 28(1):101–112, 1987. (Cited on page 12.)

[134] S. Meille, M. Saâdaoui, P. Reynaud, and G. Fantozzi. Mechanisms of crack propagation in dry plaster. *Journal of the European Ceramic Society*, 23(16):3105–3112, 2003. (Cited on page 110.)

[135] J.M. Melenk and I. Babuška. The partition of unity finite element method: basic theory and applications. *Computer Methods in Applied Mechanics and Engineering*, 139(1):289–314, 1996. (Cited on page 5.)

[136] C. Meola and G.M. Carlomagno. Recent advances in the use of infrared thermography. *Measurement science and technology*, 15(9):R27, 2004. (Cited on page 9.)

[137] C. Miehe, M. Hofacker, L.M. Schänzel, and F. Aldakheel. Phase field modeling of fracture in multi-physics problems. part ii. coupled brittle-to-ductile failure criteria and crack propagation in thermo-elastic–plastic solids. *Computer Methods in Applied Mechanics and Engineering*, 2014. (Cited on page 7.)

[138] C. Miehe, M. Hofacker, and F. Welschinger. A phase field model for rate-independent crack propagation: Robust algorithmic implementation based on operator splits. *Computer Methods in Applied Mechanics and Engineering*, 199:2776–2778, 2010. (Cited on pages 7, 20, 21, 26, 31, 34, 38, 39 and 57.)

[139] C. Miehe and M. Lambrecht. Algorithms for computation of stresses and elasticity moduli in terms of seth-hill's family of generalized strain tensors. *Comm. Num. Meth. Engng.*, 17:337–353, 2001. (Cited on pages 25 and 31.)

[140] C. Miehe and L.M. Schänzel. Phase field modeling of fracture in rubbery polymers. part i: Finite elasticity coupled with brittle failure. *Journal of the Mechanics and Physics of Solids*, 65:93–113, 2014. (Cited on page 7.)

[141] C. Miehe, L.M. Schänzel, and H. Ulmer. Phase field modeling of fracture in multi-physics problems. part i. balance of crack surface and failure criteria for brittle crack propagation in thermo-elastic solids. *Computer Methods in Applied Mechanics and Engineering*, 2014. (Cited on page 7.)

[142] C. Miehe, F. Welschinger, and M. Hofacker. A phase field model of electromechanical fracture. *Journal of the Mechanics and Physics of Solids*, 58:1716–1740, 2010. (Cited on pages 6 and 7.)

[143] C. Miehe, F. Welschinger, and M. Hofacker. Thermodynamically consistent phase-field models of fracture: Variational principles and multi-field FE implementations. *Interna-*

tional Journal for Numerical Methods in Engineering., 83:1273–1311, 2010. (Cited on pages 7 and 20.)

[144] K. Miled, R. Le Roy, K. Sab, and C. Boulay. Compressive behavior of an idealized eps lightweight concrete: size effects and failure mode. *Mechanics of Materials*, 36(11):1031–1046, 2004. (Cited on pages 42, 103 and 104.)

[145] K. Miled, K. Sab, and K. Le Roy. Particle size effect on eps lightweight concrete compressive strength: experimental investigation and modelling. *Mechanics of Materials*, 39(3):222–240, 2007. (Cited on page 103.)

[146] K. Miled, K. Sab, and R. Le Roy. Particle size effect on eps lightweight concrete compressive strength: Experimental investigation and modelling. *Mechanics of Materials*, 39:222–240, 2007. (Cited on page 47.)

[147] S. Mindess and S. Diamond. A preliminary sem study of crack propagation in mortar. *Cement and Concrete Research*, 10(4):509–519, 1980. (Cited on page 12.)

[148] A. Mitiche and P. Bouthemy. Computation and analysis of image motion: A synopsis of current problems and methods. *International journal of computer vision*, 19(1):29–55, 1996. (Cited on page 133.)

[149] N. Moës, J. Dolbow, and T. Belytschko. A finite element method for crack growth without remeshing. *International Journal for Numerical Methods in Engineering*, 46(1):131–150, 1999. (Cited on pages 5 and 61.)

[150] N. Moës, A. Gravouil, and T. Belytschko. Non-planar 3d crack growth by the extended finite element and level set part i: Mechanical model. *International Journal for Numerical Methods in Engineering*, 53(11):2549–2568, 2002. (Cited on page 5.)

[151] N. Moës, C. Stolz, P.E. Bernard, and N. Chevaugeon. A level set based model for damage growth: the thick level set approach. *International Journal for Numerical Methods in Engineering*, 86(3):358–380, 2011. (Cited on page 6.)

[152] D. Mumford and J. Shah. Optimal approximations by piecewise smooth functions and associated variational problems. *Communications on pure and applied mathematics*, 42(5):577–685, 1989. (Cited on pages 6 and 66.)

[153] A. Needleman. A continuum model for void nucleation by inclusion debonding. *Journal of applied mechanics*, 54(3):525–531, 1987. (Cited on page 6.)

[154] K.M. Nemati. Fracture analysis of concrete using scanning electron microscopy. *Scanning*, 19(6):426–430, 1997. (Cited on page 12.)

[155] K.M. Nemati, P.J.M. Monteiro, and K.L. Scrivener. Analysis of compressive stress-induced cracks in concrete. *ACI Materials Journal*, 95(5), 1998. (Cited on page 10.)

[156] TT. Nguyen, J. Yvonnet, Q-Z. Zhu, M. Bornert, and C. Chateau. On the choice of numerical parameters in the phase field method for simulating crack initiation with experimental validation. *submitted*, 2015. (Cited on pages 33 and 181.)

[157] TT. Nguyen, J. Yvonnet, Q-Z. Zhu, M. Bornert, and C. Chateau. A phase-field method for computational modeling of interfacial damage interacting with crack propagation in realistic microstructures obtained by microtomography. *submitted*, 2015. (Cited on page 60.)

[158] TT. Nguyen, J. Yvonnet, Q-Z. Zhu, M. Bornert, and C. Chateau. A phase field method to simulate crack nucleation and propagation in strongly heterogeneous materials from direct imaging of their microstructure. *Engineering Fracture Mechanics*, 139:18–39, 2015. (Cited on pages 20, 31 and 73.)

[159] M. Ortiz and A. Pandolfi. Finite-deformation irreversible cohesive elements for three-dimensional crack-propagation analysis. *International Journal for Numerical Methods in Engineering*, 44(9):1267–1282, 1999. (Cited on page 6.)

[160] S. Osher and N. Paragios. *Geometric level set methods in imaging, vision, and graphics*. Springer, 2003. (Cited on page 74.)

[161] A. Pandolfi and M. Ortiz. An eigenerosion approach to brittle fracture. *International Journal for Numerical Methods in Engineering*, 92(8):694–714, 2012. (Cited on page 4.)

[162] E. Papa and A. Taliercio. Anisotropic damage model for the multiaxial static and fatigue behaviour of plain concrete. *Engineering Fracture Mechanics*, 55(2):163–179, 1996. (Cited on page 25.)

[163] F. Paradis and W.J. Weiss. Using x-ray tomography to image cracks in cement pastes. In *Proc., Int. Conf. on High-Performance Fiber-Reinforced Concrete Composites (HPFRCC)*, page 8. Univ. of Stuttgart Stuttgart, Germany, 2007. (Cited on page 13.)

[164] R.H.J Peerlings, R. De Borst, W.A.M. Brekelmans, and M.G.D. Geers. Localisation issues in local and nonlocal continuum approaches to fracture. *European Journal of Mechanics-A/Solids*, 21(2):175–189, 2002. (Cited on page 4.)

[165] R.H.J. Peerlings, R. de Borst, W.A.M. Brekelmans, and H.P.J. de Vree. Gradient-enhanced damage for quasi-brittle materials. *International Journal for Numerical Methods in Engineering.*, 39(39):3391–3403, 1996. (Cited on pages 3 and 6.)

[166] K. Pham and J.-J. Marigo. The variational approach to damage: I. the foundations. *C. R. Mecanique*, 338:191–198, 2010. (Cited on page 6.)

[167] S.T. Pietruszczak and Z. Mroz. Finite element analysis of deformation of strain-softening materials. *International Journal for Numerical Methods in Engineering*, 17(3):327–334, 1981. (Cited on page 3.)

[168] G. Pijaudier-Cabot and Z. Bazant. Nonlocal damage theory. *Journal of Engineering Mechanics*, 113:1512–1533, 1987. (Cited on pages 3 and 4.)

[169] G. Pijaudier-Cabot and D. Grégoire. A review of non local continuum damage: Modelling of failure? *Networks and Heterogeneous Media*, 9(4):575–597, 2014. (Cited on page 4.)

[170] O. Pop, M. Meite, F. Dubois, and J. Absi. Identification algorithm for fracture parameters by combining dic and fem approaches. *International journal of fracture*, 170(2):101–114, 2011. (Cited on page 12.)

[171] W.H. Prosser, K.E. Jackson, S. Kellas, B.T. Smith, J. McKeon, and A. Friedman. Advanced waveform-based acoustic emission detection of matrix cracking in composites. *Materials evaluation*, 53(9):1052–1058, 1995. (Cited on page 8.)

[172] S. Ramtani, Y. Berthaud, and J. Mazars. Orthotropic behavior of concrete with directional aspects: modelling and experiments. *Nuclear Engineering and Design*, 133(1):97–111, 1992. (Cited on page 24.)

[173] Y.R. Rashid. Analysis of reinforced concrete pressure vessels. *Nucl. Eng. Des.*, 7:334–344, 1968. (Cited on page 3.)

[174] L. Reimer. Scanning electron microscopy: physics of image formation and microanalysis. *Measurement Science and Technology*, 11(12):1826, 2000. (Cited on page 11.)

[175] W. Ren, Z. Yang, R. Sharma, C.H. Zhang, and P.J. Withers. Two-dimensional x-ray ct image based mesoscale fracture modelling of concrete. *Engineering Fracture Mechanics.*, 133:24–39, 2015. (Cited on page 2.)

[176] J. Réthoré, A. Gravouil, F. Morestin, and A. Combescure. Estimation of mixed-mode stress intensity factors using digital image correlation and an interaction integral. *International Journal of Fracture*, 132(1):65–79, 2005. (Cited on page 12.)

[177] J. Réthoré, J.P. Tinnes, S. Roux, J.Y. Buffière, and F. Hild. Extended three-dimensional digital image correlation (x3d-dic). *Comptes Rendus Mécanique*, 336(8):643–649, 2008. (Cited on page 132.)

[178] F. Roli. Measure of texture anisotropy for crack detection on textured surfaces. *Electronics Letters*, 32(14):1274–1275, 1996. (Cited on page 12.)

[179] R. Romani. *Rupture en compression des structures hétérogènes à base de matériaux quasi-fragiles*. PhD thesis, Paris 6, 2013. (Cited on pages xix, 16, 45, 46, 110, 112, 113, 185, 189, 190, 191, 204, 205 and 238.)

[180] R. Romani, M. Bornert, D. Leguillon, R. Le Roy, and K. Sab. Detection of crack onset in double cleavage drilled specimens of plaster under compression by digital image correlation-theoretical predictions based on a coupled criterion. *European Journal of Mechanics -*

A/Solids, 51:172–182, 2015. (Cited on pages xix, 12, 33, 37, 46, 96, 110, 129, 182, 183, 184, 186, 190, 202 and 205.)

[181] J.L. Rose. *Ultrasonic waves in solid media*. Cambridge University press, 2004. (Cited on page 8.)

[182] J.G. Rots. *Computational modeling of concrete fracture*. PhD thesis, Technische Hogeschool Delft, 1988. (Cited on pages 95 and 226.)

[183] S. Roux and F. Hild. Stress intensity factor measurements from digital image correlation: post-processing and integrated approaches. *International Journal of Fracture*, 140(1-4):141–157, 2006. (Cited on pages 12 and 121.)

[184] S. Roux, F. Hild, P. Viot, and D. Bernard. Three-dimensional image correlation from x-ray computed tomography of solid foam. *Composites Part A: Applied science and manufacturing*, 39(8):1253–1265, 2008. (Cited on page 132.)

[185] S. Roux, J. Réthoré, and F. Hild. Digital image correlation and fracture: an advanced technique for estimating stress intensity factors of 2d and 3d cracks. *Journal of Physics D: Applied Physics*, 42(21):214004, 2009. (Cited on pages 14 and 132.)

[186] Yousef Saad. *Iterative methods for sparse linear systems*. Siam, 2003. (Cited on page 33.)

[187] M. Saadaoui, P. Reynaud, G. Fantozzi, F. Peronnet, and J.P. Caspar. Slow crack growth study of plaster using the double torsion method. *Ceramics International*, 26(4):435–439, 2000. (Cited on page 110.)

[188] T. Sakagami and S. Kubo. Applications of pulse heating thermography and lock-in thermography to quantitative nondestructive evaluations. *Infrared Physics & Technology*, 43(3):211–218, 2002. (Cited on page 9.)

[189] L. Salvo, P. Cloetens, E. Maire, S. Zabler, J.J. Blandin, J. Y. Buffière, W. Ludwig, E. Boller, D. Bellet, and C. Josserond. X-ray micro-tomography: an attractive characterization technique in materials science. *Nuclear Instruments and Methods in Physics*, 200:273–286, 2003. (Cited on page 2.)

[190] C.G. Sammis and W.F. Ashby. The failure of brittle porous solids under compressive stress states. *Acta Metallurgica*, 34(3):511–26, 1986. (Cited on page 33.)

[191] C. Sandino, P. Kroliczek, D.D. McErlain, and S.K. Boyd. Predicting the permeability of trabecular bone by micro-computed tomography and finite element modeling. *The Journal of Biochemistry*, 47:3129–3134, 2014. (Cited on page 2.)

[192] P.J. Schilling, B.R. Karedla, A.K. Tatiparthi, M.A. Verges, and P.A. Herrington. X-ray computed microtomography of internal damage in fiber reinforced polymer matrix composites. *Composites Science and Technology*, 65(14):2071–2078, 2005. (Cited on page 14.)

[193] A. Schlüter, A. Willenbücher, C. Kuhn, and R. Müller. Phase field approximation of dynamic brittle fracture. *Computational Mechanics*, 54(5):1141–1161, 2014. (Cited on page 7.)

[194] B. Schmidt, F. Fraternali, and M. Ortiz. Eigenfracture: an eigendeformation approach to variational fracture. *Multiscale Modeling & Simulation*, 7(3):1237–1266, 2009. (Cited on page 4.)

[195] H.W. Schreier and M.A. Sutton. Systematic errors in digital image correlation due to undermatched subset shape functions. *Experimental Mechanics*, 42(3):303–310, 2002. (Cited on page 125.)

[196] T.S. Smith, B.K. Bay, and M.M. Rashid. Digital volume correlation including rotational degrees of freedom during minimization. *Experimental Mechanics*, 42(3):272–278, 2002. (Cited on page 132.)

[197] P. Soroushian, M. Elzafraney, and A. Nossoni. Specimen preparation and image processing and analysis techniques for automated quantification of concrete microcracks and voids. *Cement and concrete Research*, 33(12):1949–1962, 2003. (Cited on page 12.)

[198] T.S. Sprague. *X-ray tomography for evaluation of damage in concrete bond*. PhD thesis, University of Washington, 2006. (Cited on page 103.)

[199] S. Stanchits, J. Fortin, Y. Gueguen, and G. Dresen. Initiation and propagation of compaction bands in dry and wet bentheim sandstone. In *Rock Physics and Natural Hazards*, pages 846–868. Springer, 2009. (Cited on page 8.)

[200] S.R. Stock, A. Guvenilir, T.M. Breunig, J.H. Kinney, and M.C. Nichols. Computed tomography part iii: Volumetric, high-resolution x-ray analysis of fatigue crack closure. *JOM*, 47(1):19–23, 1995. (Cited on page 14.)

[201] L. Struble and P. Stutzman. Epoxy impregnation of hardened cement for microstructural characterization. *Journal of Materials Science Letters*, 8(6):632–634, 1989. (Cited on page 10.)

[202] M. Suéry, J. Adrien, C. Landron, S. Terzi, E. Maire, L. Salvo, and J.J. Blandin. Fast in-situ x-ray micro tomography characterisation of microstructural evolution and strain-induced damage in alloys at various temperatures: Dedicated to professor dr. h.-p. degischer on the occasion of his 65th birthday. *International Journal of Materials Research*, 101(9):1080–1088, 2010. (Cited on page 13.)

[203] N. Sukumar and T. Belytschko. Arbitrary branched and intersecting cracks with the extended finite element method. *International Journal for Numerical Methods in Engineering*, 48:1741–1760, 2000. (Cited on page 5.)

[204] N. Sukumar, N. Moës, B. Moran, and T. Belytschko. Extended finite element method for three-dimensional crack modelling. *International Journal for Numerical Methods in Engineering*, 48:1549–1570, 2000. (Cited on page 61.)

[205] Z. Sun, J.S. Lyons, and S.R. McNeill. Measuring microscopic deformations with digital image correlation. *Optics and Lasers in Engineering*, 27(4):409–428, 1997. (Cited on page 10.)

[206] M.A. Sutton, J.J. Orteu, and H. Schreier. *Image correlation for shape, motion and deformation measurements: basic concepts, theory and applications*. Springer Science & Business Media, 2009. (Cited on page 117.)

[207] M.A. Sutton, W.J. Wolters, W.H. Peters, W.F Ranson, and S.R. McNeill. Determination of displacements using an improved digital correlation method. *Image and vision computing*, 1(3):133–139, 1983. (Cited on page 117.)

[208] T. Black T. Belytschko. Elastic crack growth in finite elements with minimal remeshing. *International Advances in Surgical OncologyJournal for Numerical Methods in Engineering*, 45:601–620, 1999. (Cited on page 5.)

[209] C.A. Tang, R.H.C. Wong, K.T. Chau, and P. Lin. Modeling of compression-induced splitting failure in heterogeneous brittle porous solids. *Eng. Frac. Mech.*, 72:597–615, 2005. (Cited on pages xii, 45, 46 and 47.)

[210] N. Triantafyllidis and E.C. Aifantis. A gradient approach to localization of deformation. i. hyperelastic materials. *Journal of Elasticity*, 16(3):225–237, 1986. (Cited on page 3.)

[211] N. Tsafnat, G. Tsafnat, and A.S. Jones. Micro-finite element modelling of oke blends using x-ray microtomography. *Fuel*, 87(13-14):2983–2987, 2008. (Cited on page 2.)

[212] C.C. Tsao and H. Hocheng. Computerized tomography and c-scan for measuring delamination in the drilling of composite materials using various drills. *International Journal of Machine Tools and Manufacture*, 45(11):1282–1287, 2005. (Cited on page 14.)

[213] V. Tvergaard. Model studies of fibre breakage and debonding in a metal reinforced by short fibres. *Journal of the Mechanics and Physics of Solids*, 41(8):1309–1326, 1993. (Cited on page 60.)

[214] V. Tvergaard and J.W. Hutchinson. The influence of plasticity on mixed mode interface toughness. *Journal of the Mechanics and Physics of Solids*, 41(6):1119–1135, 1993. (Cited on page 6.)

[215] S. Vanlanduit, J. Vanherzeele, R. Longo, and P. Guillaume. A digital image correlation method for fatigue test experiments. *Optics and Lasers in Engineering*, 47(3):371–378, 2009. (Cited on page 12.)

[216] G. Ventura, E. Budyn, and T. Belytschko. Vector level-sets for description of propagating cracks in finite elements. *International Journal for Numerical Methods in Engineering.*, 58(10):1571–92, 2003. (Cited on page 5.)

[217] C. Verhoosel and R. de Borst. A phase-field model for cohesive fracture. *International Journal for Numerical Methods in Engineering.*, 96:43–62, 2013. (Cited on page 7.)

[218] C.V. Verhoosel and R. De Borst. A phase-field model for cohesive fracture. *International Journal for numerical methods in Engineering*, 96(1):43–62, 2013. (Cited on pages xiv, 7, 61, 71, 85, 86, 96 and 233.)

[219] E. Verhulp, B. van Rietbergen, and R. Huiskes. A three-dimensional digital image correlation technique for strain measurements in microstructures. *Journal of biomechanics*, 37(9):1313–1320, 2004. (Cited on page 132.)

[220] J. Vignollet, S. May, R. De Borst, and C.V. Verhoosel. Phase-field models for brittle and cohesive fracture. *Meccanica*, 49(11):2587–2601, 2014. (Cited on page 7.)

[221] K. Wan and X. Xue. In situ compressive damage of cement paste characterized by lab source x-ray computer tomography. *Materials Characterization*, 82:32–40, 2013. (Cited on page 102.)

[222] L.L. Wang. micro-mechanical experimental investigation and modelling of strain and damage of argillaceous rocks under combined hydric and mechanical loads. 2012. (Cited on page 12.)

[223] Y.S. Wang, G.Y. Huang, and D. Gross. On the mechanical modeling of functionally graded interfacial zone with a griffith crack: plane deformation. *International journal of fracture*, 125(1):189–205, 2004. (Cited on page 60.)

[224] G.N. Wells and L.J. Sluys. A new method for modelling cohesive cracks using finite elements. *International Journal for Numerical Methods in Engineering*, 50(12):2667–2682, 2001. (Cited on pages xiv, 82, 83 and 84.)

[225] M. Wevers. Listening to the sound of materials: acoustic emission for the analysis of material behaviour. *NDT & E International*, 30(2):99–106, 1997. (Cited on pages 7 and 8.)

[226] P.J. Withers, J. Bennett, Y.C. Hung, and M. Preuss. Crack opening displacements during fatigue crack growth in ti–sic fibre metal matrix composites by x-ray tomography. *Materials science and technology*, 22(9):1052–1058, 2006. (Cited on page 14.)

[227] R.H.C. Wong, P. Lin, and C.A. Tang. Experimental and numerical study on splitting failure of brittle solids containing single pore under uniaxial compression. *Mechanics of Materials*, 38:142–159, 2006. (Cited on page 33.)

[228] P. Wright, X. Fu, I. Sinclair, and S.M. Spearing. Ultra high resolution computed tomography of damage in notched carbon fiberŮepoxy composites. *Journal of Composite Materials*, 42(19):1993–2002, 2008. (Cited on page 14.)

[229] X.-P. Xu and A. Needleman. Numerical simulation of fast crack growth in brittle solids. *Journal of the Mechanics and Physics of Solids*, 42(9):1397–1434, 1994. (Cited on page 6.)

[230] D. Yang, M. Bornert, H. Gharbi, P. Valli, and L.L. Wang. Optimized optical setup for dic in rock mechanics. In *EPJ Web of Conferences*, volume 6, page 22019. EDP Sciences, 2010. (Cited on pages 121 and 125.)

[231] J.T.P. Yao. Damage assessment and reliability evaluation of existing structures. *Engineering Structures*, 1(5):245–251, 1979. (Cited on page 9.)

[232] J. Yvonnet. A fast method for solving microstructural problems defined by digital images: a space lippmann-schwinger scheme. *International Journal for Numerical Methods in Engineering.*, 92(2):178–205, 2012. (Cited on page 2.)

[233] F. Zhou and J.F. Molinari. Dynamic crack propagation with cohesive elements: a methodology to address mesh dependency. *International Journal for Numerical Methods in Engineering.*, 59:1–24, 2004. (Cited on page 6.)

[234] G. Zi, J.H. Song, E. Budyn, S.H. Lee, and T. Belytschko. A method for growing multiple cracks without remeshing and its application to fatigue crack growth. *Modelling and Simulation in Materials Science and Engineering*, 12(5):901, 2004. (Cited on page 5.)